CEA-R-5829(E)

ISSN 0429 - 3460

COMMISSARIAT À L'ÉNERG

INFLUENCE OF THE MAGNETIC FIELD ORIENTATION ON THE MIXED STATE PROPERTIES OF HIGH TEMPERATURE SUPERCONDUCTORS: AN AC SHIELDING STUDY.

par

Beat SCHMIDT

DIRECTION DES SCIENCES DE LA MATIÈRE

DÉPARTEMENT DE RECHERCHE SUR L'ÉTAT CONDENSÉ, LES ATOMES ET LES MOLÉCULES

LABORATOIRE DES SOLIDES IRRADIÉS

CEA / Saclay

DIRECTION DES SCIENCES DE LA MATIÈRE

RAPPORT

DIRECTION DE L'INFORMATION SCIENTIFIQUE ET TECHNIQUE

RAPPORT CEA-R-5829(E)

CEA/SACLAY 91191 GIF-SUR-YVETTE CEDEX FRANCE

1999

Résumé – Ce travail porte sur l'étude de l'influence de l'orientation d'un champ magnétique statique sur les propriétés de l'état mixte des cuprates supraconducteurs à haute température critique. État qui est caractérisé par la présence de vortex (quanta de flux magnétique) dont les propriétés ont été testées via l'approche dynamique de l'écrantage d'un champ magnétique alternatif.
Dans des cristaux purs de $Bi_2Sr_2CaCu_2O_8$, nous avons étudié la transition de premier ordre du système de vortex d'un état ordonné vers un état désordonné. Il s'avère que dans ce matériau la transition est essentiellement déterminée par la composante du champ perpendiculaire aux plans supraconducteurs CuO_2. Cependant, la valeur de cette composante à la transition baisse avec l'application d'un champ parallèle aux plans. Cette diminution s'explique par la suppression du couplage Josephson entre les plans supraconducteurs par la composante parallèle du champ.
Dans des cristaux de $Bi_2Sr_2CaCu_2O_8$ irradiés aux ions lourds, nous avons examiné l'ancrage des vortex par les traces induites par l'irradiation. Ces défauts poussent la ligne d'irréversibilité vers des champs plus élevés. Dans le domaine du diagramme de phase nouvellement irréversible, l'ancrage des vortex par des défauts colonnaires est anisotrope. Cette anisotropie de l'ancrage indique qu'il y a un couplage entre les vortex 2D qui constituent une ligne de vortex, contrairement au comportement dans le matériau non-irradié dans la même gamme de champs.
$HgBa_2Ca_2Cu_3O_8$ avec des défauts colonnaires montre essentiellement le même comportement que $Bi_2Sr_2CaCu_2O_8$, les différences étant bien expliquées par l'anisotropie plus faible de $HgBa_2Ca_2Cu_3O_8$ qui confère aux vortex un caractère plus linéaire.
Finalement, nous avons montré que dans $Bi_2Sr_2CaCu_2O_8$ sans défauts, la concentration des vortex au milieu de l'échantillon est expliquée par la seule barrière de surface.

Summary – This work deals with the influence of the orientation of an applied static magnetic field on the mixed state properties of high temperature superconducting cuprates. The mixed state is characterized by the presence of vortices (quanta of magnetic flux). Their properties have been tested via the dynamic approach of the shielding of an ac magnetic field.
In pristine $Bi_2Sr_2CaCu_2O_8$ crystals the first order transition of the vortex system from an ordered to a disordered state has been studied. It has been found that in this material the transition is mainly determined by the component of the field perpendicular to the superconducting copper oxide layers. However, the value of this component at the transition diminishes with the increase of the field component parallel to the layers. This is explained by the decrease of the Josephson coupling between 2D vortices in neighbouring planes in the presence of a parallel component.
In heavy ion irradiated $Bi_2Sr_2CaCu_2O_8$ the subject under investigation has been the pinning of the vortices by the irradiation tracks. These defects push the irreversibility line towards higher fields. In the field range that has become irreversible after irradiation pinning by columnar defects is anisotropic. This anisotropy in pinning indicates that a coupling exists between the 2D vortices that form a vortex line, in contrast to the behaviour in the pristine material in the same field range.
$HgBa_2Ca_2Cu_3O_8$ with columnar defects shows essentially the same behaviour as $Bi_2Sr_2CaCu_2O_8$, the differences beeing well explained by the lower anisotropy of $HgBa_2Ca_2Cu_3O_8$ which leads to a more linear character of the vortices.
Finally, it has been shown that in pristine $Bi_2Sr_2CaCu_2O_8$ the concentration of the vortices in the center of the sample is explained by the surface barrier alone.

Thèse présentée pour obtenir le grade de

DOCTEUR DE L'ÉCOLE POLYTECHNIQUE

Spécialité : **Physique du Solide**

par

Beat SCHMIDT

INFLUENCE OF THE MAGNETIC FIELD ORIENTATION ON THE MIXED STATE PROPERTIES OF HIGH TEMPERATURE SUPERCONDUCTORS: AN AC SHIELDING STUDY

Soutenue le 15/9/1998 devant le jury composé de :

Monsieur	John Gilchrist	Président
Madame	Hélène Raffy	Rapporteur
Monsieur	Johann Blatter	Rapporteur
Monsieur	Yves Quéré	Examinateur
Monsieur	Marcin Konczykowski	Examinateur

- Rapport CEA-R-5829(E) -

CEA Saclay
Direction des Sciences de la Matière
Département de Recherche sur l'Etat Condensé, les Atomes et les Molécules
Laboratoire des Solides Irradiés

INFLUENCE OF THE MAGNETIC FIELD ORIENTATION ON THE MIXED STATE PROPERTIES OF HIGH TEMPERATURE SUPERCONDUCTORS : AN AC SHIELDING STUDY.

par

Beat SCHMIDT

- Janvier 1999 -

Remerciements

Cette thèse a été réalisée au Laboratoire des Solides Irradiés (CEA/DSM/DRECAM). Je remercie Monsieur Charles-Henri DE NOVION de m'y avoir accueilli lorsqu'il en était le Directeur.

Mes remerciements les plus sincères vont à John GILCHRIST de m'avoir fait l'honneur de présider le jury.

Madame Hélène RAFFY et Monsieur Johann BLATTER ont bien voulu prêter attention à cette recherche en assumant la tâche de rapporteurs. Je leur adresse mes plus sincères remerciements.

Je tiens à exprimer ma profonde gratitude à l'égard de Monsieur Yves QUÉRÉ qui a accepté de diriger ce travail de thèse et de faire partie du jury de soutenance.

Mes remerciements vont aussi à Monsieur Marcin KONCZYKOWSKI pour ses conseils concernant le dispositif expérimental, pour le fait qu'il m'ait permis à plusieures occasions de présenter mes résultats à la communauté scientifique internationale et pour avoir fait partie du jury.

Je suis redevable à Monsieur Kees VAN DER BEEK pour le temps qu'il a consacré à la relecture de ce mémoire. Ses critiques et ses conseils m'ont été indispensables.

Il m'est très agréable de remercier ici Monsieur Patrick LAPLACE pour son amitié et pour son aide technique au début de ma thèse. Je lui dois le cryostat utilisé dans le dispositif expérimental, sans compter le montage du moteur pas à pas.

Je tiens également à adresser mes remerciements à Serge BOUFFARD pour son assistance lors des irradiations au GANIL.

Je suis très heureux de remercier Monsieur Stéphane BERRY pour l'intérêt qu'il a porté à ce travail et pour son aide lors de la rédaction de ce manuscrit.

L'amitié et l'appui que m'ont accordé les THÉSARDS et STAGIAIRES m'ont profondément touché. Ils ont su créer un climat de solidarité que j'ai beaucoup apprécié lors des moments difficiles.

Finalement, j'aimerais remercier toutes les personnes qui m'ont fait un accueil chaleureux, facilitant mon installation en France.

Contents

1 Introduction **3**
- 1.1 Vortices and defects in type II superconductors . . . 3
- 1.2 The cuprate high temperature superconductors . . . 5
- 1.3 The $Bi_2Sr_2CaCu_2O_8$ compound . . . 6
- 1.4 The $HgBa_2Ca_2Cu_3O_8$ compound . . . 7

2 The ac shielding technique **9**
- 2.1 Introduction . . . 9
- 2.2 Apparatus description . . . 11
- 2.3 ac response of a type II superconductor . . . 13
- 2.4 Irreversibility line . . . 14
- 2.5 Modeling the signal detection . . . 18
- 2.6 Modeling the sample response . . . 20
  - 2.6.1 Ohmic response . . . 20
  - 2.6.2 The critical state model . . . 21
  - 2.6.3 Surface barrier . . . 24
  - 2.6.4 Flux creep . . . 26
- 2.7 Data analysis . . . 27
  - 2.7.1 Basic procedure . . . 27
  - 2.7.2 Shielding current . . . 28
  - 2.7.3 Angular variation . . . 28
  - 2.7.4 Onset of magnetic irreversibility . . . 30

3 Vortex lattice phase transition in pure $Bi_2Sr_2CaCu_2O_8$ **31**
- 3.1 Introduction . . . 31
- 3.2 Experimental details . . . 34
- 3.3 Results . . . 36
  - 3.3.1 Original data . . . 36
  - 3.3.2 Analysis of the paramagnetic peak . . . 39
  - 3.3.3 Peak position . . . 41
  - 3.3.4 Peak width . . . 46
  - 3.3.5 Peak height . . . 48
  - 3.3.6 Step at the peak position . . . 51

3.3.7 Irreversibility line . . . 52
3.3.8 Further observations . . . 52
3.4 Discussion . . . 54
3.5 Conclusions . . . 57

4 Anisotropy of pinning by columnar defects in $Bi_2Sr_2CaCu_2O_8$ 59
4.1 Introduction . . . 59
4.2 Experimental details . . . 66
4.2.1 Method . . . 66
4.2.2 Sample preparation . . . 67
4.3 Results . . . 69
4.3.1 Temperature dependence of the transmittivity . . . 69
4.3.2 Irreversibility line . . . 73
4.3.3 Angular dependence of the transmittivity . . . 76
4.4 Discussion . . . 84
4.5 Conclusions . . . 89

5 Anisotropy of pinning by columnar defects in $HgBa_2Ca_2Cu_3O_{8+\delta}$ 91
5.1 Introduction . . . 91
5.2 Experimental details . . . 91
5.3 Results . . . 92
5.3.1 Temperature dependence of the transmittivity . . . 92
5.3.2 Irreversibility line . . . 97
5.3.3 Angular dependence of the transmittivity . . . 99
5.3.4 Frequency dependence of the transmittivity . . . 101
5.4 Discussion . . . 103
5.5 Conclusions . . . 105

6 Angular dependence of the surface barrier in $Bi_2Sr_2CaCu_2O_8$ 107
6.1 Introduction . . . 107
6.2 Experimental details . . . 108
6.3 Results . . . 109
6.3.1 Influence of ac frequency and amplitude . . . 109
6.3.2 Polar plots of the third harmonic . . . 111
6.4 Discussion . . . 114
6.5 Conclusions . . . 118

7 General conclusions 121

Bibliography 123

A Other work 133

Chapter 1

Introduction

1.1 Vortices and defects in type II superconductors

The cuprate family of high temperature superconductors (HTSC) are type II superconductors which means that a large part of their field–temperature (H–T) phase diagram is occupied by the *mixed* state. In this state the magnetic induction B inside the material is not homogeneous, rather the field penetrates the material in the form of vortices, i.e., flux threads encircled by shielding currents. Each such vortex contains the same amount of magnetic flux, $\Phi_0 = h/2e = 2.07 \times 10^{-15}$ Wb, the flux quantum. The core of the vortex of size ξ, the coherence length, is in the normal state. The shielding currents outside this core as well as the magnetic induction decay exponentially over a characteristic length scale λ, the penetration depth. Vortices of the same orientation have a repulsive mutual interaction which makes them form a hexagonal lattice at low temperatures. At high temperatures on the other hand, thermal fluctuations of the vortices destroy the long range order of the lattice and the time average of the phase of the order parameter vanishes. Thus, two phases of the vortex system can be distinguished: the *vortex solid*, with a long range ordering of vortices, and the *vortex liquid*, in which the long range order is destroyed. A first order phase transition line separates the two regions in the H–T phase diagram (Brézin et al. 1985).

Another source of disorder in the vortex system are defects in the material. Defects are preferential locations for the vortex core because in that position the normal volume due to the defect overlaps the normal volume inside the vortex core. The energy with respect to a vortex core remaining outside the defect is lowered by the gain in core condensation energy. A force results that pins the vortex on the defect, the *pinning force*. This pinning force competes with the interaction force between vortices and tends to destroy the long range order in the solid phase, because of the random spatial distribution of the defects.

However, more important for applications is the impact of the defects on the

dynamic properties of the superconductor. An external current of density j, injected into the superconductor, generates a (Lorentz) force $\mathbf{F}_L = \mathbf{j} \times \mathbf{B}$ on the vortices which makes them move perpendicular to the current direction. This motion leads to an electric field $\mathcal{E}$ along the current path and thereby to a finite linear resistivity $\rho = \mathcal{E}/j$. This is detrimental for applications. The vortex motion is hindered though, by the pinning force of the defects. Pointlike defects are always present in the material but the pinning force of extended defects is usually much higher because the energy gain due to pinning grows linearly with the length over which the vortex is pinned.

Linear extended defects are conveniently introduced in a material by irradiating it with swift heavy ions (Groult et al. 1988). Typical ions used for the irradiation are lead (Pb) (Hardy et al. 1991; Konczykowski et al. 1991), uranium (U) (Simon et al. 1996), xenon (Xe) (Bourgault et al. 1989), iodine (I) (Gerhäuser et al. 1991), tin (Sn) (Civale et al. 1991) and gold (Au) (Krusin-Elbaum et al. 1994) with energies varying from 0.5 to 6 GeV. At an optimum energy such an irradiation creates continuous linear tracks of amorphous material with a diameter of about 8 nm depending on the ion and the material (Simon et al. 1996). This diameter is comparable to the core size of a vortex and therefore optimum to create the largest possible pinning force.

In fact, liberating a vortex from such a linear defect requires the expense of a considerable amount of energy. Only at current densities close to the pair-breaking current density can the Lorentz force overcome the pinning force and the vortices flow freely ("flux flow"). However, at non-zero temperatures thermal fluctuations give rise to a certain depinning probability of the vortices. Consequently, thermally activated motion, or *creep*, of vortices between pinning sites takes place (Anderson 1962). Nevertheless, the useful field range of the material is drastically enhanced.

The presence of columnar defects also considerably changes the equilibrium properties of the vortex system. Due to strong pinning the vortex lattice is not stable and will transform into a glassy phase in which the long range order is absent. Theoretically a vortex in a superconductor containing columnar defects can be mapped onto a two-dimensional particle on a randomly disordered substrate. The vortex system is then found to be similar to a system of 2D bosons. For this reason the glassy phase in the vortex system is called *Bose glass* (Nelson and Vinokur 1993). The localizing effect of the columns extends deep into the liquid phase, reducing the thermal fluctuations of the vortices, so that the Bose glass phase occupies a much larger part of the phase diagram than previously the solid phase. The first order melting transition line is replaced by a second order Bose glass transition line.

1.2 The cuprate high temperature superconductors

With respect to the "conventional" superconductors, which are for the greater part metals or alloys, the cuprates have a much more complex structure. They are layered compounds in which superconducting copper oxide planes are separated by insulating planes of variable composition. This layered structure leads in the normal state to a conductivity that is metallic in the layers but can be semiconducting perpendicular to them (Kadowaki et al. 1990). The electric behaviour is therefore very anisotropic with a sometimes huge ratio $\Gamma = M/m$ of the charge carrier effective masses perpendicular (M) and parallel (m) to the copper oxide planes. This anisotropy is also reflected in the parameters of the superconducting state: penetration depth λ and coherence length ξ in the two main directions differ by a factor $\gamma = \sqrt{M/m}$: $\lambda_{ab} = \lambda_c/\gamma$ and $\xi_c = \xi_{ab}/\gamma$, where the subscript ab marks the quantities in the plane and the subscript c those perpendicular to the plane. This anisotropy changes the description of the vortex state profoundly. While for moderate anisotropies an adaptation of the Ginzburg-Landau theory is possible and the vortices can still be treated as continuous objects, the strongly layered case has to be described by the Lawrence-Doniach model (Lawrence and Doniach 1971), in which the superconducting layers are coupled by the Josephson effect. In the latter case a vortex oriented perpendicular to the planes is not a continuous object but is formed out of a stack of 2 dimensional ("pancake") vortices weakly bound by magnetic (Clem 1991) and Josephson coupling (Feigel'man et al. 1990; Vinokur et al. 1990). The interaction between two pancake vortices in neighbouring layers is mainly magnetic for lateral separations less than the Josephson length $\Lambda_J = \gamma s$ with s the spacing between superconducting layers. Only at larger separations have the Josephson currents between the layers fully developed and dominate the coupling (Feigel'man et al. 1990).

A magnetic field component parallel to the layers penetrates the sample in the form of Josephson vortices. This type of vortex does not have a normal core since they traverse the sample in the insulating space between the superconducting layers which is already "normal". Perpendicular to the layers the Josephson vortices are confined by the strong currents flowing in the layers and extend a distance λ in that direction. Across the layers on the other hand, the shielding is done by the much weaker Josephson currents and the extent of the vortex along the layers is much bigger, namely $\gamma\lambda$.

In strongly layered materials thermal fluctuations can lead to the breakdown of the phase coherence perpendicular to the layers and thus of the Josephson coupling (Glazman and Koshelev 1991). The field component perpendicular to the layers then leads to a set of nearly independent pancake vortices. A field component parallel to the layers on the other hand would penetrate freely into the space between the layers.

From the above it is clear that the behaviour of the vortex system might strongly

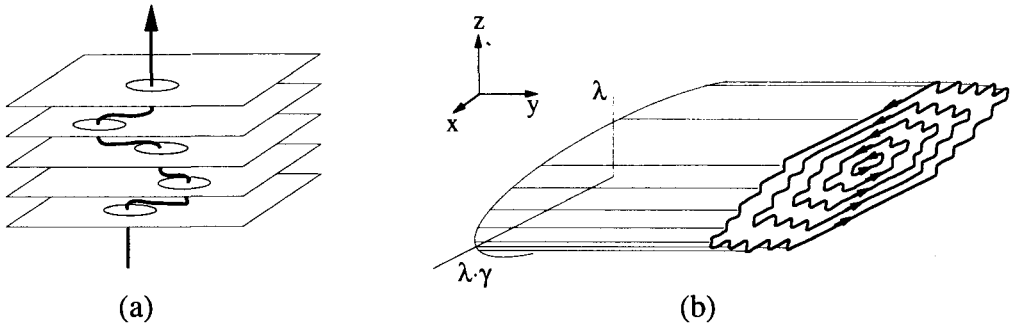

Figure 1.1: Effect of the layered structure of the cuprates on the vortices: (a) a field component perpendicular to the superconducting planes creates a stack of 2-dimensional (pancake) vortices. (b) a field component parallel to the layers penetrates in the form of a Josephson vortex.

depend on its orientation with respect to the layer structure of the material. This dependence will be studied on the example of the first order transition of the vortex matter in the absence of pinning.

The introduction of columnar defects introduces an additional anisotropy in the material. Its influence on the shielding of an ac field will be investigated as well.

1.3 The $Bi_2Sr_2CaCu_2O_8$ compound

This compound is particularly interesting because of its huge anisotropy which makes the vortices much softer (the line tension ε_1 is small) and therefore increases the importance of thermal fluctuations. As a result the vortex liquid occupies a large part of the phase diagram.

The single crystals of this compound were grown by the *travelling solvent floating zone* (TSFZ) technique in which a precursor rod of the $Bi_2Sr_2CaCu_2O_8$ material ("the feed") is zone melted under well defined atmospheric conditions. The melted zone then crystallizes while it is advanced along the precursor. The TSFZ method has the advantage that no crucible is needed. Moreover, the growth parameters are easily controlled.

The crystal structure of Bi-2212 is shown on the left hand side of Fig. 1.2. The stoichiometry $Bi_2Sr_2CaCu_2O_8$ is a theoretical one and deviations occur in the contents of Bi, Sr, Ca as well as oxygen. The latter is often reflected in the notation $Bi_2Sr_2CaCu_2O_{8+\delta}$. The contents in Bi, Sr, and Ca depend on the oxygen partial pressure during growth (Li 1995). Table 1.1 shows the respective contents for three values of the oxygen partial pressure. As can be seen from table 1.1, the highest T_c is obtained in 200 kPa pressure. The growth in elevated oxygen pressure leads to a strong increase in the Sr/Ca ratio. Taken account of the larger radius of the Sr^{2+} (0.118 nm) ion as compared to Ca^{2+} (0.100 nm) a continuous increase of the

Table 1.1: Composition of Bi-2212 single crystals grown in different oxygen pressures (from Li (1995))

Oxygen Partial Pressure	22 kPa [Air]	200 kPa	300 kPa
Bi	2.16	2.17	2.18
Sr	1.91	2.03	2.06
Ca	1.03	1.00	0.98
Cu	2.00	2.00	2.00
Sr/Ca	1.85	2.03	2.10
T_c	88	95	91
Lattice Parameters			
a [nm]	0.382	0.383	0.382
c [nm]	3.072	3.084	3.078

c-axis lattice parameter is expected. However, the enhanced oxygen pressure might lead to the incorporation of more additional oxygen ions, leading to the contraction of the Bi–O layers and thus to the reduction of the c-axis lattice parameter. The doping character of the oxygen ions would then lead to the change in T_c.

Anisotropies γ that have been measured on single crystals grown by the TSFZ method attained values >150 at $T = 77.4$ K and 0.2 T< B < 1.4 T for a crystal with a T_c of 85 K (Martinez et al. 1992) and ≈ 700 at temperatures $T \leq 20$ K and inductions $B \leq 0.15$ T for a crystal with a T_c of 91 K (Nakamura et al. 1993). This last value has been strongly contested though (Indenbom and Brandt 1994).

1.4 The $HgBa_2Ca_2Cu_3O_8$ compound

This compound is somewhat less anisotropic than Bi-2212, with an anisotropy parameter $\gamma = 52$ (Vulcanescu et al. 1996). However, its transition temperature of up to 135 K is much higher than that of Bi-2212 and is actually the highest T_c know up to date. This makes this material particularly interesting for studies in a nitrogen cryostat as used in the present work, since the superconducting transition is not easily suppressed below the working range of the cryostat by applying a strong dc field ($\approx$ 1 T).

Hg-1223 is grown by an amalgamating based synthesis method (Bertinotti et al. 1997). In this method two reactant pellets containing all the necessary elements in the correct proportions are placed next to a third precursor pellet that contains no mercury. A gold foil wrapped around these pellets serves as the amalgamating agent. During the temperature increase in the following heat treatment the gold foil absorbs the mercury vapour at temperatures below 500°C and desorps it at the higher temperature ($\approx$ 600°C) at which the Hg-1223 crystals are grown. This effect of the gold foil is crucial since it limits the formation of the parasitic phase $CaHgO_2$ at 500–550°C before the superconducting phase forms.

$HgBa_2Ca_2Cu_3O_8$ is a member of a whole family of mercury-based compound with the composition $HgBa_2Ca_{n-1}Cu_nO_{2n+2}$. The different compounds vary in the number of copper oxide planes (equal to n). Hg-1223 has three such layers per unit cell. However, during crystal growth the number of copper oxide planes is difficult to control and intergrowth of the bilayer or the monolayer compound is common.

As grown crystals of Hg-1223 usually have a (resistively determined) T_c of about 126 K. A higher T_c can be obtained by annealing the crystals in oxygen. It seems though, that the oxygen diffusion is very slow and the T_c is changed in a region near the surface only.

The crystal structure of Hg-1223 is shown on the right hand side of Fig. 1.2.

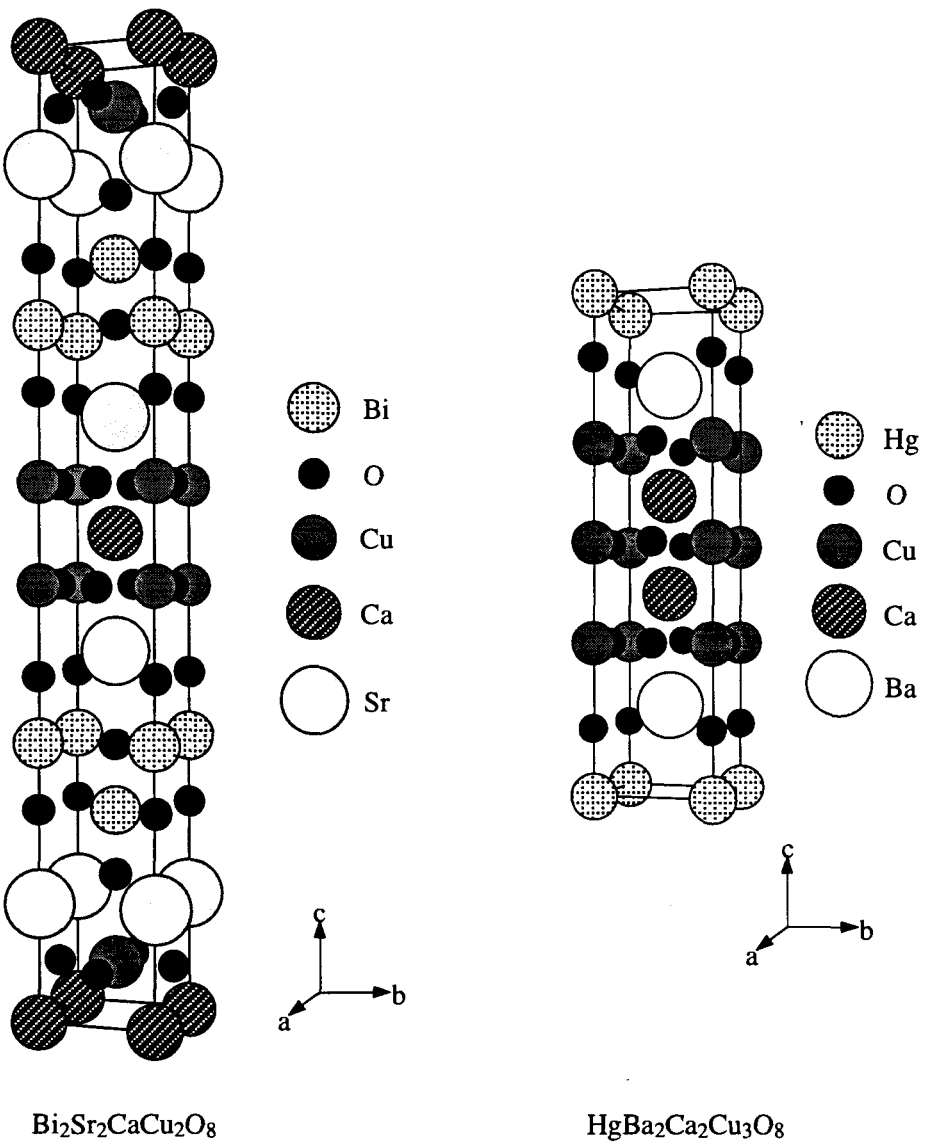

Figure 1.2: Crystal structures of $Bi_2Sr_2CaCu_2O_8$ and $HgBa_2Ca_2Cu_3O_8$.

Chapter 2

The ac shielding technique

2.1 Introduction

For all the studies presented in this work one single technique has been used which is a variation on the long known mutual inductance measurement (Kürti and Simon 1935) and which we shall henceforth call the ac shielding technique. In contrast to the usual mutual inductance technique where a pick-up coil near the sample serves to detect the flux threading the latter, a miniature Hall sensor is used in our set-up (Konczykowski et al. 1991). Mutual inductance measurements have the advantage of being a contact-free method of material analysis. Moreover, using a Hall probe for detection allows one to use very small samples. Both these facts are highly welcome for the study of the cuprate superconductors. Not only are HTSC single crystals usually tiny, but crystals of some of the cuprate materials are also very brittle, making it difficult to attach electric contacts. These advantages should of course be very useful for the analysis of other types of material, too.

In contrast to the signal from a pick-up coil which is proportional to $-\partial B/\partial t$, the time derivative of the magnetic induction B, the signal from a Hall probe measures the induction directly and "locally". The meaning of local measurements becomes apparent when we consider the active surface of Hall sensors, which are typically 100×80 μm^2 for the InSb Hall probe, but recent 2-dimensional electron gas Hall sensors have active surfaces as small as 3×3 μm^2.

A second advantage of the Hall sensors is that the signal strength is independent of the frequency of the ac field. The frequency can be chosen arbitrarily low, including dc fields.

The applied periodic magnetic field is accompanied by a periodic electric field whose amplitude is proportional to the rate of change of the magnetic field (and which is actually detected by a pick-up coil). Let us consider what voltage drop ΔV would be induced across the sample by the ac field. It is given by

$$\Delta V = -\frac{\mathrm{d}\phi}{\mathrm{d}t} = -\frac{\mathrm{d}B}{\mathrm{d}t}S = -\mu_0\frac{\mathrm{d}H}{\mathrm{d}t}S \tag{2.1}$$

where ϕ is the flux threading the sample surface S which is typically of the order of 500×500 μm (but might be much smaller). H is the magnetic field. For ac frequencies and amplitudes $0.8 < f < 2400$ Hz and $80 < h_{ac} < 1600$ A/m (1 to 20 Oe), and the above mentioned sample size we obtain values for the voltage drop ranging between $2\ 10^{-11}$ and 10^{-6} V. These values are lower than what can usually be reached in transport measurements (10^{-9} V). When interpreted in terms of electric field and current density the measurement performed with the ac Hall probe technique is in fact that of a Siemensmeter: frequency and amplitude of the applied ac field fix the electric field, and the shielding current density is obtained from the transmitted field.

The "applied" electric field exerts a force on the charge carriers in the sample, giving rise to a shielding current. This current will in its turn create a magnetic field opposed to the applied ac field and thus (by Lenz' law) alter the field detected by the Hall sensor with respect to the applied field. If the velocity of the carriers is proportional to the electric field the detected induction will have the same time dependence as the applied field exhibiting a phase shift if the shielding current leads to energy dissipation in the sample. If the carrier response to the induced electric field is non-linear, then the time dependence of the detected field will deviate from that of the applied ac field and contain higher harmonics.

The presence of a sample is reflected directly in the curve of local induction versus applied ac magnetic field or magnetization versus ac magnetic field. This is illustrated in Fig. 2.1. Without a sample B equals H and the curve lies on the bisector of the B–H diagram. A response of the charge carriers in the sample will lead to a superposed magnetization and therefore change this curve. If there is a phase lag due to a finite resistivity the loop will open and the sample displays magnetically irreversible (hysteretic) behaviour. The surface of the loop is a measure of the losses in the sample. In the case of Ohmic (linear) response the hysteresis loop is just an ellipse. If the response is non-linear, the shape will deviate from the ellipsoidal form, reflecting the presence of higher harmonics in the magnetic field created by the sample. More specifically, the existence of a critical current I_c leads to a parallelogrammatic hysteresis loop, as shown on the right hand side of Fig. 2.1.

The higher harmonics as well as the fundamental can be obtained from the total Hall voltage by means of a lock-in amplifier. The dc voltages delivered by a two-phase lock-in can be regarded as the coefficients of the real and imaginary parts of one Fourier component of the signal. Modern digital lock-ins are able to compute cosine and sine functions at any multiple of a given reference frequency and thus allow the straightforward extraction of higher harmonics. In our experiment usually only the first and third harmonic components are retained. The first because its real part (usually called in-phase component) tells us how strong the shielding is, while its imaginary part (quadrature component) is a measure of the losses in the sample. The temperature or dc field dependence of the third harmonic on the other hand allows

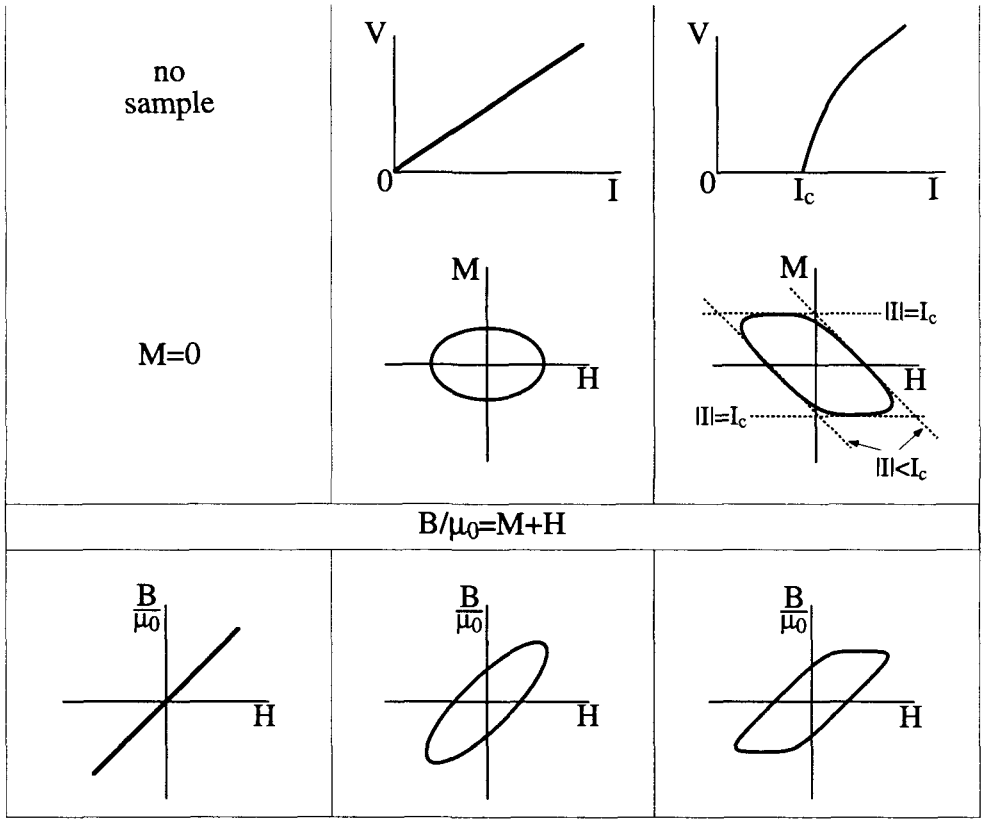

Figure 2.1: From top to bottom: I–V characteristics and corresponding magnetization versus magnetic field (M–H) and induction versus magnetic field (B–H) loop, respectively. From left to right: no sample, linear response, nonlinear response. Linear response: the elliptical shape of the loop is due to a phase shift. For a slow variation of the magnetic field, this phase shift will vanish and B will be proportional to H as in the absence of a sample. Nonlinear response: the magnetization is limited by the value of the critical current. This leads to a non-elliptical shape and to higher harmonics in the induction.

for a precise determination of the onset of non-linear and magnetically irreversible behaviour as a function of those variables, and so to trace the irreversibility line in the H–T diagram that separates the irreversible from the reversible region.

2.2 Apparatus description

Figure 2.2 gives a schematic description of sample and Hall probe together with the approximate dimensions of the sensor. A tiny slab shaped crystal of InSb, a narrow gap semiconductor, is used as Hall effect field probe. The InSb crystals usually have a length of 400-500 μm, while their width and thickness are 100 and 80 μm respectively. 20 μm-thick gold wires are attached to the ends and to two of the long sides by spot welding. The resulting active volume is approximately

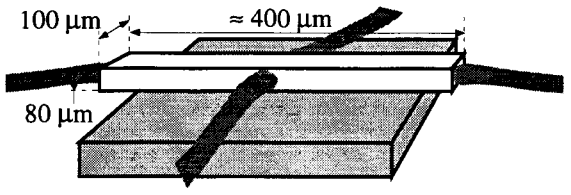

Figure 2.2: Schematic illustration of a sample with the Hall sensor on top of it. Current and voltage leads leaving the sensor are sketched as well.

$100\times80\times80$ μm^3. The two leads attached to the long sides are connected to two lock-in amplifiers in order to measure the ac Hall voltage. The first is an analog lock-in amplifier and is used to trace the fundamental component in the sample response. After an initial filtering stage that eliminates higher harmonics this lock-in uses square wave detection to extract the component at the reference frequency. A digital lock-in traces the third harmonic component. The incoming signal is digitized and then multiplied directly with a cosine or sine function at three times the reference frequency.

The InSb Hall probe is glued with General Electric varnish directly on a beryllium oxide substrate and is protected by a mica sheet onto which the sample is put. The beryllium oxide is fixed within a small coil used to generate the ac field, in such a way that the top surface of the Hall bar is perpendicular to the ac field. Coil and substrate are glued into a hole drilled into a copper support which is in contact with the nitrogen reservoir of the cryostat. The beryllium oxide ensures a good thermal contact between the sample and the copper support.

A double wall encloses this copper cold finger. The first delimits the sample space which is filled with helium gas for better thermalization and the second forms an isolation space. The whole set-up is placed between the pole caps of an electromagnet such that the sample is centered between the two poles.

The electromagnet is mounted onto a rotating table, powered by a computer controlled stepping motor with an angular precision of 1/1000 of a degree. The motor has a mechanical zero position which allows for a high reproducibility of the angular scans. Rotation speed and acceleration of the motor were adapted so as to avoid any loss of precision due to inertness of the magnet which weighs about 450 kg.

Temperature measurement is performed with platinum sensors placed onto the sample holder. The finite distance between sample and sensor might result in a slight error in the temperature measurement. Temperature is therefore continuously controlled by using a twisted heater wire wound around the sample holder. In this manner a temperature stability of about 0.05 K was obtained.

The variable parameters of our experiment are: the temperature, the frequency and amplitude of the ac field, and the orientation and strength of the dc field.

The typical configuration of the fields with respect to the sample is the following:

the ac field is always parallel to the c-axis of the HTSC single crystals, while the dc-field can have any orientation between c-axis and ab-plane (see Fig. 2.3). Usually

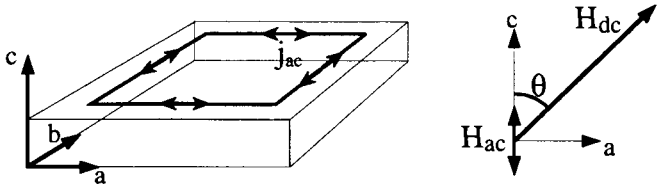

Figure 2.3: Crystal axes and orientations of ac and dc field with respect to them. Also shown: induced ac current j_{ac} in the sample.

the sample was placed such that one of its sides was parallel to the rotation plane of the dc field (as in Fig. 2.3).

The above configuration of fields has been chosen because one usually wishes to measure the characteristics of currents flowing in the ab-plane of the crystal. It is often quite difficult to put the samples on one of the sides in order to have the ac field parallel to the ab-plane, because high quality single crystals are usually very thin and may contain intergrowth leading to a c-axis mosaic.

For the measurement process an ac voltage is applied to the excitation coil. This sinusoidal signal is provided by the internal signal generator of the SR 830 lock-in amplifier. Typical amplitudes varied between 1 and 5 Vrms giving ac field amplitudes from 80 to 560 A/m (1 to 7 Oe). In some cases the signal was pre-amplified by a factor 3 which resulted in ac amplitudes of up to 1600 A/m (20 Oe). The corresponding current in the excitation coil was about 93 mA. The frequency could be chosen in the range from 0.8 to approximately 2400 Hz, the upper limit being given by inductive coupling between the excitation coil circuit and the Hall probe leads. The lower limit is set by the signal generator. Typical currents in the Hall sensor were 0.3 or 0.5 mA. For a current of 0.3 mA the sensitivity was approximately 15 μV/G which corresponds to a change of the Hall resistivity per Gauss of the order of 50 mΩ/G. If we estimate the distance between sample and Hall probe to be about 50 μm then the field created by the Hall probe current at the sample surface would be $H = I/2\pi r = 1.6$ Am^{-1} $= 0.02$ Oe. This can clearly be neglected and the limitations of the Hall probe current are rather due to heating effects.

2.3 ac response of a type II superconductor

As mentioned above, the sample is subject to two fields, an ac field along the c-axis and a dc field forming a well-defined angle with the c-axis. In case the sample is a high temperature superconducting single crystal, it will be mounted such that the ac field induces a shielding current j in the ab-plane, while the dc field creates a certain density $n_\phi = B/\Phi_0$ of vortices.

The shielding current on the sample surface acts on the vortices with a force per unit volume $F = j \times B$ (the Lorentz force). The force may lead to vortex motion with velocity v_ϕ, which causes an electric field $E = v_\phi \times B$ to appear. Vortices are pushed into the sample, thereby disturbing the equilibrium vortex distribution. The new non-equilibrium distribution mediates the further penetration of the ac field and the shielding current. Vortices are not accelerated freely, rather their motion is subject to a friction force $F = -\eta v_\phi$, arising from the motion of the charge carriers in the vortex core. It is the motion of the normal core that gives rise to a non-zero resistivity $\rho_{FF} = B^2/\eta$ and energy dissipation via Joule heating. The dissipated power is given by $P = \eta v_\phi^2 = E^2/\rho_{FF}$. The shielding current in an ac experiment will be limited to values $|j| < \frac{h_{ac}f}{\rho_{FF}}d$ (with d the dimension of the sample).

Defects in the material exert a pinning force F_p on the vortices which counteracts the Lorentz force. In the absence of thermal or quantum motion, vortices will not move until the critical current $j_c = F_p/B$ is reached. Hence, the resistivity for $j < j_c$ will be zero, while it will be equal to the flux-flow resistivity ρ_{FF} for $j > j_c$. In the presence of thermally activated or quantum motion of the vortices, the vortex velocity for $j < j_c$ will not be zero, but will still be exponentially small with respect to ρ_{FF}. The electric field generated by vortex motion will thus also be exponentially small for $j < j_c$. Thus, pinning lowers the resistivity. In an ac or dc magnetic experiment, the induced shielding current will therefore be increased for a given applied electric field $E \propto h_{ac}f$ (or $\propto \partial H/\partial t$). Changing the frequency of the applied field will change the effective applied electric field, e.g., a lower frequency will correspond to a lower electric field, and therefore to a lower induced current. The shielding current will therefore appear to depend on time. If one were to apply a static field at a given rate, and then stop the field ramp, the shielding current would truly diminish with time due to Joule heating.

2.4 Irreversibility line

The temperature and field dependence of the induced shielding current as a result of the T,B dependence of ρ, leads to the notion of an "irreversibility line" in the (B,T) diagram of the superconductor. It is the line below which the shielding current is measurable with a given apparatus, while above it the shielding current is unmeasurably small. For instance, in a magnetization experiment the shielding current cannot be measured any more when the difference in magnetization between increasing and decreasing field at constant temperature falls below the instrumental resolution. The frequency and ac amplitude dependence of the shielding current implies that the irreversibility line will also depend on these parameters, which are related to the experimental apparatus rather than to the sample under study. This is undesirable. We therefore chose another criterion to define an irreversibility line, which is intimately related to the transport properties of the sample: the irreversibility line will be defined as that set of temperatures (fields) below which

the ac response becomes nonlinear due to the appearance of a nonlinear $I(V)$ curve and a "true critical current". The onset of nonlinearity will be probed by measuring the third harmonic susceptibility. Care has to be taken however, to chose the ac excitation as low as possible, since the situation might occur that the response is linear at sufficiently low electric fields, but is nonlinear otherwise (see Fig. 2.4). It is necessary to distinguish this case from that of a E–j curve which is nonlinear at all driving fields. This can be done accurately only at low driving fields, as will be explained in more detail below.

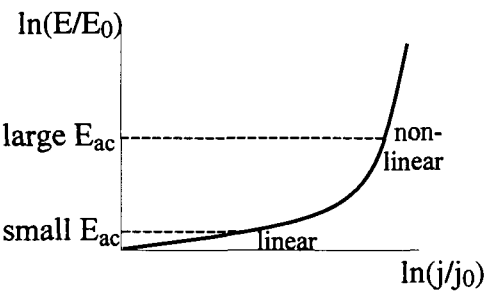

Figure 2.4: Depending on the electric field E_{ac} induced by the ac magnetic field the response can be either nonlinear at the higher value, or linear at the lower value.

The physical origin of the crossover from linear to nonlinear ac response lies in the effect of the pinning centers, which is expected to lead to a second order phase transition. The low temperature phase depends on the defect type. For point defects a vortex glass phase should occur (Fisher 1989), while columnar defects are expected to lead to the Bose glass phase (Nelson and Vinokur 1993). Model E–J curves for the case of a second order phase transition are shown in Fig. 2.5. T_{Ohm} indicates the temperature above which the voltage–current characteristics are linear at all currents. This is the (thermally assisted) flux flow regime. Below this temperature (but above another temperature T_g) the curves are expected to be linear at low driving currents, but to turn into a power-law at elevated currents, a behaviour characteristic of thermally activated flux motion. Only at a lower temperature T_g does the linear part disappear completely, i.e., below this temperature there is no linear dc resistivity, for arbitrary small current. This means that thermal fluctuations alone are not sufficient any more to unpin the vortices, which become truly pinned. This temperature would therefore indicate the transition of the vortex system into a glassy state. For such a second order transition critical regions exists above and below the transition temperature T_g. According to the scaling laws for critical phenomena the I–V curves in these regions can be scaled onto two universal curves. The transition temperature T_g separates between the two sets of curves.

How to detect this transition temperature experimentally? In principle it is possible to trace the whole set of I–V curves for each field value from transport measurements. However, this is a very time consuming way to find T_g and therefore

not practicable. An approximate value for T_g can be found in transport measurement by checking the voltage–current characteristic for the disappearance of linear behaviour. If this is done at low driving currents, a good approximation should be obtained. However, the difficulty in this type of experiment is that very low voltages have to be measured, that may easily fall below the resolution of the best voltmeters.

The other possibility, which has been adopted in this work, is to determine the onset of higher harmonic generation. At sufficiently low frequency and ac field amplitude the onset temperature is expected to lie very close to T_g (Deak et al. 1994). The method is illustrated at the bottom of Fig. 2.6. The maximum electric field is fixed by ac amplitude h_{ac} and frequency ω. The arrow marks the point where non-linear response sets in on lowering the temperature. The figure also shows how the maximum shielding current varies when the frequency ω (or the amplitude) of the ac field is changed. In the linear (ohmic) regime this induces a rather strong variation in the shielding current. In the strongly non-linear regime on the other hand, the shielding current is almost constant. Measuring the slight remaining variation with frequency gives the E–j dependence and allows one to identify the underlying creep mechanism.

The assumption of a constant $|j| = j_c$ is made in the *Bean critical state model* (Bean 1962). According to the Maxwell equations, such a constant j results in a linear field gradient inside the sample. Bean (1964) has calculated the time variation of the total flux inside a sample in the critical state when an ac magnetic field is applied and found that only odd harmonic components occur in its Fourier transform. From which the choice of the third harmonic to determine the onset of nonlinearity.

The description of the sample response in terms of the voltage–current characteristics alone is not always sufficient. As indicated in Fig. 2.7, when an ac field is

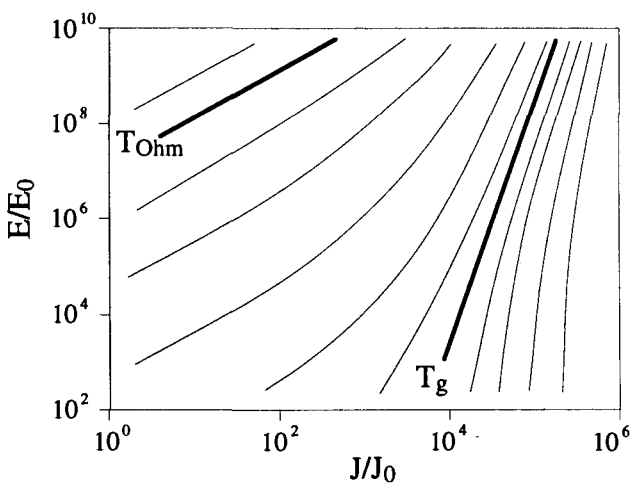

Figure 2.5: Idealized E–J isotherms. High temperature curves are in the upper left and low temperature curves in the lower right.

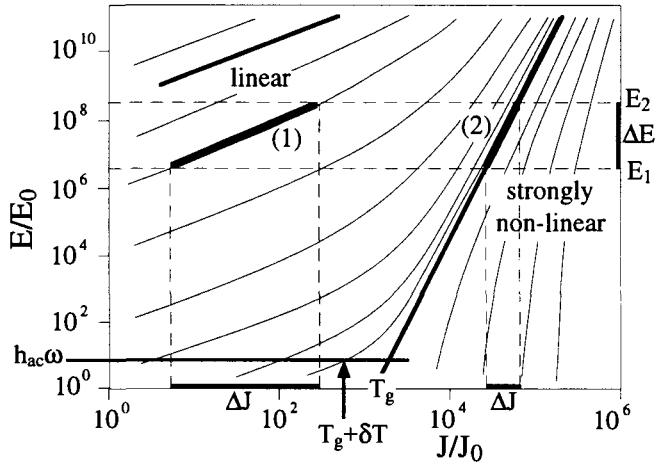

Figure 2.6: Two important facts are illustrated in this figure: (a) On changing the electric field by ΔE from E_1 to E_2 (e.g., by varying the frequency) the variation of the shielding current, ΔJ, is strong in the linear regime (1), but much weaker in the nonlinear regime (2). (b) For small voltages $h_{ac}\omega$ the temperature at which the E–j curve becomes nonlinear ($T_g + \delta T$) lies close to the real transition temperature T_g.

applied along the c-axis of the sample, there is a current flow along the edges of the sample. In principle the Lorentz forces induced by these currents are the same on the four sides when the field is applied along the c-axis only. For a dc field at a certain angle θ with respect to the c-axis two cases occur. These are illustrated in Fig. 2.7. The current is perpendicular to the field direction only on the sides per-

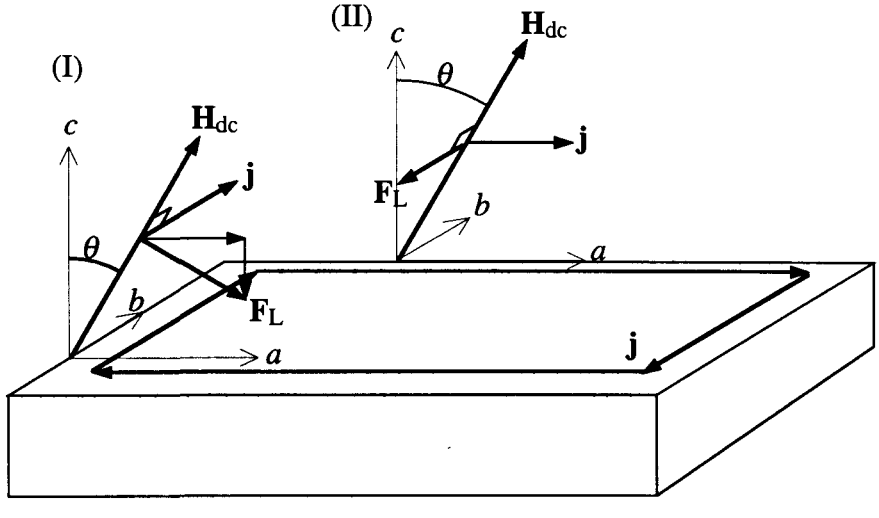

Figure 2.7: The Lorentz force on a vortex depends on the relative orientations of current and vortex. Two cases occur in Fig. 4.6: (I) current along b, (II) current along a

pendicular to the rotation plane ($j \parallel b$). The Lorentz force has then a component perpendicular to the planes $F_{L,c} = jB\sin\theta$ and a component parallel to the planes $F_{L,a} = jB\cos\theta$. For the current flowing parallel to the rotation plane ($j \parallel a$), the Lorentz force decreases as $\sin\phi$, where $\phi = 90 - \theta$ is the angle between the current and the field. The electric field is therefore not the same along the entire current path, a important detail that is lost when just the average electric field is considered.

2.5 Modeling the signal detection

We have seen above that the Hall sensor measures the induction in a small volume above the sample surface. This however does not tell us directly what happens inside the sample because the field at the Hall probe location is a function of the current distribution inside the whole sample. The complete analytical treatment of this current distribution is too complicated and should somehow be treated approximately. Gilchrist and Konczykowski proposed a description of the sample in terms of one or two inductive loops (Gilchrist and Konczykowski 1993) and we will follow here the analysis given in their paper. If the sample is represented as a single loop then its relevant physical properties are condensed into two macroscopic values, its resistance R and its inductance L. The complete system with excitation coil and Hall probe can then be analyzed by means of a few equations describing the mutual and self inductances of the different parts.

The single loop model can be expected to give a good description when peripheral currents dominate any currents in the volume. If this is not the case the sample should probably be subdivided into a large number of loops and the solution would consist in inverting the mutual inductance matrix, although in some particular case the single loop model works very well (Bean critical state, see below). A single loop actually models a particular sample realistically only in the case where the self-inductance L_2 depends on the sample size and shape alone, while R_2 might depend also on the resistivity, ρ, which is a function of the experimental parameters like temperature and magnetic field. It is a bad approximation if L_2 also changes with these parameters.

Let us turn to the single loop model in detail. In the following the excitation coil, sample and Hall probe are labelled 1, 2 and 3 respectively. We suppose that the excitation coil is supplied with a current $I_1 = I_m\cos\omega t = I_m\cos\theta$ from an infinite-impedance source. The essential properties of the loop describing the conducting sample are a self-inductance L_2, mutual inductances M_{12} with the excitation coil and M_{23} with the Hall sensor and a characteristic relation $V_2(I_2, \mathrm{d}I_2/\mathrm{d}t)$ between emf. and induced current. Note that the self inductance L_2 of the sample loop is assumed to be a constant, having no dependencies on I_2 or $\mathrm{d}I_2/\mathrm{d}t$. The Hall probe is assimilated to a loop encircling its active area and measuring Φ_3. The mutual inductances M_{13} and M_{23} are in fact notional, but their ratio contains the information of the relative contribution to the field at the probe location of currents

flowing in the sample and in the excitation coil.

The starting equations are:

$$\Phi_2 = M_{12}I_1 + L_2I_2 \tag{2.2}$$
$$\Phi_3 = M_{13}I_1 + M_{23}I_2 \tag{2.3}$$

For complete flux expulsion from the superconductor we may consider that $\Phi_2 = 0$. It follows then that $I_2 = -(M_{12}/L_2)I_1$, and $\Phi_3 = M'_{13}I_1$, where $M'_{13} = M_{13} - M_{12}M_{23}/L_2$. Even in the case of complete flux expulsion from the interior of the superconductor, the flux detected by the Hall sensor (which is placed *outside* the sample) is not zero, but has the value Φ_3. Since one is interested in the flux *inside* the superconductor, this leakage signal has to be subtracted from the full measured flux. One thus gets:

$$\Phi_3 - M'_{13}I_1 = (M_{23}/L_2)\Phi_2 \tag{2.4}$$

If the frequency ω of the applied ac field is sufficiently low so that the skin effect of the sample in the normal state can be neglected, then we can take $I_2 = 0$ above the critical temperature and get $\Phi_3 - M'_{13}I_1 = (M_{12}M_{23}/L_2)I_1$. Multiplying this with $L_2/M_{12}M_{23}I_m$, where I_m is the amplitude of the alternating current I_1, defines a normalized flux in the normal state $\phi = \cos\omega t$. This flux then essentially corresponds directly to the excitation current. For all other conditions the same normalization gives:

$$\phi = (L_2/M_{12}M_{23}I_m)(\Phi_3 - M'_{13}I_1) = (M_{12}I_m)^{-1}\Phi_2 \tag{2.5}$$

ϕ is derived solely from the measured quantity Φ_3 and is directly proportional to Φ_2. In the general case ϕ has two terms: $\phi = \cos\omega t + (L_2/M_{12}I_m)I_2$. The first term is the contribution of the current in the excitation coil to the flux at the sample position and the second term is that of the screening currents inside the superconductor. For complete screening the two terms compensate such that $\phi = 0$.

The experimental data is usually expressed in terms of the Fourier components of this normalized flux. In the following, these components will be called transmittivity components. The first harmonic components are denoted T'_H and T''_H. Its real part T'_H indicates what percentage of the field has reached the interior of the superconductor, so that with the superconductor in a highly resistive normal state $T'_H = 1$ and $T''_H = 0$. Gilchrist and Konczykowski give the following definition for T_H for a Hall probe and sine wave detection by the lock-in (which is the case for both our lock-ins):

$$T_H = T'_H - \mathrm{i}T''_H = \pi^{-1}\int_0^{2\pi} \phi\, \mathrm{e}^{-\mathrm{i}\theta}\mathrm{d}\theta \tag{2.6}$$

$\theta = \omega t$ such that the integration goes over one complete cycle of the excitation signal. In the same way higher harmonic transmittivity components can be obtained:

$$T_{Hn} = \pi^{-1}\int_0^{2\pi} \phi\, \mathrm{e}^{-\mathrm{i}n\theta}\mathrm{d}\theta \tag{2.7}$$

To go further on from this point we have to know what the relation $V_2(I_2, \mathrm{d}I_2/\mathrm{d}t)$ between emf. and induced current is. Then we will be able to substitute I_2 in 2.2 and integrate the equations 2.6 and 2.7.

In the literature the magnetic response is sometimes discussed in terms of the magnetic susceptibility χ, and one speaks also of ac susceptibility measurements. The relation between the susceptibility χ and the transmittivity is easily obtained. In the static case the susceptibility is defined as $\chi = M/H = \mu_0 B/H - 1$. In the case of an alternating field one has to differentiate between the harmonic components and their in- and out of phase parts as in the case of the transmittivity:$\chi_n = \chi'_n - \chi''_n$. Their definitions follow closely those of the transmittivity, but instead of extracting the harmonic components from the magnetic flux, which is from the magnetic induction B, one extracts those of the magnetization M. The difference between the two is just the applied field $h_{ac}\cos\omega t$ so that one gets:

$$\chi' = T'_H - 1;\ \chi'' = T''_H;\ \chi_n = T_{Hn}\ (n > 1). \tag{2.8}$$

2.6 Modeling the sample response

2.6.1 Ohmic response

In this case the sample is behaving like a normal conductor with a certain resistance R_2, as, for example, in the case of thermally assisted flux flow (TAFF). We then have to equate the emf. $-\mathrm{d}\Phi_2/\mathrm{d}t$ to $R_2 I_2$ and get:

$$\phi = \frac{R_2}{R_2^2 + \omega^2 L_2^2}(R_2\cos\omega t + \omega L_2 \sin\omega t) \tag{2.9}$$

The flux contains a resistive part which is in phase with the excitation, and an inductive part which has a phase shift of $\pi/2$. The total signal has therefore a certain phase shift with respect to the excitation signal, and the graph of flux (or B) versus applied field is an ellipse as shown in Fig. 2.1. If the frequency is sufficiently low such that $R_2 \gg \omega L_2$ we get:

$$\phi \approx \cos\omega t + \omega L_2/R_2 \sin\omega t. \tag{2.10}$$

This gives for the transmittivity:

$$T_H = 1 - \mathrm{i}\omega L_2/R_2 = (1 + \mathrm{i}\omega L_2/R_2)^{-1} = (1 + \mathrm{i}\omega\tau)^{-1} \tag{2.11}$$

No higher harmonics occur. As Gilchrist and Konczykowski mention in their paper this is the simplest way a time constant τ can get involved, τ being the L/R-time of the sample. This time constant depends on the resistivity ρ of the sample. By varying ρ (by sweeping for example the temperature), T''_H will go through a maximum when $\omega\tau \approx 1$.

2.6.2 The critical state model

The first theory to explain the response of a hard (type II) superconductor to an ac magnetic field has been made by Charles Bean in 1964 . Based on his critical state model (Bean 1962) he could calculate the harmonic components of the sample ac magnetization. In his model the current density is equal to a critical value that is independent of the field. During an ac magnetization experiment the current density in the flux-penetrated region can take on only the values $\pm j_c$. It is zero everywhere else. The resulting flux profile is linear as is shown in figure 2.8(a). The application of an ac field does not lead to the generation of even harmonics even in the presence of a steady field (Bean 1964).

The Bean model is a good approximation when either the field is small, so that interactions between the vortices are not important, or when the ac field is small as compared to the steady field such that the interaction strength remains constant. In the first case the critical current density j_c is expected to be independent on field, while in the second case it does not change very much over the ac cycle. In terms of the voltage–current characteristics of a sample the Bean model is well adapted if the I(V) curve is very steep (strongly nonlinear) and j_c = constant independent of the electric field E in a dc experiment, because then the notion of a critical current is rather well defined. This is illustrated in Fig. 2.9.

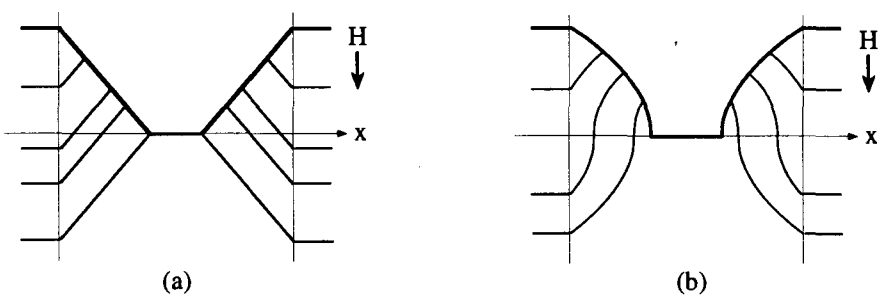

Figure 2.8: Field profiles for decreasing field. (a) Bean model with B-independent j_c. (b) Kim-Anderson model where j_c is inversely proportional to B

A model in which the current is field-dependent is the Kim-Anderson model (Kim et al. 1962; Anderson 1962). In this model it is the pinning force per unit volume that is assumed to be independent of B. This leads to a critical current density inversely proportional to the local induction and a parabolic field profile inside the superconductor (Fig.2.8(b)). The response of the superconductor to an alternating magnetic field can now contain even harmonics if an additional steady field is applied (Ji et al. 1989). In the limit of large dc fields the relative change of the field due to the superimposed ac field becomes negligible, j_c can be treated as field independent and we find again the Bean model. So with increasing dc field the even harmonics tend to disappear. Nevertheless, we should bear in mind when considering orientations of the steady field close to the ab-plane, because the c-axis

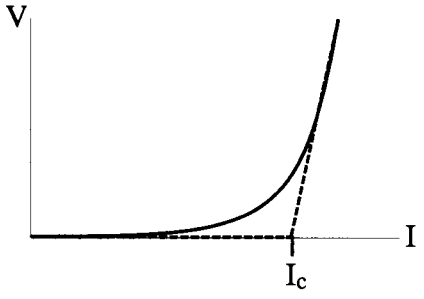

Figure 2.9: Very nonlinear voltage–current characteristics with the definition of the critical current I_c (to which corresponds a critical current density j_c).

component of the field is then low enough that a field dependence of the critical current might become important.

For a Bean-like flux profile inside the sample a Hall sensor placed at the centre of the top surface will measure zero flux unless the front of the profile reaches the centre. The total current in the sample then corresponds to the critical current density j_c of the sample integrated over half its cross section. In terms of the single loop model the Bean critical state therefore transforms to the condition that I_2 cannot exceed a value I_c, the total current at full penetration. As long as $|I_2| < I_c$ $\mathrm{d}\Phi_2/\mathrm{d}t = 0$. Hence, if $I_m \leq (L_2/M_{12})I_c$ the normalized measured flux $\phi = 0$ at all times and all transmittivities will be zero. A more interesting case occurs when I_m exceeds $(L_2/M_{12})I_c$. The corresponding cycle for the flux Φ_2 is shown in Fig. 2.10. At $\theta = 0$, $\Phi_2 = M_{12}I_m - L_2I_c$ and $\phi = 1 - J$ where $J = (L_2/M_{12})I_c/I_m$. A critical current $I_2 = -I_c$ opposes flux entry into the loop. As I_1 decreases I_2 increases in order to keep the flux Φ_2 inside the loop constant. At $\theta = \omega t = \theta_c$, I_2 equals I_c and will not increase any more. θ_c is given by $\cos\theta_c = 1 - 2J$. For $\theta_c < \theta < \pi$ we have $I_2 = I_c$, $\Phi_2 = M_{12}I_1 + L_2I_c$ and $\phi = \cos\theta + J$. So for $\theta = \pi$, $\Phi_2 = -M_{12}I_m + L_2I_c$ ($\phi = -1 + J$) and for the second half cycle the above pattern is repeated with inverted sign.

The quantity J introduced above is a normalized critical current density. It

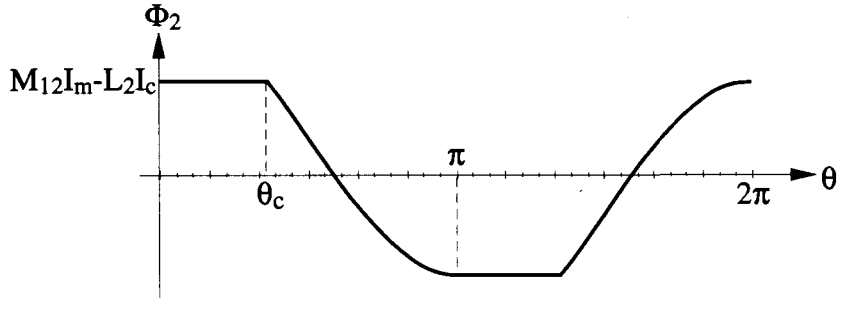

Figure 2.10: Flux Φ_2 as a function of $\theta = \omega t$. θ_c is the phase where $I_2 = I_c$.(see text)

is normalized in the sense that when J varies from 0 to 1 the response of the superconductor changes from no shielding at all ($J = 0$) to complete shielding of the applied ac field ($J = 1$). For $0 < J < 1$ the ac field is partially screened and a response as in Fig. 2.10 occurs. Complete screening means that no flux (except that leaking around the sample) is detected at the Hall probe position. In principle, J can also be bigger than 1, but this does not change anything in the detected signal, which remains that of complete shielding.

From the flux cycle depicted above the transmittivity components can now be calculated:

$$T_{Hn} = -\frac{4\mathrm{i}}{n\pi}(1-J) - \frac{2}{\pi}\int_{\theta_c}^{\pi}(\cos\theta_c - \cos\theta)\mathrm{e}^{-\mathrm{i}n\theta}\,\mathrm{d}\theta \quad \text{for odd } n \tag{2.12}$$

$$= 1 - \frac{\theta_c}{\pi} - \frac{\mathrm{i}}{2\pi}(1-\mathrm{e}^{-2\mathrm{i}\theta_c}) \quad \text{for } n = 1\,, \tag{2.13}$$

$$= -\frac{2\mathrm{i}}{n\pi}\int_{0}^{\theta_c}\sin\theta\,\mathrm{e}^{-\mathrm{i}n\theta}\,\mathrm{d}\theta \quad \text{for odd } n > 1$$

$$= \frac{2\mathrm{i}}{n(n^2-1)\pi}[1-(\cos\theta_c + \mathrm{i}n\sin\theta_c)\mathrm{e}^{-\mathrm{i}n\theta_c}]\,. \tag{2.14}$$

From the higher harmonics the third harmonic component is the most important for our purposes. In a parametric plot in which the normalized critical current J goes through the interval [0,1], the third harmonic describes a characteristic heart shape (cardioid) in the complex plane. This is shown in Fig. 2.11.

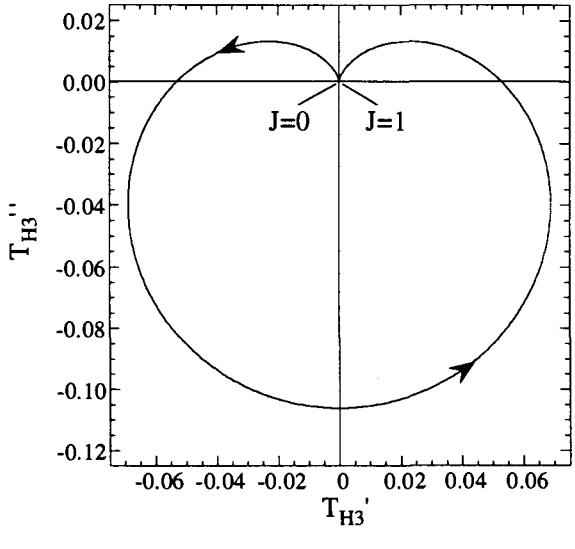

Figure 2.11: Polar plot of the third harmonic transmittivity for the critical current hypothesis. The curve is described in the counterclockwise sense on varying the normalized critical current J from 0 to 1.

2.6.3 Surface barrier

At sufficiently high temperatures bulk pinning of the vortices in the material may become negligible. For very clean samples this can already happen at temperatures as low as 0.5 T_c (Chikumoto et al. 1992). What remains is the surface barrier, as first described by Bean and Livingston (1964). This barrier is due to the attraction of the vortices to the surface. This attraction can be accounted for by replacing the surface by an image vortex of opposite orientation. The force between vortex and image is expected to decay with distance x ($x > \lambda$) from the surface as $e^{-2x/\lambda}$. However, there is also a repulsive interaction between the vortices and the Meissner currents flowing within a depth λ from the surface. These currents exert a Lorentz force on the vortices near the surface, which is proportional to the applied field and decays as $e^{-x/\lambda}$, pushing them inside the superconductor. The effect of these combined forces is to form a field dependent barrier for the vortices to pass the surface. This surface barrier or Bean-Livingston barrier manifests itself in two distinct ways: (a) the field at which the first vortex enters a superconductor is increased from H_{c1} to a higher field H_p, the field of first penetration and (b) when the external field is decreased flux cannot leave the superconductor until the surface current has vanished. The resulting induction loop is shown in Fig. 2.12. For an ideally smooth surface $H_p =$

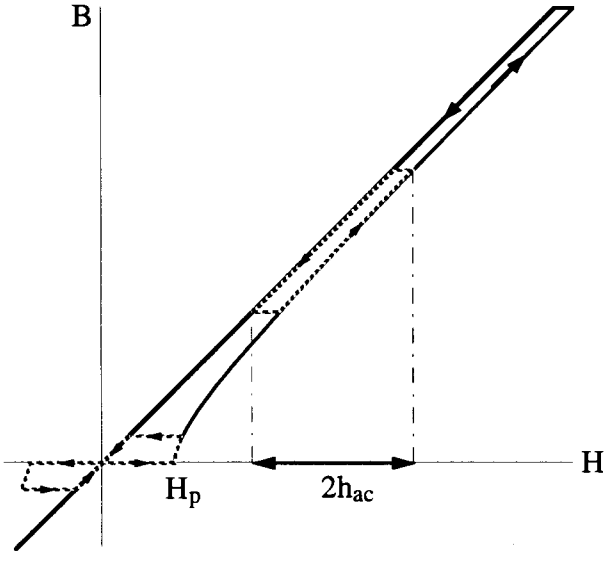

Figure 2.12: Induction loop for a sample in which flux entrance and exit are dominated by the surface barrier. H_p indicates the field at which flux starts to enter the sample on increasing field. Minor magnetization loops arising from a superimposed ac field h_{ac} are also shown for two cases: $H = 0$ and $H > 2h_{ac}$.

H_c, the thermodynamic critical field, but surface roughness of the scale of λ weakens the image force and reduces H_p to a value closer to H_{c1} (Campbell et al. 1968). In such extreme type-II superconductors as the cuprates the difference between H_p and

H_{c1} can nevertheless be important because $H_c \approx \kappa H_{c1} \gg H_{c1}$ (De Gennes 1966) due to the large Ginzburg-Landau parameter $\kappa = \lambda/\xi \gg 1$ in these materials.

Figure 2.12 also shows minor magnetization loops that occur when an ac field is superimposed on the steady field. In the single loop model the surface barrier can be treated using an alternative critical current hypothesis (Gilchrist and Konczykowski 1993). In the usual critical current hypothesis the current I_2 flows in such a way as to oppose any change in flux inside the loop. In the alternative hypothesis I_2 may oppose the entry of flux into the loop but not its exit. This means that on increasing I_1 the loop current I_2 will increase as well and the flux in the loop remains zero. Flux only starts to enter when I_2 has reached the critical value I_c. On decreasing I_1 on the other hand I_2 will decrease and the flux inside the loop remains constant but only until $I_2 = 0$. Then the loop current will remain zero and flux will leave the loop. The shape of the resulting hysteresis loop depends on the value of the applied steady field as can be seen in Fig. 2.12. The two hysteresis loops there correspond to the cases of zero steady field and a steady field exceeding twice the amplitude of the ac field respectively. In the latter case the hysteresis loop has the same shape as for the usual critical current hypothesis, the flux in the loop modeling the sample would follow a curve like in Fig. 2.10 and the same transmittivity components would be obtained.

The hysteresis loop looks quite different if there is no steady field. Now the flux inside the loop follows the curve shown in Fig. 2.13. The ac amplitude is taken to be

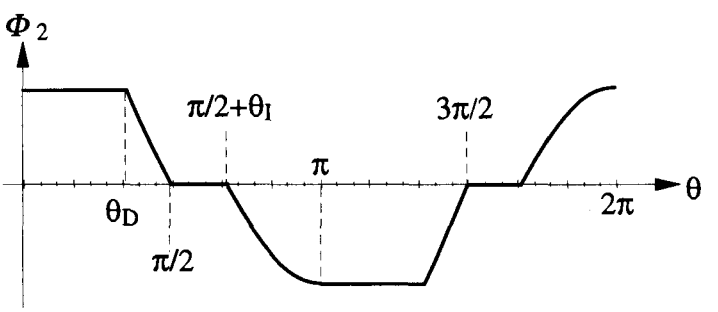

Figure 2.13: Flux Φ_2 as a function of $\theta = \omega t$ for the alternative critical current hypothesis (surface barrier).

$h_{ac} > H_p$, because otherwise the ac field is screened completely. The harmonics are now changed considerably and especially the third harmonic transmittivity is much reduced with respect to the usual critical current hypothesis (2.14). On adding a dc field component this curve is rotated, increases in size and finally turns into the usual cardioid, as the dc field equals or surpasses the ac field. This is shown in Fig. 2.15. The change in this curve reflects the change in the hysteresis loop which changes from a double parallelogram to a simple one as illustrated in Fig. 2.12.

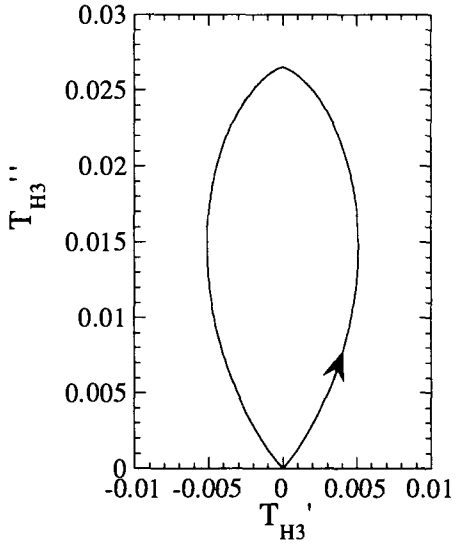

Figure 2.14: Polar plot of the third harmonic transmittivity for the alternative critical current hypothesis with zero dc field. The curve is described in the counterclockwise sense on varying the normalized critical current j from 0 to 1.

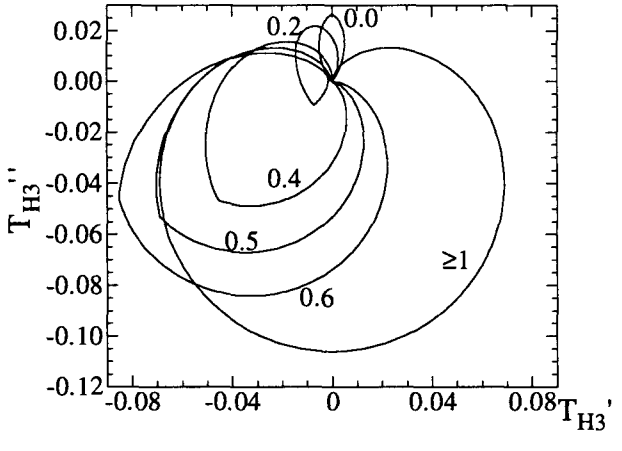

Figure 2.15: Polar plots of the third harmonic for the alternative critical-current hypothesis of Gilchrist and Konczykowski (1993). The labels next to the curves indicate the ratio H_{dc}/h_{ac}.

2.6.4 Flux creep

The critical current hypothesis can be a good approximation to the voltage–current characteristics of a superconductor, but the assumption of a critical current below which there is no resistance is never completely correct. The $V(I)$ curve can be very nonlinear but V will have a finite value for any current. This is due to flux creep: there is always a certain probability that the vortices unpin under the influence of the Lorentz force. This leads to the smoothed I(V) curve as shown in Fig. 2.9 and

to exponentially low voltages for current densities $j < j_c$.

In the single loop model flux creep can be modelled by introducing a nonlinear relation between voltage and current: $V_2 = B|I_2|^\sigma I_2$. This relation leads to an increased dissipation as compared to the critical current hypothesis and to a reduction in the harmonic content (Gilchrist and Konczykowski 1993).

Flux creep gives rise to the relaxation of the flux profile inside the sample. This effect will be the stronger the more time the system is given to relax. Since the frequency of the ac field determines a time scale the response of the superconductor should depend on frequency. This is actually what is observed (van der Beek et al. 1995). With increasing frequency relaxation should become less and less important and the response is expected to approach a critical current behaviour (Prozorov et al. 1995).

2.7 Data analysis

2.7.1 Basic procedure

The measurement with the Hall sensor gives voltage values corresponding to the fundamental (V) and third harmonic (V_{H3}) components in the voltage over the width of the sensor. These components are proportional to the corresponding components in the induction at the Hall probe location (B_{ac} and B_{ac3}). We differentiate also between in-phase (V') and out of phase component (V'') of the measured signal which are available to us due to the phase sensitivity of lock-in measurements. They are sometimes also referred to as real and imaginary part of the voltage under consideration. The task now is to normalize this data and to obtain the transmittivity. The starting point of any experiment is to perform a temperature scan of the in-phase component of the first harmonic beginning at a temperature well above its drop and terminating well below, in order to obtain $M'_{13}I_m$ and $L_2/(M_{12}M_{23}I_m)$ (compare section 2.5). The curve obtained by the temperature scan not only contains the temperature dependence of the superconducting properties of the sample but also the temperature dependence of the Hall probe sensitivity. The change in sensitivity results from the variation of the carrier density with temperature. It is linear in the temperature range of interest here. In order to correct for it the curve has to be divided by a linear fit to its high temperature part. The resulting curve has flat parts at high temperatures and at low temperatures. Let us denote the corresponding voltage values by V'_{max} and V'_{min}. Following the single loop model we can identify $V'_{min} \equiv kM'_{13}I_m$ and $V'_{max} \equiv k(M_{12}M_{23}I_m/L_2 + M'_{13}I_m)$ with k an undetermined constant describing the sensitivity of the sensor. The difference of the two voltages gives $V'_{max} - V'_{min} = kM_{12}M_{23}I_m/L_2$. With this knowledge we can actually express ϕ in terms of the measured voltages:

$$\phi = \frac{1}{V'_{max} - V'_{min}}(V(\theta) - V'_{min}\cos\theta) \tag{2.15}$$

The constant k falls out naturally. The formulae for the transmittivity components now follow immediately:

$$T'_H = \frac{V' - V'_{min}}{V'_{max} - V'_{min}} \tag{2.16}$$

$$T''_H = \frac{-V''}{V'_{max} - V'_{min}} \tag{2.17}$$

$$T'_{H3} = \frac{V'_{H3}}{V'_{max} - V'_{min}} \tag{2.18}$$

$$T''_{H3} = \frac{-V''_{H3}}{V'_{max} - V'_{min}} \tag{2.19}$$

$$|T_{H3}| = \sqrt{T'^2_{H3} + T''^2_{H3}} \tag{2.20}$$

Negative signs were used in equations 2.17 and 2.19 in order to be in agreement with the definitions in (Gilchrist and Konczykowski 1993). In reality this analysis is slightly complicated by secondary effects of the measurement. For frequencies above 200 Hz, for example, an offset in V'' appears due to inductive coupling of the voltage leads to the excitation coil.

2.7.2 Shielding current

In general it is not possible to get the current distribution inside the sample from the simple knowledge of the induction at some point at the sample surface. However, in the case of strongly nonlinear $V(I)$ characteristics the flux penetrated region has a sharp boundary. Its position depends on the magnitude of the shielding current density which is now well defined. It is then possible to get the normalized shielding current density J from the measurements. In good approximation it is given by (van der Beek et al. 1995):

$$J = \frac{1}{\pi} \arccos(2T'_H - 1) \tag{2.21}$$

2.7.3 Angular variation

A form of measurement often performed is the angular scan which consists in tracing the transmittivity as a function of the orientation of the static field with respect to the sample and Hall probe. Amplitude of the static magnetic field and temperature are held constant during field rotation. Such scans are taken for several temperatures spanning the range from some Kelvin above the transition to a few below such that these data can be transformed into functions of temperature. For each angle the procedure described in the previous subsection can then be applied. Each angle has to be treated separately because of the dependence of the Hall probe sensitivity together with its temperature derivative on field orientation. This procedure can be simplified only if the static field does not exceed a few hundred Oersted.

The dependence of the Hall coefficient on field orientation is due to several factors. One is that the finite probe thickness together with a probable misalignment of the contacts can lead to a voltage that depends not only on the field component perpendicular to the sensor top surface but also on the parallel component. The periodicities on these two components might have a mutual phase shift. Moreover magnetoresistive effects might arise and add to the complexity of the angular dependence of the Hall probe sensitivity.

An additional difficulty arises because of the limited temperature range of our nitrogen cryostat: often we cannot reach V'_{min} for all angles but for those near the *ab*-plane orientation of the sample. In that case an approximation for the low temperature curve has to be found. In general we adopt the following procedure: the angular scans usually span an angular range of 270 degrees. Thus we have a range of 90 degrees for which we have both positive and negative field. By taking the difference in V' for positive and negative sign of the field at the lowest available temperature and dividing it by two we get the difference function for the angular interval from 0 to 90 degrees:

$$V_1(\theta) = \frac{V'(\theta) - V'(\theta + 180)}{2} \quad (O < \theta < 90)$$

Then we copy the inverted values to the interval from 180 to 270 degrees. The interval from 90 to 180 degrees remains to be interpolated. This can be done for example by fitting the available data with the function:

$$A\cos(\theta - \theta_0) + B\cos^3(\theta - \theta_0) + C\cos^5(\theta - \theta_0)$$

Finally the mean offset from zero of the lowest temperature angular scan is added to this curve in order to obtain our $V'_{min}(\theta)$.

The method to obtain V'_{min} is somewhat arbitrary but the error that is introduced can be estimated and is not very large. The voltage V_1 as defined above covers a range of typically only 3% of full scale which gives 6% for the voltage difference that appears in its definition. The real curve should be a smooth function of θ and we might thus estimate the error introduced by our fit to be of the order of 1% or less.

Data analysis gets even more complicated if the parameter for the angular scans is not the temperature but the frequency. Increasing the frequency actually has a similar effect in high T_c anisotropic samples as decreasing the temperature: the field gets screened over a broader and broader angular range. However, in addition to the frequency dependence of the Hall probe sensitivity one now also has to deal with an angular dependent phase shift of the signal, especially at the highest frequencies ($f > 700$ Hz). This is a big hindrance since the high frequency data is necessary for the normalization (it corresponds to the low temperature voltage in the above example).

The exact orientation of the crystal axes with respect to the zero position of the stepping motor was usually obtained easily. The layered structure of the sample materials gives rise to a pronounced angular dependence of the transmittivity when

the dc field is almost parallel to the sample *ab*-plane. In order to have the sharpest structure we chose a field of a few hundred Oersted and a temperature only 2 or 3 K below the zero field onset of the third harmonic transmittivity. Then, using higher and higher angular resolution in increasingly restricted intervals we could in principle fix the angle of the *ab* plane with a precision of $\frac{1}{1000}$ of a degree. In practice we actually never went beyond $\frac{1}{100}$ of a degree.

2.7.4 Onset of magnetic irreversibility

An important piece of information is the onset of the third harmonic which indicates the onset of magnetically irreversible behaviour. The signification of the line in the H–T phase diagram that this onset defines will be discussed in the following chapters. Here only the method to find this onset will be given.

The exact definition of the onset temperature is illustrated in Fig.2.16. As can be seen there we actually define two onset temperatures, the first corresponding to the point where the signal deviates from zero and the second as the intersection point of the linear extrapolation of the high temperature part of the peak with the x-axis. The figure shows some temperature scan where both points are easily identified. However, often some noise is present which makes the definition of T_{onset1} difficult and only T_{onset2} is retained.

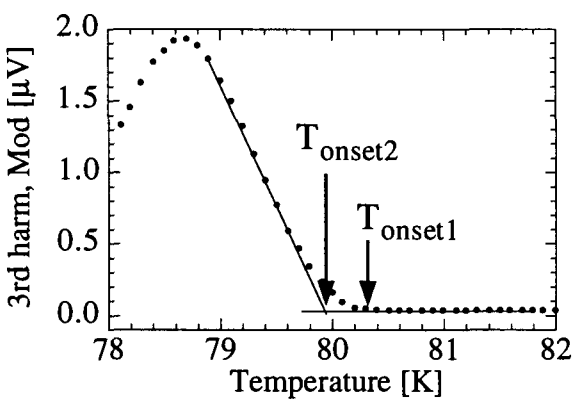

Figure 2.16: Determination of the onset temperatures from the amplitude of the third harmonic. These values are used for the definition of the irreversibility line. The data was taken on a 6 GeV Pb-ion irradiated BSCCO crystal with a matching field of 5 kG. H_{DC} = 126 Oe, H_{AC} = 7 Oe, f = 7.75 Hz

Chapter 3

Vortex lattice phase transition in pure $Bi_2Sr_2CaCu_2O_8$

3.1 Introduction

Even before the discovery of the high temperature superconducting oxides thermal fluctuations were thought to destabilize the Abrikosov vortex lattice above a certain temperature T_m. (Huberman and Doniach 1979) and (Fisher 1980) first discussed this for the case of thin films. Brézin, Nelson and Thiaville (1985) actually showed a few years later that in dimensions lower than 6 fluctuation effects are strong and change the second order mean-field transition from the normal state to the vortex-lattice into a first order transition (FOT). However, in conventional superconductors the FOT is very close to H_{c2} because thermal fluctuations are unimportant except close to $T_c(H)$ and only in the cuprate superconductors are the critical temperature and anisotropy high enough for thermal fluctuations to determine a large part of the mixed state phase diagram. Quantitatively the importance of thermal fluctuations is reflected in the Ginzburg number $Gi = \frac{1}{8}(\frac{k_B T_c}{\varepsilon\varepsilon_0 \xi})^2 = \frac{1}{2}(\frac{2\pi\mu_0 k_B T_c \lambda^2}{\Phi_0^2 \varepsilon \xi})^2$. In conventional superconductors $Gi \approx 10^{-8}$, whereas in $YBa_2Cu_3O_7$, for example, $Gi \approx 10^{-2}$, and in the extremely anisotropic $Bi_2Sr_2CaCu_2O_8$, $Gi \approx 1$. In Bi-2212 the importance of thermal fluctuations is actually better accounted for by the two-dimensional Ginzburg number, $Gi^{2D} \approx T_c/\varepsilon_0(0)s$, which takes the value $Gi^{2D} = 0.1$.

The new phase appearing between the first order transition and H_{c2} is called the vortex liquid state. This vortex liquid is characterized by a linear resistance and the vanishing of the superconducting phase coherence due to strong positional fluctuations of the vortex cores.

In layered superconductors the situation might be even more complicated. As Glazman and Koshelev (1991) pointed out, the transition from the pinned vortex solid to an unpinned vortex liquid could be separated into two stages. At low fields, on raising the temperature, first a transition from the vortex lattice to the vortex liquid occurs. Then, at a somewhat higher temperature, independent liquid

systems of 2D vortices in different layers are formed. This second transition is called decoupling and is characterized by the loss of interlayer coherence. The new phase that appears above the decoupling line and that consists of a system of completely independent 2D (pancake) vortices (Clem 1991), is called the pancake gas. At high fields the decoupling is expected to occur in the solid phase.

First indications of a vortex liquid phase in BSCCO (Palstra et al. 1988) and of a phase transition of the vortex system in BSCCO and YBCO (Gammel et al. 1988) were found soon after the discovery of the cuprate family of superconductors. However, these findings were made on crystals of rather poor quality and the transition in YBCO was subsequently well described in terms of a disorder induced freezing into a vortex glass state (Koch et al. 1989; Gammel et al. 1991). Then, untwinned YBCO crystals became available that showed a transition in the magnetically reversible regime, as revealed by torsional oscillator experiments (Farrell et al. 1991; Beck et al. 1992). Resistive measurements on the same type of crystals seemed to indicate that the transition was of first order (Safar et al. 1992; Kwok et al. 1992; Safar et al. 1993; Charalambous et al. 1993). The low temperature phase in pure BSCCO crystals was first identified as a vortex lattice by small angle neutron scattering (SANS) (Cubitt et al. 1993) and muon spin rotation (μSR) (Lee et al. 1993) experiments. None of these experiments measured a thermodynamic quantity at the transition and the resistive hysteresis that had been observed (Kwok et al. 1992; Safar et al. 1993; Charalambous et al. 1993) could not be taken as clear evidence for a first order transition (Jiang et al. 1995). In 1994 SQUID magnetometry finally revealed a jump in the equilibrium magnetization at the transition in a $Bi_2Sr_2CaCu_2O_8$ single crystal (Pastoriza et al. 1994). This jump in the magnetization, which is a first derivative of the free energy, clearly indicated the first order nature of the transition. Soon after this discovery the transition in BSCCO:2212 was investigated by local induction measurements at the sample surface with a 2-dimensional electron gas Hall sensor array (Zeldov et al. 1995).

In general, the induction profile across the sample is non-uniform, and therefore the FOT takes place at different applied fields in different parts of the sample. This causes an artificial broadening of the magnetization jump in global (SQUID) magnetization measurements, which is avoided by using a local measurement of B (such as by the Hall probe array).

It has to be noted that these local measurements with 10 μm or 3 μm Hall sensors showed a clear step in the magnetization without any additional peaks. This is insofar important as the step reflects an abrupt change in vortex density that must be accompanied by a current sheet separating the two phases. In thin samples this current sheet gives rise to a decrease of the magnetic induction on one side of it and an increase on the other side. In addition to a mere step there would therefore be a dip and a peak on either side of this step. The step measured by Zeldov et al. (1995), not showing these structures, is indicative of a relatively thick sample. In that case the measured jump in local induction ΔB equals the jump in the magnetization ΔM. Application of the Clausius-Clapeyron relation for first

order transitions yields the entropy change per unit volume ΔS at the transition:

$$\Delta S = -\mu_0 \Delta M \frac{dB_m}{dT} \tag{3.1}$$

where B_m is the value of the local induction at the FOT. Replacing ΔM with ΔB gives:

$$\Delta S = -\frac{1}{\mu_0} \Delta B \frac{dB_m}{dT} \tag{3.2}$$

expressing the entropy jump completely through the measurable quantity B. Using this equation Zeldov et al. (1995) obtained values for ΔS between 0 and 2 k_B per vortex per CuO_2 double layer depending on temperature.

The jump in B can also be measured using ac measurements on the Hall sensor array. In these measurements the discontinuity in B gives rise to a paramagnetic peak, i.e., an enhanced signal in the ac response (Morozov et al. 1996), which clearly indicates that the vortex system is in equilibrium since any nonequilibrium due to pinning must result in a diamagnetic signal. Moreover, using ac fields with phase sensitive detection increased the sensitivity with respect to the dc induction measurements and allowed the extension of the accessible temperature range to temperatures closer to T_c. Morozov et al. (1996) obtained values for the entropy change in BSCCO exceeding 6 k_B per vortex per CuO_2 double layer close to T_c, a value considered abnormally high. In $YBa_2Cu_3O_7$ in contrast, the entropy jump ΔS at the transition is about 0.5 k_B per vortex per copper oxide layer as consistently derived from both magnetization and calorimetric measurements (Schilling et al. 1996). It should be mentioned that according to more recent work by Rae, Forgan and Doyle (1998) some change has to be made to the equation for ΔS as used by Zeldov et al. (1995). In their calculations Rae et al. show that the jump in local induction at the sample surface is only 1/2 the magnetization jump inside the sample, which means that the entropy jump would actually be twice the value calculated in Zeldov et al. (1995). The reason for the additional factor 2 is that the induction jump induced by a current sheet extending into one half-space (i.e., at a surface) is only half the jump at a sheet extending into the whole space.

In another recent analysis by Dodgson et al. (1998) a theoretical form for the temperature dependence of the jump in local induction in strongly layered superconductors has been found. Following this work the $\Delta B(T)$ dependence exhibits two regimes due to a change in the relative importance of the interlayer Josephson coupling with respect to the electromagnetic one. Below a certain temperature T^{em} interactions are dominated by the electromagnetic coupling while above it the Josephson coupling becomes relevant. From the experiment one has $T^{em} \approx 0.92 T_c$ (Zeldov et al. 1995). The growth of the Josephson coupling increases the length L of the dominant fluctuations of the vortex line. Below T^{em} this length is equal to s, the interlayer spacing. Above T^{em} $L = \varepsilon \lambda_{ab}$. This leads to the following dependences for the induction jump:

$$\Delta B \approx \begin{cases} \mu' \frac{\mu_0}{4\pi} \frac{k_B T_m}{\Phi_0 s}, & T_m < T^{em}, \\ \mu' \frac{\mu_0}{4\pi} \frac{k_B T_m}{\Phi_0 \varepsilon \lambda_0} \sqrt{1 - (T_m/T_c)^2}, & T^{em} < T_m. \end{cases} \tag{3.3}$$

As above s is the interlayer distance, and $\mu' \approx 1$.

However, the interpretation of the observations in terms of a first order transition has been questioned not only because of the unexpectedly high entropy values but also because, in torque magnetometry measurements, a suppression of the magnetization step by an in-plane field was reported (Farrell et al. 1996). Although torque magnetometry is well adapted, the ac Hall sensor technique has proven to be more sensitive. Moreover, turning the magnetic field with respect to the sample is a very convenient way to gradually add an in-plane component to the static field. It was therefore decided to study the behaviour in an inclined magnetic field, and to measure its influence on the first order transition in Bi-2212. This could also be expected to provide a good test of the nature of the vortex system. The influence of tilting the magnetic field away from the c-axis should be rather different depending on whether the system behaves in a two dimensional manner or as a three dimensional but anisotropic medium. The former would occur if there was essentially no Josephson coupling between the copper oxide double layers and the interaction of 2D vortices in different layers was purely electromagnetic. An additional in-plane field would then penetrate completely freely and without affecting the field component parallel to the c-axis. For any orientation of the applied dc field the transition would be observed when the c-axis component reaches the first order transition field. The result is a simple scaling of the transition field with $1/\cos\theta$, where θ is the tilt of the field away from the c-axis.

In the case of a three dimensional behaviour a finite anisotropy $\varepsilon = \sqrt{m/M} \ll 1$ has to be taken into account, where m, M are the in-plane and c-axis effective mass, respectively. According to the scaling rules of Blatter, Geshkenbein, and Larkin (1992) we then expect the angular dependence to be described by the scaling factor $1/\varepsilon_\theta$, where ε_θ in the present case is given by $\varepsilon_\theta^2 = \cos^2\theta + \varepsilon^2 \sin^2\theta$.

3.2 Experimental details

The sample used for this study has a T_c of 91.5 K and approximate dimensions of $500\times500\times40$ μm^3. It had been cut out of the same larger crystal as the sample one investigated in Zeldov et al. (1995).

The experiment was arranged in such a way that the ac magnetic induction perpendicular to the sample was measured by the Hall sensor. In order to measure the applied dc field, the Hall sensor of a commercial Gaussmeter was placed outside but close to the tube enclosing the sample holder. Figure 3.1 shows the orientations of the applied ac and dc fields with respect to the sample. Whereas the dc field could be turned to any angle between c-axis direction and ab-plane, the ac field was always parallel to the c-axis. The field sweeps have been performed in the following way: after turning the electromagnet producing the dc field to the desired angle, the sample was cooled down in a field well in excess of the first order transition field. Once the temperature was stabilized, data was taken on decreasing the field. We adopted this procedure to keep the difference between field and induction small when

the FOT field was reached because only the applied field was measured, not the local induction. In addition an alternative procedure to study the angular dependence of

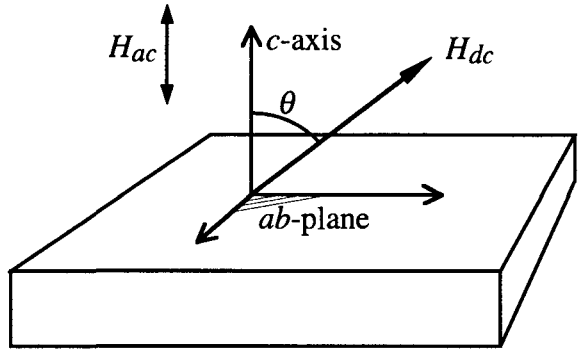

Figure 3.1: Orientations of the dc and ac fields with respect to the sample. The ac field is always parallel to the sample c-axis. The dc field orientation can be chosen freely in a plane spanned by the c-axis and a given vector of the ab-plane.

the phase transition was used. This procedure consisted in rotating a constant dc magnetic field at a given temperature. The rotation changes the projection of H_{dc} on the direction parallel to the c-axis. This procedure will be called angular scan in contrast to the first one that will be referred to as field scan. As can be seen from Fig. 3.2 the two procedures are more or less equivalent.

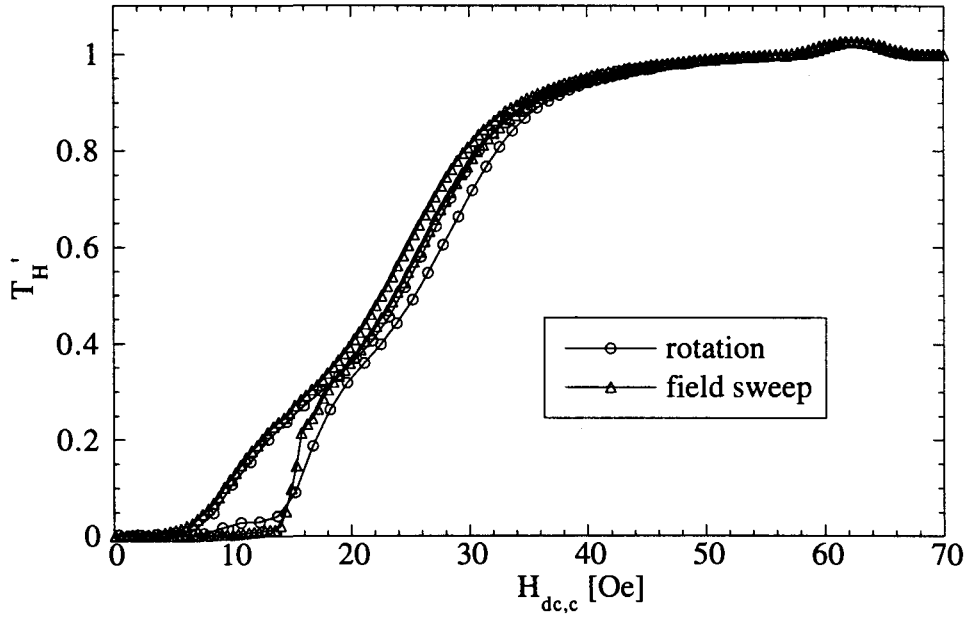

Figure 3.2: Comparison of an ordinary field sweep with an angular scan. For the angular scan the measured signal is traced versus the c-axis component of the field. $T = 80$ K.

3.3 Results

3.3.1 Original data

Typical results of the magnetic field scans at various angles are presented in Fig. 3.3. For large angles, the increased field necessary to get the transition influenced the

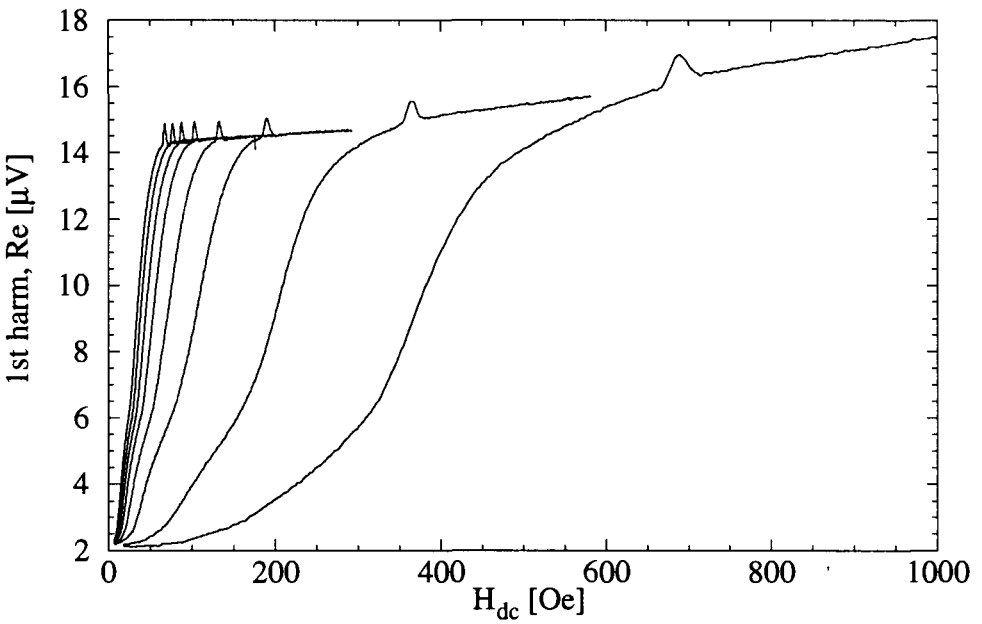

Figure 3.3: In-phase part of the measured Hall voltage as a function of applied dc-field for different angles θ between c-axis and dc-field direction, $\theta = 0°$, 30°, 40°, 50°, 60°, 70°, 80°, and 85°. $T = 80$ K, H_{ac}= 1 Oe, f = 7.75 Hz.

sensitivity of the Hall sensor. However, the linear growth of the sensitivity with applied field which the data exhibits can easily be corrected. After correction and normalization to the ac amplitude, curves as shown in Fig. 3.4 are obtained. The ac response B'_{ac} shows a gradual transition from a fully shielded state at low H_{dc} to a fully transparent state at higher dc fields. A very well defined paramagnetic peak in B'_{ac} appears at a dc field labelled $H_m(\theta)$, which increases with increasing tilt θ from the c-axis. This paramagnetic peak is the hallmark of the first order transition.

As mentioned before, instead of keeping the angle fixed and changing the dc field it also possible to fix the field and to change the angle. As we saw in Fig. 3.2 such angular scans correspond very closely to a field cycle of the c-axis field. This means that the in-plane field has almost no importance and enters the sample completely freely. As will be seen later, this is true to a good approximation, but some influence of the in-plane field exists. ac measurements on the increasing and the decreasing field branch of a cycle of the c-axis field give the same results only when the ac field is sufficient to connect the two branches (see Fig. 3.5). Otherwise the ac response is different. This is also the reason why the angular scans exhibit a slight asymmetry around the ab-plane direction since the two sides correspond to decreasing and in-

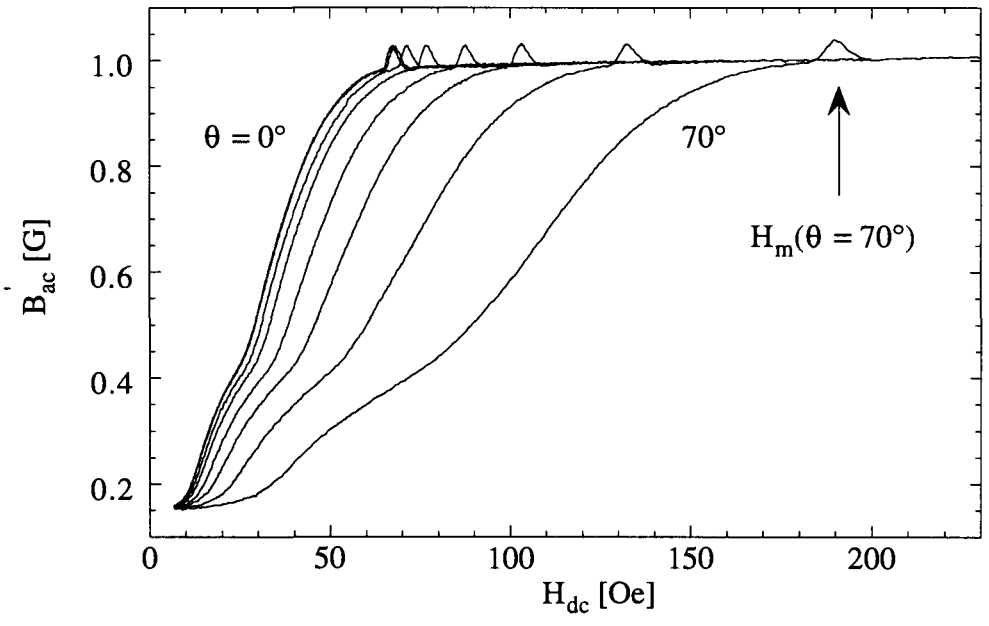

Figure 3.4: Transmitted ac-field as a function of applied dc-field for different angles θ between c-axis and dc-field direction, $\theta = 0°$ to 70° in 10° intervals. $T = 80$ K, H_{ac}= 1 Oe, f = 7.75 Hz.

creasing c-axis field, respectively. This can be seen in Fig. 3.6 , where angular scans for a few temperatures are shown. Screening sets in first for alignment of the dc field with the ab-plane since this corresponds to the zero in the c-axis field. With decreasing temperature screening sets in for angles closer and closer to the c-axis because of efficient pinning at higher and higher (c-axis) fields. At the same time the first order transition is shifted to higher (c-axis) fields.

The choice of the ac field is crucial for the observation of the paramagnetic peak. Figure 3.7 shows angular scans on a different pure sample with a T_c of 90.1 K that have been made earlier, but for which a much higher ac field (20.8 Oe) had been chosen. From these curves the presence of the paramagnetic peak can be hardly guessed. The strong ac field has wiped out all the details. Even the asymmetry around ab has disappeared.

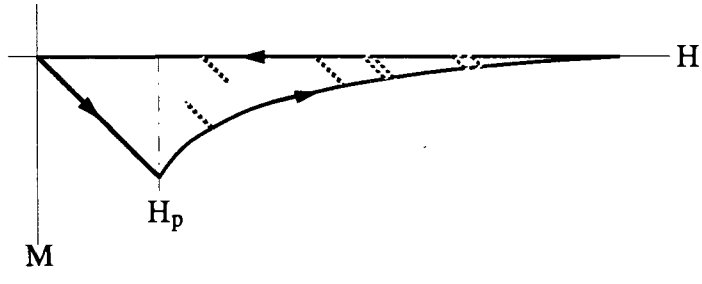

Figure 3.5: dc magnetization loop and superimposed minor ac magnetization loops.

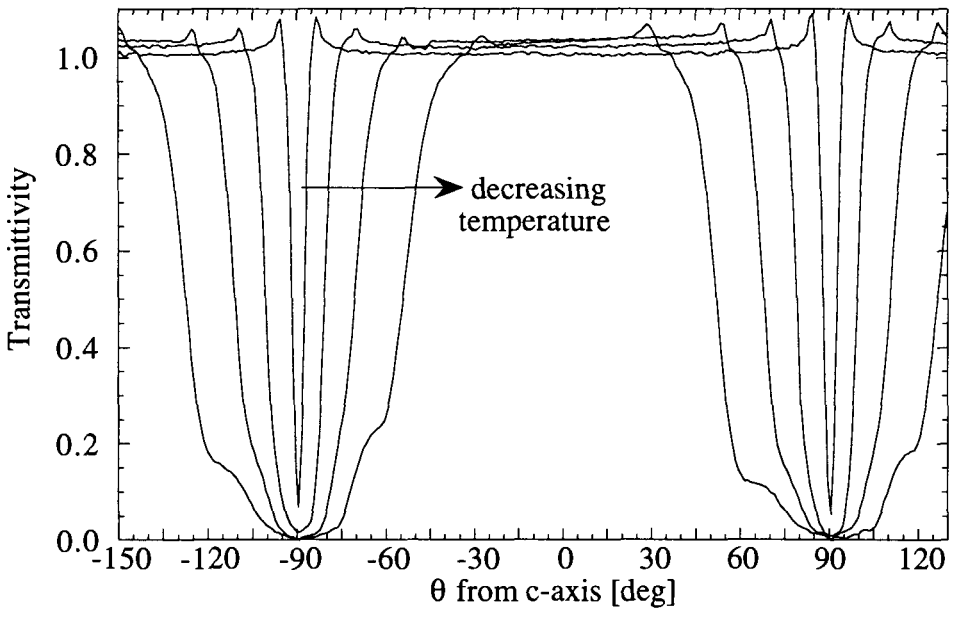

Figure 3.6: Angular variation of the transmittivity. f = 7.75 Hz. H_{ac} = 1.4 Oe. H_{dc}=138 Oe. Temperatures: 90, 84, 78, and 72 K.

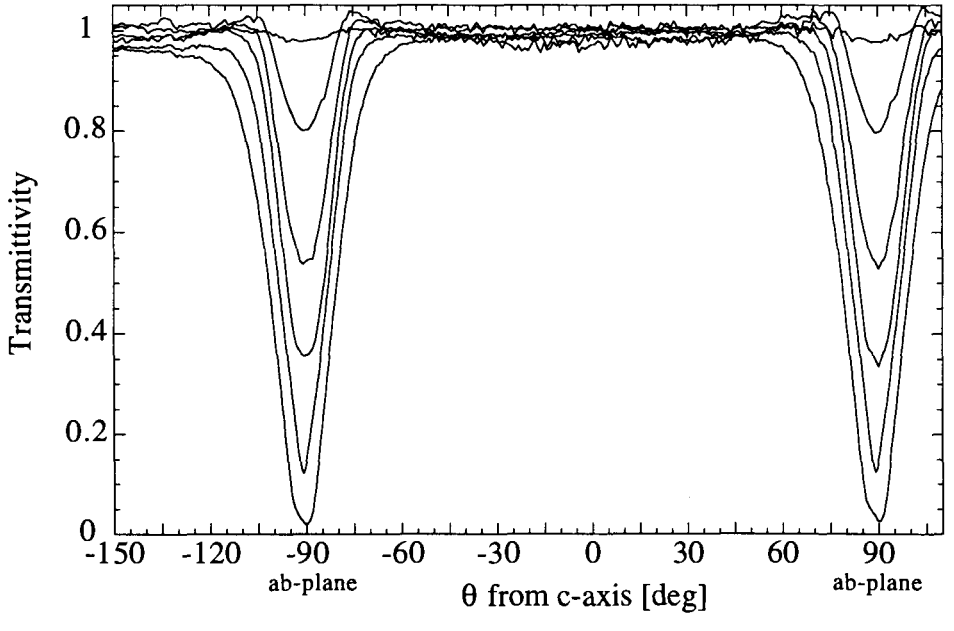

Figure 3.7: Angular variation of the transmittivity for a pristine sample with T_c = 90.1 K. The ac field has an amplitude of 20.8 Oe and a frequency of 7.75 Hz. H_{dc} = 100 Oe. On decreasing the temperature the transmittivity decreases around the *ab*-plane. The temperatures shown are: 90, 88, 84, 80, 76, and 72 K.

3.3.2 Analysis of the paramagnetic peak

The paramagnetic peak that we are going to study has first been observed by Morozov et al. (1996). They show that for a sharp step in the local dc induction the in-phase component of the ac response has the following form:

$$B'_{ac} \simeq \mu_0 H_{ac} + \frac{2\Delta B}{\pi}\sqrt{1-\left(\frac{H_{dc}-H_m}{H_{ac}}\right)^2} \simeq \mu_0 H_{ac} + \frac{2\Delta B}{\pi}\left(1-\frac{1}{2}\left[\frac{H_{dc}-H_m}{H_{ac}}\right]^2\right) \tag{3.4}$$

for $|H_{dc} - H_m| \leq H_{ac}$, where H_{dc} is the applied static field, H_m the melting field and H_{ac} the ac field. See Fig. 3.8 for illustration. It follows that the height of the

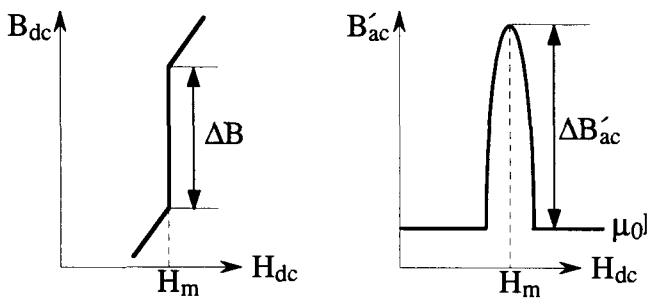

Figure 3.8: Schematic illustration of the induction step at the vortex-lattice transition and the resulting paramagnetic peak in the ac induction.

paramagnetic peak, $\Delta B'_{ac}$, is given by $\Delta B\, 2/\pi$. For B'_{ac} measured as RMS value this transforms into $\Delta B\sqrt{2}/\pi$. The height does not depend on the amplitude of the ac excitation and it allows a precise determination of the height of the magnetization jump. However, the magnetic signal decreases rapidly with distance from the surface. Our InSb sensor is 80 μm thick and the measured signal thus corresponds to the average induction over the thickness. As a result the height of our paramagnetic peak is reduced by a factor of about 3 as compared to the value close to the surface (Morozov et al. 1996). The full width at half maximum of the peak is $\Delta H = \sqrt{3}H_{ac}$ (it equals $\sqrt{6}H_{ac}$ if H_{ac} is given as RMS value). For the present experiment no narrowing of the peak was found for ac amplitudes less than 1 Oe due to the relatively large size of our Hall sensor, which resulted in some smearing of the peak because of the spatial inhomogeneity of B (see Fig 3.9). For higher ac amplitudes a broadening was observed in accordance with the calculation. A finite out-of-phase component B''_{ac} may occur at the peak due to possible hysteresis at the transition (Morozov et al. 1996). In our measurements we were unable to detect any out-of-phase signal related to the peak at temperatures above 70 K.

A more practical problem is that of the determination of the peak parameters. A first approach is illustrated in Fig. 3.10. In this approach the first step consists in drawing the baseline of the peak. Then a parallel to this line is laid tangentially to the peak in order to identify the maximum. The intersection of a vertical line

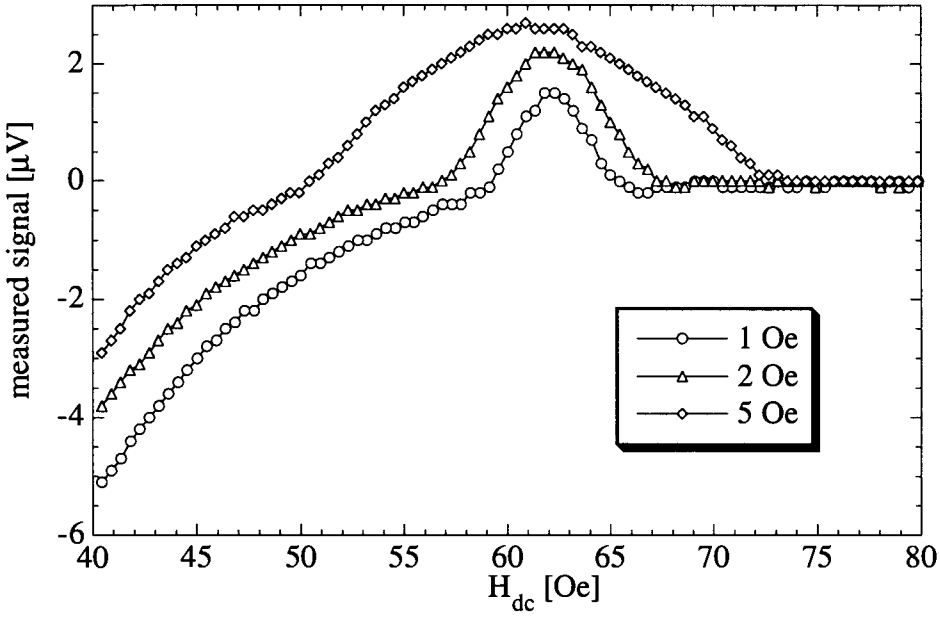

Figure 3.9: Paramagnetic peak measured at different ac amplitudes.

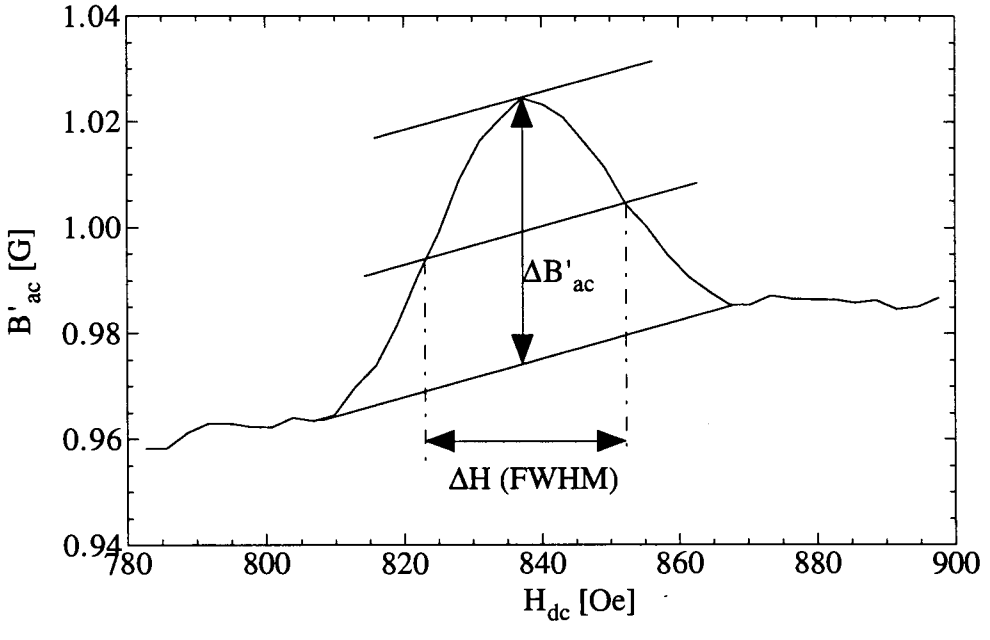

Figure 3.10: Illustration of the first method for the determination of the peak dimensions.

through this point and the baseline gives the point from where the height has to be measured. Another parallel to the baseline through the midpoint of the height determines the width at half maximum. This is the procedure that was used for the results as published in Schmidt et al. (1997). The difficulty with this procedure is, that the choice of the baseline is somewhat arbitrary, resulting in some fluctuations in the measured heights.

A more stable criterion for the peak dimensions is achieved by fitting the peak as well as the main transition curve. A first choice for a function to fit the peak is of course given by equation 3.4. However, this formula correctly describes the shape of the peak near its summit only. It can therefore not account for the tails that are observed at the base of the peak. The origin of these tails lies probably in the fact that the transition is not completely sharp as it has been supposed for the derivation of eq. 3.4. A pragmatic choice for the fitting function, which also reproduces the tails, is given by a Gaussian:

$$\Delta B\, \mathrm{e}^{\frac{(H-H_m)^2}{w}} \tag{3.5}$$

where ΔB is the peak height, H_m is its center and w is a measure for the width. By developing in a Taylor series one obtains:

$$\Delta B \left(1 - \frac{(H - H_m)^2}{2w}\right) \tag{3.6}$$

For dc fields parallel to the c-axis this is equal to eq.3.4, with $w \approx H_{ac}^2$. The full width at half maximum (FWHM) will be given by:

$$\Delta H = 2\sqrt{w \ln 2} \tag{3.7}$$

Again, for fields along c:

$$\Delta H \approx 2\sqrt{\ln 2} H_{ac} \approx 2H_{ac} \tag{3.8}$$

A reasonable fit for the main curve, at least for a certain range of field values around the peak, is obtained with the function:

$$C_1 - C_2\, \mathrm{e}^{-|H/H_0|^p} \tag{3.9}$$

C_1 is the constant value of B_{ac} well above the phase transition and C_2 is the amount by which the ac-field is screened at low temperatures. The two other variables should be merely regarded as fitting parameters although H_0 indicates approximately the mid-point of the shielding transition if this curve is fitted as a whole. The combination of the main-curve function and the Gaussian gave good fits for most of the curves and a typical fit is shown in figure 3.11.

3.3.3 Peak position

As could be seen in Fig. 3.4 the peak position is shifted to higher applied fields as the field is tilted away from the c-axis. One could naively think that the position

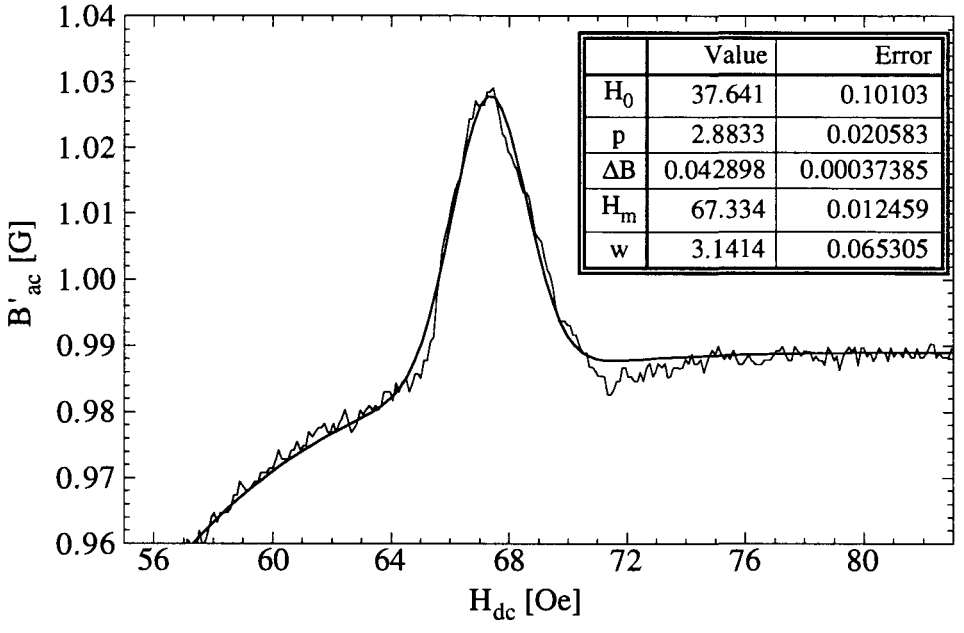

Figure 3.11: Illustration of a fit of the peak with a Gaussian. The main shielding transition is fitted with an exponentially decreasing function. A description of the parameters is given in the text.

just follows a $1/\cos\theta$ law and that the transition still occurs at the same c-axis field $H_m \cos\theta$. Figure 3.12 shows a closer view of the paramagnetic peak of Fig. 3.4 with the measured ac induction now traced against the c-axis component of the field. As can be seen from this figure the naive assumption made above is not correct. The peak height remains almost constant but the peak shifts to slightly lower c-axis fields. To go beyond this qualitative impression the fitting procedure explained above is applied to the data and height, width and position are obtained. First let us consider the angular dependence of the transition field H_m. This is shown in Fig. 3.13a with temperature fixed at 70, 80 and 88 K respectively. The same data, re-scaled to the c-axis component of the field at which the paramagnetic peak is observed, is shown in Fig. 3.13b. In the case of a perfect 2D behaviour the value $H_m(\theta)\cos(\theta)$ should be a constant. This is quite accurately the case for low tilt angles, but as can be seen in Fig. 3.13b the 2D scaling fails for field orientations close to the ab-plane. The angular range around the ab-plane in which deviations are important increases with decreasing field: at the highest temperature (88 K) the 2D scaling seems to describe the data well up to a few degrees from the ab-plane, but at 70 K the deviations start at about 70°.

One might think that the angular dependence of the transition field would be better described by the anisotropic scaling function of Blatter, Geshkenbein and Larkin (1992) which takes into account a non-zero coupling between the superconducting layers giving rise to a non-zero anisotropy $\varepsilon = \sqrt{\frac{m}{M}}$ with m and M being

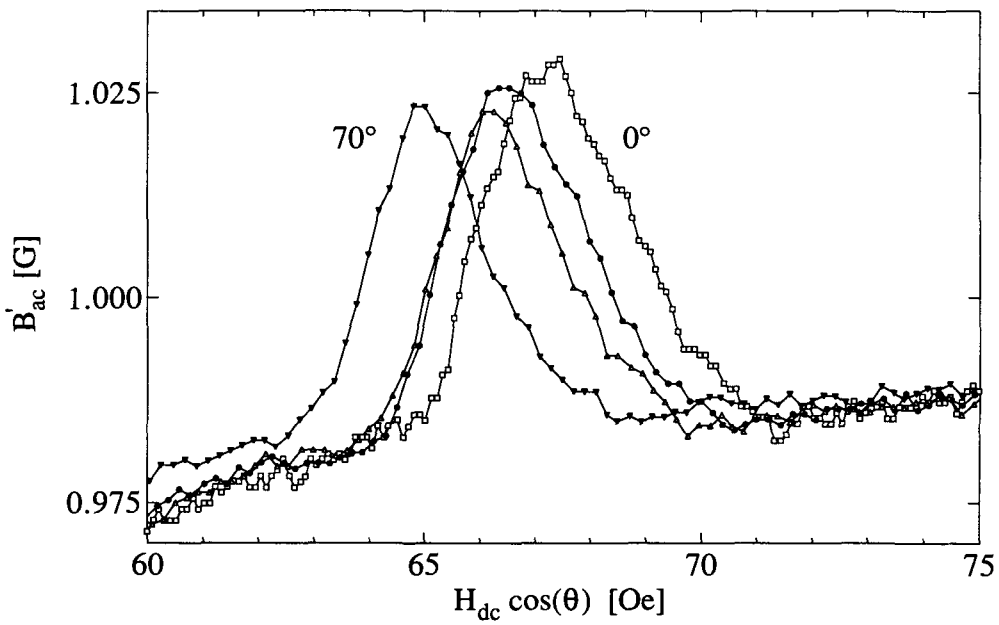

Figure 3.12: Paramagnetic peaks of Fig. 3.4 as a function of the c-axis component of the applied dc-field ($H_{dc}\cos\theta$) for $\theta = 0°, 30°, 60°$ and $70°$. The peak shows a tendency to shift slightly to lower c-axis fields at large angles.

the in and out of plane charge carrier effective masses. However, the difference with a pure cosine scaling is expected to be small for very anisotropic materials like BSCCO. In our case (with θ being the angle between the field and the c-axis) this anisotropic scaling is given by:

$$H_m(\theta) = H_m(0)/\sqrt{\cos^2\theta + \varepsilon^2 \sin^2\theta} \tag{3.10}$$

In order to estimate the anisotropy coefficient we tried several ways of fitting the data. First we kept $H_m(0)$ as a free parameter in addition to ε and allowed also for some error θ_0 in the angle so that the fitting function took the following form:

$$H_{m,0}/\sqrt{\cos^2(\theta - \theta_0) + \varepsilon^2 \sin^2(\theta - \theta_0)} \tag{3.11}$$

With this function we fitted either the left branch or the right branch or the whole angular range of the curves that can be seen in the upper part of Fig. 3.13.

For this temperature as for all the other cases the fits on only one of the branches gave unphysical negative values for ε^2 and values for θ_0 of the order of 0.3–0.4 degrees which is about one order of magnitude higher than the precision with which we determined the orientation of the ab-plane. When fitting both branches θ_0 was of the order of 0.01–0.02 degrees in agreement with our precision and the ε^2 values were positive. In this latter case however, the fit gave values for the transition field that were too low for orientations near the c-axis. This resulted from the fact that the

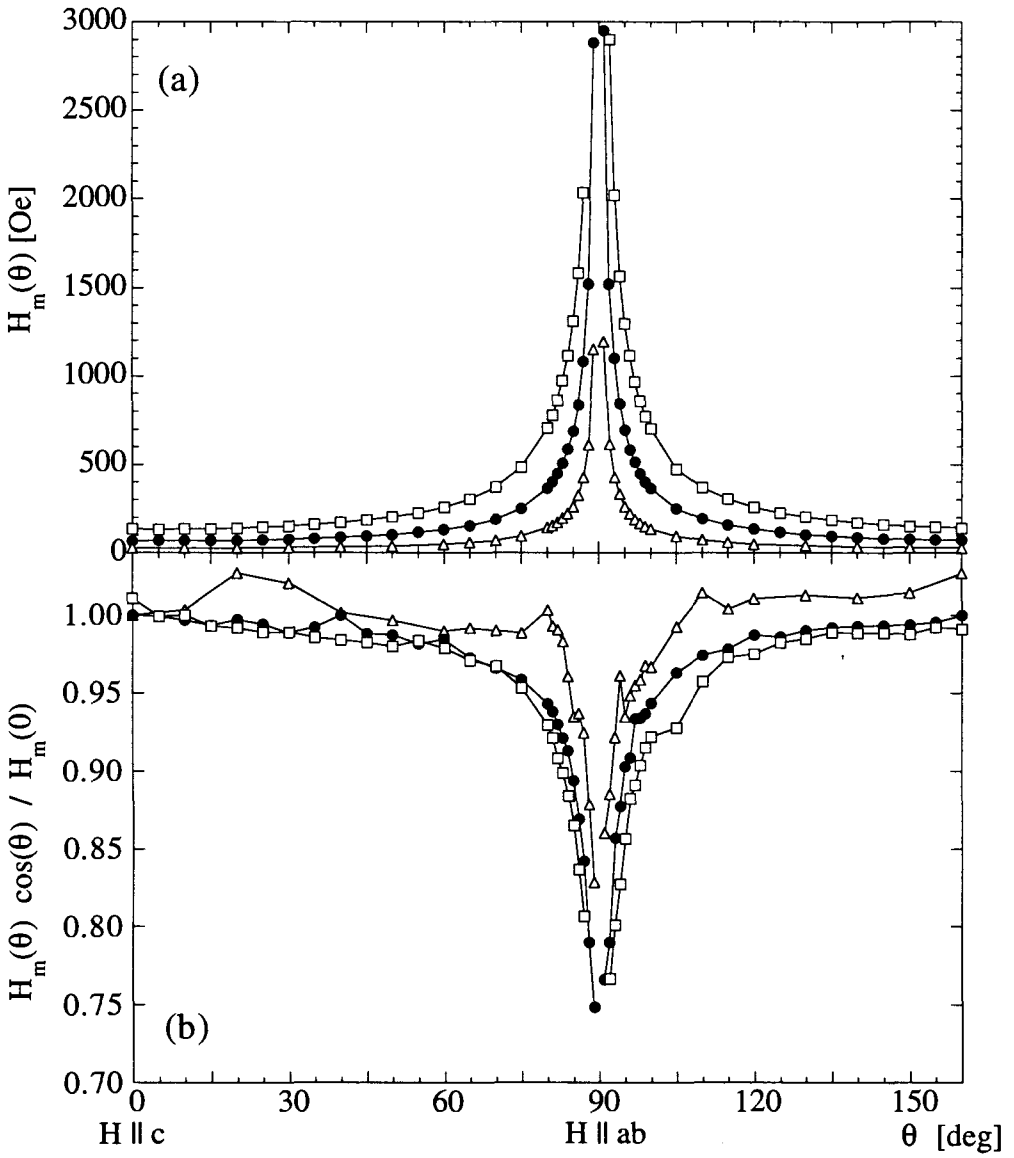

Figure 3.13: (a) Angular dependence of the transition field $H_m(\theta)$ recorded at temperatures of 88 K (△), 80 K (•), and 70 K (□). (b) The same data represented in terms of the normalized c-axis component of the field at the transition $H_m(\theta)\cos(\theta)/H_m(0)$.

curve is very steep near the *ab*-plane giving the points there more weight. It seemed thus more reasonable to fix $H_{m,0}$ to the measured value and to adapt only ε^2 and θ_0. The resulting curve fit and the pure cosine fit for the 80 K data as well as the data points are plotted in Fig. 3.14. The difference between the two functions is very small

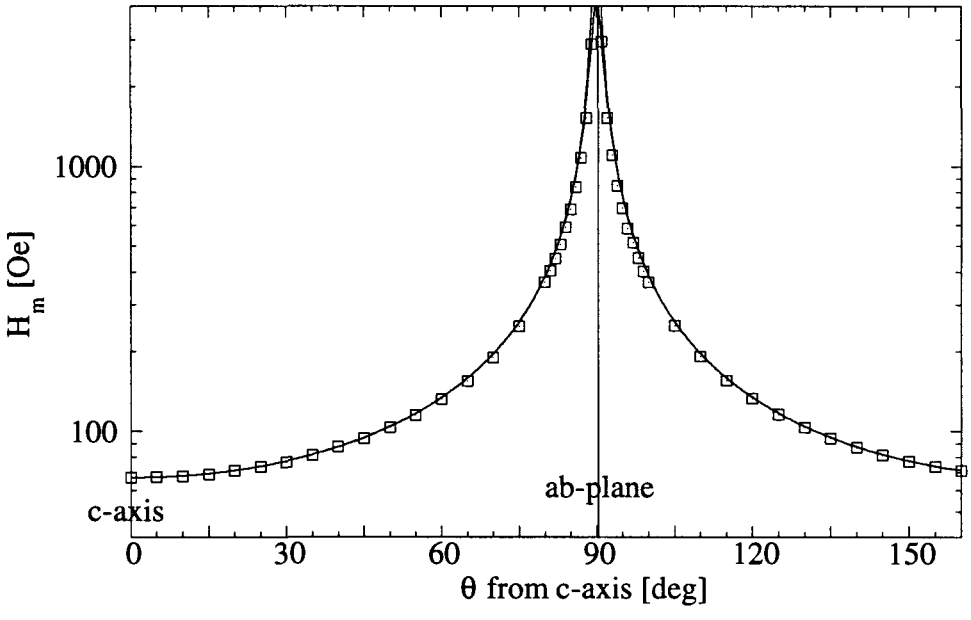

Figure 3.14: Curve fits to the transition field H_m at 80 K. Cosine law and anisotropic law are plotted. The difference is very small and can only be seen very close to the *ab*-plane.

and shows up only very close to the *ab*-plane. This can be seen more clearly in figure 3.15, where the data has been scaled according to the two laws. The curves for 88 K and 70 K look similar. The anisotropic scaling gives slightly better results than the 2D-scaling, but neither of them can account completely for the angular dependence of the transition field. The values of the anisotropy coefficient obtained from these fits should thus be taken with care. They are shown in table 3.1. The apparent

temperature [K]	θ_0 [deg]	ε^2	$1/\varepsilon$
88	0.02±0.01	1.31(7) 10^{-4}	87(2)
80	0.02±0.02	2.53(16) 10^{-4}	63(2)
70	-0.02±0.04	1.03(6) 10^{-3}	31(1)

Table 3.1: Estimated anisotropies (curve fits to H_m)

anisotropy determined from the curve fits diminishes with decreasing temperature. This explains the fact that the high temperature data is better described by the cosine-law: the stronger the anisotropy the more the behaviour is 2D-like.

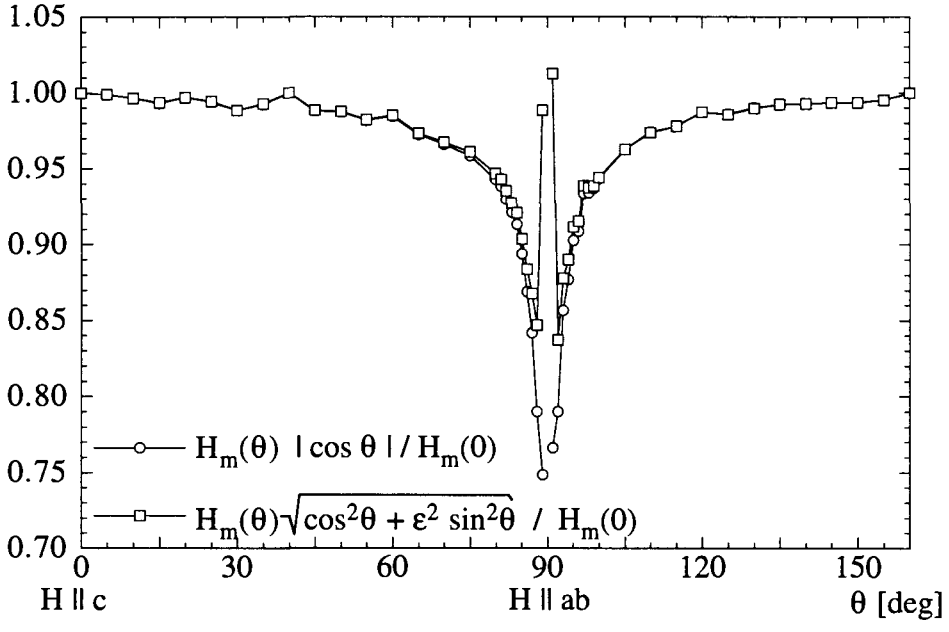

Figure 3.15: The graph shows the measured transition field H_m at 80 K divided by the cosine law on the one hand and by the fitted anisotropic law on the other hand.

3.3.4 Peak width

In the following we will not consider the anisotropic scaling any more, but just investigate the data for deviations from the cosine-law.

One actually might expect that the width of the peak more or less scales in the same way, too. The peak has a finite width even if the dc field is aligned with the c-axis. This is partly due to the finite amplitude of the ac excitation. However, as mentioned before, even for vanishing ac amplitude the width of the peak would not decrease below a certain value because of the finite size of the Hall probe. Therefore, in order to move the front of the transition over the whole probe width, the external field has to be changed by a finite amount. Then, if only the c-axis component of the field is important, the broadening of the peak with increasing tilt has a purely geometric origin. In order to change the c-axis field by the necessary amount to move the transition front over the sample width, the tilted field has to be changed by an amount that is increased by a factor $1/\cos\theta$. Figure 3.16a shows the full width at half maximum of the peak as a function of angle. The same data multiplied by $\cos\theta$ is shown in Fig. 3.16b. As can be seen from this figure the peak width also follows a cosine-law up to 10° or less from the ab-plane. Close to the ab-plane the width grows faster than $1/\cos\theta$.

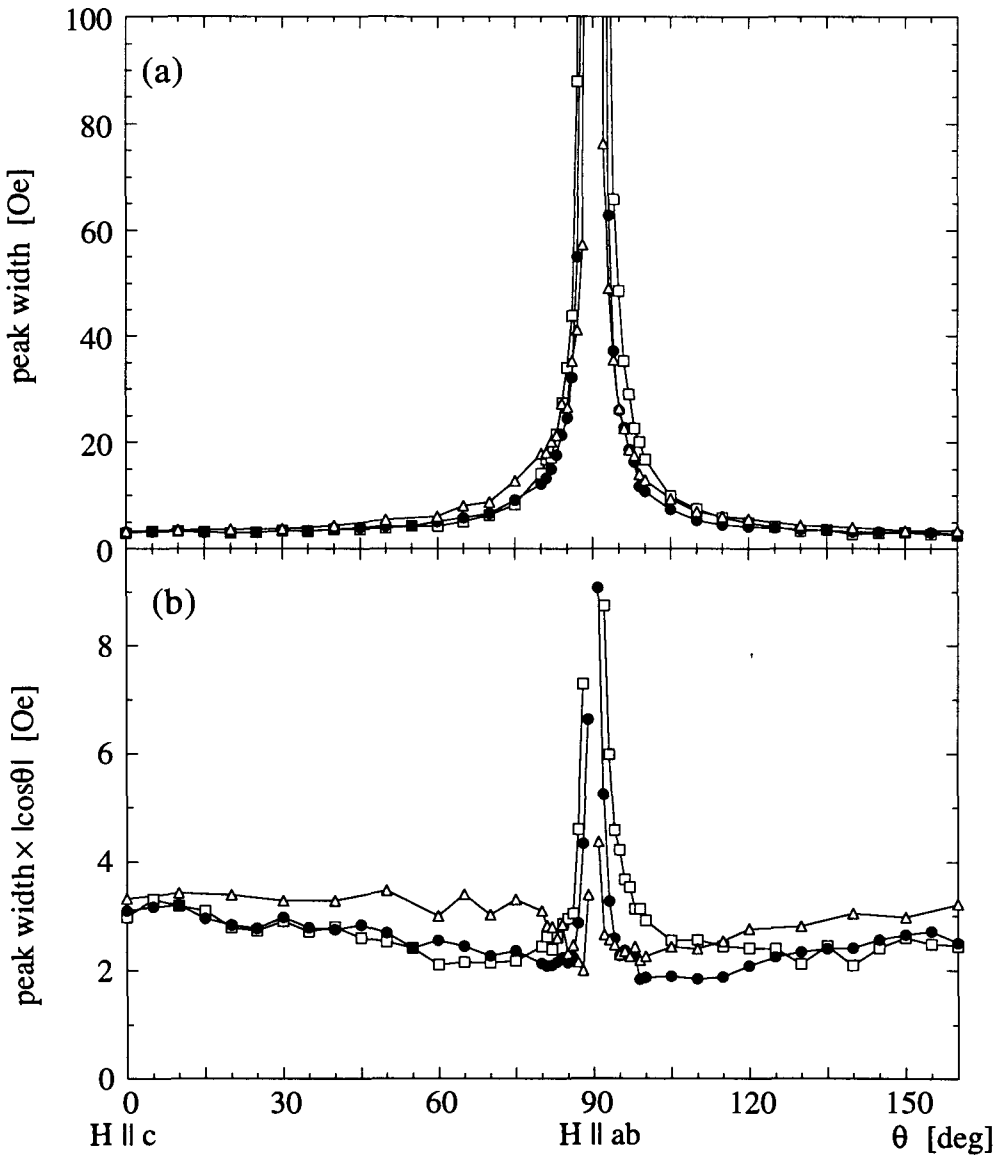

Figure 3.16: (a) The width of the paramagnetic peak as a function of angle for temperatures of 88 K (△), 80 K (•), and 70 K (□). (b) Peak width times $|\cos(\theta)|$ as a function of angle.

3.3.5 Peak height

The peak heights as determined by the curve fit at the three temperatures considered are shown in Figures 3.17, 3.18 and 3.19. The error in the measurement of the height is estimated as 1.5 mG. This estimation is based on the noise level appearing in the data.

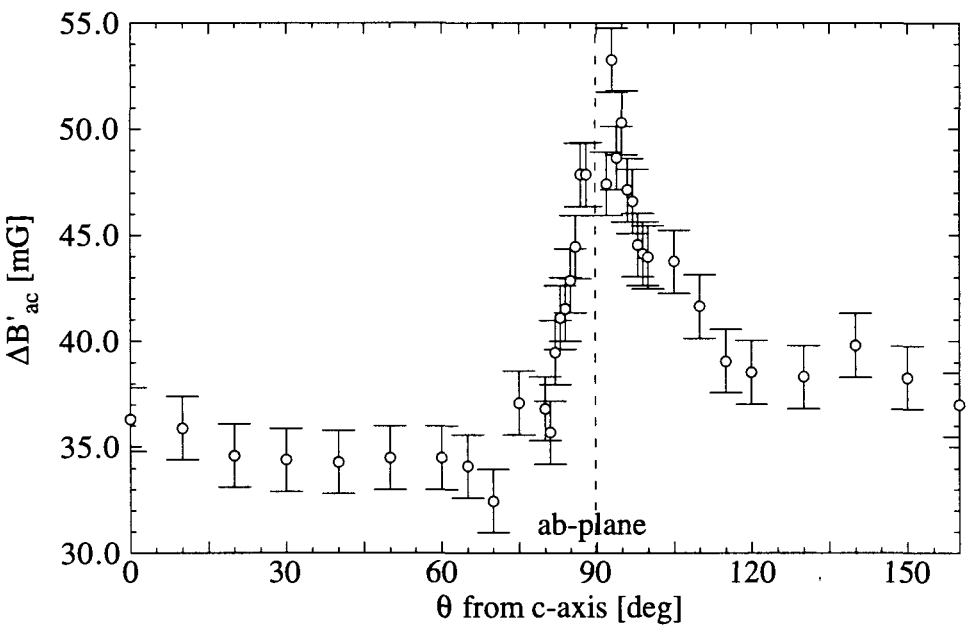

Figure 3.17: Paramagnetic peak height $\Delta B'_{ac}$ as a function of the applied field angle θ with respect to the c-axis at $T = 88$ K.

A common feature of the different curves is the slight asymmetry with respect to the ab-plane. It is not clear what causes this asymmetry. Another common feature is the increase of the peak height on approaching the ab-plane.

As we have seen above, the effective c-axis first order transition field $H_{m,c} = H_m(\theta)\cos\theta$ decreases on increasing the ab-plane field. This decrease in transition field can be translated into an increase in transition temperature. This effective increase in transition temperature should in its turn correspond to a variation of the peak height (Zeldov et al. 1995; Morozov et al. 1996). In order to check this we gathered some data in order to be able to trace the transition line in the field and temperature range of interest (see Fig. 3.20). In this range the decoupling prediction $H_D(T) = H_0(T_c - T)/T$ gives a good description of the transition line. A fit to the data of Fig. 3.20 gives $T_c = 93.2$ K and $H_0 = 396$ Oe. With this information it is now possible to translate the angular dependent transition field into an angular dependent transition temperature. Plotting the entire peak height data against this effective temperature allows for a comparison with existing data (Zeldov et al. 1995; Morozov et al. 1996). The result is shown in Fig. 3.21. In a global manner the

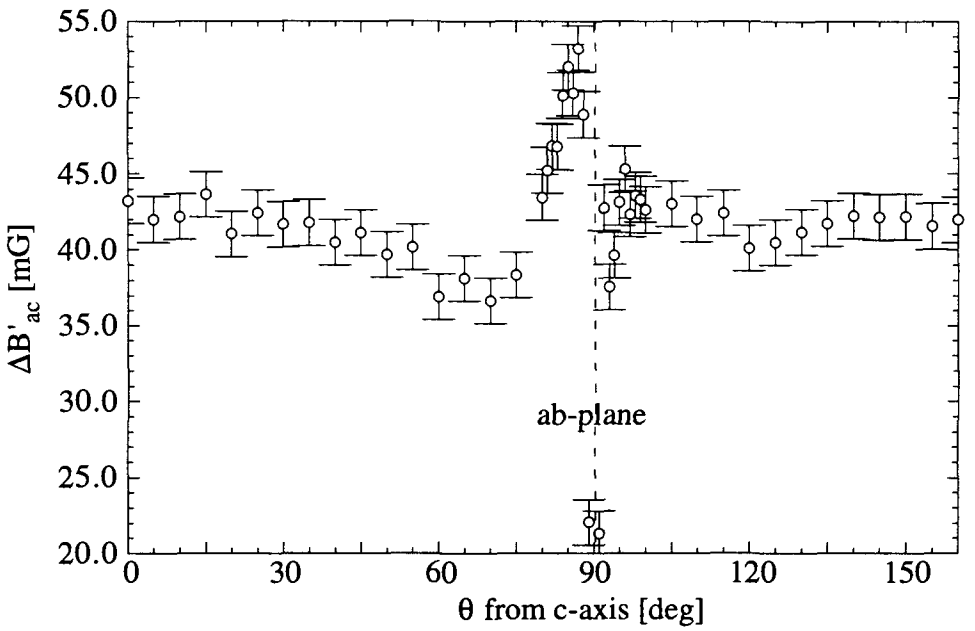

Figure 3.18: $\Delta B'_{ac}$ as a function of the applied field angle θ at $T = 80$ K.

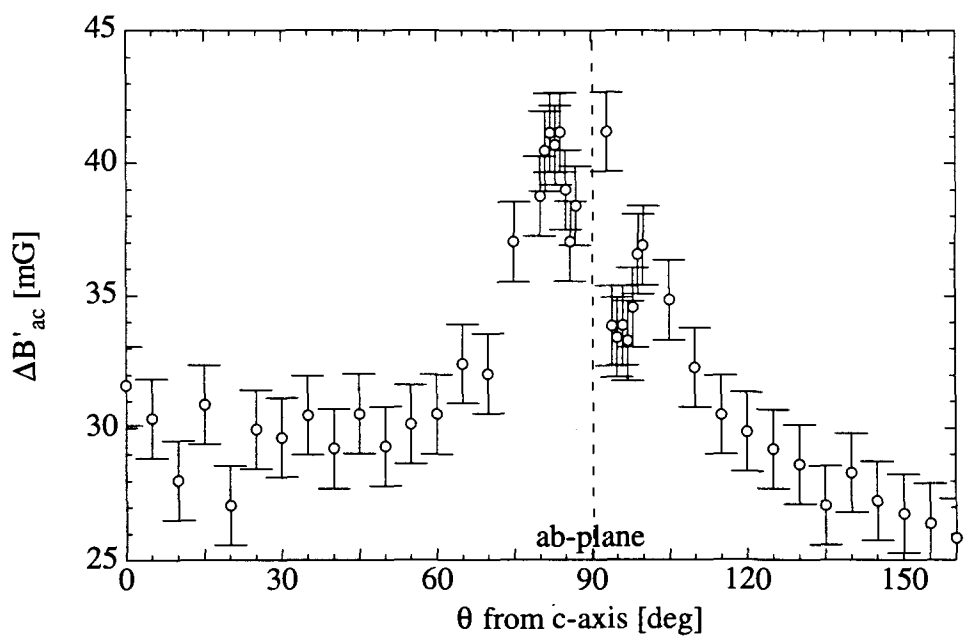

Figure 3.19: $\Delta B'_{ac}$ as a function of the applied field angle θ at $T = 70$ K.

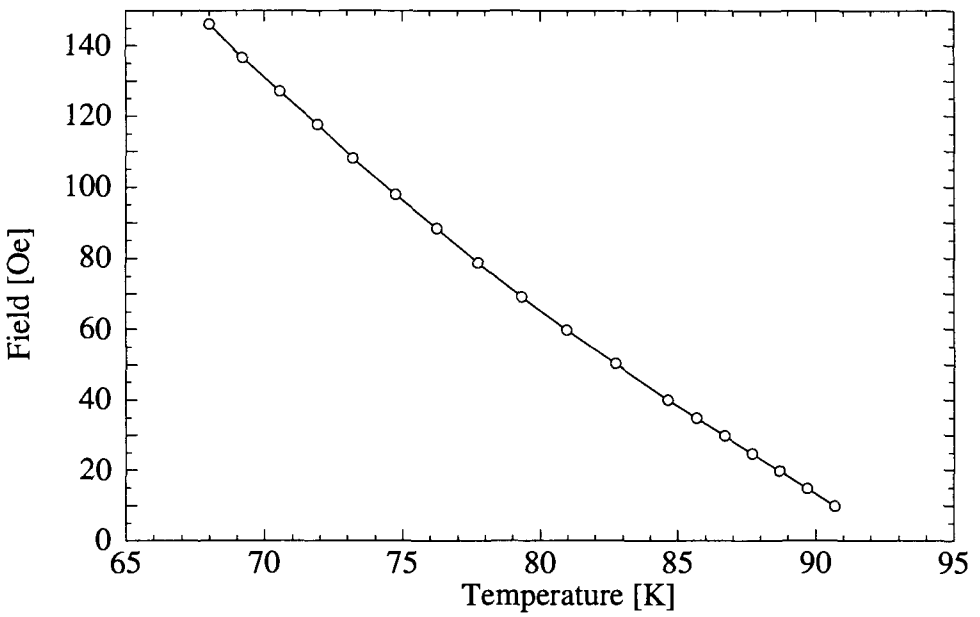

Figure 3.20: H_m as a function of temperature.

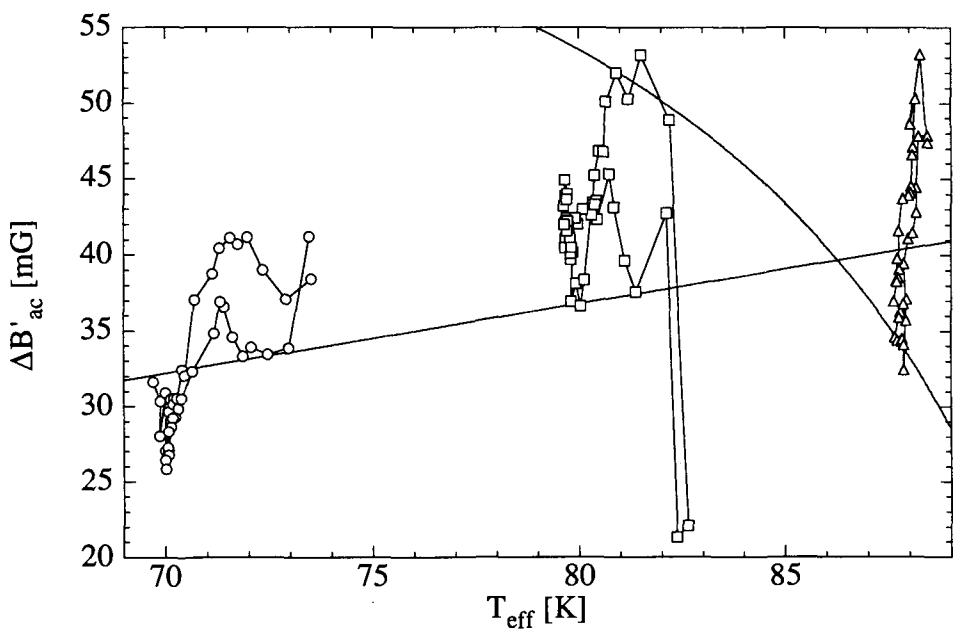

Figure 3.21: Peak heights plotted against the effective transition temperature (see text). The figure shows also the theoretical curves of Dodgson et al. (1998), eq. 3.3

data at 70 and 80 K show the same trend as earlier observations: an increase of the peak height with temperature. However, this effect seems stronger in the present measurements than what has been observed before. The 88 K data on the other hand does not follow the same trend and moreover exhibits a very big change in a narrow temperature range. Even if there is some influence of the change in transition field, it seems completely negligible compared to some more direct influence of the in-plane field.

3.3.6 Step at the peak position

When the dc field is tilted by about 80 degrees or more, a step is observed in the ac screening just below the FOT (see Fig. 3.22 for an example). Such a step corresponds to a rapid decrease of the pinning- or barrier-related critical current or activation barrier near the FOT. The sudden disappearance of shielding current is reminiscent of observations by Chikumoto et al. (1992) and Khaykovich et al. (1997). The height

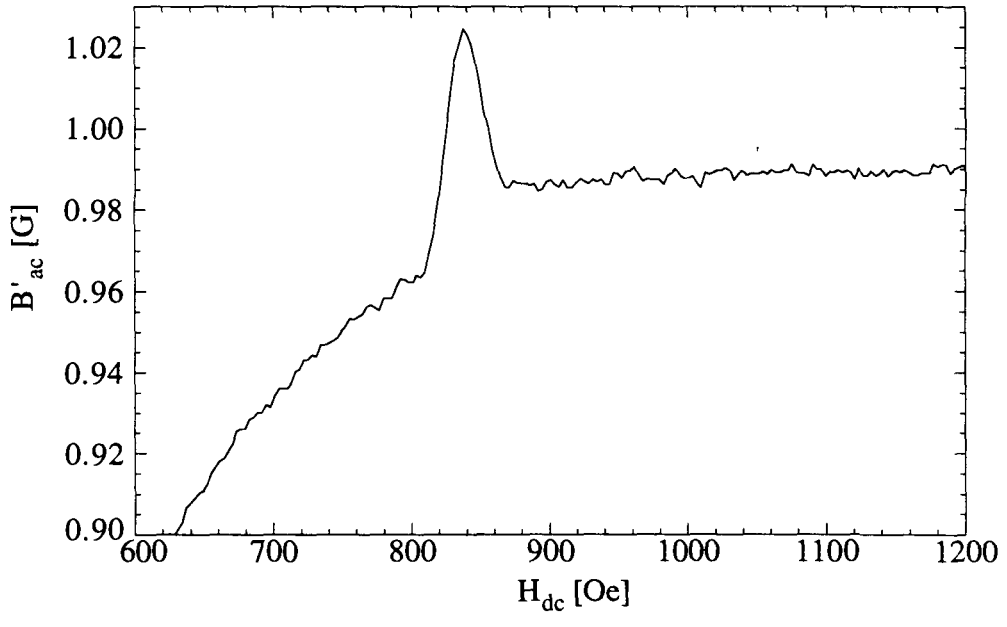

Figure 3.22: For orientations of the dc field close to the *ab*-plane (here θ=86 deg) a step coincides with the peak.

of this step, as obtained from the curve fit, is shown in Fig. 3.23. The error bars are based on the noise level in the signal. However, the fluctuations in the curves infer that the uncertainty might be even greater. Despite these fluctuations it seems clear that the step increases on approaching the *ab*-plane. The abrupt appearance of the step is due to the fact that very small steps are not easily detected.

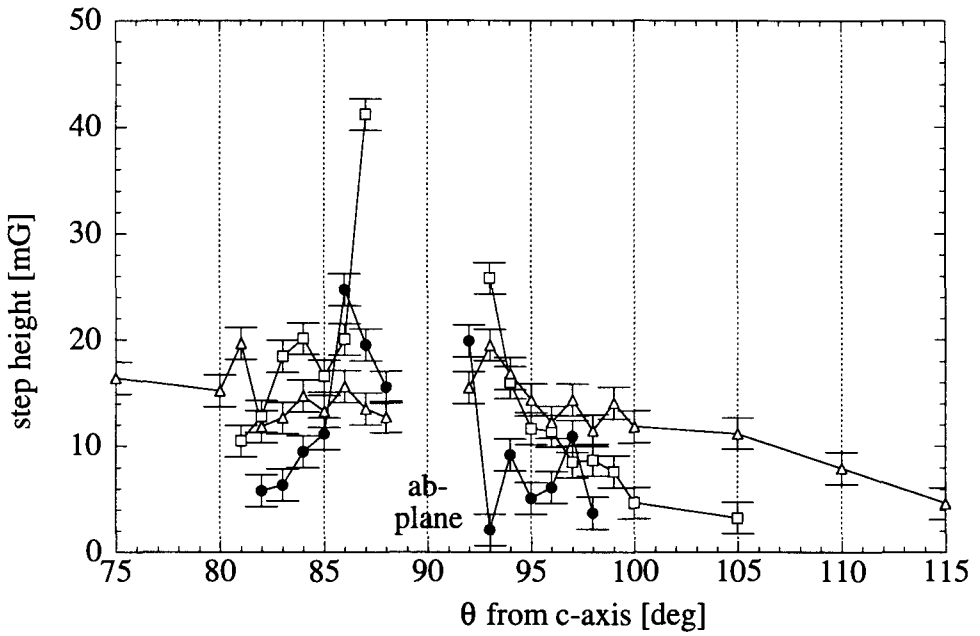

Figure 3.23: The step at the peak position as a function of angle for temperatures of 88 K (△), 80 K (•), and 70 K (□).

3.3.7 Irreversibility line

As shown in Fig. 3.24 the paramagnetic peak in the ac induction is accompanied by a small peak in the third harmonic response. It follows clearly from this figure that the peaks in the ac induction and the third harmonic fall together with the onset of irreversibility. First order transition line and irreversibility line are identical.

3.3.8 Further observations

In the large majority of the cases the background curve did not present any interesting features. However, there is one noticeable exception. At 70 K and at ± 2 degrees from the *ab*-plane a step in the main curve was found that did not coincide with the peak. Figure 3.25 shows the corresponding data. In spite of the slight differences in the two curves the position of this step is almost identical for the two orientations of the static field. A comparison with the 80 K data shows that the step is not an artifact due to the Hall probe, since it does not appear for that temperature and the same fields. This shows also that the elevated in-plane field alone is not sufficient to produce this step as it occurs only at the lowest temperature.

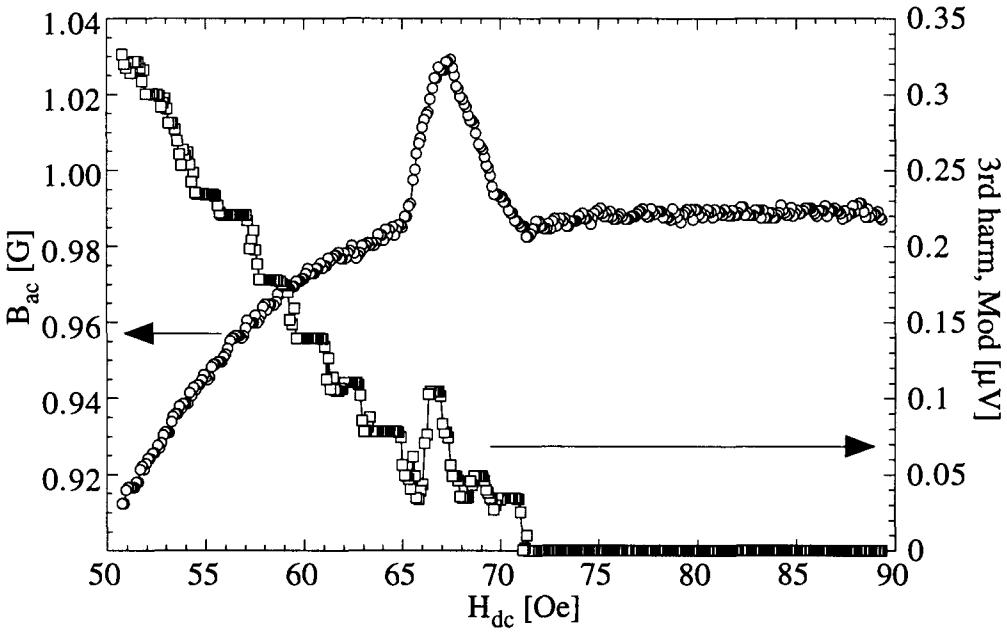

Figure 3.24: Measured ac induction and third harmonic voltage as a function of field. The third harmonic shows a small peak related to the paramagnetic peak in the ac induction. H_{dc} is parallel to the c-axis. The steps in the third harmonic are due to the instrumental resolution.

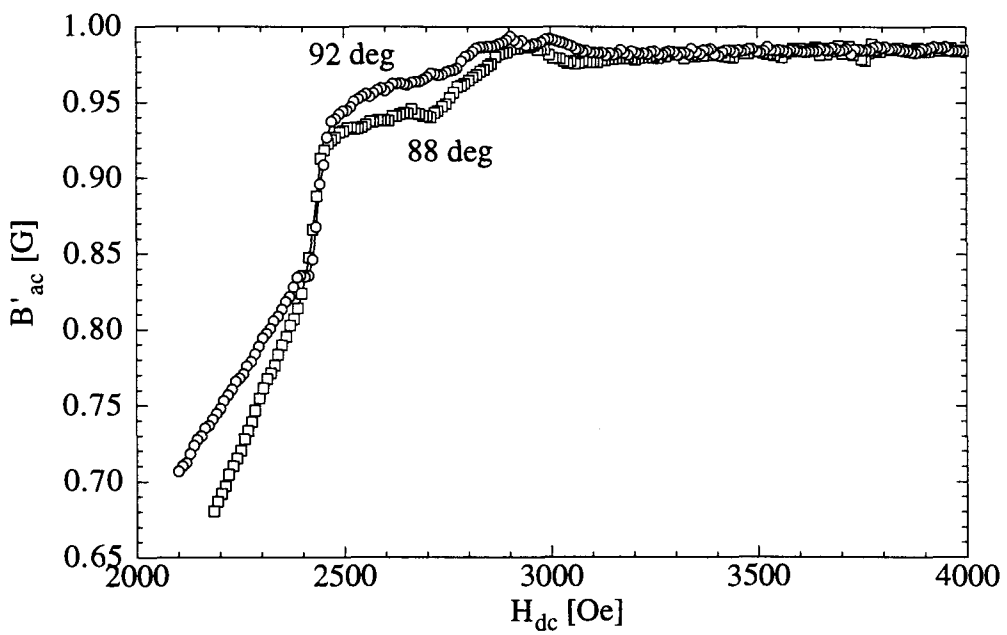

Figure 3.25: The step in the main transition curve at 70 K. $\theta = 88$, 92 deg ($\pm$ 2 deg from ab-plane).

3.4 Discussion

Taking account of all the facts of the previous section it is clear that the c-axis melting is not completely independent of an additional in-plane field. Obviously the ab-plane field has some influence in terms of which the data has to be discussed. Its influence becomes even more apparent when the c-axis melting field is traced as a function of the field component in the ab-plane, as it is shown in figures 3.26, 3.27 and 3.28. These figures show that the ab-plane field reduces the transition

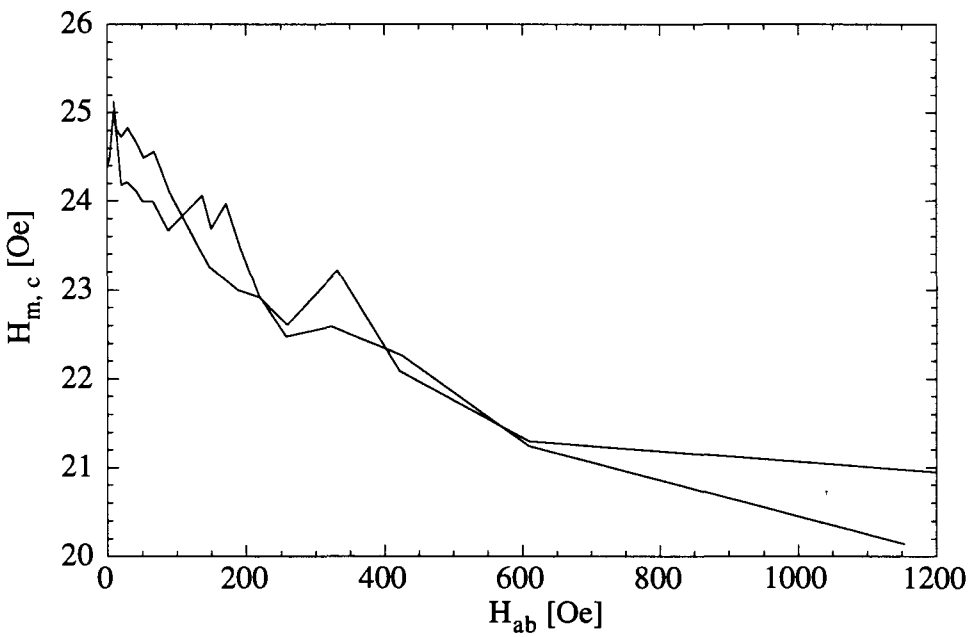

Figure 3.26: c-axis melting field as a function of the applied in-plane field at $T = 88$ K.

field. The rightmost points in Fig. 3.26 and 3.27 are those where the field is only 1 degree away from the ab-plane. They deviate appreciably from the other data. In Fig. 3.28, corresponding to a temperature of 70 K, the data includes only angles up to 88 degrees. Beyond that angle correct fits were not possible any more. Therefore the flattening of the curve is not observed at this temperature. If, in a first time, those points very close to the ab-plane are neglected the reduction of H_m can be regarded as approximately linear in field with perhaps some slight positive curvature.

An influence of the in-plane field on the transition along c can be understood in terms of the Josephson coupling between the layers. This coupling remains important up to fields of the order of B_{cr}, the 2D to 3D crossover field. The 2D to 3D crossover roughly occurs when the inter-vortex distance $a_0 = (\Phi_0/B)^{1/2}$ becomes comparable to the Josephson length $\lambda_J = \gamma s$. s is the interlayer distance and $\gamma = 1/\varepsilon$ the anisotropy. This leads to $B_{cr} = \Phi_0/(\gamma s)^2$. Taking for γ the rather high value of 200 we get for BSCCO $B_{cr} \approx 170$ G. More accurate estimates would actually lead to upward corrections of this value (e.g. equation (5) in Glazman and

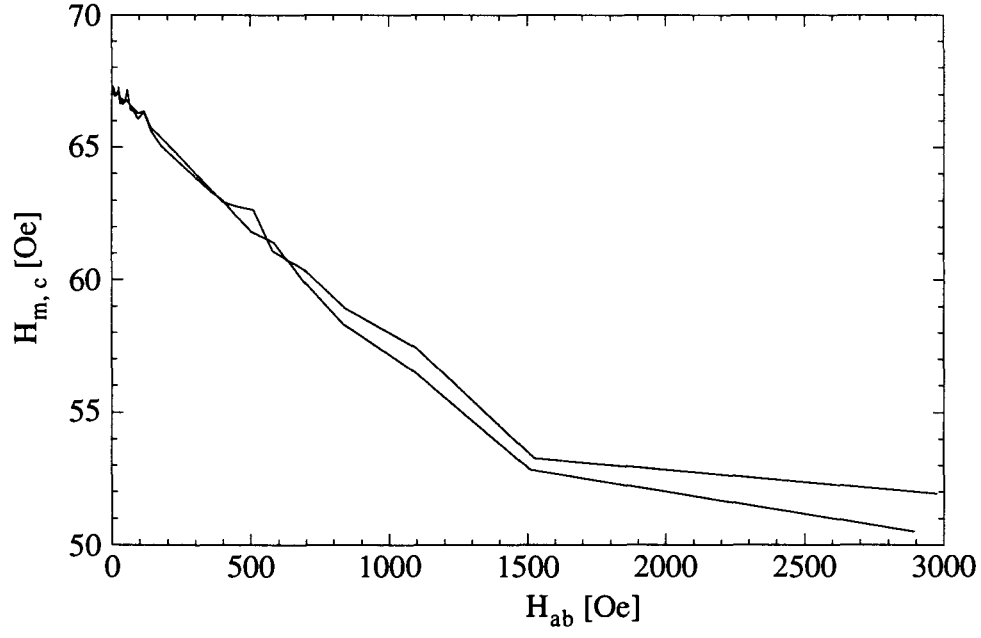

Figure 3.27: c-axis melting field as a function of the applied in-plane field at $T = 80$ K.

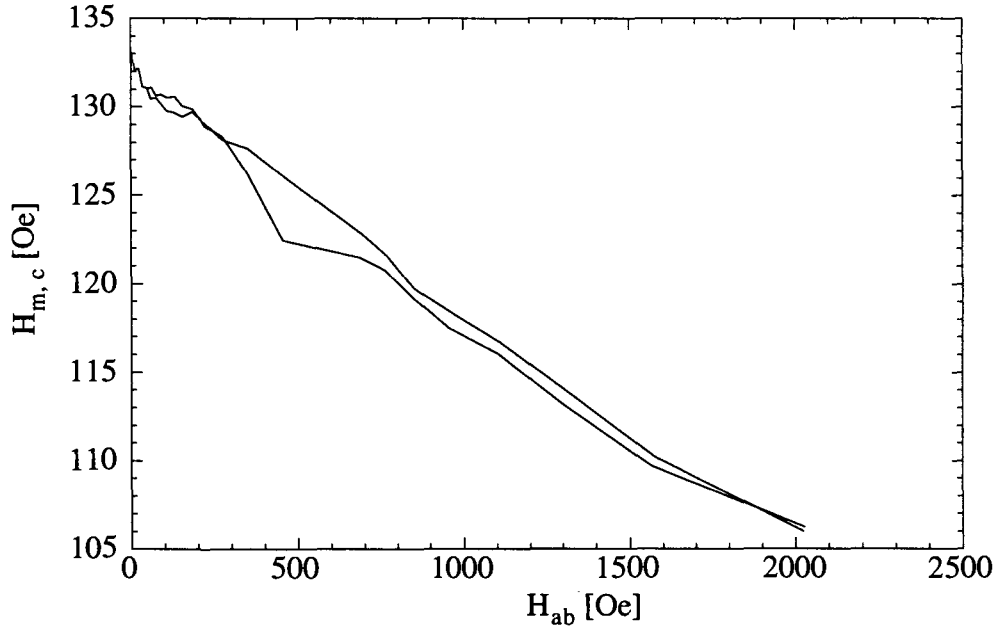

Figure 3.28: c-axis melting field as a function of the applied in-plane field at $T = 70$ K.

Koshelev (1991)). The same is true if we take lower values for γ. Anyway, in every observed case the c-axis field lies below the rough estimate such that the Josephson coupling is always important.

Usually the coupling between the layers is expressed in terms of a coupling constant ρ to which the maximal Josephson current is proportional. Coherence length and penetration depth are given by Bulaevskii et al. (1992)

$$\xi_c^2 = s^2\rho/2,\ \lambda_c^2 = \Phi_0^2/8\pi^2 H_c^2 \xi_c^2 = \Phi_0^2/4\pi^2 H_c^2 s^2 \rho \tag{3.12}$$

It follows that the penetration depth λ_c increases as the coupling between the layers decreases. This leads to a coupling dependent anisotropy as the planar coherence length and penetration depth will remain unperturbed:

$$\varepsilon = \frac{\lambda_{ab}}{\lambda_c} = \frac{2\pi\lambda_{ab} H_c s}{\Phi_0}\sqrt{\rho} \tag{3.13}$$

Suppose now that the coupling between the layers is influenced by a field component parallel to the planes. Most probably one would expect a weakening. It is then immediately clear why the fits of the angular dependence of H_m failed. The cosine-fit fails because the material has some finite anisotropy, i.e., there is some coupling between the layers. The anisotropic model on the other hand fails due to the field-dependence of this anisotropy.

For the case of simultaneous electromagnetic and Josephson coupling between the layers, which is very likely the case here, Blatter, Geshkenbein, Larkin, and Nordborg (1996) give the following line shape for the melting line for fields parallel to the c-axis direction:

$$B_m^{em,J} \approx \frac{\Phi_0}{\lambda_{ab}} \frac{\pi c_L^2 \sqrt{\ln(1 + 4\lambda_{ab}^2/c_L^2 a_0^2)}}{4} \frac{\varepsilon\varepsilon_0}{k_B T} \tag{3.14}$$

This shows explicitly how the transition field depends on anisotropy. λ_{ab} is the temperature dependent planar penetration depth and c_L the Lindemann number. However, the dependence of the coupling constant ρ on the in-plane field B_{ab} is not clear. A possible guess might be based on the field dependence of a (short) planar Josephson junction (see for example Tilley and Tilley (1994)). There the maximal Josephson current depends on the field in the plane like $\sin(\pi\Phi/\Phi_0)/(\pi\Phi/\Phi_0)$. The oscillations with the number of vortices in the junction are likely to be a characteristic of the single junction only. Even if it would be correct for the coupling between one pair of layers, the effect would be smeared out due to the shear number of such pairs and the slightly varying local field contained within them. The $1/B$ dependence of the maximal current (and thus the coupling constant) might nevertheless survive in the system of coupled layers. This would lead to a B-dependence of the anisotropy ε as $1/\sqrt{B}$ and the same would be true for the transition field B_m.

The simple $1/\sqrt{B}$-form cannot be used to fit the data due to its divergence. A form that does not diverge and that is much closer to the shape for a single junction

is given by $1/\sqrt{B/B_0+1}$. A fit to the data with this formula is possible but it is not clear up to now if this is pure coincidence and how one could cross check if the values of B_0 are reasonable or not. The values that have been obtained from the fits are: (3680±65) G at 70 K, (2670±40) G at 80 K, and (1680±110) G at 88 K

An alternative to the above dependence of B_m on B_{ab} is given by the decoupling prediction of Glazman and Koshelev (1991). According to Blatter et. al. (1996) a strong anisotropy $\varepsilon < s/\lambda_0$ would lead to a decoupling line that is determined by the electromagnetic coupling alone and only in the case of an intermediate anisotropy Josephson coupling could be determinating. Recent experiments by Lee et. al. (1997) seem to indicate that the latter case nevertheless occurs in BSCCO:2212 at high temperatures. They obtain a good fit above 70 K ($T_c \approx$84 K) with the formula

$$B_{dc}^J = \frac{\Phi_0}{\lambda_{ab}^2} c_D \frac{\varepsilon^2 \varepsilon_0 \lambda_{ab}^2}{k_B T s} \tag{3.15}$$

In this decoupling scenario the constant c_D plays the role of the Lindemann constant for melting. According to formula 3.15 the transition field $H_m = \frac{1}{\mu_0} B_{dc}^J$ depends on the in-plane field as $1/B_{ab}$ which means an even stronger curvature. For a curve fit the same problems of interpretation as before would occur.

The growth of the magnetization step on approaching the *ab*-plane can also be understood in terms of the above reasoning. Due to the in-plane field the transition occurs at lower vortex densities. However, as the melting coincides with the decoupling of the layers the strength of the coupling has no importance in the pancake gas so that the same density of (pancake) vortices is recovered independently of the in-plane field. It follows that the magnetization step grows as the field component parallel to the layers increases.

Let us turn now to the step at the peak position. This step signifies a rather abrupt increase of screening at the transition. Due to its absence at low in-plane fields one might conclude that it is not connected to the *c*-axis field but to the in-plane field. Supposing that there is some creep of Josephson vortices via kink sliding then the freezing of the pancake gas might make the sliding more difficult. This would decrease the resistance and increase the shielding.

No explanation could be found for the additional step observed at 70 K.

3.5 Conclusions

The susceptibility measurements presented in this chapter show that the first order transition in the vortex lattice persists in the presence of large in-plane fields contrary to an earlier report based on torque magnetometry (Farrell et al. 1996). However, the in-plane field effectively increases the anisotropy of the system, and thus leads to the observed changes in the characteristic quantities of the first order transition. The state of the vortices perpendicular to the planes seems to influence in its turn

the dynamics of the parallel vortices. This can be understood if creep of parallel vortices happens via kink sliding involving pancake vortices.

In order to go beyond the rather qualitative results outlined above, a much more rigorous treatment would be necessary. Especially should the vortices be treated as tilted lines and not as independent parallel and perpendicular vortices. This extreme case of combined lattices has actually been studied by Bulaevskii et al. (1992), but it is not obvious that this configuration is a stable one (Blatter et al. 1994).

Chapter 4

Anisotropy of pinning by columnar defects in $Bi_2Sr_2CaCu_2O_8$

4.1 Introduction

Columnar tracks produced by heavy ion irradiation increase the current carrying capabilities of $YBa_2Cu_3O_7$ (Y-123) (Civale et al. 1991; Konczykowski et al. 1991a; Konczykowski et al. 1991b; Hardy et al. 1991) and $Bi_2Sr_2CaCu_2O_8$ (Bi-2212) (Gerhäuser et al. 1991; Thompson et al. 1992). Moreover, in Y-123 the defects introduced an anisotropy in addition to the intrinsic one due to the layered structure: the sustainable current density has been found in magnetization measurements to be highest for alignment of the field with the columnar defects (Civale et al. 1991; Hardy et al. 1991). These experimental results prompted a theoretical description of the vortex system in the presence of a set of parallel columnar defects (CDs) by Nelson and Vinokur (1993). These authors mapped the problem of a vortex in the presence of columnar defects onto that of localization of a quantum particle in two dimensions. The vortex trajectory along the defect direction then corresponds to the temporal trajectory of the two-dimensional particle in a random potential, and the calculations can be conveniently done in the particle system. If more than one vortex is present in the system then each of them gives a positive contribution to the partition function of the system, i.e., the vortex system obeys Bose statistics. Nelson and Vinokur (1993) showed that at low temperatures and fields a glassy phase, the *Bose glass*, is possible in which the vortices are localized by the columnar defect potential. The Bose glass theory could indeed account for the anisotropy of pinning. This is in contrast to the vortex glass model (Fisher 1989) in which isotropic pinning by point defects is considered and where no anisotropy is expected.

When the local field is aligned with the columnar defects the vortex can follow a defect over its entire length. It can then only move by thermal excitation and subsequent growth of vortex loops. Depending on current density the nucleation mechanism of creep is expected to be either half loop unbinding or double-kink

excitation. These two mechanisms are illustrated on the left hand side of Fig. 4.1. A: half loop unbinding, B: double kink excitation. For large currents $j_1 < j < j_c$ the thermal unbinding of a small vortex half loop is sufficient for the Lorentz force F_L to depin the vortex, which escapes into the space between columns. For smaller current density the size of the critical loop grows until at a current density $j_1 = U_0/\Phi_0 d$ its lateral extend equals the mean intercolumn spacing d. For currents below j_1 the critical nucleus is expected to be a double kink configuration stretching out to a nearby column. Under the action of the Lorentz force the two kinks slide towards the surface and a net motion of the vortex results.

These flux creep mechanisms, half loop unbinding and double kinks, give rise to the following E–j law:

$$E \approx \rho_0 J \exp[-(E_k/k_B T)(J_0/J)^{\mu}] \tag{4.1}$$

The exponent μ is 1 for half loop activation and 1/3 for double kink excitation.

The critical current density j_c above which the vortex can be depinned under the action of the current only is estimated at low temperature to be close to the depairing current j_0. This follows from an estimate of the maximal pinning force, which is the derivative of the pinning potential. The depinning current is obtained by dividing this force by the flux quantum Φ_0. For a potential of depth U_0 that decays over a distance b_0, the column radius, this estimate gives $j_c = U_0/\Phi_0 b_0$. b_0 is of the order of ξ, the coherence length, and U_0, which is the difference in free energy between the situations where the vortex is on a column and where it is off a column (at $T = 0$), is of the order of ϵ_0, the energy of vortex formation. Making these substitutions, the expression for the current becomes $\epsilon_0/\Phi_0\xi = j_0$, the depairing current, apart from a numerical factor.

For tilts of the external field with respect to the columnar defects smaller than a critical angle θ_c the vortices remain locked on the defect, because the increase in energy due to misalignment of B and H is more than compensated by the pinning energy. Beyond this lock-in angle the competition between these energies leads to the formation of kinks by which the vortex jumps from one column to another and thus is able to follow on the average the direction of the external field. This is illustrated on the right hand side of Fig. 4.1. A current perpendicular to these kinks and to the columns exerts the same Lorentz force per unit length $f_L = j\Phi_0$ on the kinks and on the trapped sections, but the kinks move much more easily under the action of this force since their motion is only hindered by the much weaker background pinning by point defects. This is the situation that naturally arises in magnetization experiments since the bending of the vortices is given by $\vec{\nabla} \times \vec{B} = \vec{j}$, which means that the vortex bends perpendicular to the current direction. When the field is tilted the different situation of current flowing parallel to the kinks also occurs. The Lorentz force on the kinks is then zero. If the anisotropy of pinning is tested with a transport current, the observed result is rather different, depending on which of the two cases applies. This is illustrated in Fig. 4.2(a) with schematic angular dependences for the two cases.

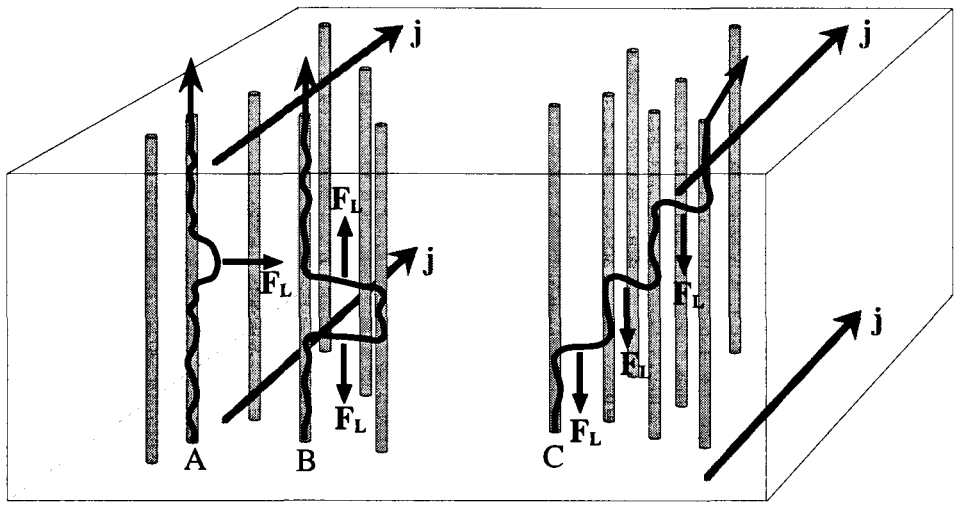

Figure 4.1: Creep mechanisms for vortices pinned by columnar defects. (A,B): field parallel to the columns. (A) half loop unbinding. (B) double kink structure. (C) field at an angle to the columns.

During flux penetration into a rectangular shaped sample both situations occur on different sides of the sample. The result is an anisotropic flux penetration as illustrated in Fig. 4.2(b). For a long slab in which the current parallel to the long edges dominates the behaviour the observed anisotropy should therefore strongly depend on the sense in which the field is tilted, and care has to be taken when orienting the sample.

When the columnar defects are tilted with respect to the normal of the sample top surface (usually the c-axis) the kinks that occur when the field is not aligned with the columns are not expected to be parallel to the sample top surface and the force free situation should not arise. However, an anisotropy in flux penetration remains, since the kink motion along the defects is easier than the motion perpendicular to the defects (see Fig. 4.3). This anisotropy has been observed by magneto-optics in $DyBa_2Cu_3O_{7-\delta}$ (Schuster et al. 1994).

In contrast to the observations in Y-123, magnetization measurements at 20 K on Bi-2212 (Thompson et al. 1992) did not show a directional effect of the columns on pinning. This was taken as a confirmation of the existing picture of Bi-2212 as a quasi 2-dimensional material (Kes et al. 1990), a consequence of its extremely high anisotropy. It was supposed that the pancake vortices are pinned independently from those in the neighbouring layers so that only the density of pancakes per layer is important and not the direction of the external field. An additional in plane field was found to penetrate freely into the material. This interpretation was also used to explain the small activation energies at low temperatures that had been found from magnetization measurements (Thompson et al. 1992; Gerhäuser et al. 1992) and from magneto-optically measured flux profiles (Schuster et al. 1992) and which were attributed to depinning of 2D-vortices.

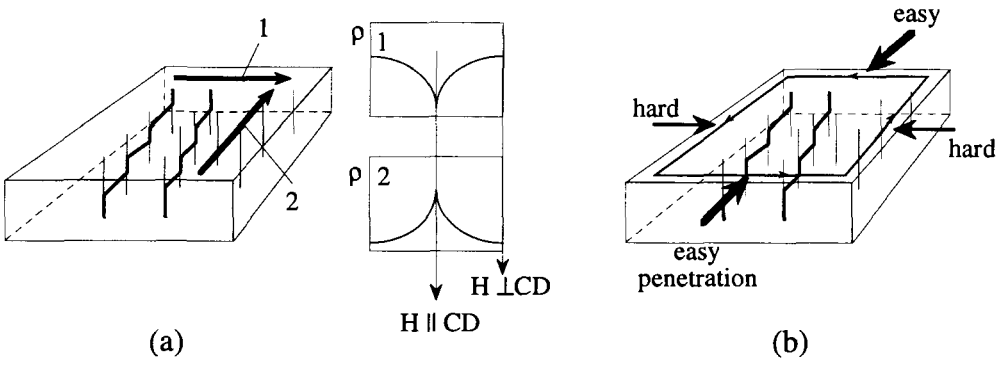

Figure 4.2: Tilted field in the presence of columnar defects. (a) In transport measurements an anisotropy in the resistivity is observed for both current directions. However, while the resistivity is minimal for alignment of field and columnar defects (CD) in the case of a current perpendicular to the vortex kinks (1), it is maximal if the current is parallel to the kinks due to the vanishing Lorentz force (2). (b) Flux penetration is anisotropic since the current is parallel to the vortex kinks along two edges such that there is no force on them. Along the other two edges the current is perpendicular to the kinks, a force results and penetration is easy.

Magnetization measurements at 60 K, in a regime that has been found to be 2-dimensional in previous experiments, showed a slight anisotropy in the magnetization loops for field parallel or perpendicular to the defects which formed an angle of 45 degrees with the c-axis (Klein et al. 1993). Since the density of pancake vortices was the same for the two orientations of the field, the alignment of the field with the defect orientation had to be an important factor. This means that pancakes are aligned along the columns and that this alignment increases the pinning force. Hence, a coupling between the pancakes has appeared.

At low fields ($\lesssim$ 100 Oe) Klein et al. observed a magnetization that was inde-

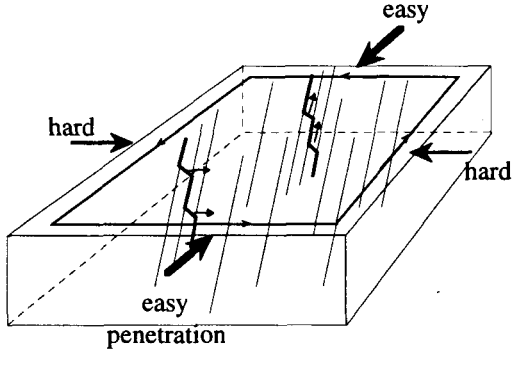

Figure 4.3: Anisotropic flux penetration in the case of tilted columnar defects. Parallel to the defects the kink motion is easier than perpendicular to them.

pendent of the orientation of the applied field. This was explained by the reduced influence of the magnetic pressure at low fields. It is then possible for the flux lines to follow the columnar defects.

How is it possible that pancakes that were thought to be pinned independently in each layer line up along a column? The first possibility is that some coupling already existed between the pancakes. However, this is difficult to reconcile with the earlier observations. The second possibility is that it is an effect of the columns alone, i.e., there exist differences in the strength of the pinning potential among the columns such that the pancakes, which will be pinned preferentially by the strongest pinning potential, will naturally line up. The third possibility is that the remaining magnetic interaction between the pancakes is important, in the sense that a pancake vortex prefers a columnar defect already occupied by a pancake in the neighbouring plane to an empty columnar defect.

Klein et al. (1993) also noticed in their measurements that the observed pinning anisotropy became weaker on decreasing the temperature and disappeared completely for all fields at 40 K. This was surprising in the sense that there seemed to be pancake-like (2D) behaviour at low temperatures and line-like (3D) behaviour at high temperatures, contrary to what was expected (Glazman and Koshelev 1991). According to theory the vortex system should be driven from 3D to 2D behaviour (decoupling) by vortex thermal fluctuations, which *increase* with temperature and field. However, theory did not take into account the effect of disorder. In fact, the anisotropy in pinning is absent in the regime where pinning was important even before the irradiation with heavy ions. There are two possible explanations for this: either a thermodynamic one in the sense that there might be competition in pinning between point and line defects which destroys the pancake alignment, or the "dynamic" explanation that at elevated currents pancakes might be unpinned individually.

Figure 4.4 summarizes the results of Thompson et al. and of Klein et al. Thompson et al. have also determined the irreversibility lines of their sample before (pristine) and after irradiation from the onset of ac response in ac magnetometer measurements. These lines are indicated schematically in Fig. 4.4. Note however, that the corresponding lines for Klein's sample might be slightly different.

After evidence had been found that the vortices in Bi-2212 could manifest line-like behaviour, several questions remained:

1. is this behaviour induced by the columns or are the pancakes aligned in the pristine material also
2. in what field and temperature range can line-like behaviour be observed
3. are vortex pinning by and creep from columnar defects in a very anisotropic layered superconductor the same as in an isotropic one, i.e.,
   (a) are the vortices actually pinned as lines always or do they just move in stacks of pancakes

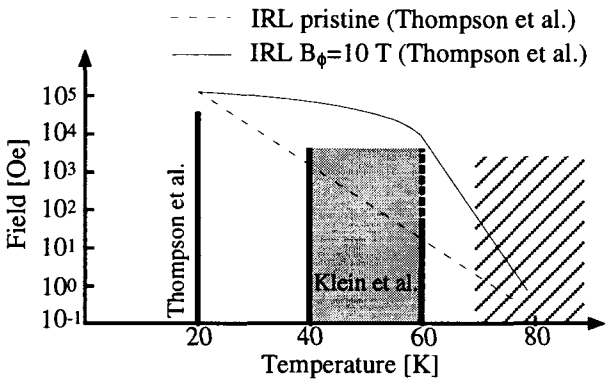

Figure 4.4: H–T phase diagram for Bi-2212. Indicated are the measurements of Thompson et al. (1992) and of Klein et al. (1993). Thick lines mean isotropic pinning, the thick dashed line means anisotropic pinning. The thin lines are the irreversibility lines of Thompsons sample before and after irradiation. The dashed region indicates the working range of the present set-up.

(b) do vortex kinks exist and how do they move

(c) if they do not exist, what is the origin of anisotropy

4. does the pinning change when the columns are tilted

5. could the pinning efficiency be further enhanced by a special arrangement like crossed columns as suggested by the splay glass theory (Hwa et al. 1993).

Fig. 4.5 illustrates how such an enhancement could come about. (A) A vortex kink that connects defects with a different orientation cannot move without increasing its length which requires a considerable amount of energy. (B) Kinks connecting two parallel defects still occur, but their gliding should be stopped when they encounter a defect with a different orientation.

Introducing a splay in the defect orientation could actually be used to test the nature of the vortices, since the enhancement effect is based on the existence of vortex kinks. It cannot work for pancakes, even if they are aligned.

In Klein's experiment the anisotropy in pinning was identified via changes in the magnetization curves for three orientations of the applied field. With the set-up used for this study it is possible to vary the orientation of the dc field continuously. This allows one to study in detail how the pinning efficiency changes on tilting the field direction away from the defects. Because of the high sensitivity of the technique even very small changes in the strength of the shielding current can be detected.

The field and temperature range that can be explored with the present set-up is indicated as the dashed region in Fig. 4.4. In this region pinning in the pristine sample is very weak, see chapter 3.

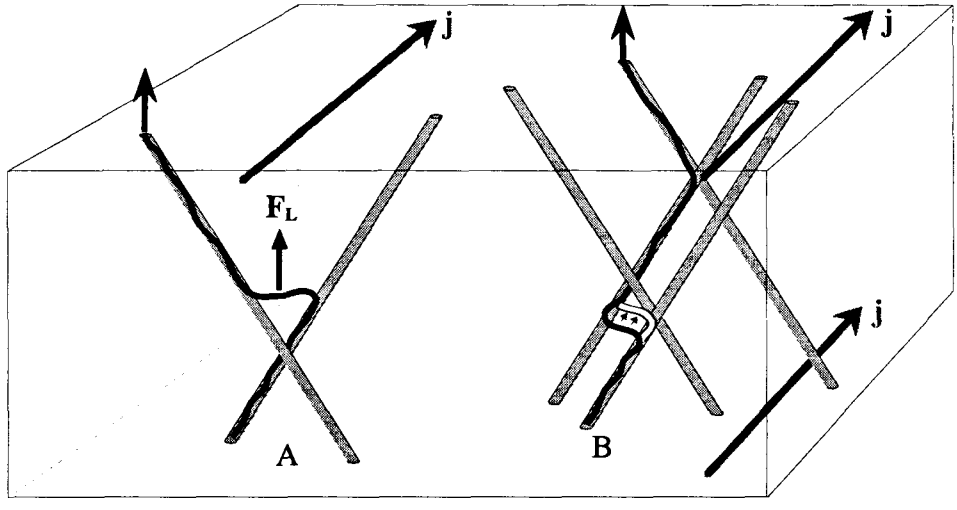

Figure 4.5: Pinning of vortices by splayed columnar defects. A: vortex kink connecting two non-parallel columns, B: Vortex kink connecting parallel columns, stopped by non-parallel defect.

Moreover, using an ac field introduces the frequency, "the inverse of time", as additional parameter. By changing the frequency the time available to the system to follow the external field change can be tuned. The way in which the supported shielding current is influenced by this change contains information on the mechanisms of flux creep. The variation of the frequency of the ac field gives therefore access to the dynamics of the vortex system.

The starting point of the present work on columnar defect pinning in Bi-2212 will be the shielding transition, i.e., the improvement in shielding of an ac field when the temperature is lowered. First it will be made sure that the nature of the transition does not depend on the amplitude of the additional dc field. Then the influence of frequency and amplitude of the ac field will be checked. After this preliminary work the irreversibility lines for field along c of most of the samples will be determined. It is found that the dose is important but not so much the arrangement of the defects, i.e., crossed defects do not shift the irreversibility line to higher temperatures and fields. Then, the anisotropy of pinning by columnar defects will be investigated. Usually, the shielding current, when it is measurable, is found to be strongest for alignment of the field with the defects, if they are parallel to the c-axis or at 30 degrees. For columns with a splay of ± 15 degrees from the c-axis the strongest shielding current is found along the c-direction. This is found to be true for ± 45 degree splay also, but only for certain fields.

4.2 Experimental details

4.2.1 Method

As explained in chapter 2 the ac response of the samples is measured using a InSb Hall probe placed on the top surface of the sample. In addition to the ac field, which is oriented along the c-axis and therefore induces an ac shielding current j in the ab-plane of the sample, a dc field is also applied. Because of this dc field vortices are present in the sample. The dc field can be rotated in a plane which is chosen such that it contains the normal to the sample plane and is parallel to two of the sample edges. If the sample contains tilted or crossed defects, the rotation plane is chosen to be parallel to the irradiation plane as well. The direction of the dc field is then defined by the angle θ it forms with the c-axis. The orientations of ac and dc field with respect to the sample are illustrated in Figure 4.6.

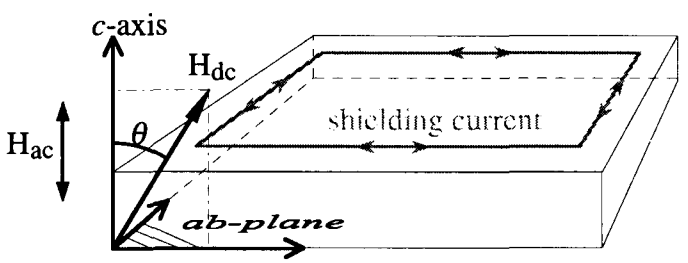

Figure 4.6: Orientations of dc and ac field with respect to the sample. The shielding current is indicated schematically.

Recall that the Lorentz force on a vortex depends on the relative orientations of vortex and current. For vortices that are not perpendicular to the sample top surface it will therefore depend on the sample edge under consideration (see chapter 2): the force will be weaker on the edges where the current is not perpendicular to the vortex direction. The result is an anisotropic flux penetration as for example observed in $YBa_2Cu_3O_7$ (Indenbom et al. 1994b). However, the same effective force will result along all sample sides if the field component parallel to the ab-plane penetrates the sample freely as supposed by Kes et al. (1990), because then only the component of the force parallel to the planes is of importance. An isotropic penetration from the four sides is observed (Indenbom et al. 1994b). It should be noted also, that the orientation of the local induction can be different from that of the applied field, so that the local Lorentz force might differ from what would be expected from the orientation of the external field.

4.2.2 Sample preparation

The Bi-2212 crystals used for this study were grown by the *travelling solvent floating zone* (TSFZ) technique, either at the University of Tokyo by S. Ooi and T. Tamegai or at Leiden University by T. W. Li. They have been left as grown which means that no annealing stage followed the growth. The Tokyo crystals were grown under normal conditions. The Leiden crystals on the other hand, are the result of a growth in excess pressure of oxygen. This increases the Sr/Ca ratio with respect to the growth in air, leading to a higher T_c (see chapter 1). However, the elevated oxygen pressure is also suspected to give rise to inclusions of the Bi-2223 phase.

These crystals were cut into smaller pieces in order to ensure the homogeneity of the physical properties among several samples. Then the samples were subjected to different irradiations.

Heavy ion irradiation has been performed at the *Grand Accélérateur National d'Ions Lourds (GANIL)*, Caen, France. The ions used for the irradiations were lead (Pb), uranium (U), and xenon (Xe) with energies of 5.8 or 1 GeV. The ions are accelerated in a separated sector cyclotron. This assures a very small uncertainty in energy, since deviations in energy would lead to an altered trajectory in the cyclotron such that the ion would not appear at the beam exit. The ion flux is controlled during irradiation by measuring the flow of electrons induced by the passage of the ion beam through a titanium foil of a few micron thickness. Before starting the irradiation this electron flow is calibrated against the direct measurement of the ion flux with a Faraday cage. The remaining uncertainty on the ion flux is about 5%. The irradiation is stopped automatically when the desired dose is reached. The flux did not exceed $\approx 10^8$ ions per second in order to assure that no heating of the sample occurred. A homogeneous irradiation is obtained by sweeping the beam over the irradiation area with incommensurate horizontal and vertical frequencies. In addition, the homogeneity of the irradiation has been verified on mica samples. An etching procedure on these samples confirmed the homogeneity of the defect distribution created by the ions.

TEM studies have shown that Pb and U ions introduce continuous linear tracks in Bi-2212 with an amorphous core of a diameter of about 70 Å(Hardy et al. 1992). Around the amorphous core there is a highly disordered zone of 20 Å thickness (Hardy et al. 1994). The irradiation with Xe ions, on the other hand, gives rise to discontinuous tracks of elongated defects (Bourgault et al. 1989). This has been observed for an ion energy of 3.5 GeV, a little higher than the 1 GeV used for one of the samples.

The irradiation dose of a sample is often given in terms of the matching (or dose equivalent) field B_ϕ. At $B = B_\phi$ the vortex density equals the density of columnar defects. A defect density of 10^{15} m^{-2} for example, is matched by the density of vortices B/Φ_0 when $B = 2$ T.

For irradiation under an angle the samples have been fixed on an inclined stage such that the beam direction was lying in a plane that contained the c-axis and

that was perpendicular to one of the sample edges. For *crossed* irradiation the sample was then rotated by 180 degrees and irradiated again. For *doubly crossed* irradiation this procedure was repeated four times with intermittent rotation by 90 degrees. The different irradiation geometries are illustrated in Fig. 4.7.

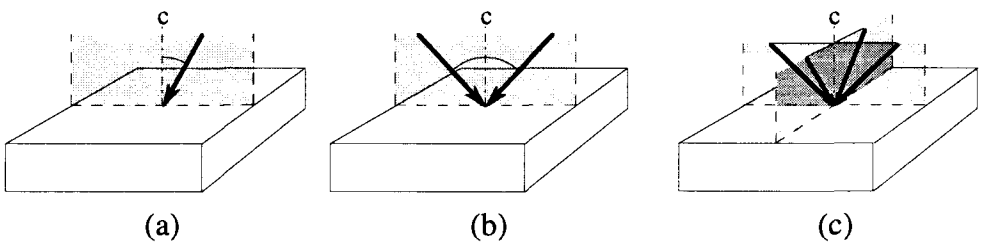

Figure 4.7: Irradiation geometries: (a) simple irradiation under an angle from the c-axis, (b) crossed irradiation, (c) doubly crossed irradiation.

Table 4.1 gives an overview of all the samples used in this work. Samples cut from the same bigger crystal are grouped together. The names of the samples indicate

Table 4.1: Parameters of the different samples studied. Samples stemming from the same crystal are grouped together.

sample	T_c [K]	B_ϕ [T]	ions	energy [GeV]	source	remarks
irr-c-0.5	≈ 86	0.5	Pb	5.8	Tokyo	as grown
irr-c-2-86	86.3	2	Pb	5.8		
irr-X15-2	86	2×1	Xe	1		
irr-c-2-91	91.3	2†	U	5.8	Leiden	as grown
irr-30-0.4	≈ 91	0.4	Pb	5.8		in excess
irr-XX15-2	91.3	4×0.5†	U	5.8		pressure
						of oxygen
irr-X45-0.4	88	2×0.2	Pb	5.8	Tokyo	as grown

†The ion beam was unstable during the irradiation run so that the real value of the dose is uncertain and probably lower than indicated. However, irr-c-2-91 and irr-XX15-2 have received exactly the same total dose since they have been irradiated together.

how the sample was irradiated: *irr-c-0.5* — irradiation along the c-axis with a matching field of 0.5 T, *irr-30-0.4* — irradiation at 30 degrees from the c-axis with a total dose of 0.4 T, etc. For the samples named irr-c-2-x, the x indicates the T_c, to distinguish between the samples.

An X in the sample name means that the sample was subject to crossed irradiation. XX means doubly crossed irradiation.

For the measurements of the irreversibility line the frequency was kept fixed at 7.75 Hz and the dc field was always parallel to the c-axis. The onset is determined from the $|T_{H3}(T)|$ curve as described in chapter 2.

4.3 Results

4.3.1 Temperature dependence of the transmittivity

The simplest case to study is a collinear arrangement of columnar defects and external field direction, both oriented along the c-axis. This case will serve as reference for the more complex arrangements of columnar defects and orientations of the dc field.

Figure 4.8 shows the in-phase component of the fundamental (T'_H) and the amplitude of the third harmonic transmittivity $|T_{H3}|$ of sample irr-c-2-86 cooled in applied fields of 100, 200, 400 and 600 Oe. The in-phase component of the first harmonic, T'_H, which measures the ratio $|b_{ac}|/\mu_0 h_{ac}$ of the RMS amplitude of the detected ac induction $|b_{ac}|$ to the applied ac field $\mu_0 h_{ac}$, decreases monotonically with decreasing temperature. The ac shielding current that creates a field opposite to the external ac field grows. The normalized shielding current J can be calculated easily using eq. 2.21. However, a good first estimate of J can be obtained simply by inverting the T'_H-axis. Minima in the transmittivity then show up as maxima in the shielding current and vice versa.

As is seen in Fig. 4.8, increasing the dc field shifts the transition to lower temperatures, but its width approximately remains the same.

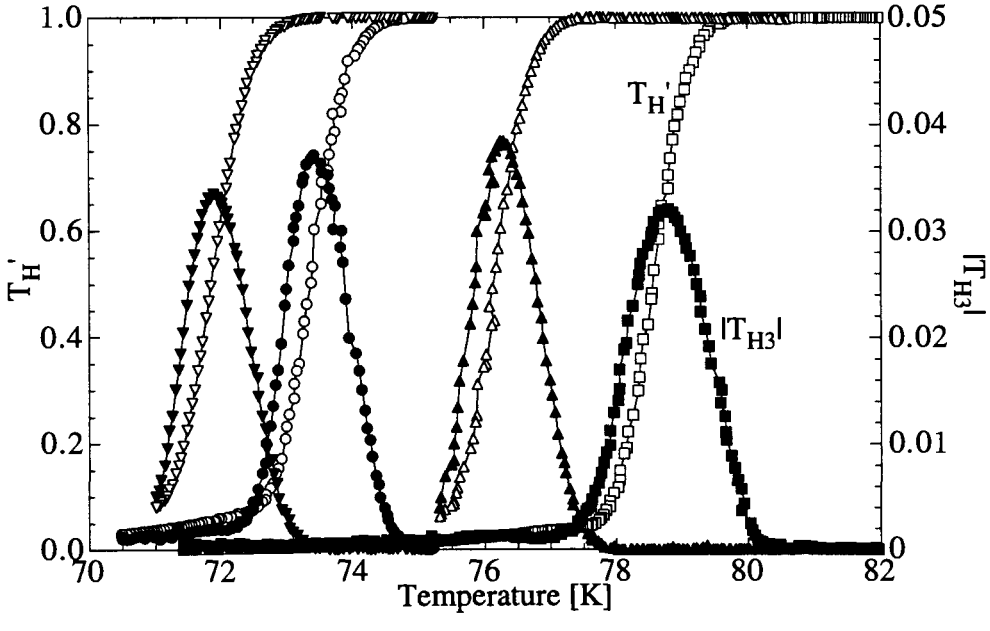

Figure 4.8: In-phase component T'_H of the first harmonic (empty symbols) and amplitude $|T_{H3}|$ of the third harmonic transmittivity (full symbols) for a sample with defects along the c-axis. $B_\phi = 2$ T, $T_c = 86.3$ K (irr-c-2-86). The dc field H_{dc} has been kept parallel to c. H_{dc} values: 102 Oe (□), 200 Oe (△), 402 Oe (○), and 594 Oe (▽). $H_{ac} = 7.1$ Oe, $f = 7.75$ Hz.

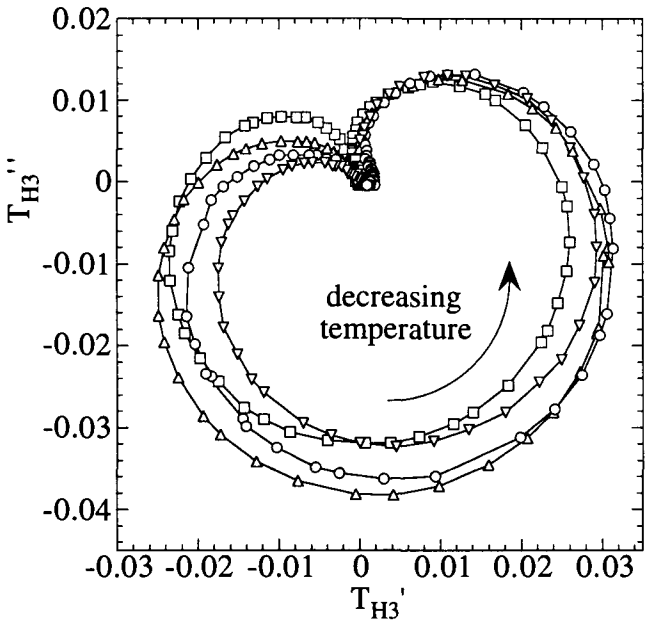

Figure 4.9: Polar plot of the third harmonic of Fig. 4.8. H_{dc} values: 102 Oe (□), 200 Oe (△), 402 Oe (○), and 594 Oe (▽). H_{ac} = 7.1 Oe, f = 7.75 Hz. Sample: irr-c-2-86.

The third harmonic transmittivity on the other hand, is a measure of the non-linearity of the sample I–V characteristic. It is present during the whole transition. Its onset defines the irreversibility temperature (see section 2.7.4). The field dependence of this onset will be studied in more detail below. A polar plot of the third harmonic (out-of-phase component T''_{H3} against in-phase component T'_{H3}) is shown in Fig 4.9. The shape of this curve is typical for minor hysteresis loops in the form of a parallelogram as it occurs for example in the Bean critical state (compare Fig. 2.11) or for the surface barrier when an additional dc field is present. The detailed shape changes only slightly with field. Thus it is verified that the sample response does not change fundamentally.

For fields above 200 Oe the amplitude of the third harmonic slowly decreases with field at high temperatures. For the whole field range shown here the amplitude of the third harmonic is reduced with respect to the theoretical curve by a factor 2–3. This is most likely due to flux creep (Gilchrist and Konczykowski 1993).

The effects of flux creep can be measured directly by changing the time scale of the experiment, i.e., the frequency of the applied ac field. Figure 4.10 shows the effect of increasing the frequency of the ac field. The third harmonic onset and thus the onset of the transition are shifted to higher temperatures. For not too high frequencies the shift is only weak, and at the same time the transition becomes sharper. Above 200 Hz on the other hand, the shift becomes substantial and the transition broadens again. The third harmonic peak height decreases continuously. This means that the harmonic content of the sample response diminishes, the response becomes

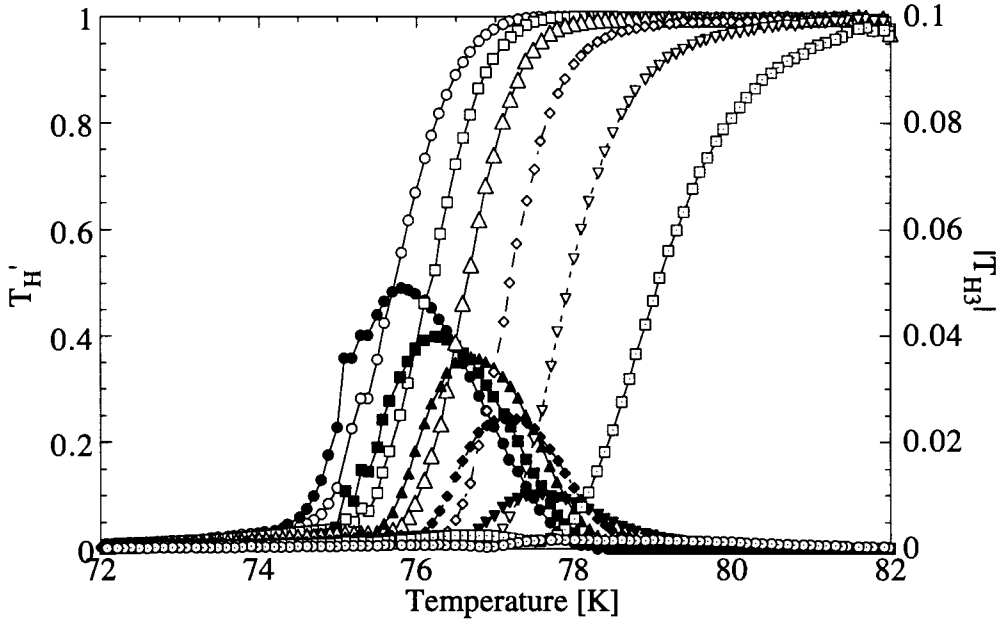

Figure 4.10: Influence of the frequency of the ac field on the transition curves. H_{dc} = 200 Oe, H_{ac} = 20.8 Oe. Frequencies: 7.75 Hz (circles), 24.29 Hz (squares), 76.1 Hz (triangles), 238 Hz (diamonds), 747 Hz (inverted triangles), and 2340 Hz (dotted symbols). Sample: irr-c-2-86.

more linear. At 2 kHz the third harmonic is nearly gone, the transition occurs practically in the linear regime and should therefore just be triggered by the increasing friction that the vortex flow is subject to in the vortex liquid/pancake gas.

In a polar plot (not shown here) the shape of the third harmonic curve remains almost the same, only its size changes.

Increasing the amplitude of the ac field (by a factor of approximately 3 in Fig. 4.11) not only shifts the third harmonic onset to higher temperatures but also widens the transition and increases the third harmonic content of the signal. The shape of the polar plot remains unchanged.

The above results can be summarized as follows: increasing the dc field shifts the transition quickly to lower temperatures; increasing the frequency narrows the transition and leads to a slight increase of the onset temperature of the third harmonic if the frequency is not increased too much; when the frequency becomes of the order of a few hundred Hertz the friction of the free vortex flow becomes important and the shielding transition occurs in the linear regime, in which the transition broadens again. Increasing the ac amplitude also induces a slight shift of the onset to higher temperatures, but at the same time broadens the transition. All these changes do not influence the shape of the polar plot of the third harmonic which always presents the characteristics of a parallelogrammatic ac induction loop. In chapter 2 it has been shown that such a shape of the third harmonic occurs either for a critical state

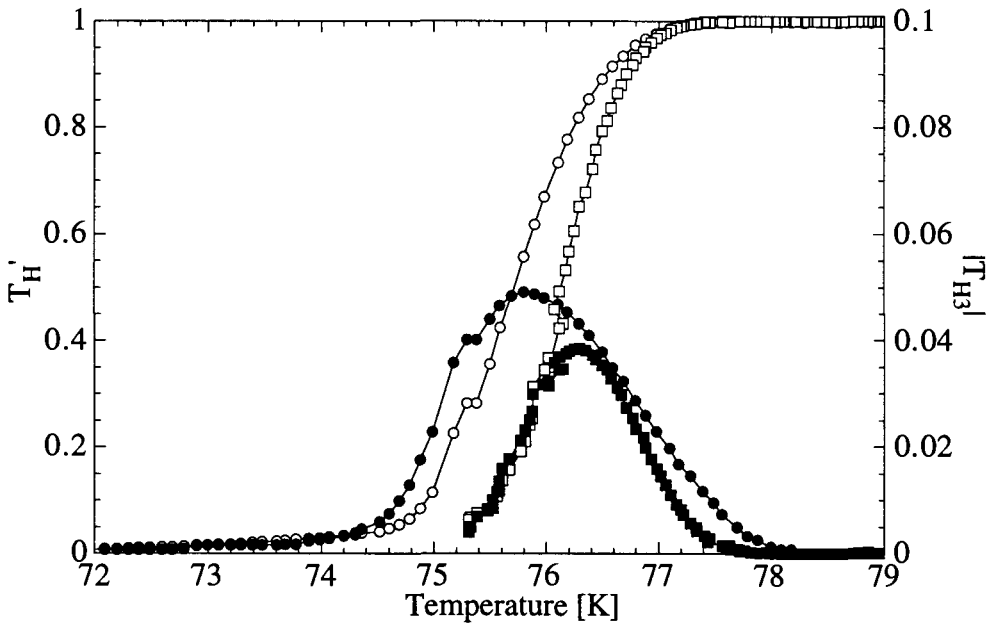

Figure 4.11: Influence of the amplitude of the ac field on the transition curves. H_{dc} = 200 Oe, f = 7.75 Hz. H_{ac} = 20.8 Oe (circles), 7.1 Oe (squares). Sample: irr-c-2-86.

or for a surface barrier. Since the field and temperature values of interest here fall into a regime that is completely reversible in a pristine sample, one concludes that a critical state is formed. The reduced amplitude of the third harmonic with respect to the theoretical value is due to flux creep. The existence of the critical state thus established, it follows that the shielding current can be determined from the transmittivity using the model by van der Beek et al. (1995) presented in chapter 2. The electric field is determined by the amplitude and frequency of the ac field so that it is possible to determine the E–J characteristic. From the E–J characteristic a creep mechanism can possibly be identified.

This type of analysis has been tried on many of the samples, but it has turned out to be very difficult. Very often the transition is so strongly shifted by the change in frequency, that at a given temperature the transmittivity passes from 0 to 1 over just one decade. This is much to rapid to allow for an exact interpretation. Moreover, the strong temperature shift may drive the transition out of the useful temperature range. A sample for which this analysis could be completed despite the difficulties is that with crossed defects with a 45 degree tilt. The dc field is 590 Oe, the value where a minimum in the transmittivity is observed around c. The curves of $\log j$ vs. $\log f$ are shown in Fig. 4.12. As the straight lines indicate, frequency and shielding current are related by a power law, the power of which depends on temperature. The representation on the right hand side has swapped axes in order to resemble more closely an E–j characteristic. The current range is limited on the high current side by the disappearance of the ac signal due to full shielding and on the low current side by noise.

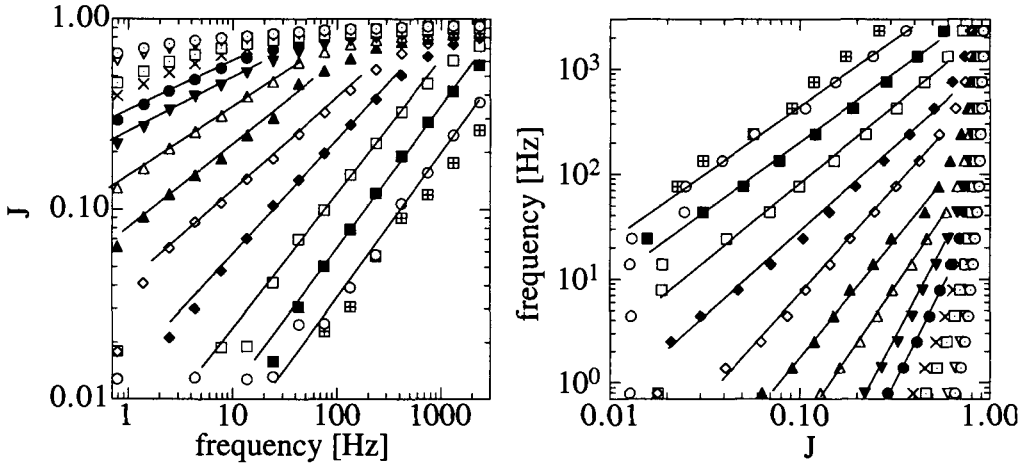

Figure 4.12: Two representations of the frequency dependence of the normalized shielding current, J, for sample irr-X45-0.4, irradiated at $\pm$ 45 degrees. B_ϕ = 2×0.2 T, H_{dc} = 590 Oe, H_{ac} = 20.8 Oe. Temperatures: 77.8 (⊞), 77.3 (○), 76.8 (■), 76.3 (□), 75.8 (♦), 75.3 (◊), 74.8 (▲), 74.3 (△), 73.8 (▼), 73.3 (•), 72.8 (×), 72.3 (⊡), 71.8 (▽),71.3 (⊙). In the representation on the right hand side the axes are swapped.

4.3.2 Irreversibility line

As has been shown in the previous section, the onset of the third harmonic shifts to lower temperatures on increasing the field, but a polar plot of its components keeps the same shape indicating that the electrodynamics that govern the sample response remain the same.

Figure 4.13 shows the strong influence of the heavy ion irradiation on the IRL. The lower line is the vortex first order transition in the sample studied in chapter 3. As has been shown there, the IRL of that sample practically coincides with this line. The upper line is the IRL of sample irr-c-2-91. This sample has been irradiated along the c-axis with a matching field of 2 T. Both samples have a critical temperature of 91.3 K (the pristine sample stems from the same bigger crystal). Despite the heavy ion irradiation the T_c of sample irr-c-2-91 has almost remained the same. The irreversible regime on the other hand, has increased considerably. Even at temperatures very close to the transition temperature the two lines are still separated.

Remarkable is the sudden rise of the irreversibility field at 76.7 K. Such steeply rising parts have been observed before in heavy ion irradiated Bi-2212 (Zech et al. 1995; Zech et al. 1996; Seow et al. 1996). Above this temperature the IRL of the irradiated sample decreases nearly exponentially with temperature.

Two important results on the influence of the density and the arrangement of the columnar defects follow from Fig. 4.14 which collects the IRLs of the samples with T_c = 86 K: irr-c-0.5 (B_ϕ = 0.5 T), irr-c-2-86 (B_ϕ = 2 T), and irr-X15-2 (B_ϕ = 2×1 T). First, the increase of the column density from 2.5 10^{14}m^{-2} (B_ϕ = 0.5 T) to 10^{15}m^{-2}

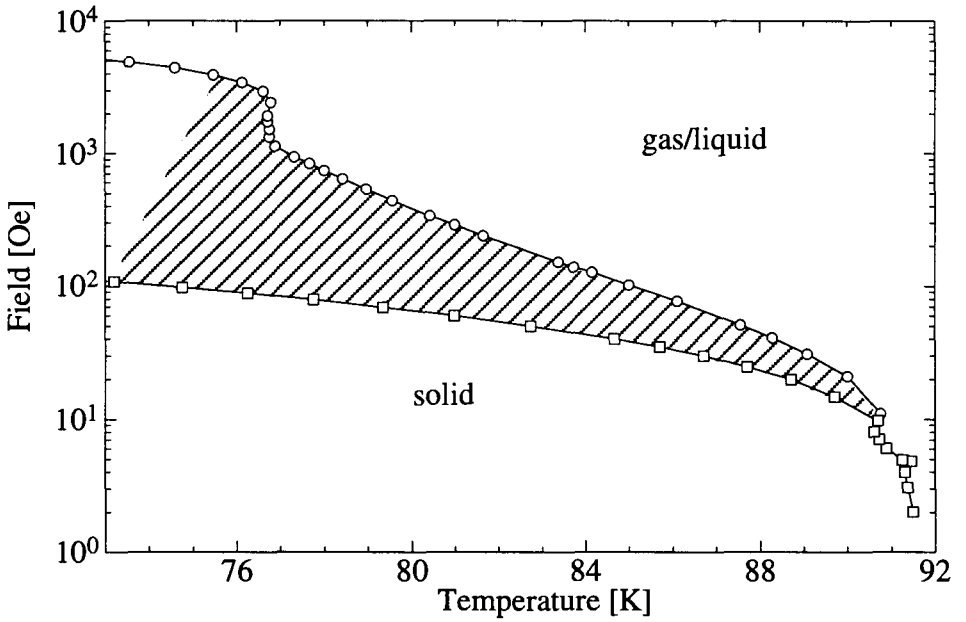

Figure 4.13: High temperature part of the irreversibility line (onset of third harmonic) of sample irr-c-2-91 (o) in a log-plot. The first order transition line (□) is also shown for comparison. The irreversible regime is strongly enhanced by the irradiation (dashed region).

(B_ϕ = 2 T) leads to an extension of the exponential temperature dependence to lower temperatures. The vertical rise in the IRL for the matching field of 2 T occurs at a lower temperature, inaccessible with the present set-up. Second, crossed defects with a 15 degree tilt from the c-axis instead of defects along c but with the same total defect density of $10^{15}\mathrm{m}^{-2}$ do not increase the irreversible regime, rather it is slightly reduced.

Even doubly crossed defects do not enhance the irreversible regime beyond that of the straight defects as shown in Fig. 4.15. There the IRLs of samples irr-c-2-91 and irr-XX15-2 are compared. Also here the IRL of the sample with CDs along c lies slightly above that of the more elaborate defect arrangement. However, the two IRLs are quite close and both show the vertical rise.

For crossed defects with a tilt of 45 degrees on the other hand a vertical part is absent in the IRL (see Fig. 4.16). Nevertheless it contains a part that rises more steeply than the high temperature exponential part.

The horizontal bars in all the figures indicate the fields and temperature ranges for which the influence of the dc field orientation on the screening current has been studied (see the following section).

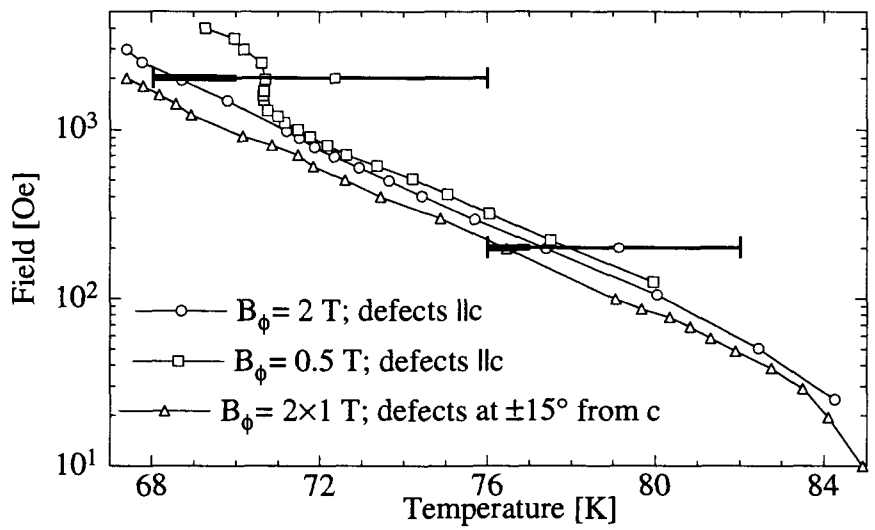

Figure 4.14: Semilogarithmic plot of the IRLs of samples irr-c-0.5 (□), irr-c-2-86 (o) and irr-X15-2 (△) with the same T_c (86 K) but a different density or arrangement of defects. The ac amplitudes are 7.1 Oe (irr-c-0.5, irr-X15-2) and 1.4 Oe (irr-c-2-86); f = 7.75 Hz. The horizontal bars indicate the temperature range and dc field value for which the anisotropy in pinning by the columnar defects has been checked. Thick lines indicate where such an anisotropy has been observed.

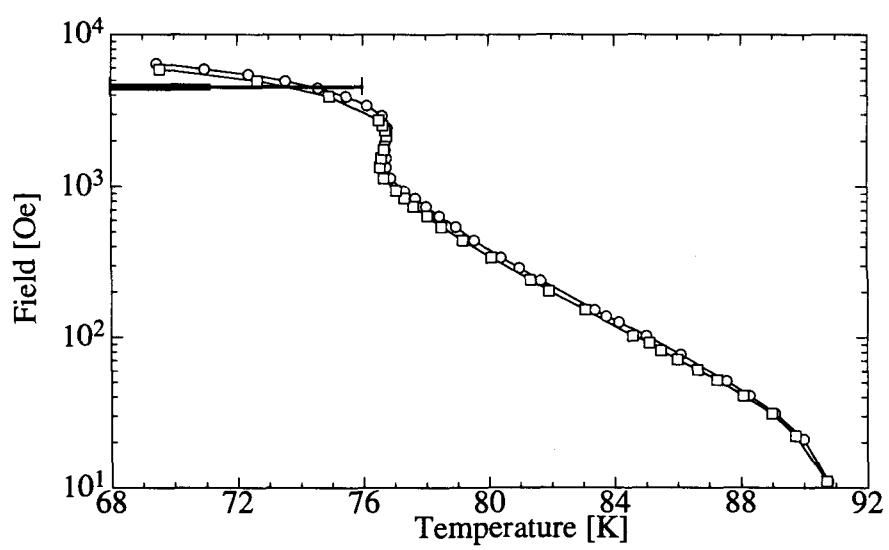

Figure 4.15: IRLs of samples irr-c-2-91 (o) and irr-XX15-2 (□) with the same T_c and the same total dose, but a different defect arrangement (doubly crossed columns). The horizontal bar indicates the temperature range and dc field value for which the anisotropy in pinning by the columnar defects has been checked for sample irr-XX15-2. The thick line indicates where such an anisotropy has been observed.

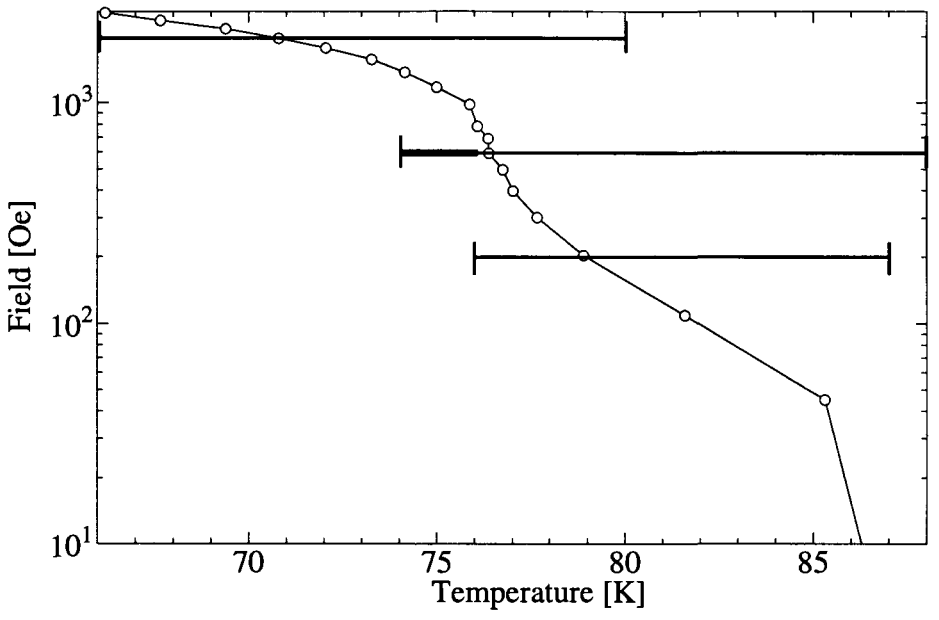

Figure 4.16: Irreversibility line of the sample with crossed defects at 45 degrees (irr-X45-0.4). The horizontal bars indicate the temperature range and dc field value for which the anisotropy in pinning by the columnar defects has been checked. Thick lines indicate where such an anisotropy has been observed.

4.3.3 Angular dependence of the transmittivity

Different regimes have been identified in the IRLs presented above. With the following measurements of the angular dependence of the transmittivity it shall be checked, in which of these regimes an anisotropy in pinning caused by the columns can be found. First, defects along the c-axis will be studied, then tilted defects, and finally crossed defects.

For these measurements the angle θ between the dc field and the c-axis (see Fig. 4.6) has been swept over a broad range of angles. For each measured position the first and third harmonic components of the Hall probe signal have been recorded. A detailed description of the procedure and of the normalization of the data is given in section 2.7.3.

The samples have been positioned in such a way so as to make the rotation plane as closely aligned as possible with the irradiation plane (or with one of them if there are two). The misalignment can be estimated to be of the order of a few degrees. This means that the field direction, when rotated by 180 degrees, probably misses the exact alignment with the defects and with the c-axis by a few degrees.

Defects parallel to the c-axis

Figure 4.17 shows typical curves for the angular dependence of the transmittivity, measured on sample irr-c-2-86 for various temperatures and in a dc field of 200 Oe. At the highest temperatures screening is important only when the dc field is turned

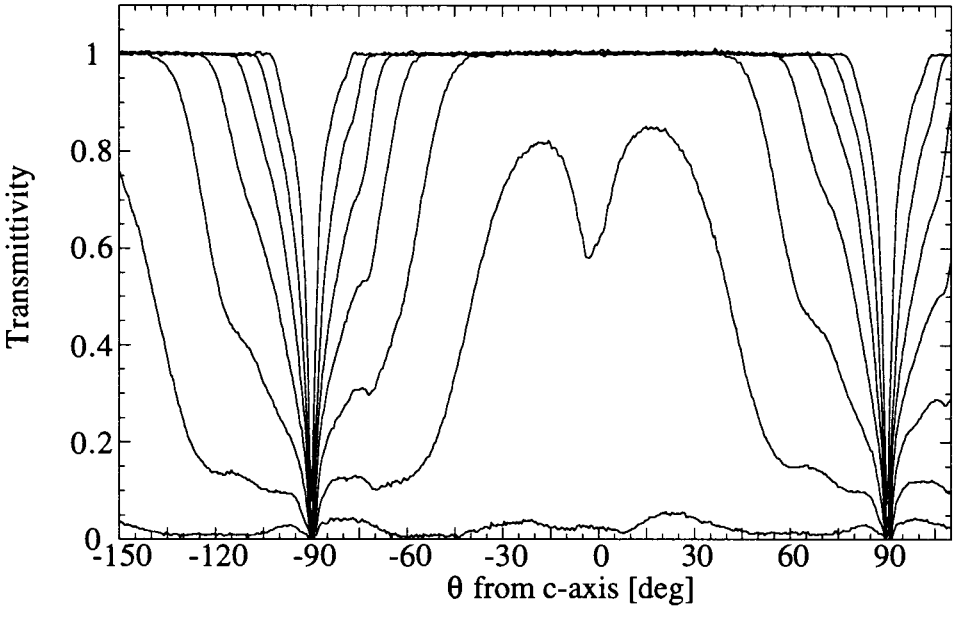

Figure 4.17: Dependence of the transmittivity of sample irr-c-2-86 on the angle between the applied field and the c-axis. $B_\phi = 2$ T, $T_c = 86$ K. $H_{dc} = 200$ Oe, $H_{ac} = 1.4$ Oe, $f = 7.7$ Hz. Temperatures: 82 K to 76 K in steps of 1 K (from top to bottom).

close to the ab-plane ($\pm 90°$), where a sharp minimum is observed. On decreasing the temperature the transmittivity diminishes around the ab-plane, and the minimum becomes broader. At a given temperature a dip appears for alignment of the field with the defects, meaning that for this orientation of the field a higher shielding current is supported by the sample. At sufficiently low temperatures screening is strong for all angles.

Such a dip in heavy ion irradiated Bi-2212 has already been reported by van der Beek et al. (1995). A similar dip on rotating the field through the c-axis has also been observed in resistive measurements in Bi-2212 single crystals (Doyle et al. 1996), and $Tl_2Ba_2CaCu_2O_8$ thin films (Budhani et al. 1994; Gray et al. 1996), a material with a similarly high anisotropy.

The curves in Fig. 4.17 have to be compared to the angular dependence of the transmittivity for an unirradiated sample (Figs. 3.6 and 3.7). There, no dip along c was present at the even lower fields of 140 and 100 Oe, respectively. Down to 72 K no screening of the ac field could be observed for a dc field along the c-axis. For the irradiated sample on the other hand, a sharp dip is observed for temperatures below 78 K (the extrapolation of the high temperature part of the third harmonic

gives an onset temperature of $T_{onset2} = 77.4$ K at this field). At 76 K the ac field is almost perfectly screened for any direction of the dc field, and this despite the somewhat higher value of the dc field (200 Oe, as compared to 100/140 Oe for the pristine samples). The dip in the angular dependence is visible at least down to a dc field of 40 Oe for sample irr-c-2-86.

It has been shown in chapter 3 that at low applied dc fields a field scan with $H_{dc} \parallel c$ and a rotation of a constant applied field $H_{dc,0}$ give the same curves when the transmittivity T' is traced against H_{dc} and $H_{dc,0} \cos\theta$, respectively. This scaling law indicated, that only the c-axis component of the dc field is important.

The presence of a dip in the angular dependence of the transmittivity immediately implies that such a scaling is not possible any more. Decreasing a dc field aligned with the c-axis will always produce a transition curve similar to the ones seen in Section 4.3.1 for decreasing the temperature, and never leads to an increasing transmittivity. The latter would imply a reentrant IRL, which is not observed.

Figure 4.18 shows that a dip is also observed for fields in the vertical part of the IRL of sample irr-c-0.5. The dc field here was 2 kOe. Because of the limitations of the cryostat the angular dependence in the low temperature regime could not be measured for this sample.

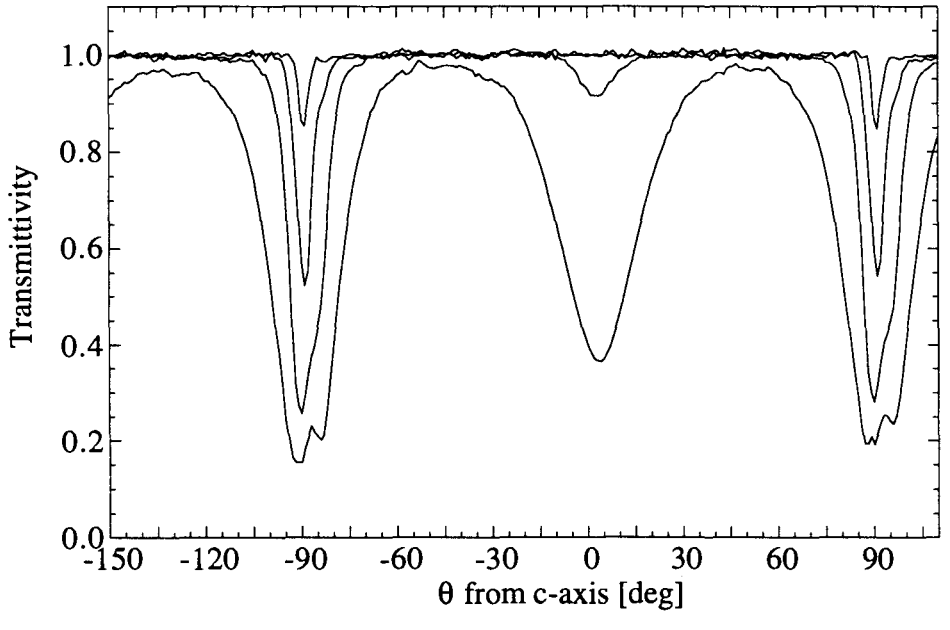

Figure 4.18: Dependence of the transmittivity of sample irr-c-0.5 on the angle between the applied field and the c-axis: $B_\phi = 0.5$ T. $T_c = 86$ K. $H_{dc} = 2000$ Oe, $H_{ac} = 7.1$ Oe, $f = 7.75$ Hz. Temperatures: 76 K to 68 K in steps of 2 K (from top to bottom).

A further question that has to be checked, is how the appearance of the dip is related to the onset of a third harmonic response. The third harmonic transmittivity corresponding to the data just presented (Fig. 4.18) is shown in Figure 4.19. Above

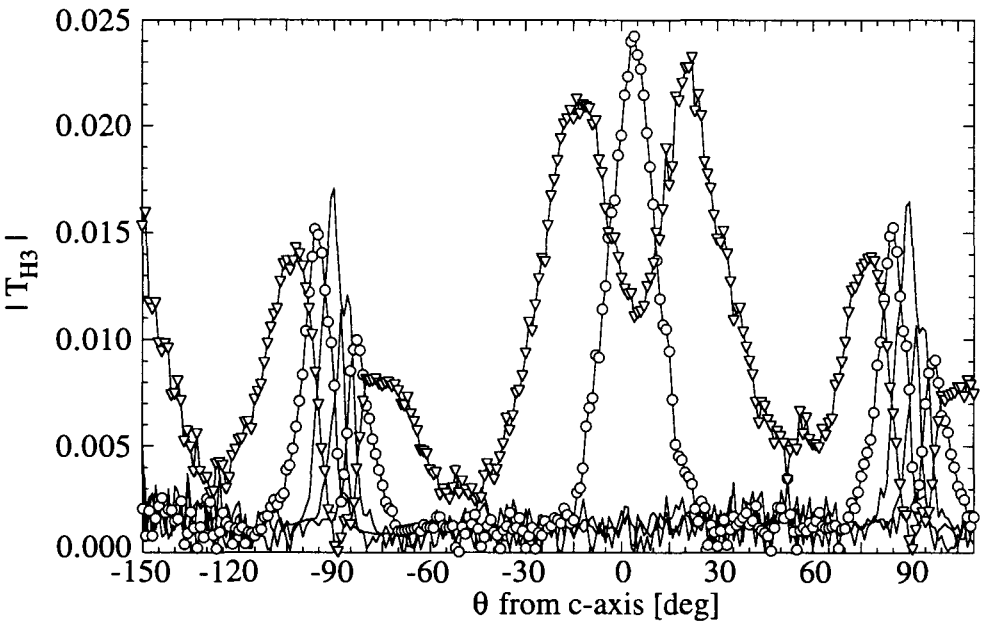

Figure 4.19: Dependence of the third harmonic transmittivity of sample irr-c-0.5 on the angle between the applied field and the c-axis: $B_\phi = 0.5$ T, $T_c = 86$ K. $H_{dc} = 2000$ Oe, $H_{ac} = 7.1$ Oe, $f = 7.75$ Hz. Temperatures: 76 K to 68 K in steps of 2 K. Circles: 70 K, triangles: 68 K.

70 K there is no measurable screening of the ac field. Up to 80 degrees from c the transmittivity equals 1, and the third harmonic component is zero. At 70 K on the other hand, when the dip in the first harmonic is still rather small, a peak is visible in the third harmonic transmittivity which attains a height of 0.03, i.e., close to the maximum value seen for example in Fig. 4.8. A closer look at the 70 K data reveals that screening and the third harmonic component become unobservable at approximately the same angle, even though the borders of the dip in the first harmonic are much smoother.

On further decrease of the temperature the third harmonic peak shifts to higher angles.

Tilted defects

The same questions can now be addressed with respect to a system with tilted defects. Tilted defects forming an angle of 30 degrees with the c-axis have been studied. They also give rise to a minimum in transmittivity for dc fields parallel to the defects. This has been verified for field magnitudes ranging from 500 to 2000 Oe. Figure 4.20 representatively shows the observed angular dependence of sample irr-30-0.4 for a field of 500 Oe.

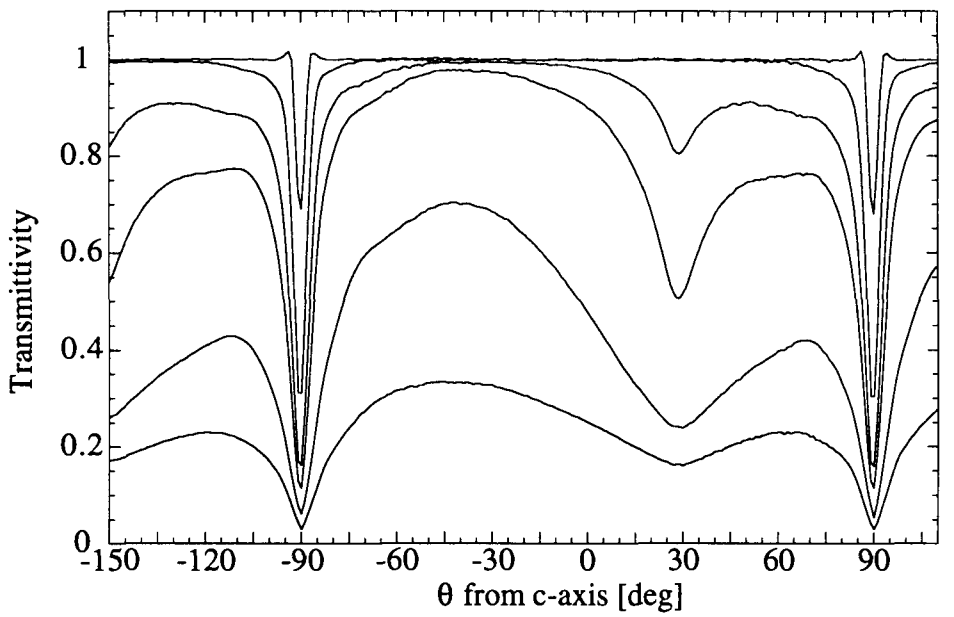

Figure 4.20: Dependence of the transmittivity of sample irr-30-0.4 on the angle between the applied field and the c-axis. $B_\phi = 0.4$ T, $T_c = 91$ K. $H_{dc} = 500$ Oe, $H_{ac} = 20.8$ Oe, $f = 7.75$ Hz. Temperatures: 86 K, 78 K, 76 K, 75 K, 73 K, and 71 K (from top to bottom).

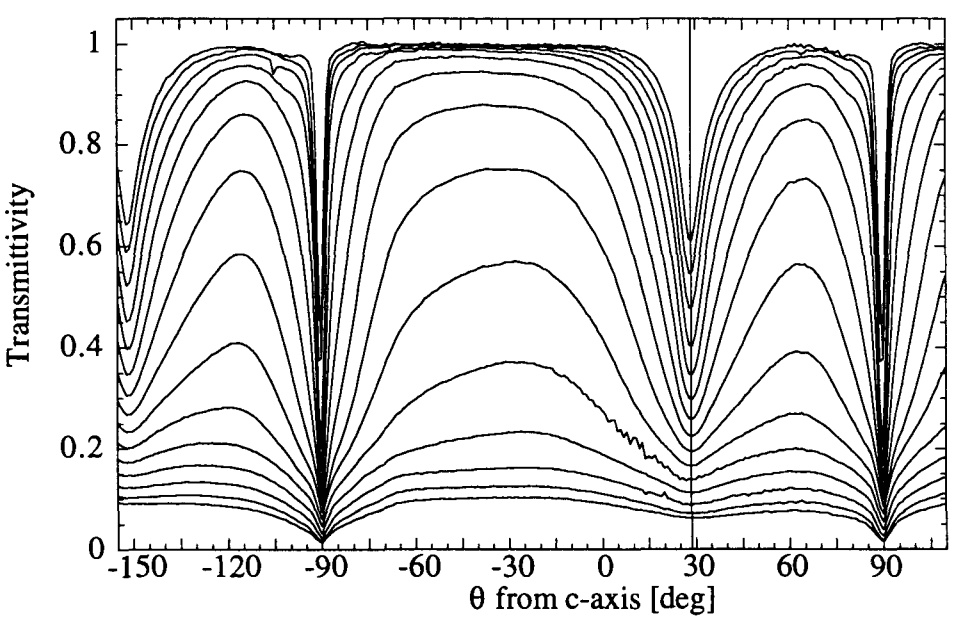

Figure 4.21: Dependence of the transmittivity of sample irr-30-0.4 on the angle between the applied field and the c-axis. $B_\phi = 0.4$ T, $T_c = 91$ K. $H_{dc} = 1000$ Oe, $H_{ac} = 20.8$ Oe, $T = 74$ K. The frequencies are (from top to bottom): 0.79, 1.4, 2.47, 4.38, 7.75, 13.7, 24.3, 43, 76.1, 134.7, 238.4, 422, 747, 1322, and 2340 Hz.

Several studies on samples with tilted defects can be found in the literature. The work of Klein et al. (1993), for example, was done on a sample with defects tilted 45 degrees away from the c-axis. Above 50 K they found a stronger magnetization current for alignment of the field with the columnar defects (+45°), than for fields parallel to the c-axis, or even less for fields perpendicular to the defects (−45°). Kummeth et al. (1994) made a similar observation for defects with a 60 degree tilt away from the c-axis. They studied the angular dependence of the magnetization current in more detail and found a peak, i.e., a stronger current, for alignment of the field with the defects at 60 K as well as 77 K. An enhancement for alignment of the field with 45 degree tilted columns was also found for the irreversibility field (Zech et al. 1995) and temperature (Seow et al. 1996).

The presence of the dip in transmittivity along the defects is independent of the frequency of the ac field. Figure 4.21 illustrates this, still on sample irr-30-0.4, but in a dc field of 1000 Oe. The range of frequencies extends from 0.79 to 2340 Hz and over this whole range the dip is present. With increasing frequency the shielding improves more strongly along the defects at first, but then becomes better for any orientation of the field with respect to the defects so that the directional enhancement becomes less pronounced at high frequencies.

Crossed columnar defects

This is a special case in the sense that crossed columns are expected to give rise to entanglement of the vortices. It is not clear however, what this induces in a layered high temperature superconductor.

The experiments show that crossed columnar defects lead to an improved shielding not for alignment of the field with the defect direction, but for field along the c-axis. This is exemplified in Fig. 4.22 for sample irr-XX15-2. The dc field in this measurement is 4560 Oe and therefore well above the vertical part of the IRL. In this sample a dip is also observed for fields of 2200 and 400 Oe, representing the vertical and the exponential part, respectively.

The minimum for field along c is observed even for a 45 degree tilt of the crossed defects (see Fig. 4.23; sample irr-X45-0.4 in a field of 590 Oe). The dip is broader for this arrangement of the defects than for the crossed defects with only 15 degrees tilt. Moreover it is only visible in the steep part of the IRL. In the low temperature part and in the exponential, high temperature part the c-axis direction actually presents the highest transmittivity (see Figs.4.24 and 4.25 for 200 and 2000 Oe applied field, respectively).

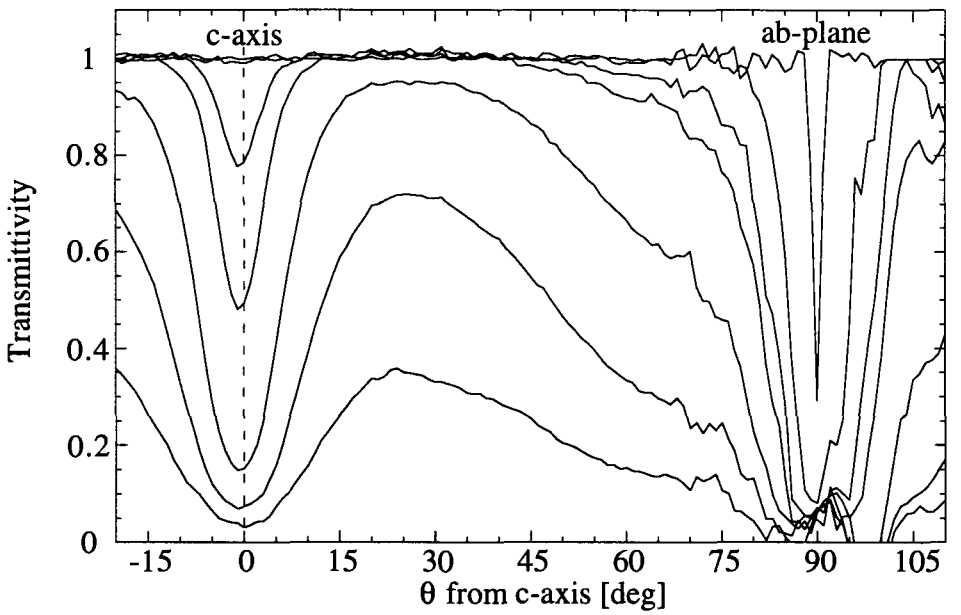

Figure 4.22: Dependence of the transmittivity of sample irr-XX15-2 on the angle between the applied field and the c-axis. $B_\phi = 2$ T, $T_c = 91.3$ K. $H_{dc} = 4560$ Oe, $H_{ac} = 7.1$ Oe, $f = 7.75$ Hz. Temperatures (from top to bottom): 74 K, 70.5 K, 69.5 K, and from 69 K to 66 K in steps of 1 K.

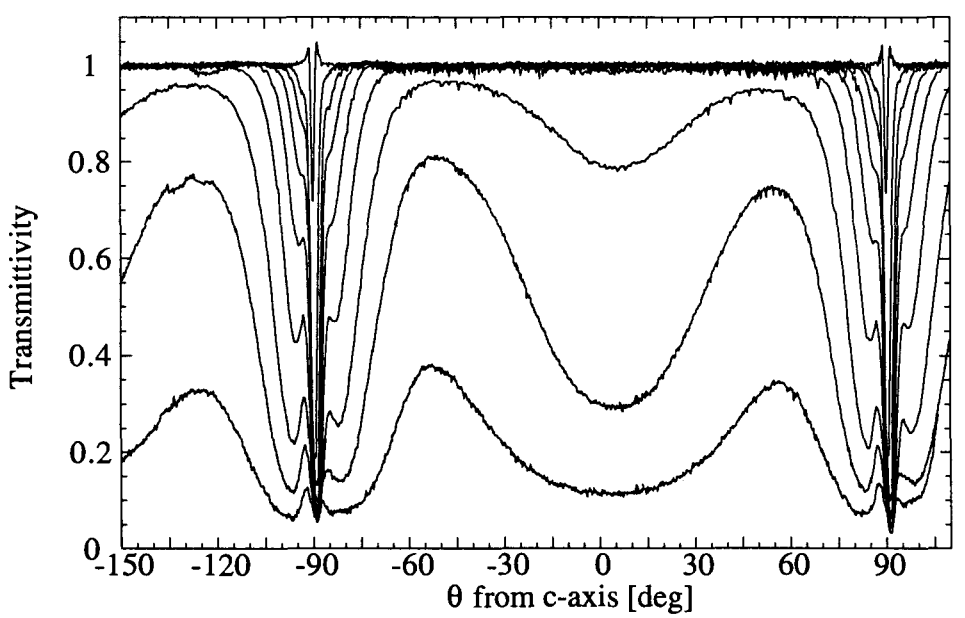

Figure 4.23: Dependence of the transmittivity of sample irr-X45-0.4 on the angle between the applied field and the c-axis. Defects are at $\pm$ 45 deg from the c-axis. $B_\phi = 2 \times 0.2$ T, $T_c \approx 88$ K. $H_{dc} = 590$ Oe, $H_{ac} = 7.1$ Oe, $f = 7.75$ Hz. Temperatures (curves from top to bottom): 88 K, and 81 K to 74 K in steps of 1 K.

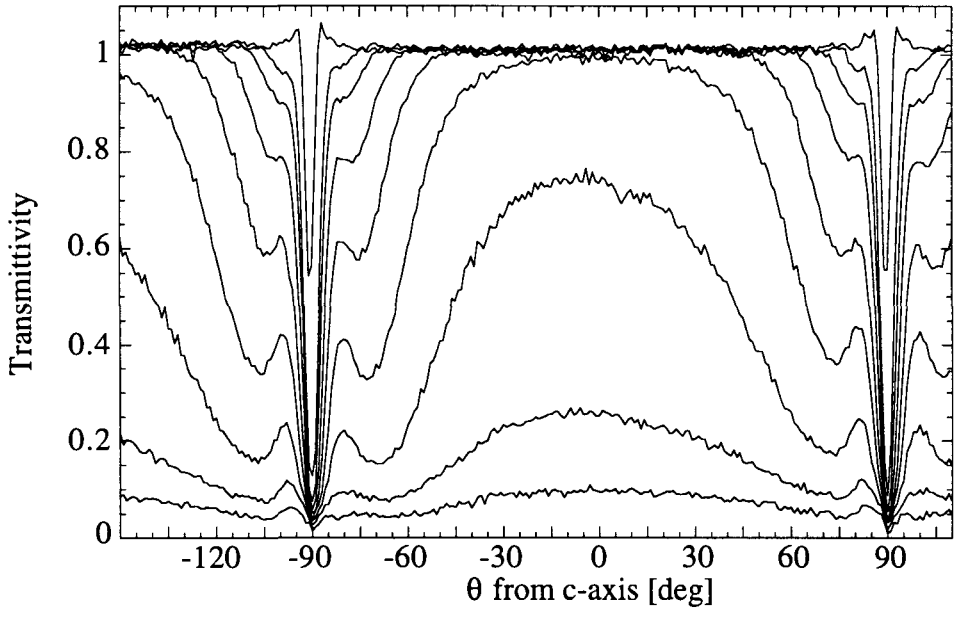

Figure 4.24: Dependence of the transmittivity of sample irr-X45-0.4 on the angle between the applied field and the c-axis. Defects are at $\pm$ 45 deg from the c-axis. B_ϕ =2×0.2 T, $T_c \approx$ 88 K. H_{dc} = 200 Oe, H_{ac} = 7.1 Oe, f = 7.75 Hz. Temperatures (from top to bottom): 87 K and from 83 K to 76 K in steps of 1 K.

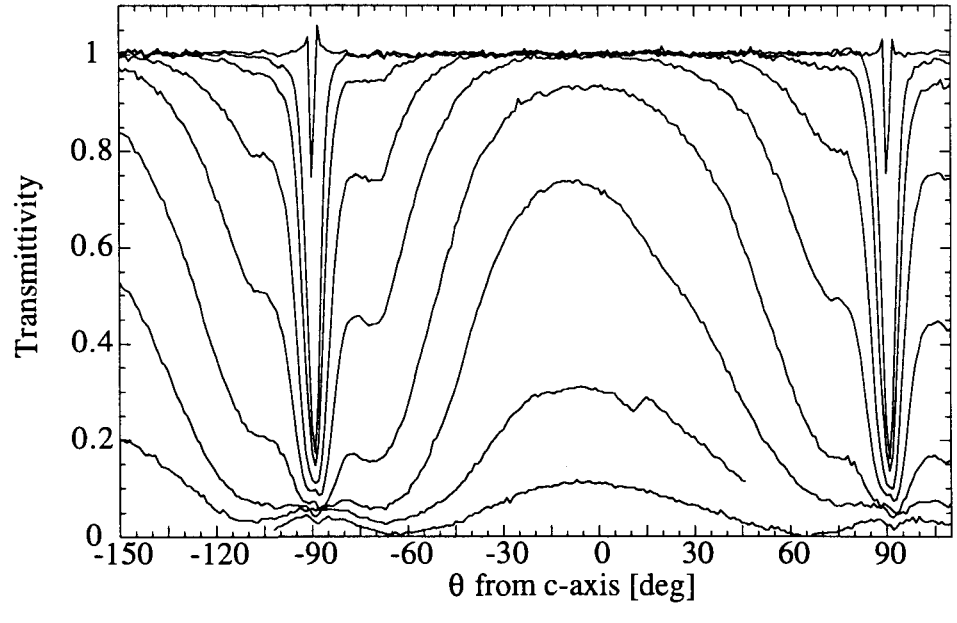

Figure 4.25: Dependence of the transmittivity of sample irr-X45-0.4 on the angle between the applied field and the c-axis. Defects are at $\pm$ 45 deg from the c-axis. B_ϕ =2×0.2 T, $T_c \approx$ 88 K. H_{dc} = 2000 Oe, H_{ac} = 7.1 Oe, f = 7.75 Hz. Temperatures (from top to bottom): 80 K, from 74 K to 68 K in steps of 1 K and 66 K.

4.4 Discussion

The main observations that can be made from the data are:

(a) pinning is enhanced by the introduction of columnar defects up to the highest investigated temperatures

(b) no further enhancement of the IRL is observed for crossed defects

(c) an enhanced shielding for alignment of the field with the columnar defects is observed for a set of columns of a single orientation

(d) for crossed defects that are symmetric to the c-axis, the enhancement is along c

(e) the directional enhancement is observed as soon as the I–V characteristic becomes nonlinear (i.e., below the IRL)

(f) the IRL essentially shows three parts: a high temperature, exponential part, a vertical part, and a high field, low temperature part.

Before discussing the anisotropy in pinning, the situation where the field is parallel to the defects should be considered first. Obviously the vortices are pinned by the defects. However, the irreversibility line displays three parts with apparently different behaviour of the vortex system. Most remarkable is the vertical part that separates between high temperature and low temperature regime. Such a vertical part means that the pinning energy is field independent, i.e., the vortices are pinned independently. This independent pinning regime is limited by two factors. On the high field side the increasing interactions lead to the appearance of interstitial vortices which are much less pinned (van der Beek et al. 1995). Some pinning remains due to their interaction with the pinned vortices. On the low field side on the other hand the vortices can gain positional entropy by delocalizing: the pancakes that form the vortex are distributed over several columns (Larkin and Vinokur 1995). The vortex is then localized by the fluctuations in the distribution of pinning centers. In this regime the pinning energy is again field dependent, because the variations in pin density lead to a distribution in pinning energies. On increasing the field the vortices occupy the pinning sites in the order of increasing energy. In the vertical part the pinning energy is constant which means that every vortex is probably pinned by just one columnar defect.

We now proceed to the discussion of the anisotropy in pinning by the columnar defects. A stronger pinning for alignment of the field with the columnar defects is what one would expect for a strongly coupled system, where the vortices behave as lines. This becomes clear from Fig. 4.26.

In this figure the properties of a crystal with point defects is compared to that of a crystal containing columnar defects. For both cases a vortex parallel to the

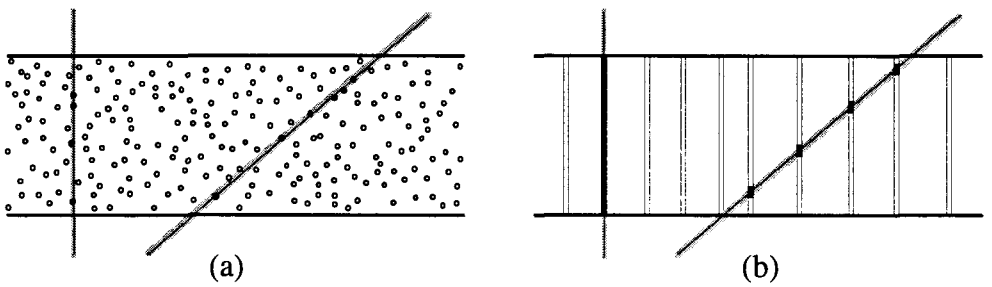

Figure 4.26: Pinning efficiency of different defects for rigid vortices: (a) For point defects the pinned volume per unit length of the vortex is independent of the direction. However, for completely rigid lines the pinning force is zero, because the line cannot adapt to the pinning potential. (b) For columnar defects the pinned volume is maximal for alignment of the vortex with the defect.

c-axis and a tilted vortex are considered. In the case of point defects a vortex line encounters on the average the same amount of pinning sites per unit length of the vortex, independent of its direction. Therefore the pinning force per unit length does not depend on the orientation of the vortex. In fact, a completely rigid vortex line cannot adapt to the pinning potential and the total force from the different point defects is zero on average.

In the case of columnar defects on the other hand, the volume of intersection between the vortex and the columnar defects grows when the vortex direction approaches that of the columnar defects. The pinning force per unit length of the vortex increases on decreasing the angle between vortex and defect and so should the current carrying capabilities.

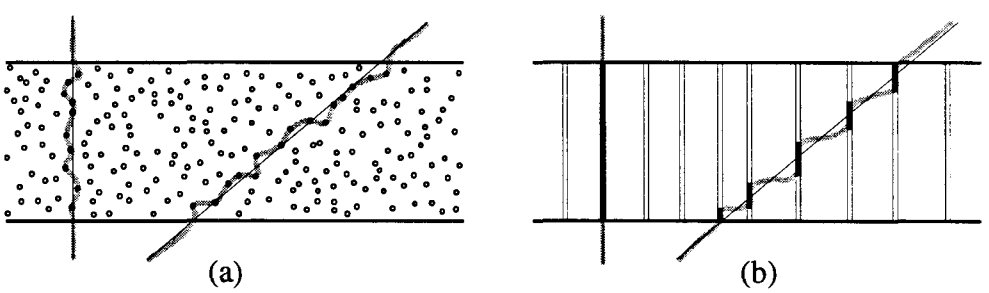

Figure 4.27: Pinning efficiency of different defects for soft vortices: (a) point defects, (b) columnar defects.

For soft vortices, i.e., vortices with a finite line tension ε_1, the situation is slightly different in that the vortices can adapt more easily to the pinning potential (see Fig. 4.27). Even in this case the conclusion remains the same: enhancement of pinning in the case of columnar defects, for alignment of the field with the columns.

In Bi-2212 without columnar defects the vortices do not behave as lines in the field and temperature range under consideration. The strong thermal fluctuations

lead to the suppression of the Josephson coupling such that a field component parallel to the layers penetrates freely due to the spontaneous nucleation of Josephson vortices. The vortex decouples into independent pancake vortices in the different layers. Note however, that a magnetic interaction always exists between pancakes in neighbouring layers although it is weak compared to the thermal fluctuations. Introducing columnar defects into the material leads to pinning sites for the pancake vortices that are not only strong, but moreover correlated in the different planes. This correlation could naturally give rise to a certain alignment of the pancakes which would be further strengthened by the magnetic interaction (at least for not too strong tilt of the defect with respect to the c-axis). Moreover, the strong pinning effect of the columns is expected to suppress the thermal fluctuations of the pancake vortices which should lead to the reestablishment of the Josephson coupling (Koshelev et al. 1996). Strong intralayer vortex interactions (stronger than the interlayer coupling) on the other hand can lead to a decoupling of the layers. According to these considerations a system of pancakes in the presence of columnar defects can adopt several configurations:

- totally ordered — a column is completely occupied by pancakes
- aligned but on different columns
- totally random

These configurations are illustrated in Figs.4.28 and 4.29.

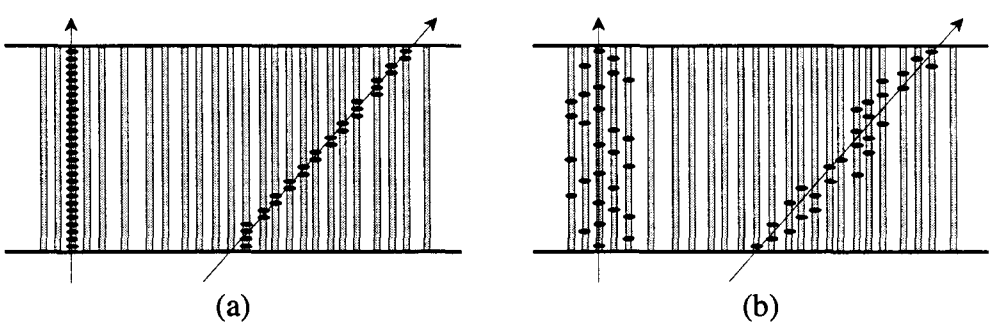

Figure 4.28: Correlated pinning of pancakes on columnar defects for two orientations of the external field. (a) strong correlations, (b) weak correlations.

Before comparing these simplified pictures to the presented experimental results one remark should be made: measuring the ac shielding current does not yield information on how vortices are pinned, but on how vortices depin in the presence of a current. Two cases are possible: one pancake depins independently from its neighbours, or pancakes depin collectively. Both modes are possible in either the correlated pinning configuration or in the uncorrelated pinning configuration.

Let us just recall when independent depinning occurs in the case of correlated pancakes: this case is expected for sufficiently high currents, when the size of the

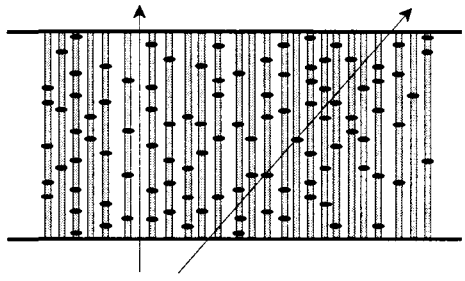

Figure 4.29: Completely random distribution of pinned pancakes. No enhancement of pinning for field along the defects is expected.

vortex loop that must be liberated by thermal excitations to initiate the movement can be smaller than the interlayer spacing s and then corresponds to just one pancake vortex (Koshelev et al. 1996). The current above which this decoupled motion occurs is $j_{dec} = \sqrt{\varepsilon_1 U_0}/\Phi_0 s$. ε_1 is the line tension, U_0 the pinning energy per unit length, and s the interlayer spacing. For an anisotropy $\gamma = 150$ the elastic tension is approximately $1.1\,10^{-15}$ J/m. U_0 is estimated from the pinning energy of a pancake vortex given by Gerhäuser et al. (1992) (70 meV) divided by s which gives in MKSA units 7.36×10^{-12} J/m. It follows that the decoupling current is $j_{dec} = 3.1 \times 10^{10}\mathrm{Am}^{-2}$. Note that the strongest measurable currents in the present set-up are of the order of 10^7 Am^{-2}.

It was observed by Kummeth et al. (1994) that this could explain the absence of anisotropy in pinning by columnar defects at low temperatures, since the magnetization currents are then so high that the size of the critical loop for vortex depinning falls below the interlayer spacing.

On the other hand, an anisotropy in (de-)pinning as it is evidenced by the dip in the transmittivity necessarily means that pancake motion occurs in a collective manner, via depinning of packets of several pancakes.

From the possible pancake distributions the completely random distribution can now be eliminated: it does not give rise to a higher probability of depinning packets of pancakes when the field is aligned with the columns. The two other distributions, totally ordered and aligned, but on different columns, are still possible. The different parts in the IRL suggest that they probably occur both, albeit at different vortex densities.

Therefore an anisotropy in pinning is observed over the whole accessible temperature range for defects along the c-axis. This is true as well for defects inclined by 30 degrees with respect to the c-axis, and for crossed defects with a 15 degree tilt. For crossed defects tilted by 45 degrees it is true in a limited field and temperature range only.

The direct comparison of the IRLs of samples with defects along c, and samples with crossed defects, but the same total dose, shows that the splay does not enhance the irreversible regime (Figs. 4.14 and 4.15), rather it is slightly reduced. This is in

accordance with the splay glass model if the IRL traces the glass transition, since a splay in the columnar defects is expected to degrade the glass transition temperature only when the splay angle exceeds the average thermal tilt in the flux liquid phase (Hwa et al. 1993). However, if the IRL is determined by the creep rate then a splay should push it to higher temperatures and fields. This would at least be the case for line-like vortices, it is not clear what should happen in a strongly layered compound. For line-like vortices the splay in the defect orientation is expected to hinder the free propagation of vortex kinks by which vortices jump between columns in the Bose glass phase. But how does such a kink look like in a strongly layered superconductor? Imagine that part of a pancake stack has shifted to a neighbouring column. The kink is the connecting field and current distribution between the top pancake of the lower part and the bottom pancake of the higher part of the stack. For closely spaced columns the kink induces only a slight perturbation in the field and current distribution and the interaction between the two pancakes is mainly magnetic (Bulaevskii et al. 1992). A Josephson string between the two pancakes develops only when their separation exceeds the Josephson length $\lambda_J = \gamma s$. For an anisotropy $\gamma = 150$ and an interlayer distance $s = 1.5$ nm this length equals 225 nm. The matching field that would correspond to a mean spacing between columnar defects of the same size is 450 G. This is much lower than in the samples used for this work and the interdefect distance therefore much smaller than λ_J.

Such a kink in a pancake stack can propagate along the defects simply by a series of jumps of pancake vortices.

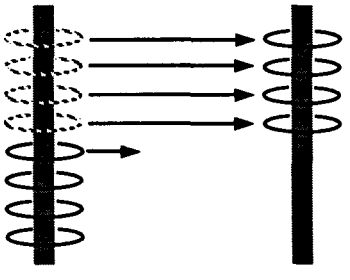

Figure 4.30: Kink in a pancake stack and its propagation

Studies of the magnetization current in the critical state give diverging results with respect to the effect of splay. Schuster et al. (1996) claim that the field profiles observed with a magneto-optical technique give a constant ratio of approximately 1.5 between the current for crossed defects with a 45 degree tilt and that for defects along c, and this in the whole temperature range from 5 K to 80 K. Such a difference could in fact be explained by the increased defect size in the copper oxide planes that results from the oblique irradiation (the defect is a factor $\sqrt{2}$ longer in one direction for an irradiation under 45 degrees). Magnetization measurements at 6 K and 40 K by Hardy et al. (1996) point rather towards a weaker pinning by splayed defects. An enhanced critical current was only observed for the very large tilt angle

of 75 degrees. Note that even this large angle would still be negligible in the rescaled isotropic frame (Blatter et al. 1992).

In summary, for small-angle splayed defects there is a slight lowering of the IRL, but no clear enhancement of the critical current. Together with the observed anisotropy in the transmittivity the following picture emerges: although the vortices exhibit line-like features in their creep from columnar defects, no further increase of the supported current at a given voltage is observed for splayed defects at low and intermediate temperatures.

Apparently a misalignment between families of columns seems to slightly enhance the creep rate. This could be understood if the two sets of columns were in competition with each other in pinning stacks of pancakes. In order to follow an average direction of the field intermediate between the directions of the different sets of columns, the vortex has to hop several times between the two sets of columns. This could limit the maximal size of a pancake stack and lead to kinks that are absent when the columns are along c. It could be this increased number of kinks that leads to a enhanced creep.

The effect should be stronger for the crossed defects with a 45 degree tilt than for those tilted by 15 degrees. This could explain why the steep part in the IRL for such a defect arrangement is not completely vertical. For this tilt of the crossed defects the dip in the transmittivity curves is absent in the high and low field regime (Fig. 4.24). At low fields one deals with delocalized pancake stacks and at high fields with interstitial pancakes. In both cases a potential which is constant along the c-axis is absent, so that this direction is not preferential any more. In the intermediate field regime on the other hand an anisotropy is still present. The vortex stacks should then be localized on the columns, but in order to follow the field direction the vortex has to jump between the two sets.

In this situation the E–j characteristics shows power law behaviour. This is not what is expected in the case of splay glass or Bose glass dynamics, where the electric field has a stretched exponential dependence on the current density (compare also Fig. 5a in the paper of van der Beek et al. (1995)). Such a behaviour should be observed though, if the relevant energy is that which is needed to move one of the pancakes at the end of a stack (i.e., to move a kink by one pancake), because this energy does not depend on the current density.

4.5 Conclusions

It has been found, that pinning by columnar defects is anisotropic in the region of the H–T phase diagram that has become irreversible after the introduction of these defects. This means more precisely, that the pancakes which constitute a vortex depin in a correlated manner, i.e., in packets of pancakes or as kinks, at least for current densities below $\approx 10^7 \mathrm{Am}^{-2}$. Such correlated depinning is observed for fields along the c-axis in the case where the columnar defects also follow this direction,

but also in the case of crossed columns, arranged symmetrically with respect to the c-axis. It is moreover observed for other orientations of the applied field, if this orientation coincides with that of a set of tilted columns.

The irreversibility line does not seem to be very sensitive to the exact arrangement of the columnar defects. In particular is the IRL not shifted to higher temperatures and fields by a splay in the defects. This is probably due to the strongly layered nature of the material.

A lot of problems are still waiting to be solved before vortex dynamics in layered superconductors in the presence of columnar defects will be completely understood. One of these problems is whether the Josephson coupling is reestablished after introduction of columnar defects. Such a coupling should in fact become important in vortex creep when the mean distance between columnar defects exceeds the Josephson length. By studying samples with sufficiently low irradiation doses it should be possible to shed some light at least on this question.

Chapter 5

Anisotropy of pinning by columnar defects in $HgBa_2Ca_2Cu_3O_{8+\delta}$

5.1 Introduction

The materials that are most often used to study pinning of vortices by columnar defects are $YBa_2Cu_3O_8$ (Y-123) and $Bi_2Sr_2CaCu_2O_8$ (Bi-2212). While the first is only slightly anisotropic ($\gamma = 7$), with vortices that behave as lines, the second is a layered material ($\gamma \gtrsim 150$) for which the vortices have lost most of their line-like character and are better described as stacks of 2D-vortices. $HgBa_2Ca_2Cu_3O_{8+\delta}$ (Hg-1223), which has been discovered more recently by Schilling et al. (1993), is a material with an anisotropy that lies between those of Y-123 and Bi-2212, $\gamma = 52$ according to Vulcanescu et al. (1996). Its study can shed light on the depinning of vortices with a behaviour intermediate between true vortex lines and pancake stacks. Moreover, with a maximal T_c of 135 K Hg-1223 is the material with the highest critical temperature known up to date. This allows to apply rather high magnetic fields without degrading the superconducting transition temperature below the working range of a nitrogen cryostat.

5.2 Experimental details

The single crystal with dimensions $150 \times 250 \times 70 \mu m^3$ used for this work was synthesized by Dorothée Colson at SPEC/CEA-L'Orme-les-Merisiers via a gold amalgamating technique described in more detail in chapter 1. It has then been annealed in oxygen in order to increase its oxygen content. This procedure lead to a T_c of 134.4 K (an optimal T_c of 135 K is obtained for a stoichiometry of $HgBa_2Ca_2Cu_3O_{8.19}$, according to Bertinotti et al. (1995)). However, the oxygenation of Hg-1223 under low pressure of oxygen is a very slow process and the annealed crystals are suspected to have an optimal oxygen content in a limited volume close to the surface only. Another source of inhomogeneity in Hg-1223, which has three copper oxide layers

per unit cell, is the intergrowth of the crystal phases Hg-1212 and Hg-1201 with two or one copper oxide layer. Apparently it is difficult to exactly control the number of copper oxide layers per unit cell by the growth conditions. Note that Hg-1201 has a T_c of approximately 95 K, as-grown Hg-1212 a such of 120 K, which can be pushed to 126 K by annealing in oxygen, and as-grown Hg-1223 has a T_c of 120 K (Bertinotti et al. 1997).

After a characterization of the pristine crystal by tracing the transmittivity transition curves in zero as well as several applied fields, the sample was irradiated along its c-axis with a dose of 10^{15} m^{-2} 6 GeV Pb ions resulting in a matching field of 2 T. This slightly lowered the critical temperature to 132.6 K.

The discussion of the results obtained on this crystal will follow the lines of chapter 4. First, the superconducting transition of the pristine and the irradiated crystal as reflected in the increased shielding of an ac field will be discussed. It reveals a sample inhomogeneity that probably has to be ascribed to the incomplete oxygenization mentioned above, although cracks in the crystal can not completely be ruled out. This will be followed by an analysis of the additional observations made on the crystal after irradiation. The irreversibility line exhibits two regimes, and its shape confirms that the vortex physics of Hg-1223 in the presence of columnar defects are intermediate between those observed in Y-123 and Bi-2212. An anisotropy of pinning by the columnar defects is observed in both regimes of the IRL. It appears as soon as a shielding current becomes measurable as seen in chapter 4 for Bi-2212. The investigation of vortex dynamics via measurements at variable frequency (E–j characteristics) finally showed that the high field part of the IRL is rather determined by the vortex creep rate than by a phase transition.

5.3 Results

5.3.1 Temperature dependence of the transmittivity

Before irradiation

Figure 5.1 shows the transition in zero field of the pristine crystal. As can be seen in the first harmonic, the signal drops steeply over a temperature interval of 1.6 K, but only to a value of 0.2. Also is a slight shoulder visible at about 90% of full signal. To this sharp drop in the in-phase component of the first harmonic corresponds a peak in the third harmonic. This peak also has a shoulder coinciding with that in the first harmonic. This structure may reflect a sample inhomogeneity which might be due to the incomplete oxygenization process.

On decreasing the temperature further the shielding continuously increases, but much more slowly. The third harmonic signal in turn remains at a very low level, then goes through a weak maximum and finally drops to zero at 126.5 K. Such a weak third harmonic signal is sometimes also seen in Bi-2212 where it can be ascribed to a surface barrier. In the present case, the barrier like behaviour is due to the

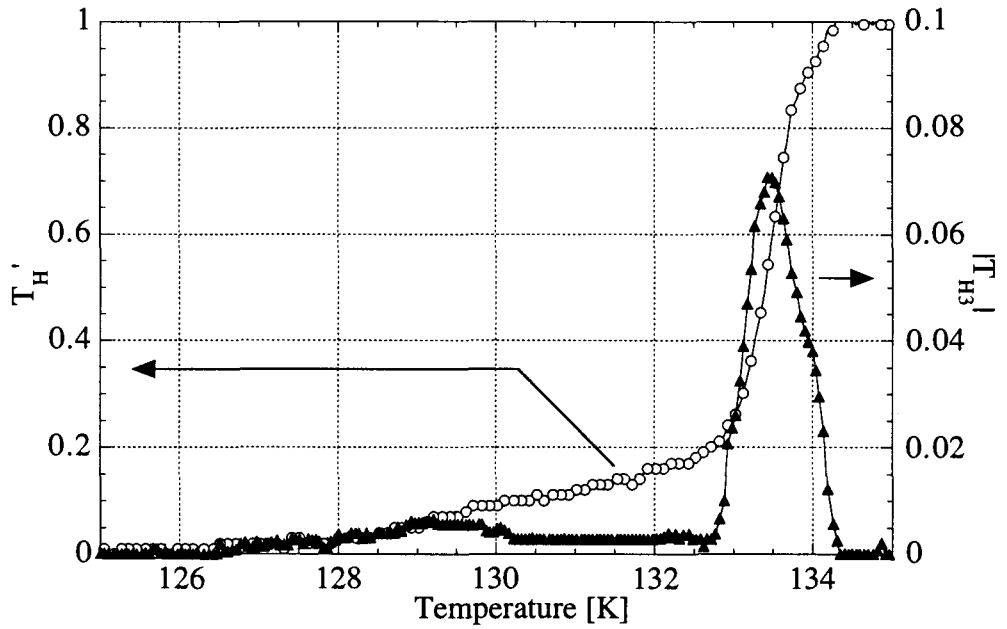

Figure 5.1: In-phase component of the first (o) and amplitude of the third harmonic transmittivity (▲) as measured on the pristine Hg-1223 crystal during a temperature decrease in zero dc field. $H_{ac} = 7.1$ Oe, $f = 7.75$ Hz.

full oxygenization of the sample perimeter, with respect to the poorly oxygenated interior.

Transition curves for several applied dc fields are shown in Fig. 5.2. For the measurements shown in this figure the field was at an angle of approximately 13 degrees with respect to the c-axis of the crystal. Several changes can be observed in the transition curves of the third harmonic when a field is applied: its onset temperature decreases slightly and the transition widens. Moreover, the small second peak in the third harmonic at 129 K becomes much larger for an applied field of 50 Oe. At higher fields this second peak merges with the principal one.

After irradiation

The real part of the first harmonic and the modulus of the third for the transition in zero field after irradiation are shown in Fig. 5.3. The transition curve of the first harmonic looks still quite the same after irradiation, there is just a slight decrease of the critical temperature to 132.6 K to be noted. The third harmonic on the other hand has undergone striking changes: all the substructures observed before have completely disappeared. This might be due to the increased importance of bulk pinning as compared to the surface barrier. The structures partly recover when a dc field is applied (see Figs. 5.4 and 5.5). In particular, the second peak in $|T_{H3}|$ appears again. It is clearly separated from the first peak even though the applied field has the same value as the highest field shown in Fig. 5.2. In the first harmonic

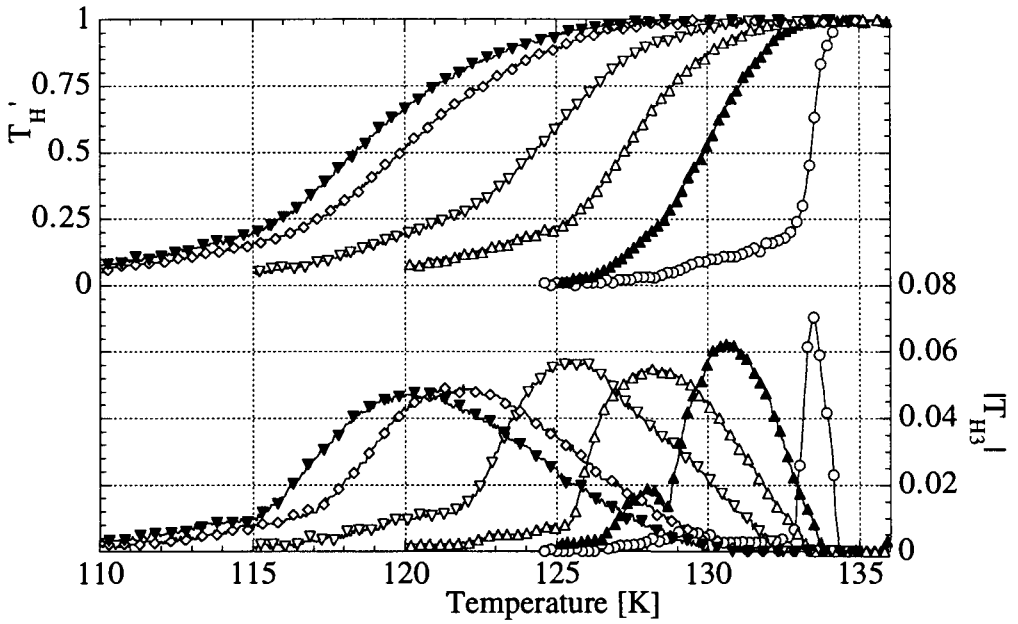

Figure 5.2: Temperature dependence of the in-phase component of the first and amplitude of the third harmonic transmittivity of the pristine Hg-1223 crystal for different fields: 0 Oe (○), 50 Oe (▲), 100 Oe (△), 200 Oe (▽), 400 Oe (◇), 500 Oe(▼). The field orientation is tilted by 13 degrees with respect to the c-axis. $H_{ac} = 7.1$ Oe, $f = 7.75$ Hz.

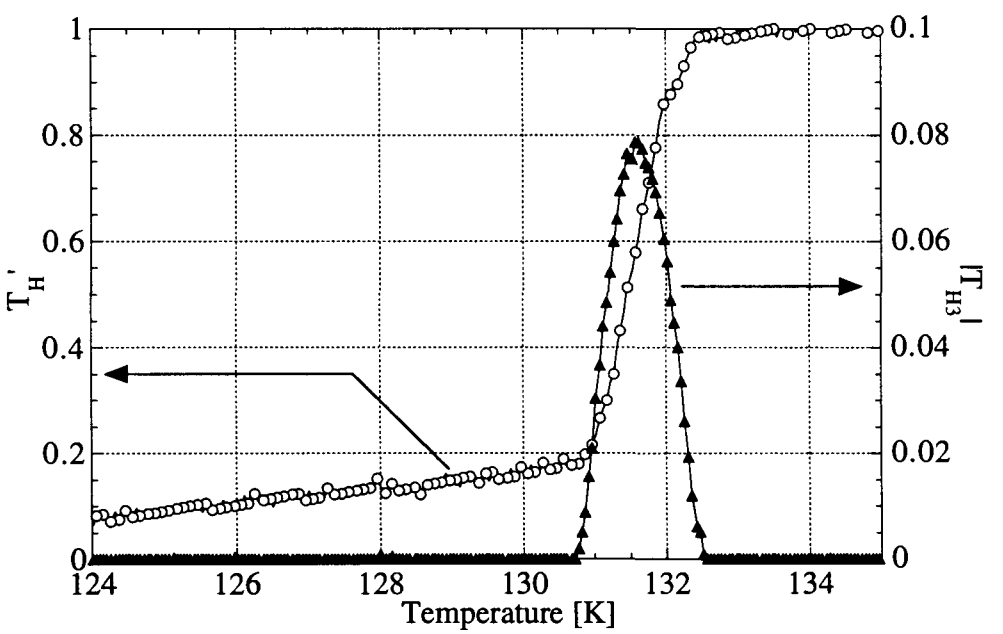

Figure 5.3: In-phase component of the first (○) and amplitude of the third harmonic transmittivity (▲) during a temperature decrease in zero dc field as measured on the Hg-1223 crystal after irradiation with a dose corresponding to $B_\phi = 2$ T. $H_{ac} = 7.1$ Oe, $f = 7.75$ Hz.

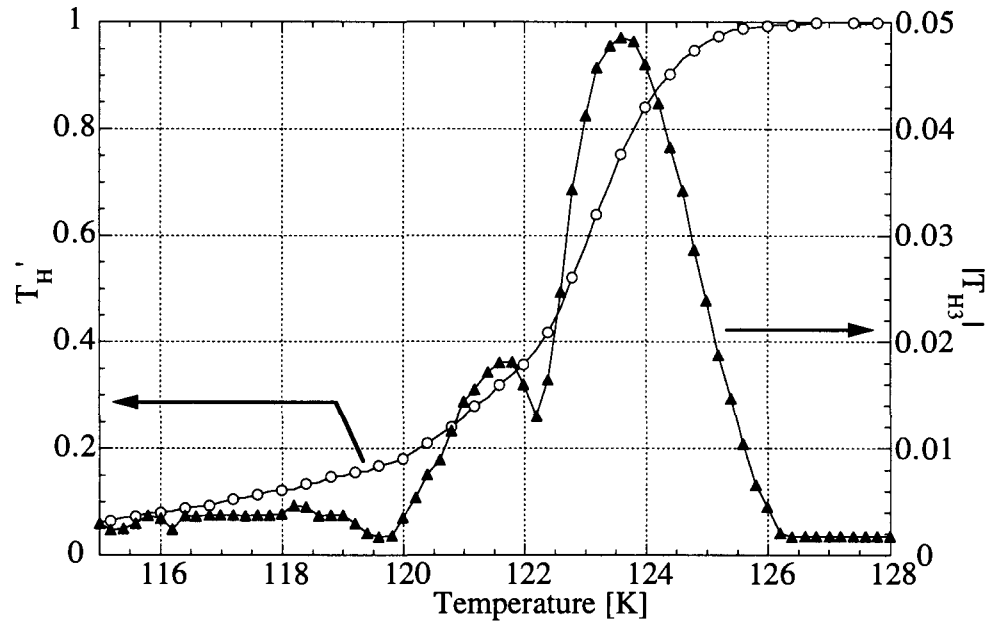

Figure 5.4: In-phase component of the first (o) and amplitude of the third harmonic transmittivity (▲) measured on the irradiated Hg-1223 sample (B_ϕ = 2 T) during a temperature scan in an applied dc field of 500 Oe. H_{ac} = 7.1 Oe, f = 7.75 Hz.

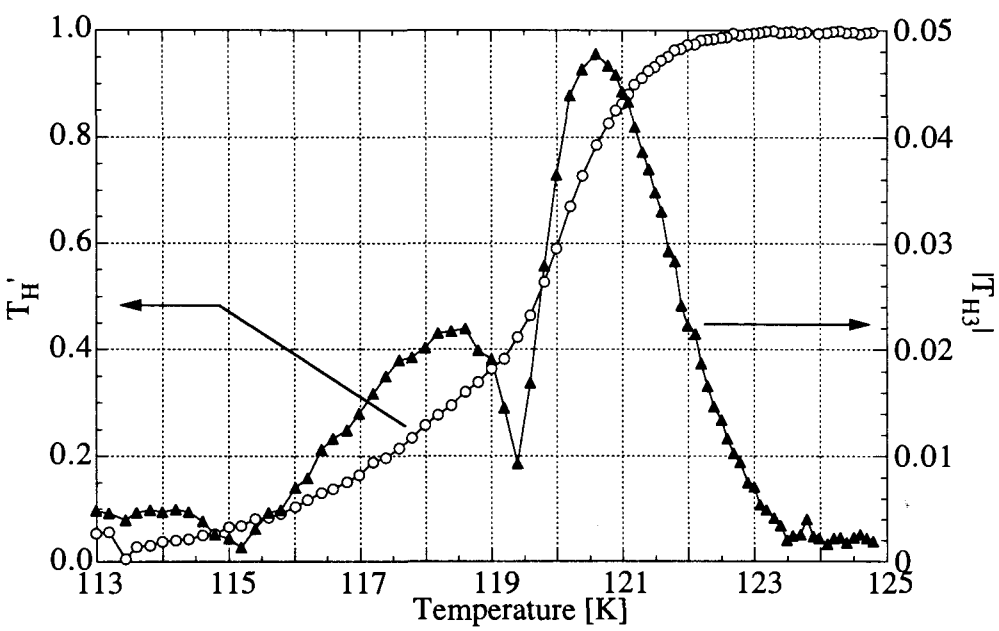

Figure 5.5: In-phase component of the first (o) and amplitude of the third harmonic transmittivity (▲) measured on the irradiated Hg-1223 sample (B_ϕ = 2 T) during a temperature scan in an applied dc field of 5000 Oe. H_{ac} = 7.1 Oe, f = 7.75 Hz.

this double peak structure is only visible as a change in slope. Even in the presence of a dc field as high as 5000 Oe the two peaks remain rather well separated (Fig. 5.5).

When drawn in a polar plot with the temperature as parameter the double peak structure in the third harmonic turns out to be a minor loop inside a main loop (Fig. 5.6). The main loop resembles those observed in Bi-2212 with columnar defects, and is expected for a parallelogrammatic ac magnetization loop. Two explanations are possible for the double loop: (a) there is a crack in the sample separating it in two parts, from either of which a magnetic response is picked up. The superposition then gives the observed signal. (b) part of the sample has a lower T_c due to incomplete oxygenization giving rise to a double transition. The main loop is then due to the part of the sample with the higher T_c. At a certain temperature T_1, the part of the sample with the lower T_c starts to screen the ac field, leading to a second loop, superposed on the first one.

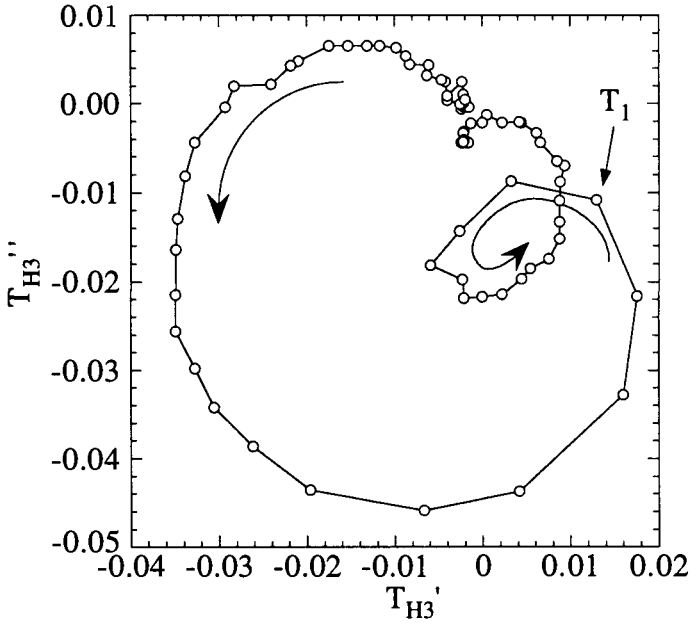

Figure 5.6: Polar plot of the third harmonic transmittivity that is observed during the shielding transition of the irradiated Hg-1223 sample ($B_\phi = 2$ T) during a temperature scan in an applied dc field of 5000 Oe. $H_{ac} = 7.1$ Oe, $f = 7.75$ Hz. The arrows indicate the sense given to the curve by decreasing the temperature. T_1 is the temperature at which the minor loop starts.

5.3.2 Irreversibility line

Even if a double transition is present in this crystal, the *onset* of the third harmonic is solely determined by the onset of nonlinearity at the sample edge, i.e., in the high T_c phase. Therefore it is still useful to study the variation of the third harmonic onset with amplitude of the applied dc field.

The onset has been determined as explained in chapter 2. The IRL after irradiation is shown in Fig. 5.7 in semi-logarithmic scale. As compared to Bi-2212, the

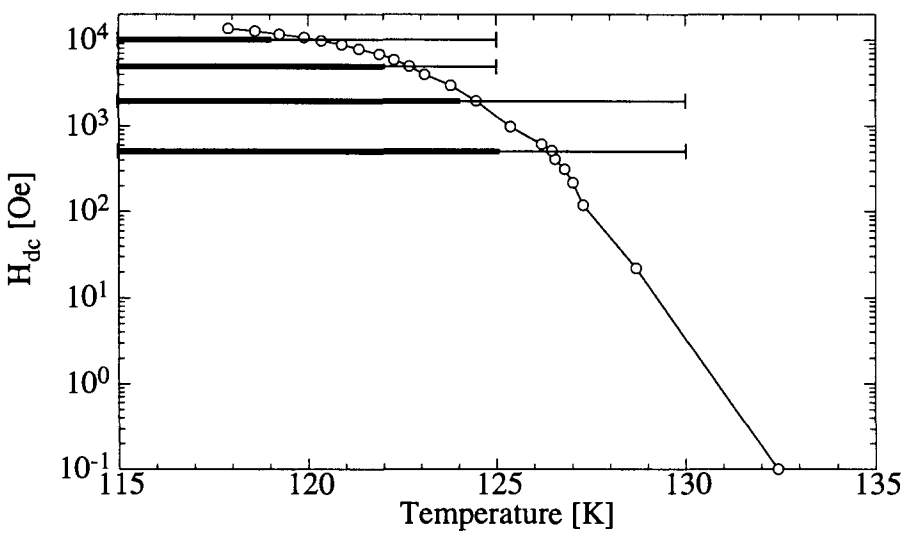

Figure 5.7: Irreversibility line of the irradiated Hg-1223 sample in a semi-logarithmic plot. The horizontal bars indicate the field values for which the dependence of the transmittivity on the field direction has been investigated. Thick lines mark the temperatures where an anisotropy of pinning by the columnar defects has been found.

absence of the vertical part is striking. As a result the distinction of different parts in the IRL is much less obvious than in Bi-2212. A tentative separation in different parts is shown in Fig. 5.8, in which the irreversibility field is plotted against reduced temperature. Three parts have been distinguished: (1) a high temperature part above 126.5 K where the irreversibility field drops exponentially with temperature, (2) an intermediate part extending down to 121.6 K, and (3) a "low" temperature part. Intermediate and low temperature part are fitted by a power law in $(1 - t)$, where $t = T/T_c$. It is not clear what the origin of these two parts is. Neither are they comparable to the IRL of Y-123, which is linear in T, except very close to T_c (Samoilov et al. 1996), nor have they counterparts in the IRL of low dose irradiated Bi-2212, although the IRL there has a shape which superficially resembles that of Hg-1223 (see van der Beek et al. (1995)).

The high temperature part on the other hand has the same exponential temperature dependence as in the IRL of Bi-2212 (chapter 4 and van der Beek et al. (1995)).

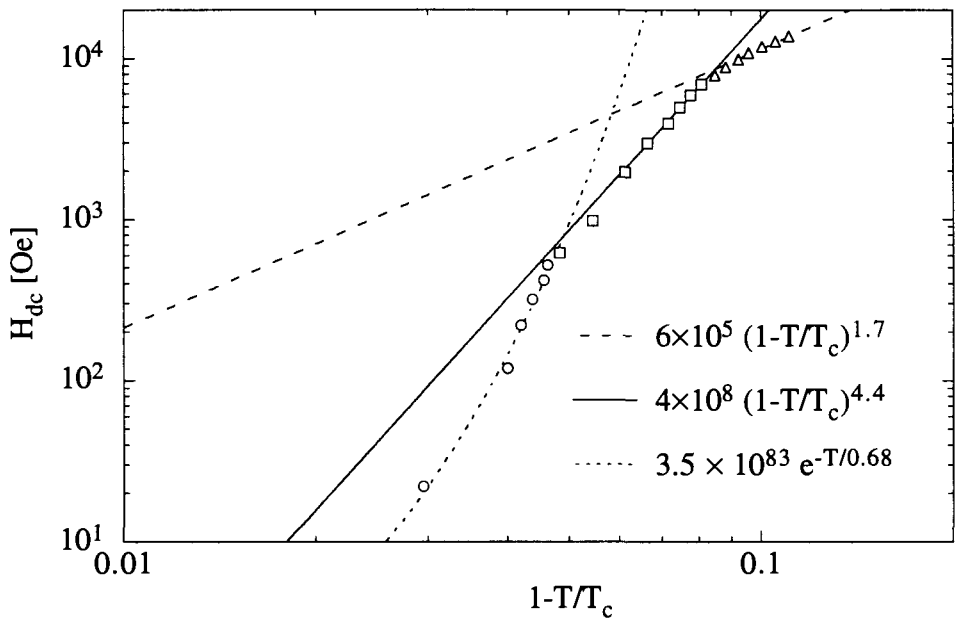

Figure 5.8: Irreversibility field of the irradiated Hg-1223 sample against reduced temperature. Curve fits have been applied to the different parts.

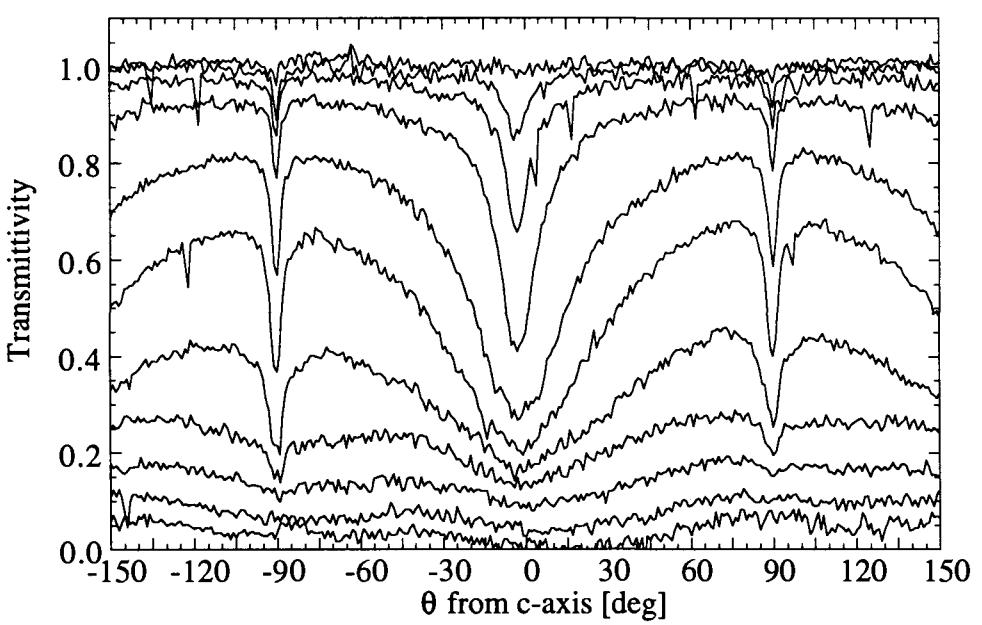

Figure 5.9: Dependence of the transmittivity of the irradiated Hg-1223 crystal on the angle θ between the applied field and the c-axis. $B_\phi = 2$ T, $H_{dc} = 500$ Oe, $H_{ac} = 7.1$ Oe, $f = 7.75$ Hz. Temperatures: 126 to 119 in steps of 1 K, 117, 114, and 111 K (from top to bottom).

5.3.3 Angular dependence of the transmittivity

Angular scans of the transmittivity have been taken for fields ranging from 500 Oe to 10 kOe. In this whole range anisotropy of pinning induced by the columnar defects is observed. The field values and temperature ranges for which the dependence of the transmittivity on the angle between dc field direction and c-axis have been studied and at which temperatures an anisotropy in pinning by the columnar defects has been found is indicated in the IRL (Fig. 5.7). As in heavy-ion irradiated Bi-2212 an anisotropy in shielding due to the pinning by columnar defects sets in slightly below the irreversibility temperature. Figs. 5.9 and 5.10 represent the low field region (H_{dc} = 500 Oe) and the intermediate field region (H_{dc} = 5000 Oe) of the IRL, respectively. The corresponding curves for 2 kOe and 10 kOe look similar and are not shown here. The anisotropy of pinning by the columnar defects ($\parallel c$) is reflected by the central dip. Note that this dip is deeper than those occurring for alignment of the dc field with the ab-plane of the sample ($\pm$90 degrees). This is in contrast to the observation made in Bi-2212 where shielding always first sets in for alignment of the dc field with the ab-plane and where the dips for $H \parallel ab$ are deeper than for H parallel to the columns. The increased shielding very close to the ab-plane could be due to intrinsic pinning of the vortices by the layered structure (Feinberg and Villard 1990). The broader minimum around ab, which is more pronounced at higher fields, can be ascribed to the material anisotropy. Similar observations have been made in Y-123 and scaled perfectly with the anisotropy (Yeh et al. 1995).

The dip due to pinning by the columnar defects has a similar shape and width for all the field values, although these values correspond to quite different ratios between the number of vortices and the number of defects. A comparison of angular scans at different fields but approximately the same temperature is shown in Fig. 5.11. The effect of increasing the field on the pinning by the columnar defects is very similar to increasing the temperature: screening decreases for all directions and the pinning dip becomes sharper. However, increasing the field and increasing the temperature are not completely equivalent. This becomes evident from Fig. 5.12. In this figure the temperatures of the curves at different fields have been chosen such that the transmittivity for alignment of the field with the columns equals 0.4. In this representation one can see clearly that the dip becomes sharper when the field is increased. The approximate angles above which the signal is independent of angle are 78 (500 Oe), 50 (2000 Oe), 37 (5000 Oe), and 21 degrees (10 kOe).

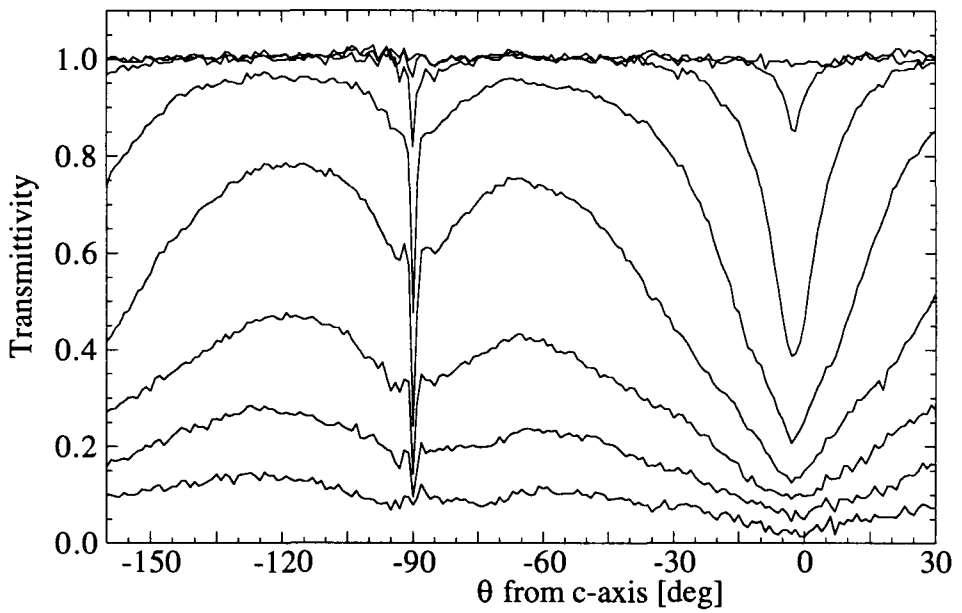

Figure 5.10: Dependence of the transmittivity of the irradiated Hg-1223 crystal on the angle θ between the applied field and the c-axis. $B_\phi = 2$ T, $H_{dc} = 5000$ Oe, $H_{ac} = 7.1$ Oe, $f = 7.75$ Hz. Temperatures: 124 to 110 in steps of 2 K (from top to bottom).

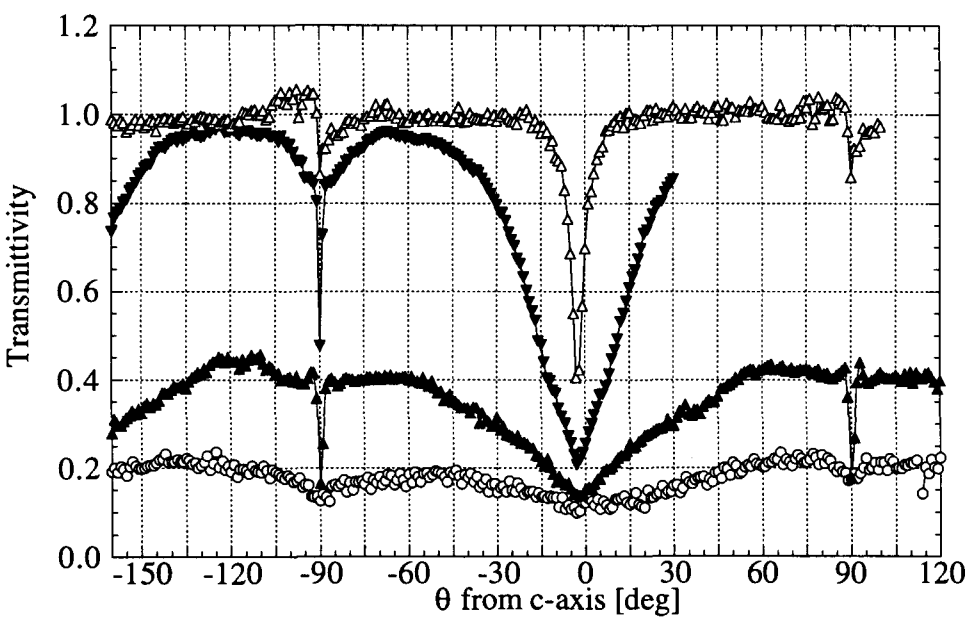

Figure 5.11: Comparison of angular scans at different fields. Temperatures are 118 K for the scans at 500 (○), 2000 (▲), and 5000 Oe (▼), and 117 K for 10000 Oe (△). $H_{ac} = 7.1$ Oe, $f = 7.75$ Hz.

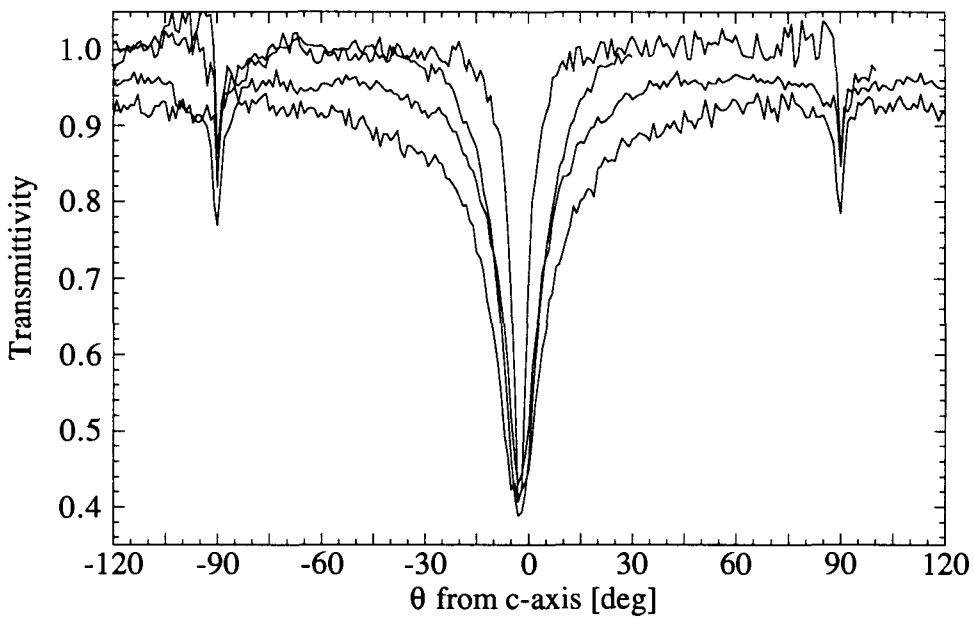

Figure 5.12: Comparison of angular scans at different fields. The temperatures were chosen so that the transmittivity for field parallel to c and to the columnar defects is reduced to 0.4. Temperatures are 123 K for 500 Oe (bottom curve), 122 K for 2000 Oe, 120 K for 5000 Oe, and 117 K for 10 kOe (top curve). $H_{ac} = 7.1$ Oe, $f = 7.75$ Hz.

5.3.4 Frequency dependence of the transmittivity

It has been shown in the previous section, that the pinning by columnar defects is anisotropic in both parts of the IRL. In a next step one would like to know if the vortex dynamics are the same in the low and intermediate field regions as well. In an attempt to answer this question temperature scans at different frequencies of the ac field have been performed for 100, 200, and 5000 Oe dc field. However, for the low field values the noise level was too high to obtain useful results, so only the 5000 Oe data are presented here. This corresponds to the intermediate region in the IRL. Fig. 5.13 shows a log-log plot of the frequency dependence of the normalized shielding current j, obtained from the transmittivity as explained in chapter 2. First it has to be noted that the lines above the bold dashed line stem from the temperature region where the second peak in the third harmonic is observed. The dynamics there are dominated by the screening by the low T_c phase in the interior. Below the dashed line the dynamics can be expected to be purely those of the high T_c phase at the perimeter. The lines in Fig. 5.13 are power law fits to the data without taking into account the lowest frequencies, where systematic deviations occur. A power law dependence of j on frequency were also observed at high fields in Bi-2212 by C. J. van der Beek et al. (1995).

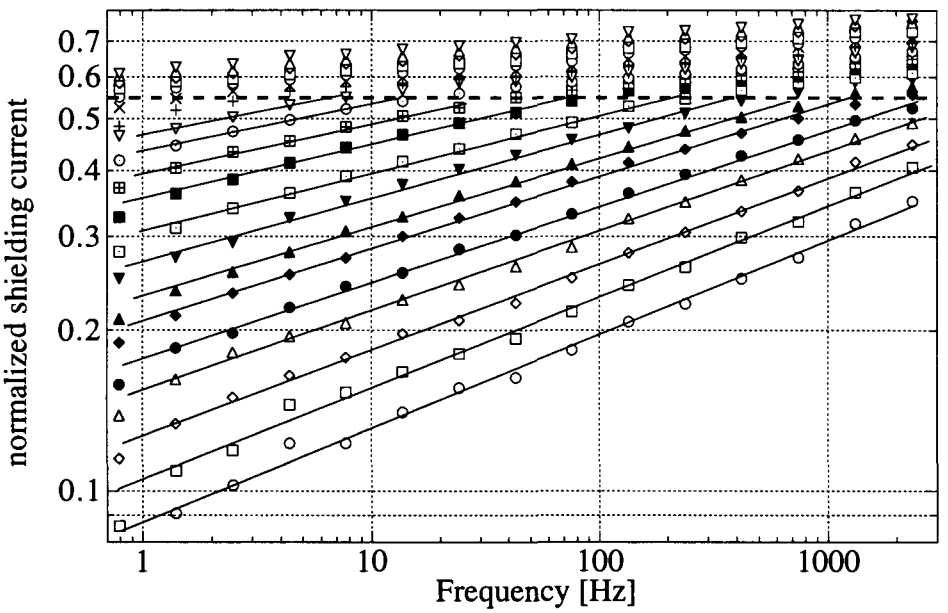

Figure 5.13: Frequency dependence of the shielding current for on applied dc field of 5000 Oe. H_{ac} = 7.1 Oe. Temperatures in Kelvin: 121.8 (○), 121.6 (□), 121.4 (◊), 121.2 (△), 121.0 (●), 120.8 (♦), 120.6 (▲), 120.4 (▼), 120.2 (⊡), 120.0 (■), 119.8 (⊞), 119.6 (⊙), 119.4 (▽), 119.2 (+), 119.0 (×), 118.8 (○), 118.6 (□), 118.4 (◊), 118.2 (△), 118.0 (▽). Lines are power law fits (see text).

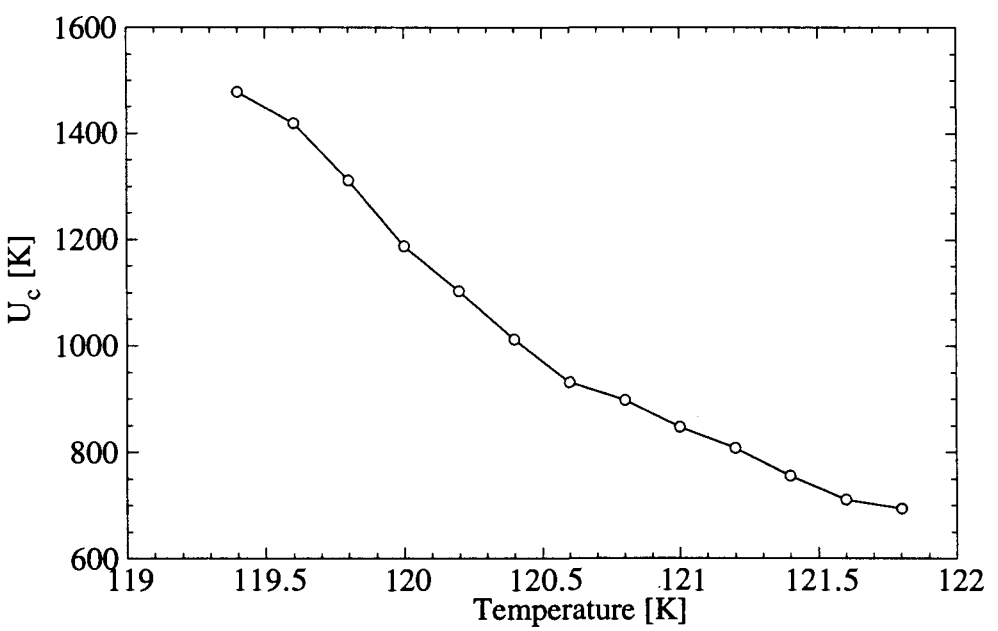

Figure 5.14: Flux creep activation energy, U_c, as a function of temperature as extracted from the power law fits on the j vs. f data.

As argued there, such a power law dependence with a temperature dependent power does not correspond neither to the creep predictions of the Bose glass theory, nor to a critical scaling analysis of the Bose glass transition, nor to the expectations for collective creep. They can be explained if one assumes that the activation barrier against flux motion depends logarithmically on J, $U(J,T) = U_c(T)\ln(J_c/J)$. The prefactor $U_c(T)$ then corresponds to k_BT divided by the slope of the data in Fig. 5.13. $U_c(T)$ is shown in Fig. 5.14. The temperature dependence of U_c for Hg-1223 seems to be quite different from that observed in Bi-2212 where a linear dependence has been observed(van der Beek et al. 1995). However, the temperature range over which this dependence could be traced here is very limited ($\gtrsim$ 2 K) and much smaller than that observed by (van der Beek et al.). A direct comparison has therefore to be taken with care.

5.4 Discussion

The temperature variation of the transmittivity components at the transition shows quite clearly that the transition to a complete shielding occurs in two steps. Apparently the sample is not homogeneous. A has been mentioned in the introductory part of this chapter a strong source of inhomogeneity is the slow diffusion of oxygen during annealing, which most likely results in an enhanced T_c in a surface layer only. However, bad sample quality could lead to a similar observation. A crack in the material separating the sample into two domains could lead to a shielding signal composed of the responses of the two sample parts, and also result in a double transition.

Evidence against this second possibility comes from the transition curve in zero field after the irradiation. In fact, the irradiation cannot turn a sample that consists of two parts into a simply connected sample, and should therefore not lead to the disappearance of the double transition with a second small maximum in the third harmonic.

In the case of inhomogeneous oxygenation on the other hand, the irradiation enhances the shielding current in the high T_c surface layer to a level that is sufficient to completely shield the interior of the sample. The transition of the inner part with a lower T_c then happens in the (local) absence of any ac signal, and can therefore not be detected. Before irradiation the shielding would not have been complete, and a small signal could be detected. The second transition is again visible when a dc field is applied, because this reduces the supported shielding current under otherwise equal conditions (temperature, ac amplitude and frequency) and the ac signal penetrates to the central region.

Despite the fact that the sample is not homogeneous, it is nevertheless possible to study some of the properties of the high critical temperature phase. Over a certain temperature range below the onset of superconductivity it is only this phase that makes a contribution to the ac response (if one neglects any contribution of the

normal electrons). This means that the flux inside is only determined by the outer perimeter and the single loop model should be very well applicable.

In particular, the onset of the third harmonic can be expected to contain information about this high T_c phase only so that the IRL keeps its significance. When compared to the IRLs of heavy ion irradiated samples of Y-123 (see for example Samoilov et al. (1996)) or Bi-2212 (previous chapter), that of Hg-1223 exhibits differences with respect to both. While a vertical part is absent as in the case of Y-123, there is nevertheless a high temperature exponential part as in Bi-2212, which is not observed in Y-123.

As in the case of Bi-2212 the exponential part can be explained by delocalization of the vortices, when the creep is dominated by the most weakly pinned vortices. However, the absence of a vertical part probably signifies that the depinning mechanism is not that of single pancakes, which in Bi-2212 gives rise to a field independent irreversibility temperature. Apparently in Hg-1223 the vortices are lines, even though they might be very soft. This corresponds well to the observed anisotropy of Hg-1223 which is intermediate between those of Y-123 and Bi-2212.

The angular dependence confirms this conclusion. Indeed, if one considers the angular dependence of the transmittivity for a dc field of 500 Oe (Fig. 5.9), then it is seen that as the field is tilted towards the *ab*-plane, and the *c*-axis component of the field decreases, the shielding does not improve until the field is almost parallel to the *ab*-plane. An improvement of shielding when the field direction approaches that of the *ab*-plane has also been observed in Y-123 (Jiang et al. 1994). This effect is due to the anisotropy of the superconducting properties: on approaching the *ab*-plane direction the vortex core (ξ) becomes smaller and the extend of the screening currents (λ) increases. This results in a stiffening of the vortex and hence a better pinning. The characteristic angle where this effect sets in should move closer to the *ab*-direction as the anisotropy is increased. This is what one observes in Hg-1223. The observation that in Bi-2212 on the other hand the dip around *ab* extends again to larger angles has a different origin. Here the vortices are practically decoupled into stacks of pancakes oriented along the *c*-axis and a freely penetrating *ab*-component of the field. The in-plane component does not contribute to the dissipation, which is determined by the density of pancakes alone. This density decreases as the field is turned towards *ab*. In Bi-2212, with its very high anisotropy, it is this decreasing pancake density that leads to an improvement of shielding even far from alignment with the *ab*-plane. In this point, which tests specifically the line-like nature of the vortices, Hg-1223 appears to be closer to Y-123 than to Bi-2212.

In the high field part of the IRL a power-law frequency dependence of the screening current is observed with a temperature dependent power. As has been said before, this cannot be explained by critical scaling near the Bose glass transition, since the power should be constant in the critical region below the transition. The IRL is determined by creep, as in the low field part. It is not clear though, what the creep mechanism is.

5.5 Conclusions

Columnar defects have been found to give rise to an anisotropic pinning in Hg-1223 crystals. The irreversibility line for this material has a feature that is also found in the IRL of Bi-2212: an exponentially decreasing part. This part is supposed to occur for delocalized vortices that are not pinned by a single column, but by a fluctuation in pin density. Apparently the anisotropy of Hg-1223 is still sufficiently high to allow the vortices to wander between the columns and to take advantage of a locally increased density of columns. However, the dependence of the transmittivity on the angle between the defects/c-axis and the field direction suggests that the vortices keep their line-like character in this material. The behaviour of the vortices is therefore intermediate between those observed in Y-123, where the vortices are rather stiff, and those of Bi-2212, where the vortex is very soft and is better regarded as a stack of pancakes.

Only one sample of this material has been measured, which moreover seems to be inhomogeneous. The results of this chapter should therefore be checked on other samples of better quality in order to get certainty about the physics of the vortex matter in Hg-1223.

Chapter 6

Angular dependence of the surface barrier in $Bi_2Sr_2CaCu_2O_8$

6.1 Introduction

Even in the absence of an effective pinning of the vortices by defects in the bulk of a superconducting material other sources of irreversibility still remain; such as the competition between the attractive force on the vortices exerted by the sample surface and their repulsive interaction with the surface screening currents. Together these interactions are at the origin of the Bean-Livingston surface barrier (Bean and Livingston 1964).

Another type of barrier arises in non-ellipsoidally-shaped samples where the vortices enter first at sharp sample corners. The interaction with the shielding current pushes them towards the sample center, but in order to advance they have to increase their length, at a considerable energy cost. There is therefore a barrier against flux entry. This is the geometrical barrier (Indenbom et al. 1994a; Zeldov et al. 1994).

The geometrical barrier, as its name indicates, depends on the geometry under consideration. The usual geometry to study this barrier has been to apply the magnetic field along the normal to the top surface of a rather flat sample of rectangular cross section as illustrated in Fig. 6.1.

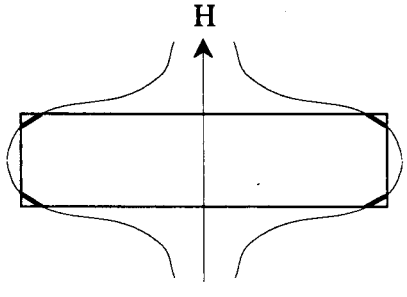

Figure 6.1: Flux penetration from the corners in a flat sample of rectangular cross section.

In this chapter flux exit and entry of a c-axis field into a Bi-2212 crystal will be studied in the presence of an additional in-plane field. The in-plane field might be expected to alter the geometry of the flux penetration process with respect to that shown in Fig. 6.1. It will be shown though, that the observed local induction loop can be understood in terms of a barrier for flux entry as it is observed in the presence of a c-axis field only. This means that in this material the vortices are so soft (the Josephson coupling so small), that a geometrical barrier effect is negligible. It is proposed that the origin of the barrier is the ordinary Bean-Livingston barrier and not the geometrical barrier as claimed by Zeldov et al. (1994).

6.2 Experimental details

Two samples grown via the "travelling solvent floating zone" technique have been used for this study: a pristine Bi-2212 crystal of approximate dimensions $700 \times 200 \times 30$ μm^3, and a T_c of 90.1 K and a sample of size $450 \times 250 \times 30$ μm^3 and $T_c = 78$ K, which was irradiated with 6 GeV Pb ions at $\pm$ 15 degrees from the c-axis with a dose of $5 \times 10^{14} m^{-2}$ in each direction. The experimental set-up is that described in

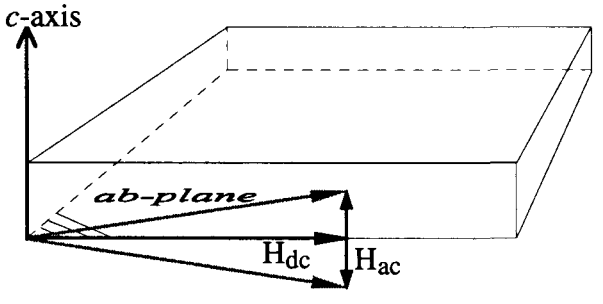

Figure 6.2: Orientations of ac and dc magnetic field with respect to the sample. The dc field is shown to lie completely parallel to the *ab*-plane of the sample. In the experiments slight deviations of perfect alignment have been explored as well.

chapter 2 with the specialty that the dc magnetic field orientation is close to the *ab*-plane (see Fig. 6.2). The action of the ac field is that of a periodic tilting of the vortices already present in the sample. It thus induces a periodic entry and exit of a field component parallel to the c-axis. Moreover, since in the following experiments the ac magnetic field amplitude is of the same order of magnitude as the dc field, it cannot be regarded as a minor perturbation. For this reason the data will not just be analysed via the transmittivity components, but the "full" signal will be reconstructed from these components.

6.3 Results

The onset of screening for dc field orientations closely aligned with the *ab*-plane (θ is the angle between the field direction and the *ab*-plane), as it shows up in the transmittivity components of the pristine sample with $T_c = 90.1$ K, is shown in Fig. 6.3. As the temperature is lowered the in-phase component of the first harmonic develops a dip that continuously deepens while its width remains almost the same (Fig. 6.3(a)). The out of phase component on the other hand shows more structure (Fig. 6.3(b)): next to a central peak there are plateaus on either side. Moreover, the angular extent of the whole structure increases noticeably as the temperature is lowered. What is most intriguing however, is the angular dependence of the third harmonic component. This is illustrated in Fig. 6.3(c), where $|T_{H3}|$ is traced as a function of θ. The third harmonic shows a central peak and two satellite peaks centered at e$\pm$9 degrees. Surprisingly the third harmonic signal vanishes when the dc field forms an angle of 6 degrees with the *ab*-plane. On decreasing the temperature the height of the peaks grows and the secondary peaks broaden towards higher angles. The minimum at $\theta = 6$ degrees persists, independently of the temperature. At this angle the *c* component of the static field is 10.5 Oe. This is surprisingly close to half the ac field amplitude (20.8 Oe). As will become clear later, this is a pure coincidence. Note that when the third harmonic signal vanishes the total *c*-axis field still changes sign over one cycle.

As the temperature is very close to T_c, H_{c1}, or more exactly H_p, the field of first penetration, is very small, of the order of 1 Oe, much smaller than both ac field and the *c*-axis component of the dc field at the minimum in T_{H3}. The Meissner effect can therefore be eliminated as a possible origin of the minimum. Note that H_p increases approximately linearly from zero as the temperature is decreased below T_c and might become important. At the lowest temperature shown in Fig. 6.3, 78 K, it is approximately 10 Oe (Chikumoto et al. 1992).

6.3.1 Influence of ac frequency and amplitude

The triple peak structure in the third harmonic was also observed in the irradiated sample with a T_c of 78 K. At 75 K the triple peak structure in the third harmonic is still clearly resolved. Apparently pinning by the columnar defects does not yet dominate the dynamics at this temperature and a study of the ac amplitude and frequency dependence of the minimum position is therefore possible, even in this irradiated sample.

Let us first consider the influence of the frequency of the ac excitation. As can be seen from Fig. 6.4 the position of the minimum does not change with frequency. The peaks however, change drastically. The central peak is strongly suppressed when the frequency is increased. The satellite peaks decrease slightly but broaden very much with increasing frequency. From this figure it can also be seen that the position of the minimum depends on ac field amplitude. The ac amplitude here is 1.19 Oe and

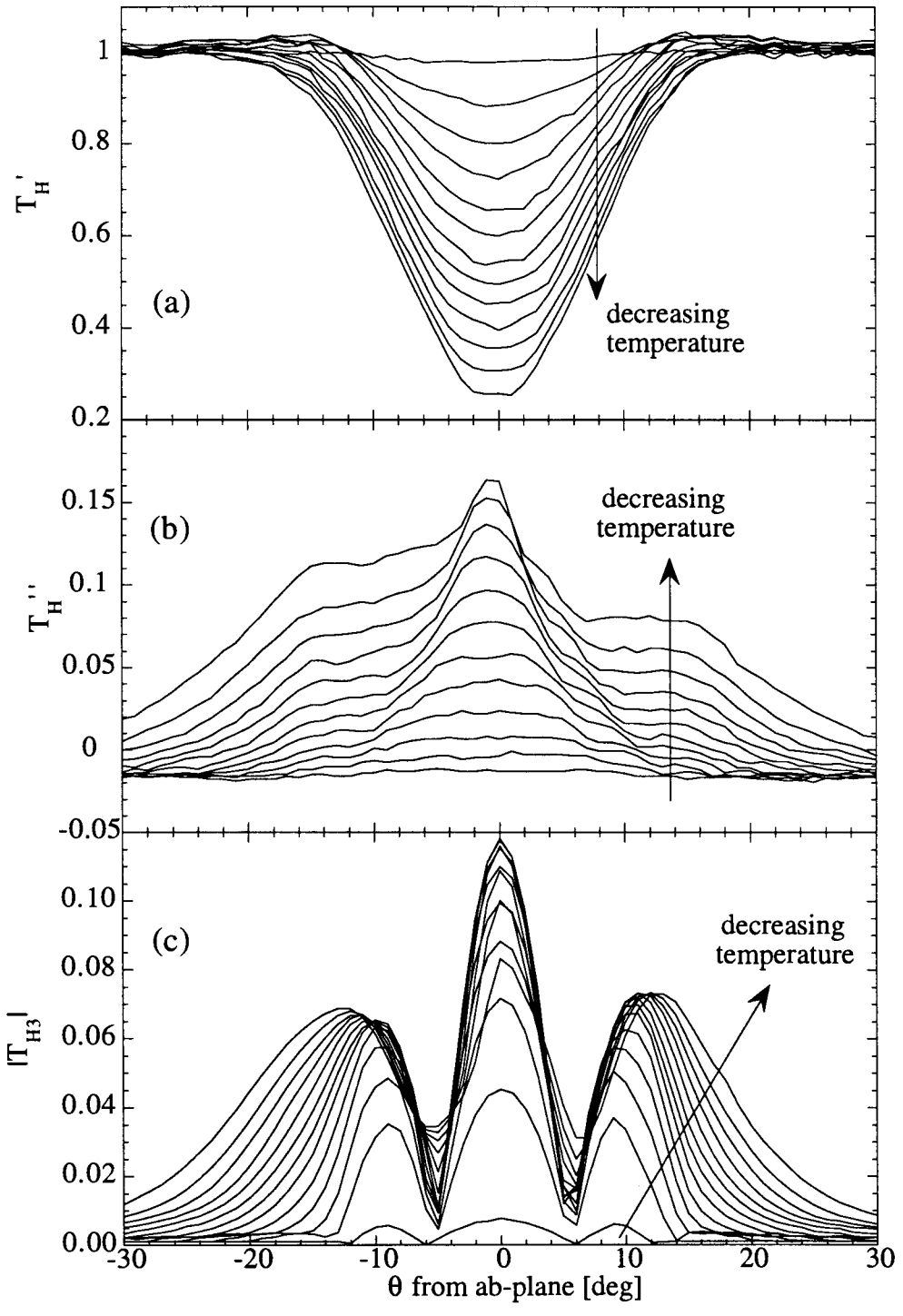

Figure 6.3: Dependence of (a) the in-phase and (b) out-of phase components of the first harmonic and (c) of the amplitude of the third harmonic transmittivity on the angle between the dc field direction and the *ab*-plane of a pristine sample with $T_c = 90.1$ K. $H_{dc} \approx 101$ Oe, $H_{ac} = 20.8$ Oe, $f = 7.75$ Hz. Temperatures: 90 K to 78 K in steps of 1 K.

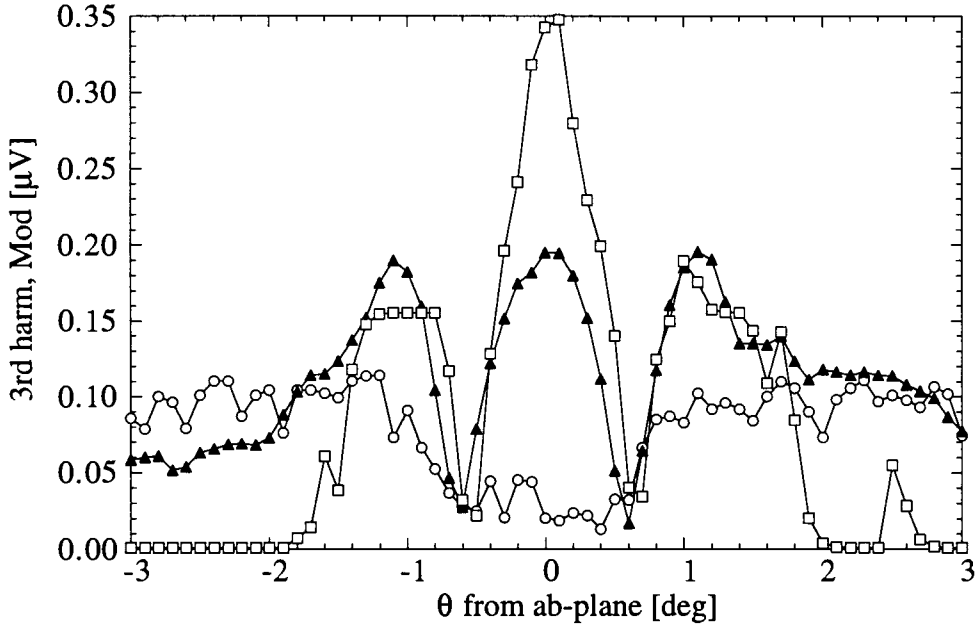

Figure 6.4: Dependence of the triple peak structure around *ab* on the frequency of the ac field at an ac amplitude of 1.19 Oe in an irradiated sample with crossed defects at ±15 degrees. $T_c = 78$ K. $H_{dc} = 101$ Oe, $T = 75$ K. Frequencies: 7.75 Hz (□), 76.1 Hz (▲), and 747 Hz (○).

the minimum lies at approximately 0.6 degrees. This has to be compared with the 20.8 Oe ac amplitude and the angle of 6 degrees observed for the pristine sample. The dc field is in both cases 100 Oe. That the shift is not just due to the presence of the columnar defects is shown in Fig. 6.5. The minimum position can actually be shifted towards higher angles in the irradiated sample as well, by increasing the ac amplitude. The angles obtained from these curves are collected in table 6.1. As becomes clear from this table the ratio between ac and dc field is not a constant. This excludes a simple arithmetic origin of the minimum, due only to the ratio of the two fields as suggested in the work of (Ji et al. 1989).

6.3.2 Polar plots of the third harmonic

Only the amplitude of the third harmonic has been considered up to now. In order to gain more insight into the angular dependence one should look at its real and imaginary parts. Figure 6.6 shows polar plots of the third harmonic for the pristine sample and a field of 100 Oe. The angle is held fixed and the temperature varied for each curve. Here, a crossover is clearly visible. For dc field parallel to the planes (Fig.6.6a) the response of the sample is very different from the one at 16 degrees (Fig.6.6f). On increasing the angle, and thus the *c*-axis field, the amplitude of the third harmonic response diminishes but the polar plot keeps its shape. Then,

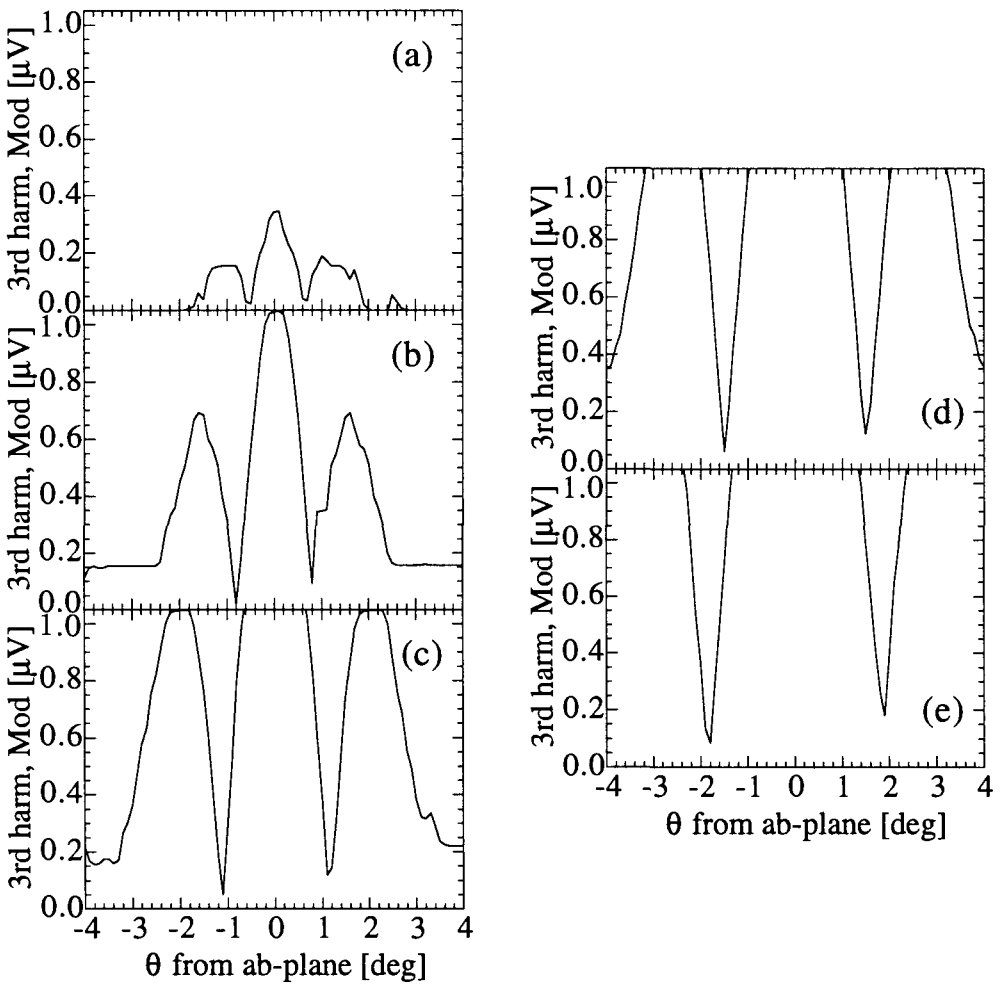

Figure 6.5: Dependence of the triple peak structure around *ab* on the amplitude of the ac field with frequency 7.75 Hz in an irradiated sample with crossed defects at ±15 degrees. $T_c = 78$ K. $H_{dc} = 101$ Oe, $T = 75$ K. ac field values: 1.19 (a), 2.59 (b), 4.01 (c), 5.41 (d), and 7.17 Oe (e).

Table 6.1: Variation of the position of the minimum in the third harmonic with third harmonic amplitude. The position is given as the angle θ measured from the *ab*-plane. The corresponding *c*-axis dc field is given as well as the ratio to the ac field.

H_{ac} [Oe]	θ [deg]	$H_{dc,c}$ [Oe]	$H_{dc,c}/H_{ac}$
1.19	0.6	1.047	0.880
2.59	0.8	1.396	0.539
4.01	1.13	1.972	0.492
5.41	1.5	2.618	0.484
7.17	1.85	3.228	0.450

around 6 degrees in the present case (Fig.6.6c), the whole figure turns and the third harmonic response evolves into a second type. On increasing the angle further, the third harmonic response increases again. The second response type, exemplified by the polar plot at 16 degrees, comes close to the ideal cardioid, although the full cycle has not yet been described. This reflects a parallelogrammatic hysteresis loop (see chapter 2).

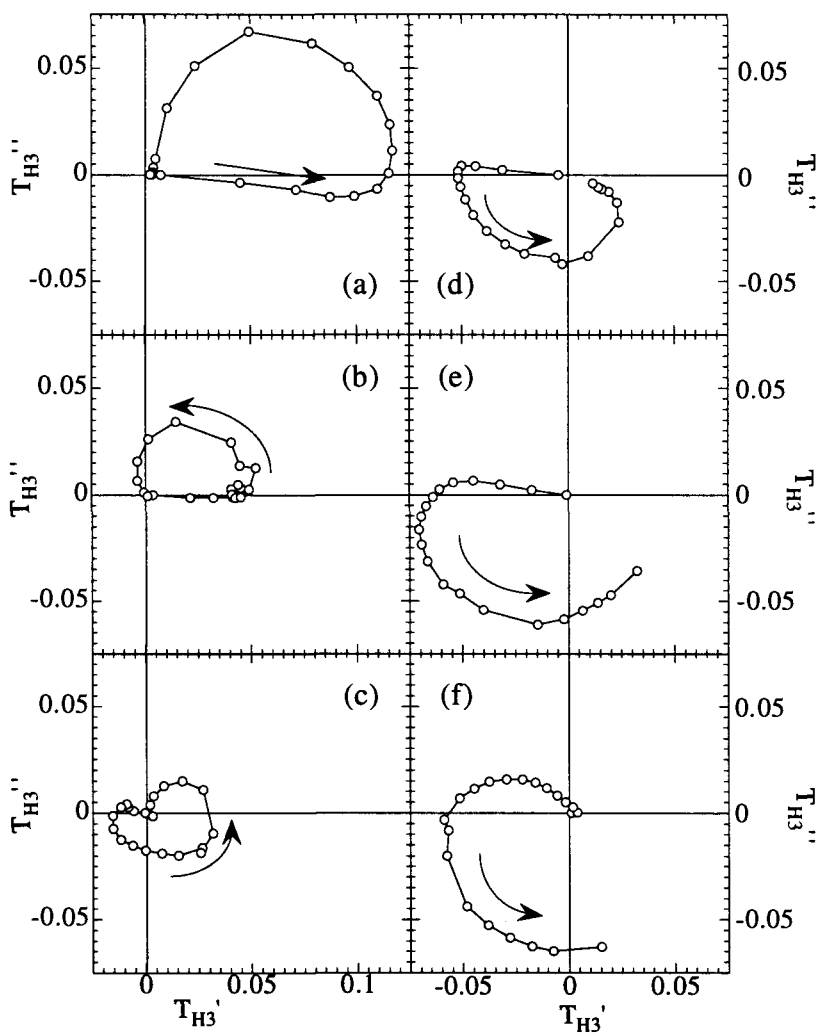

Figure 6.6: Polar plots of the third harmonic as a function of temperature. For each curve the temperature varies between 88.8 K and 67.8 K. The curves are traversed in the positive sense as the temperature is decreased (arrows). The different curves correspond to different angles θ between the dc field direction and the ab-plane: (a) parallel to ab, (b) 4 degrees, (c) 6 degrees (minimum), (d) 8 degrees, (e) 12 degrees, (f) 16 degrees. $H_{dc} = 101$ Oe, $H_{ac} = 20.8$ Oe, $f = 7.75$ Hz

around 6 degrees in the present case (Fig.6.6c), the whole figure turns and the third harmonic response evolves into a second type. On increasing the angle further, the third harmonic response increases again. The second response type, exemplified by the polar plot at 16 degrees, comes close to the ideal cardioid, although the full cycle has not yet been described. This reflects a parallelogrammatic hysteresis loop (see chapter 2).

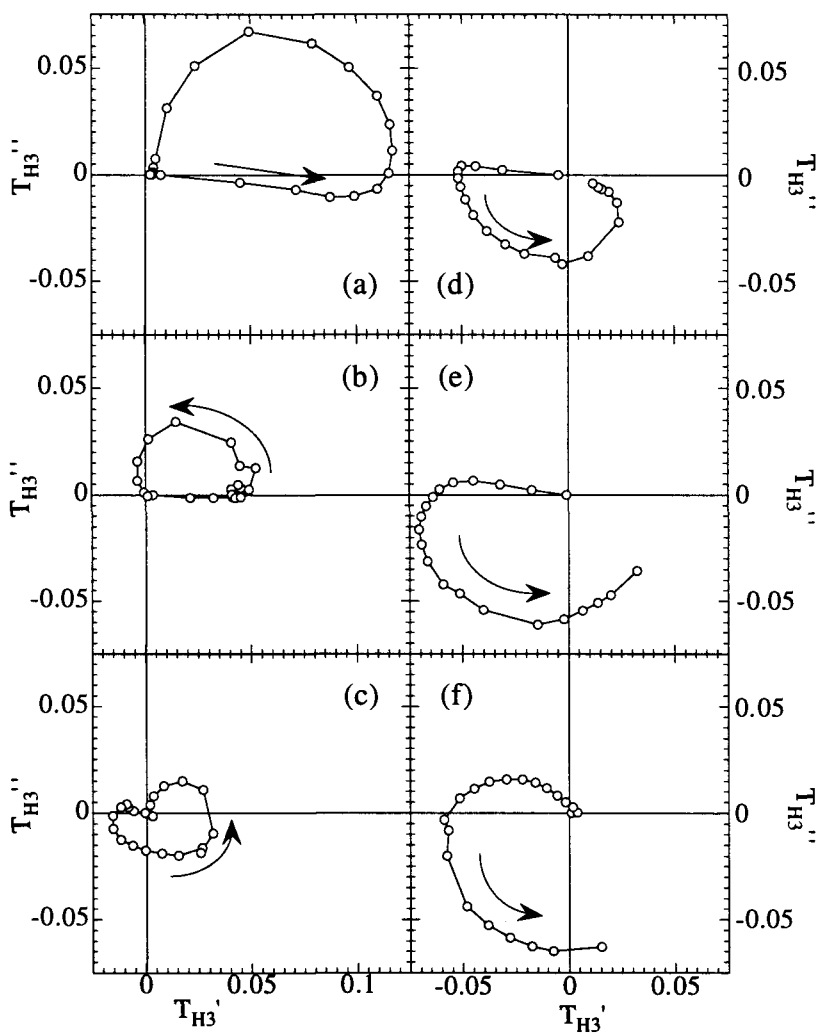

Figure 6.6: Polar plots of the third harmonic as a function of temperature. For each curve the temperature varies between 88.8 K and 67.8 K. The curves are traversed in the positive sense as the temperature is decreased (arrows). The different curves correspond to different angles θ between the dc field direction and the ab-plane: (a) parallel to ab, (b) 4 degrees, (c) 6 degrees (minimum), (d) 8 degrees, (e) 12 degrees, (f) 16 degrees. $H_{dc} = 101$ Oe, $H_{ac} = 20.8$ Oe, $f = 7.75$ Hz

6.4 Discussion

It has already been mentioned that bulk pinning can be excluded as the source of the observed behaviour since irradiation with heavy ions does not change the response for $H \parallel ab$ at high temperatures appreciably. A surface or geometrical barrier however, cannot be neglected. Such a barrier is present up to the highest temperatures and is independent of the presence of columnar defects. Therefore, this source of nonlinearity should be examined more carefully. The surface barrier has actually already been treated by Gilchrist and Konczykowski (1993) in their alternative critical-current hypothesis. We reproduce here the polar plot of the third harmonic (Fig. 6.7) as it was given in their paper. The different curves in this figure represent different ratios H_{dc}/h_{ac} of dc and ac field. The curves are described in the positive sense as the normalized surface current j varies from 0 (no shielding) to 1 (complete shielding). It is obvious that this result is somewhat different from

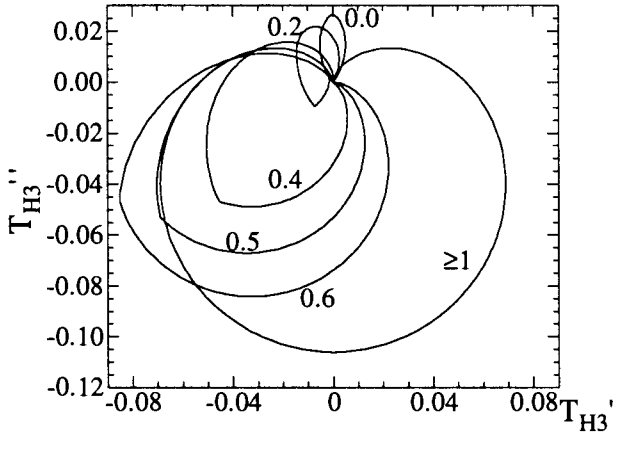

Figure 6.7: Polar plots of the third harmonic for the alternative critical-current hypothesis of Gilchrist and Konczykowski (1993), which models surface pinning of vortices. The labels next to the curves indicate the ratio H_{dc}/h_{ac} between static and alternating magnetic field.

what has been shown in Fig. 6.6. A reason for this could be that the single loop model does not accurately describe the present case.

In order to gain more insight into the details of the nonlinearities of the sample response, a reconstruction of the original signal has been attempted based on the measured components. The reconstructed signal is given by:

$$B(\theta) = T' \cos\theta - T'' \sin\theta + T_3' \cos 3\theta - T_3'' \sin 3\theta \tag{6.1}$$

The negative signs for the out of phase components are due to the definition of the complex transmittivities (see chapter 2).

For an arbitrary signal such a reconstruction would be far from giving the original signal shape. However, for the two cases to which this method shall be applied here,

there is a good chance that the reconstructed signal is not very far from the real one as will be outlined in the following. The two cases are: alignment of the dc field with the *ab*-plane and the dc field at 16 degrees from *ab*. In the first case the excitation is symmetric since there is no offset. Therefore even harmonics cannot occur. In the second case on the other hand, the cardioid shape of the polar plot of the third harmonic indicates a parallelogrammatic hysteresis loop. The situation corresponds exactly to the alternative critical current hypothesis of Gilchrist and Konczykowski (1993) with an applied dc field $H > h_{ac}$. Again, no even harmonics should occur. As to the higher odd harmonics, they are usually much smaller than the third harmonic. For the usual critical current hypothesis and for harmonic detection with a Hall sensor the amplitude of the harmonics is expected to decrease approximately with the square of the harmonic number (Gilchrist and Konczykowski 1993). The fifth harmonic would then be about three times smaller than the third. For the alternative critical current hypothesis (describing the surface barrier) without a dc field the fifth harmonic is actually bigger than the third one, but in that model the third harmonic is very small, contrary to what is observed experimentally. The fact that the third harmonic is as big as where the cardioid is observed, indicates a transfer of weight from the higher harmonics to the third one. The necessary corrections can therefore be expected to be small.

The simpler of the two cases is the one where the dc field is at 16 degrees from the *ab*-plane. The reconstructed signal for this case is shown in Fig. 6.8. On lowering the temperature the signal diminishes, which means that the screening becomes stronger, but at the same time a slight broadening of the $B(\theta)$ peaks is observed. This is exactly what one expects for the critical current hypothesis (compare with Fig. 2.10).

When the dc field is parallel to the *ab*-plane the reconstruction of the signal gives the curves in Fig. 6.9. Here the signal diminishes rapidly with decreasing temperature. Its shape is rather conclusive: the plateaus near the abscissa indicate the presence of a barrier to flux entry. However, no broadening of the $B(\theta)$ peak is seen, contrary to what is expected for the surface barrier (compare with Fig. 2.13).

In order to understand this second fact it has to be remembered that the Hall sensor gives a local measurement of the flux. The local response can be quite different from the global one as has been shown by Morozov et al. (1996). They observed that locally the transmittivity can attain negative values which means that the field change inside the sample can be opposite to the change in external field. This was attributed to the dome shaped flux profile inside the superconductor due to the geometrical barrier (Indenbom et al. 1994c; Zeldov et al. 1994). The active surface of the Hall sensor used for the present work is much larger though, than that of the 2D electron gas Hall sensors used by Morozov et al. It can therefore not be expected that the same details in local response will be observed. Nevertheless, there remains a difference with global measurements which can be explained as follows. The sensor is placed approximately in the center of the sample top surface. On decreasing the

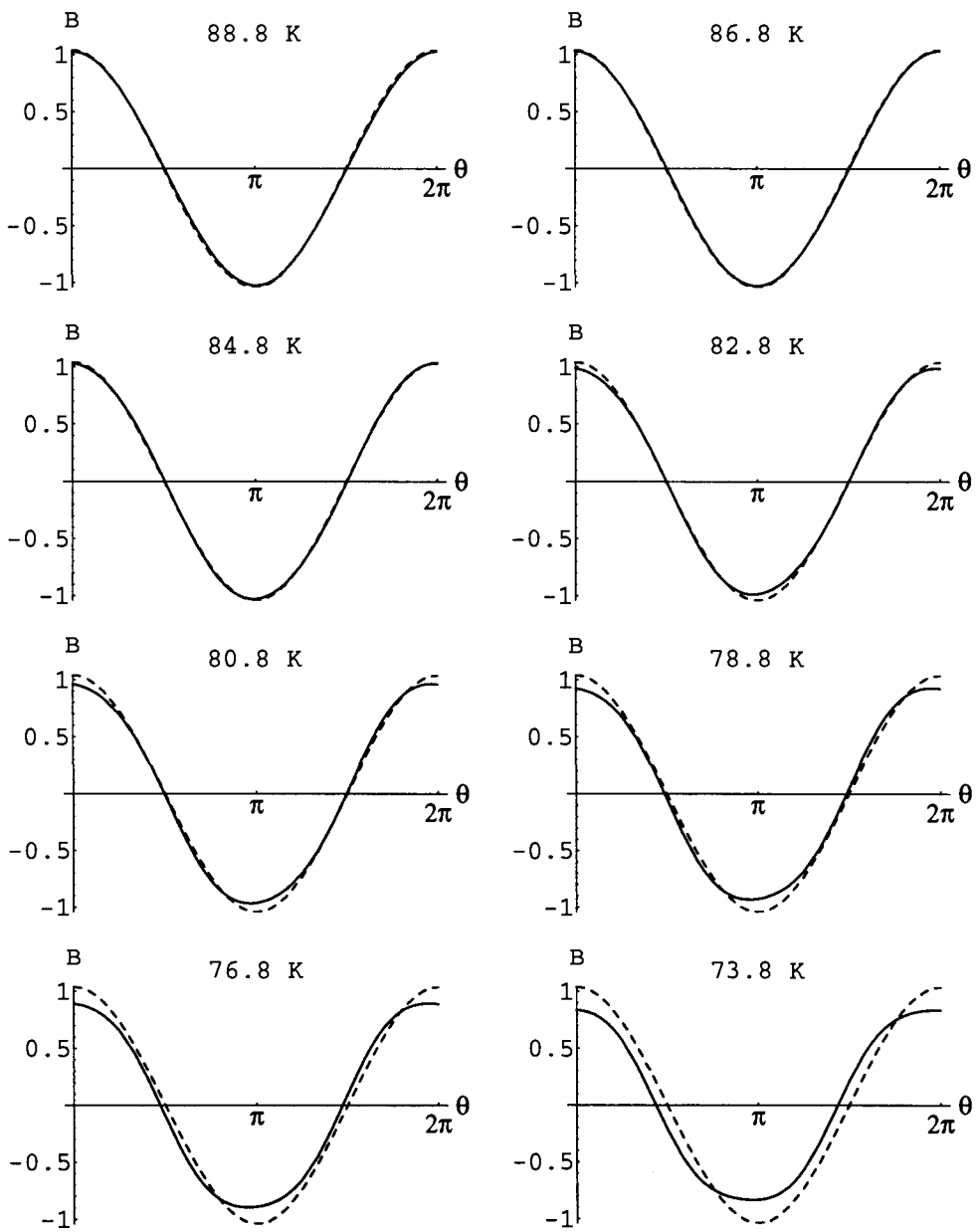

Figure 6.8: Reconstructed signals for several temperatures and dc field at 16 degrees from the *ab*-plane direction. For clarity the reference signal is drawn as well (dashed curve).

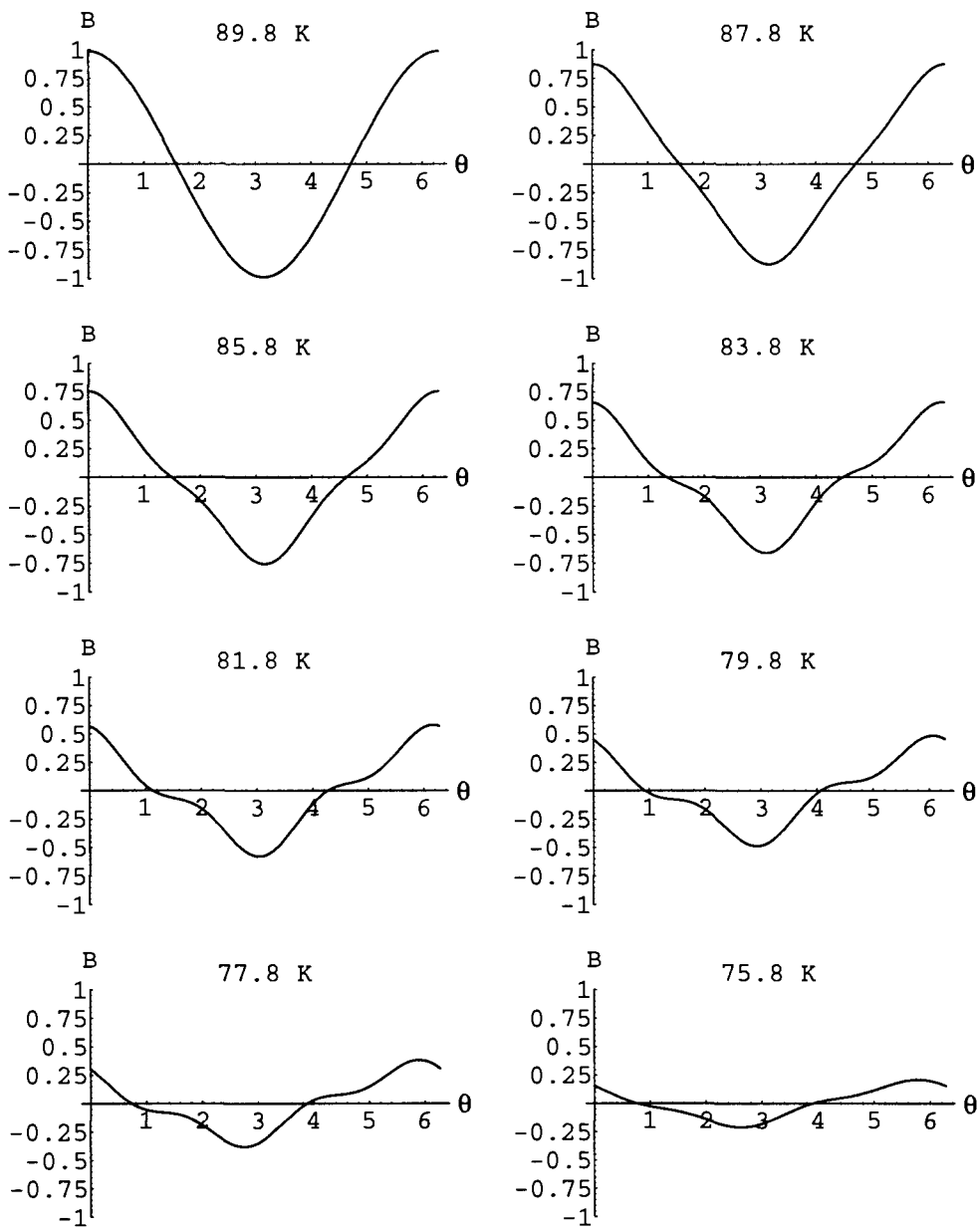

Figure 6.9: Reconstructed signals for several temperatures and alignment of the dc field with the *ab*-plane of the sample.

applied field the surface current decreases and initially no flux leaves the sample unless the current has disappeared completely. However, the internal distribution of the flux changes in this phase: the dome spreads out and the flux in the center of the sample decreases. So no broadening of the peak should be observed for the local measurement.

Now that the two extreme cases have been identified, an interpretation of the crossover can be attempted. By tilting the field away from the *ab*-plane the *c*-axis component of the dc field is increased and this apparently drives the crossover. For small dc fields along *c* the third harmonic content decreases. This can be understood in the following way: in that half of the ac cycle where dc and ac field are opposite the signal is reduced just because there is better screening. For the rest of the cycle ac and dc field add up, the dome is more extended and the local flux change at the sensor position will reflect more closely the global response. The description by Gilchrist and Konczykowski will then again become more adequate. However, due to the spreading of the dome the hysteresis loop is not exactly a parallelogram, but is smoothed. The third harmonic content is therefore reduced.

Upon further increase of the *c*-axis field the total field will, at a given point, cease to change sign during the cycle, and, as Gilchrist and Konczykowski pointed out, the response then approaches that of an ordinary critical state, so that the curve finally turns into the usual cardioid.

The increasing perpendicular component of the dc field not only changes the nature of the curve in the complex plane but increases also the density of pancake vortices in the sample. This will finally lead to the decrease of the screening current. The third harmonic will therefore be zero beyond a limiting angle that depends on temperature.

The description of the flux cycle given above does not make use of the presence of an in-plane field, it is the *c*-axis component of the dc field which triggers the change in the harmonic content of the measured signal. This reflects the extremely small line tension of the vortices (because of the huge anisotropy). In fact, pancakes that appear at the surface of the sample can be regarded as kinks of the already existing Josephson vortices. However, these kinks apparently move immediately to the center of the sample.

The same should happen in the absence of an additional in-plane field: a pancake that penetrates the sample is immediately pushed to the sample center. This however means that a geometrical barrier is not effective in Bi-2212.

6.5 Conclusions

The sample response in very low fields along the *c*-axis has been discussed via the change of third harmonic content with angle and temperature. It has been found that the behaviour can be understood in terms of the alternative critical current hypothesis of Gilchrist and Konczykowski (1993) which describes the effect of a surface

barrier. For the description of the observed signal it is crucial that the Hall probe measures the induction locally. This makes the response different from the global response, invalidating partly the single loop model of Gilchrist and Konczykowski (1993) in this special case. The presence of the in-plane field did not alter the penetration cycle of the perpendicular flux component. This could be explained by the extremely small line tension of the vortices in Bi-2212. From this it follows that a geometrical barrier should not be effective in this material, but that it is the Bean-Livingston barrier alone that determines the hysteresis in the magnetization. As a result, the observations of Zeldov et al. (1994) have to be discussed in terms of the Bean-Livingston barrier, and not in terms of a geometrical barrier.

This page is intentionally left blank.

Chapter 7

General conclusions

The shielding of an ac magnetic field has been used to test the properties of the superconducting mixed state of the high temperature superconducting materials $Bi_2Sr_2CaCu_2O_8$ (Bi-2212) and $HgBa_2Ca_2Cu_3O_8$ (Hg-1223).

In such experiments, the vortex arrangement in the mixed state is perturbed by the ac current induced by the temporally varying field. The response of the vortices, which determines the penetration of the applied ac field into the sample, gives clues as to pinning, vortex interactions, and the nature of the thermodynamic state of the vortex system. In specific, the nonlinearity of the response induced by pinning has been characterized by measurements of the higher harmonic ac response.

The first subject of study concerns the influence of an in-plane field on the first order vortex-solid to liquid transition in pristine Bi-2212. It is found that to a good approximation this transition is only determined by the c-axis component of the field, i.e., the density of pancake vortices. This is due to the very high anisotropy of this material. However, as the in-plane field is increased, the c-axis component of the field at which the transition takes place decreases linearly in the applied in-plane field. In order to account for this, it has to be supposed that the in-plane field suppresses the (already very weak) Josephson coupling between the layers. It should be noted however, that since Josephson coupling between the plane exists, the in-plane field does not penetrate the material homogeneously, but in the form of Josephson vortices. The exact influence of the in-plane field is therefore certainly more complicated.

Second, pinning of the vortices by columnar defects has been investigated in Bi-2212 and Hg-1223 single crystals.

In Bi-2212 several configurations of the columnar defects have been studied: a single family of defects aligned with the c-axis (perpendicular to the CuO_2 planes), or at an angle of 30 degrees with respect to this axis; two families of columnar defects arranged symmetrically with respect to the c-axis and forming the same angle with it, which was fixed to either 15 or 45 degrees; four families of symmetrically arranged columnar defects forming an angle of 15 degrees with the c-axis, and 90 degrees with each other.

An anisotropy of pinning caused by the columnar defects has been found for all these arrangements, although in the case of two sets of columns crossing at an angle of 45 degrees with the c-axis the field range where such an anisotropy can be observed has been found to be rather limited. For a single family of defects maximum pinning occurs for alignment of the field with the defect direction. For crossed families of defects on the other hand, maximum pinning is observed along the intermediate direction, here, along the c-axis.

The anisotropy of pinning is revealed by an improved shielding of the ac signal along the preferential direction, and is only observed at temperatures at which a nonlinear ac response due to pinning can be detected. Moreover, anisotropic pinning is found in the field and temperature range where the pristine crystals are magnetically reversible, and in which the vortex system is better described as a set of independent 2D (pancake) vortices. On the other hand, the anisotropic pinning by columnar defects is expected for coupled line-like vortices. In order to reconcile these observations in Bi-2212, one has to assume that pancakes move in packets and not independently. This motion is not equivalent to a real line-like behaviour, since a splay in the columnar defects does not lead to a further enhancement of pinning. It can therefore be concluded that columnar defects introduce a correlation between pancake vortices in neighbouring layers, but cannot wipe out the nearly two-dimensional character of the vortices.

In Hg-1223 the anisotropy of the material is less important and the character of the vortices thus more line-like than in Bi-2212. In fact, the shape of the irreversibility line is intermediate between those of Bi-2212 and $YBa_2Cu_3O_7$. However, the vortices are still sufficiently soft to allow for a delocalization at high temperatures, similar to the observations in Bi-2212.

Finally, flux entry and exit has been studied in Bi-2212 crystals in the presence of a constant field component closely aligned with the ab-plane of the crystal. It is found that the local ac induction cycle is the same as that observed in the presence of a field component along c only. This means that the influence of the in-plane field is negligible, despite the fact that the experimental geometry is quite different in the two cases. This observation is in conflict with the geometrical barrier model, which predicts a large sensitivity to the relative orientation between the flat sample and the magnetic field. It can therefore be concluded, that the observed induction cycle has to be explained in terms of the Bean-Livingston surface barrier for pancake vortices only.

These studies illustrate the consequences of a strong layering on the vortex physics: vortices are not well described in terms of true strings. The picture of a stack of pancake vortices is more adapted to describe the vortex physics near the first order transition as well as in the presence of columnar defects. However, the interlayer Josephson coupling, though weak, is not completely absent and should, in the end, be taken into account.

Bibliography

Anderson, P. W. (1962). Theory of flux creep in hard superconductors. *Phys. Rev. Lett. 9*, 309.

Bean, C. P. (1962). Magnetization of hard superconductors. *Phys. Rev. Lett. 8*, 250.

Bean, C. P. (1964). Magnetization of high field superconductors. *Rev. Mod. Phys. 36*, 31.

Bean, C. P. and J. D. Livingston (1964). Surface barrier in type II superconductors. *Phys. Rev. Lett. 12*, 14.

Beck, R. G., D. E. Farrell, J. P. Rice, D. M. Ginsberg, and V. G. Kogan (1992). Melting of the Abrikosov flux lattice in anisotropic superconductors. *Phys. Rev. Lett. 68*, 1594.

Bertinotti, A., D. Colson, J. Hammann, J.-F. Marucco, D. Luzet, A. Pinatel, and V. Viallet (1995). X-ray single crystal analysis of $HgBa_2Ca_2Cu_3O_{8+\delta}$ and influence of oxygen stoichiometry on the superconducting properties. *Physica C 250*, 213.

Bertinotti, A., D. Colson, J.-F. Marucco, V. Viallet, G. L. Bras, L. Fruchter, C. Marcenat, A. Carrington, and J. Hammann (1997). Single crystals of mercury based cuprates: growth, structure and physical properties. In A. V. Narlikar (Ed.), *Studies of High Temperature Superconductors*, Volume 23, pp. 27–85. Nova Science Publishers (New York).

Blatter, G., M. V. Feigel'man, V. B. Geshkenbein, A. I. Larkin, and V. M. Vinokur (1994). Vortices in high-temperature superconductors. *Rev. Mod. Phys. 66*, 1125.

Blatter, G., V. Geshkenbein, A. Larkin, and H. Nordborg (1996). Low-field phase diagram of layered superconductors: The role of electromagnetic coupling. *Phys. Rev. B 54*, 72.

Blatter, G., V. B. Geshkenbein, and A. I. Larkin (1992). From isotropic to anisotropic superconductors: A scaling approach. *Phys. Rev. Lett. 68*, 875.

Bourgault, D., S. Bouffard, M. Toulemonde, D. Groult, J. Provost, F. Studer, N. Nguyen, and B. Raveau (1989). Modifications of the physical properties of

the high-T_c superconductors $YBa_2Cu_3O_{7-\delta}$ ($0.1 \leq \delta < 0.7$) by 3.5-GeV xenon ion bombardment. *Phys. Rev. B 39*, 6549.

Brézin, E., D. R. Nelson, and A. Thiaville (1985). Fluctuation effects near H_{c2} in type-II superconductors. *Phys. Rev. B 31*, 7124.

Budhani, R. C., W. L. Holstein, and M. Suenaga (1994). Columnar-defect-induced resistivity minima and Bose glass scaling of linear dissipation in $Tl_2Ba_2CaCu_2O_8$ epitaxial films. *Phys. Rev. Lett. 72*, 566.

Bulaevskii, L. N., M. Ledvij, and V. G. Kogan (1992). Vortices in layered superconductors with Josephson coupling. *Phys. Rev. B 46*, 366.

Campbell, A. M., J. E. Evetts, and D. Dew-Hughes (1968). Pinning of flux vortices in type II superconductors. *Phil. Mag. 18*, 313.

Charalambous, M., J. Chaussy, P. Lejay, and V. Vinokur (1993). Superheating of the Abrikosov flux lattice. *Phys. Rev. Lett. 71*, 436.

Chikumoto, N., M. Konczykowski, N. Motohira, and K. Kishio (1992). Temperature dependence of the lower critical field under the effect of surface barriers in $Bi_2Sr_2CaCu_2O_8$ crystal. *Physica C 199*, 32.

Chikumoto, N., M. Konczykowski, N. Motohira, and A. P. Malozemoff (1992). Flux-creep crossover and relaxation over surface barriers in $Bi_2Sr_2CaCu_2O_8$ crystals. *Phys. Rev. Lett. 69*, 1260.

Civale, L., A. D. Marwick, T. K. Worthington, M. A. Kirk, J. R. Thompson, L. Krusin-Elbaum, Y. Sun, J. R. Clem, and F. Holtzberg (1991). Vortex confinement by columnar defects in $YBa_2Cu_3O_7$ crystals: Enhanced pinning at high fields and temperatures. *Phys. Rev. Lett. 67*, 648.

Clem, J. R. (1991). Two-dimensional vortices in a stack of thin superconducting films: A model for high-temperature superconducting multilayers. *Phys. Rev. B 43*, 7837.

Cubitt, R., E. M. Forgan, G. Yang, S. L. Lee, D. M. Paul, H. A. Mook, M. Yethiraj, P. H. Kes, T. W. Li, A. A. Menovsky, Z. Tarnawski, and K. Mortensen (1993). Direct observation of magnetic flux lattice melting and decomposition in the high-T_c superconductor $Bi_{2.15}Sr_{1.95}CaCu_2O_{8+x}$. *Nature 365*, 407.

De Gennes, P. G. (1966). *Superconductivity of Metals and Alloys*. Frontiers in Physics. New York: W. A. Benjamin, Inc.

Deak, J., M. McElfresh, J. R. Clem, Z. Hao, M. Konczykowski, R. Muenchausen, S. Foltyn, and R. Dye (1994). Irreversibility line in $YBa_2Cu_3O_7$ thin films: Correlation of transport and magnetic behavior. *Phys. Rev. B 49*, 6270.

Dodgson, M. J. W., V. B. Geshkenbein, H. Nordborg, and G. Blatter (1998). Characteristics of first-order vortex lattice melting: jumps in entropy and magnetization. *Phys. Rev. Lett. 80*, 837.

Doyle, R. A., W. S. Seow, Y. Yan, A. M. Campbell, T. Mochiku, K. Kadowaki, and G. Wirth (1996). Local electrodynamics in heavy ion irradiated $Bi_2Sr_2CaCu_2O_{8+\delta}$. *Phys. Rev. Lett. 77*, 1155.

Farrell, D. E., E. Johnston-Halperin, L. Klein, P. Fournier, A. Kapitulnik, E. M. Forgan, A. I. M. Rae, T. W. Li, M. L. Trawick, R. Sasik, and J. C. Garland (1996). Magnetization jumps and irreversibility in $Bi_2Sr_2CaCu_2O_8$. *Phys. Rev. B 53*, 11807.

Farrell, D. E., J. P. Rice, and D. M. Ginsberg (1991). Experimental evidence for flux-lattice melting. *Phys. Rev. Lett. 67*, 1165.

Feigel'man, M. V., V. B. Geshkenbein, and A. I. Larkin (1990). Pinning and creep in layered superconductors. *Physica C 167*, 177.

Feinberg, D. and C. Villard (1990). Intrinsic pinning and lock-in transition of flux lines in layered type-II superconductors. *Phys. Rev. Lett. 65*, 919.

Fisher, D. S. (1980). Flux lattice melting in thin-fim superconductors. *Phys. Rev. B 22*, 1190.

Fisher, M. P. A. (1989). Vortex-glass superconductivity: A possible new phase in bulk high-T_c oxides. *Phys. Rev. Lett. 62*, 1415.

Gammel, P. L., L. F. Schneemeyer, and D. J. Bishop (1991). SQUID picovoltmetry of $YBa_2Cu_3O_7$ single crystals: evidence for a finite-temperature phase transition in the high-field vortex state. *Phys. Rev. Lett. 66*, 953.

Gammel, P. L., L. F. Schneemeyer, J. V. Waszczak, and D. J. Bishop (1988). Evidence from mechanical measurements for flux-lattice melting in single-crystal $YBa_2Cu_3O_7$ and $Bi_{2.2}Sr_2Ca_{0.8}Cu_2O_8$. *Phys. Rev. Lett. 61*, 1666.

Gerhäuser, W., H.-W. Neumüller, W. Schmidt, G. Ries, O. Eibl, G. Saemann-Ischenko, and S. Klaumünzer (1991). Correlation of flux line pinning and irradiation damage in Bi-2212 single crystals after 0.5 GeV iodine irradiation. *Physica C 185-189*, 2339.

Gerhäuser, W., G. Ries, H.-W. Neumüller, W. Schmidt, O. Eibl, G. Saemann-Ischenko, and S. Klaumünzer (1992). Flux-line pinning in $Bi_2Sr_2CaCu_2O_x$ crystals: Interplay of intrinsic 2D behavior and irradiation-induced columnar defects. *Phys. Rev. Lett. 68*, 879.

Gilchrist, J. and M. Konczykowski (1993). Superconductor screen viewed as one or two inductive loops. *Physica C 212*, 43.

Glazman, L. I. and A. E. Koshelev (1991). Thermal fluctuations and phase transitions in the vortex state of a layered superconductor. *Phys. Rev. B 43*, 2835.

Gray, K. E., J. D. Hettinger, D. J. Miller, B. R. Washburn, C. Moreau, C. Lee, B. G. Glagola, and M. M. Eddy (1996). Interaction of two-dimensional vortices with linear ion tracks in the highly anisotropic layered cuprates. *Phys. Rev. B 54*, 3622.

Groult, D., M. Hervieu, N. Nguyen, and B. Raveau (1988). 3.1 GeV-xenon ion latent tracks in $Bi_2Fe_4O_9$: high resolution electron microscope observations. *J. Solid State Chem. 76*, 260.

Hardy, V., D. Groult, M. Hervieu, J. Provost, B. Raveau, and S. Bouffard (1991). Latent track formation induced by high energy heavy ions in superconductive copper oxides. *Nucl. Instr. and Meth. B54*, 472.

Hardy, V., J. Provost, D. Groult, M. Hervieu, B. Raveau, S. Durčok, E. Pollert, J. C. Frison, J. P. Chaminade, and M. Pouchard (1992). Strong shift of the irreversibility line in bismuth and thallium based 2212 HTSC single crystals irradiated by 6.0 GeV Pb ions. *Physica C 191*, 85.

Hardy, V., A. Ruyter, J. Provost, D. Groult, and C. Simon (1994). Columnar defects and relaxation in Bi-2212 single crystals Dual analysis by the single-barrier model and the Hagen and Griessen inversion scheme. *Physica C 224*, 143.

Hardy, V., A. Ruyter, A. Wahl, A. Maignan, D. Groult, J. Provost, C. Simon, and H. Noël (1996). Splayed configurations of columnar defects in $YBa_2Cu_3O_7$, (Tl, Bi)$Sr_2CaCu_2O_7$ and $Bi_2Sr_2CaCu_2O_8$ single crystals Study of the enhanced pinning efficiencies for different characteristic angles. *Physica C 257*, 16.

Huberman, B. A. and S. Doniach (1979). Melting of two-dimensional vortex lattices. *Phys. Rev. Lett. 43*, 950.

Hwa, T., P. Le Doussal, D. R. Nelson, and V. M. Vinokur (1993). Flux pinning and forced vortex entanglement by splayed columnar defects. *Phys. Rev. Lett. 71*, 3545.

Indenbom, M. V. and E. H. Brandt (1994). Comment on "field induced 3D to 2D crossover of shielding current path in $Bi_2Sr_2CaCu_2O_x$". *Phys. Rev. Lett. 73*, 1731.

Indenbom, M. V., G. D'Anna, M.-O. André, V. V. Kabanov, and W. Benoit (1994a). Edge-shape barrier irreversibility and decomposition of vortices in $Bi_2Sr_2CaCu_2O_8$. *Physica C 235-240*, 201.

Indenbom, M. V., A. Forkl, B. Ludescher, H. Kronmüller, H.-U. Habermeier, B. Leibold, G. D'Anna, T. W. Li, P. H. Kes, and A. A. Menovsky (1994b). Anisotropy of perpendicular field penetration into high-T_c superconductors induced by strong longitudinal field. *Physica C 226*, 325.

Indenbom, M. V., H. Kronmüller, T. W. Li, P. H. Kes, and A. A. Menovsky (1994c). Equilibrium magnetic properties and Meissner expulsion of magnetic flux in $Bi_2Sr_2CaCu_2O_x$ single crystals. *Physica C 222*, 203.

Ji, L., R. H. Sohn, G. C. Spalding, C. J. Lobb, and M. Tinkham (1989). Critical-state model for harmonic generation in high-temperature superconductors. *Phys. Rev. B 40*, 10936.

Jiang, W., N.-C. Yeh, D. S. Reed, U. Kriplani, D. A. Beam, M. Konczykowski, T. A. Tombrello, and F. Holtzberg (1994). Evidence of a Bose-glass transition in superconducting $YBa_2Cu_3O_7$ single crystals with columnar defects. *Phys. Rev. Lett. 72*, 550.

Jiang, W., N.-C. Yeh, D. S. Reed, U. Kriplani, and F. Holtzberg (1995). Possible origin of anisotropic resistive hysteresis in the vortex state of untwinned $YBa_2Cu_3O_7$ single crystals. *Phys. Rev. Lett. 74*, 1438.

Kadowaki, K., A. A. Menovsky, and J. J. M. Franse (1990). Magnetoresistivity in superconducting state of single crystalline $Bi_2Sr_2CaCu_2O_{8+\delta}$. *Physica B 165*, 1159.

Kes, P. H., J. Aarts, V. M. Vinokur, and C. J. van der Beek (1990). Dissipation in highly anisotropic superconductors. *Phys. Rev. Lett. 64*, 1063.

Khaykovich, B., M. Konczykowski, E. Zeldov, R. A. Doyle, D. Majer, P. H. Kes, and T. W. Li (1997). Vortex-matter phase transitions in $Bi_2Sr_2CaCu_2O_8$: Effects of weak disorder. *Phys. Rev. B 56*, R517.

Kim, Y. B., C. F. Hempstead, and A. R. Strnad (1962). Critical persistent currents in hard superconductors. *Phys. Rev. Lett. 9*, 306.

Klein, L., E. R. Yacoby, Y. Yeshurun, M. Konczykowski, and K. Kishio (1993). Evidence for line vortices in $Bi_2Sr_2CaCu_2O_8$. *Phys. Rev. B 48*, 3523.

Koch, R. H., V. Foglietti, W. J. Gallagher, G. Koren, A. Gupta, and M. P. A. Fisher (1989). Experimental evidence for vortex-glass superconductivity in Y-Ba-Cu-O. *Phys. Rev. Lett. 63*, 1511.

Konczykowski, M., F. Holtzberg, and P. Lejay (1991). Local hall probe magnetometry: a new technique for investigation of magnetic flux penetration, exclusion and trapping in HTSC. *Supercond. Sci. Technol. 4*, S331.

Konczykowski, M., F. Rullier-Albenque, E. R. Yacoby, A. Shaulov, Y. Yeshurun, and P. Lejay (1991a). Effect of 5.3-GeV Pb-ion irradiation on irreversible magnetization in Y-Ba-Cu-O crystals. *Phys. Rev. B 44*, 7167.

Konczykowski, M., F. Rullier-Albenque, Y. Yeshurun, E. R. Yacoby, A. Shaulov, and P. Lejay (1991b). Flux pinning enhancement near tc in $YBa_2Cu_3O_7$ crystals irradiated by 5.3 GeV Pb ions. *Physica C 185-189*, 2347.

Koshelev, A. E., P. Le Doussal, and V. M. Vinokur (1996). Columnar defects and vortex fluctuations in layered superconductors. *Phys. Rev. B 53*, R8855.

Krusin-Elbaum, L., L. Civale, G. Blatter, A. D. Marwick, F. Holtzberg, and C. Feild (1994). Bose-glass melting in YBaCuO crystals with correlated disorder. *Phys. Rev. Lett. 72*, 1914.

Kummeth, P., C. Struller, H.-W. Neumüller, and G. Saemann-Ischenko (1994). Dimensionality of flux pinning in $(Bi,Pb)_2Sr_2Ca_2Cu_3O_{10+\delta}Ag$ tapes with colum-

nar defects—Crossover from two-dimensional to three-dimensional behavior. *Appl. Phys. Lett. 65*, 1302.

Kürti, N. and F. Simon (1935). Experiments at very low temperatures obtained by the magnetic method I - the production of the low temperature. *Proc. Roy. Soc. (London) A 149*, 152.

Kwok, W. K., S. Fleshler, U. Welp, V. M. Vinokur, J. Downey, G. W. Crabtree, and M. M. Miller (1992). Vortex lattice melting in untwinned and twinned single crystals of $YBa_2Cu_3O_{7-\delta}$. *Phys. Rev. Lett. 69*, 3370.

Larkin, A. I. and V. M. Vinokur (1995). Bose and vortex glasses in high temperature superconductors. *Phys. Rev. Lett. 75*, 4666.

Lawrence, W. E. and S. Doniach (1971). Theory of layer structure superconductors. In E. Kanda (Ed.), *Proceedings of the Twelfth International Conference on Low Temperature Physics*, Kyoto, pp. 361. Academic Press of Japan.

Lee, S. L., C. M. Aegerter, H. Keller, M. Willemin, B. Stäuble-Pümpin, E. M. Forgan, S. H. Lloyd, G. Blatter, R. Cubitt, T. W. Li, and P. H. Kes (1997). Role of electromagnetic coupling in the low-field phase diagram of $Bi_{2.15}Sr_{1.85}CaCu_2O_{8+\delta}$. *Phys. Rev. B 55*, 5666.

Lee, S. L., P. Zimmermann, H. Keller, M. Warden, I. M. Savic, R. Schauwecker, D. Zech, R. Cubitt, E. M. Forgan, P. H. Kes, T. W. Li, A. A. Menovsky, and Z. Tarnawski (1993). Evidence for flux-lattice melting and a dimensional crossover in single-crystal $Bi_{2.15}Sr_{1.85}CaCu_2O_{8+\delta}$ from muon spin rotation studies. *Phys. Rev. Lett. 71*, 3862.

Li, T. W. (1995). *Studies of crystal growth, oxygen diffusion, flux pinning and flux lattice melting on $Bi_2Sr_2CaCu_2O_8$ single crystals.* Ph. D. thesis, Leiden University.

Martinez, J. C., S. H. Brongersma, A. E. Koshelev, B. Ivlev, P. H. Kes, R. P. Griessen, D. G. de Groot, Z. Tarnavski, and A. A. Menovsky (1992). Magnetic anisotropy of a $Bi_2Sr_2CaCu_2O_x$ single crystal. *Phys. Rev. Lett. 69*, 2276.

Morozov, N., E. Zeldov, D. Majer, and B. Khaykovich (1996). Negative local permeability in $Bi_2Sr_2CaCu_2O_8$ crystals. *Phys. Rev. Lett. 76*, 138.

Morozov, N., E. Zeldov, D. Majer, and M. Konczykowski (1996). Paramagnetic ac susceptibility at the first-order vortex-lattice phase transition. *Phys. Rev. B 54*, R3784.

Nakamura, N., G. D. Gu, and N. Koshizuka (1993). Field induced 3D to 2D crossover of shielding current path in $Bi_2Sr_2CaCu_2O_x$. *Phys. Rev. Lett. 71*, 915.

Nelson, D. R. and V. M. Vinokur (1993). Boson localization and correlated pinning of superconducting vortex arrays. *Phys. Rev. B 48*, 13060.

Palstra, T. T. M., B. Batlogg, L. F. Schneemeyer, and J. V. Waszczak (1988). Thermally activated dissipation in $Bi_{2.2}Sr_2Ca_{0.8}Cu_2O_{8+\delta}$. *Phys. Rev. Lett. 61*, 1662.

Pastoriza, H., M. F. Goffman, A. Arribére, and F. d. l. Cruz (1994). First order phase transition at the irreversibility line of $Bi_2Sr_2CaCu_2O_{8+\delta}$. *Phys. Rev. Lett. 72*, 2951.

Prozorov, R., A. Shaulov, Y. Wolfus, and Y. Yeshurun (1995). Frequency dependence of the local ac magnetic response in type-II superconductors. *Phys. Rev. B 52*, 12541.

Rae, A. I. M., E. M. Forgan, and R. A. Doyle (1998). The interpretation of magnetisation and entropy jumps in the mixed state of high-temperature superconductors. *Physica C 301*, 301.

Safar, H., P. L. Gammel, D. A. Huse, D. J. Bishop, W. C. Lee, J. Giapintzakis, and D. M. Ginsberg (1993). Experimental evidence for a multicritical point in the magnetic phase diagram for the mixed state of clean, untwinned $YBa_2Cu_3O_7$. *Phys. Rev. Lett. 70*, 3800.

Safar, H., P. L. Gammel, D. A. Huse, D. J. Bishop, J. P. Rice, and D. M. Ginsberg (1992). Experimental evidence for a first-order vortex-lattice-melting transition in untwinned single crystal $YBa_2Cu_3O_7$. *Phys. Rev. Lett. 69*, 824.

Samoilov, A. V., M. V. Feigel'man, M. Konczykowski, and F. Holtzberg (1996). Upper limit of the Bose-glass transition in $YBa_2Cu_3O_7$ at high density of columnar defects. *Phys. Rev. Lett. 76*, 2798.

Schilling, A., M. Cantoni, J. D. Guo, and H. R. Ott (1993). Superconductivity above 130 K in the Hg-Ba-Ca-Cu-O system. *Nature 363*, 56–58.

Schilling, A., R. A. Fisher, N. E. Phillips, U. Welp, D. Dasgupta, W. K. Kwok, and G. W. Crabtree (1996). Calorimetric measurement of the latent heat of vortex-lattice melting in untwinned $YBa_2Cu_3O_{7-\delta}$. *Nature 382*, 791.

Schmidt, B., M. Konczykowski, N. Morozov, and E. Zeldov (1997). Angular dependence of the first-order vortex-lattice phase transition in $Bi_2Sr_2CaCu_2O_8$. *Phys. Rev. B 55*, R8705.

Schuster, T., M. V. Indenbom, H. Kuhn, H. Kronmüller, M. Leghissa, and G. Kreiselmeyer (1994). Observation of in-plane anisotropy of vortex pinning by inclined columnar defects. *Phys. Rev. B 50*, 9499.

Schuster, T., M. R. Koblischka, H. Kuhn, H. Kronmüller, M. Leghissa, W. Gerhäuser, G. Saemann-Ischenko, H.-W. Neumüller, and S. Klaumünzer (1992). Observation of flux penetration in $Bi_2Sr_2CaCu_2O_{8+\delta}$ crystals with irradiation-induced columnar defects. *Phys. Rev. B 46*, 8496.

Schuster, T., H. Kuhn, M. V. Indenbom, G. Kreiselmeyer, M. Leghissa, and S. Klaumünzer (1996). Direct observation of stronger flux-line pinning of crossed compared to parallel linear defects. *Phys. Rev. B 53*, 2257.

Seow, W. S., R. A. Doyle, A. M. Campbell, G. Balakrishnan, K. Kadowaki, and G. Wirth (1996). Influence of columnar defects on vortex dynamics in $Bi_2Sr_2CaCu_2O_8$ from out-of-plane and flux transformer measurements. *Phys. Rev. B 53*, 14611.

Simon, C., J. Provost, D. Groult, V. Hardy, A. Wahl, C. Goupil, and A. Ruyter (1996). Vortex pinning and columnar defects in superconducting oxides. *Nucl. Instr. and Meth. B107*, 384.

Thompson, J. R., Y. R. Sun, H. R. Kerchner, D. K. Christen, B. C. Sales, B. C. Chakoumakos, A. D. Marwick, L. Civale, and J. O. Thomson (1992). Enhanced current density J_c and extended irreversibility in single-crystal $Bi_2Sr_2Ca_1Cu_2O_8$ via linear defects from heavy ion irradiation. *Appl. Phys. Lett. 60*, 2306.

Tilley, D. R. and J. Tilley (1994). *Superfluidity and Superconductivity* (3rd ed.). Graduate Student Series in Physics. Bristol, UK: Institute of Physics Publishing.

van der Beek, C. J., M. Konczykowski, V. M. Vinokur, G. W. Crabtree, T. W. Li, and P. H. Kes (1995). Vortex dynamics in a $Bi_2Sr_2CaCu_2O_8$ crystal with columnar defects. *Phys. Rev. B 51*, 15492.

van der Beek, C. J., M. Konczykowski, V. M. Vinokur, T. W. Li, P. H. Kes, and G. W. Crabtree (1995). Vortex line pinning and Bose-glass dynamics in heavy-ion irradiated $Bi_2Sr_2CaCu_2O_{8+\delta}$ single crystals. *Phys. Rev. Lett. 74*, 1214.

Vinokur, V. M., P. H. Kes, and A. E. Koshelev (1990). Flux pinning and creep in very anisotropic high temperature superconductors. *Physica C 168*, 29.

Vulcanescu, V., L. Fruchter, A. Bertinotti, D. Colson, G. L. Bras, and J.-F. Marucco (1996). Magnetization and anisotropy of a $HgBa_2Ca_2Cu_3O_{8+d}$ single crystal. *Physica C 259*, 131.

Yeh, N.-C., W. Jiang, D. S. Reed, U. Kriplani, T. A. Tombrello, M. Konczykowski, F. Holtzberg, and C. C. Tsuei (1995, June 26-30). Experimental investigation of the critical vortex dynamics in extreme type-II— superconductors with controlled static disorder. In *Workshop on Low-Energy Electrodynamics in Solids*, Třešt, Czech Republic.

Zech, D., S. L. Lee, H. Keller, G. Blatter, B. Janossy, P. H. Kes, T. W. Li, and A. A. Menovsky (1995). Correlation of flux lines in single-crystal $Bi_2Sr_2CaCu_2O_8$ with columnar defects. *Phys. Rev. B 52*, 6913.

Zech, D., S. L. Lee, H. Keller, G. Blatter, P. H. Kes, and T. W. Li (1996). Phase diagram of $Bi_{2.15}Sr_{1.85}CaCu_2O_{8+\delta}$ in the presence of columnar defects. *Phys.*

Rev. B 54, 6129.

Zeldov, E., A. I. Larkin, V. B. Geshkenbein, M. Konczykowski, D. Majer, B. Khaykovich, V. M. Vinokur, and H. Shtrikman (1994). Geometrical barriers in high-temperature superconductors. *Phys. Rev. Lett. 73*, 1428.

Zeldov, E., D. Majer, M. Konczykowski, V. B. Geshkenbein, V. M. Vinokur, and H. Shtrikman (1995). Thermodynamic observation of first-order vortex-lattice melting transition in $Bi_2Sr_2CaCu_2O_8$. *Nature 375*, 373.

This page is intentionally left blank.

Appendix A

Other work

Origin of the irreversibility line in thin $YBa_2Cu_3O_{7-\delta}$ films with and without columnar defects

R. Prozorov
Institute of Superconductivity, Department of Physics, Bar-Ilan University, 52900 Ramat-Gan, Israel

M. Konczykowski and B. Schmidt
Laboratoire des Solides Irradiés, Ecole Polytechnique, 91128 Palaiseau, France

Y. Yeshurun and A. Shaulov
Institute of Superconductivity, Department of Physics, Bar-Ilan University, 52900 Ramat-Gan, Israel

C. Villard* and G. Koren
Department of Physics, Technion, Haifa, Israel
(Received 12 June 1996)

We report on measurements of the angular dependence of the irreversibility temperature $T_{irr}(\theta)$ in $YBa_2Cu_3O_{7-\delta}$ thin films, defined by the onset of a third-harmonic signal and measured by a miniature Hall probe. From the functional form of $T_{irr}(\theta)$ we conclude that the origin of the irreversibility line in unirradiated films is a dynamic crossover from an unpinned to a pinned vortex liquid. In irradiated films the irreversibility temperature is determined by the trapping angle. [S0163-1829(96)01245-3]

I. INTRODUCTION

The origin of the irreversibility line (IRL) in the field-temperature (H-T) phase diagram of high-temperature superconductors (HTS's) is intriguing and still a widely discussed topic.[1–9] Experimentally, this line is defined as the borderline at which the magnetic response of the sample changes from irreversible to reversible. In HTS's, large fluctuations and relatively weak pinning lead to a rich H-T phase diagram with a variety of dynamic and static transitions which can be responsible for the appearance of magnetic reversibility.[3–5,10–12] Thus, a thorough experimental investigation of the IRL is important for the understanding of the vortex-lattice behavior in superconductors in general and of the mechanisms responsible for the onset of irreversible magnetic response, in particular.

Several models, like thermally activated depinning,[2,3,6,13,14] vortex-lattice melting,[15–21] and a transition from vortex glass to vortex fluid,[22–24] were proposed to identify the origin of the IRL in HTS's. Also, attention was given to the possibility of pinning in the vortex-liquid phase[5,10,11,25] and to different dissipation mechanisms above the melting line.[5,13,26–28] Irreversibility due to geometrical[7,9] or surface barriers[29] has also been proposed, but this mechanism is less probable in thin $YBa_2Cu_3O_{7-\delta}$ films with strong pinning. The irreversibility line may be affected by sample-dependent properties such as the nature and density of pinning centers and by intrinsic or extrinsic anisotropy. For example, in superconductors with columnar defects, the irreversibility line may either be identified with the Bose-glass transition[5,28–37] or related to the concept of a trapping angle.[38] The configuration of the columnar defects is also very important, since it affects the possibility for different types of depinning mechanism. A splayed configuration, for example, inhibits creep from columnar defects.[39,40] Similarly "crossed" defects (i.e., defects at angles $\pm\theta$) were shown to act collectively; i.e., they introduce unidirectional anisotropy such that the current density reaches its maximum for magnetic field directed in a midangle between defects.[41,42]

Experimentally, the situation is even more complex, since different techniques (magnetization loops, field-cool vs zero-field-cool dc magnetization, peak in the imaginary part of the first harmonic, etc.) yield different IRL's.[24,43] To a great extent, the reliability of the determination of the IRL depends on the criterion for the onset of the irreversibility. We determine the irreversibility temperature at a given dc field by the onset of the third harmonic in the ac response, which, we believe, is one of the most reliable methods for contactless determination of the IRL.[44] In most experiments T_{irr} is measured as a function of the external field H. This information is insufficient to distinguish between different models for the origin of the irreversibility. Additional information, like the frequency dependence of the IRL (Refs. 24 and 45) or its angular variation,[18,20,21,32,34,36,46] is needed.

In this paper we report on a study of the angular dependence of the irreversibility temperature $T_{irr}(\theta)$ in thin $YBa_2Cu_3O_{7-\delta}$ (YBCO) films before and after irradiation with Pb ions.

II. EXPERIMENT

The 1500 Å YBCO films were "sandwiched" between $SrTiO_3$ layers.[47] First, a 500 Å layer of $SrTiO_3$ was deposited on a MgO substrate. Then, the YBCO film was laser ablated on top of the $SrTiO_3$ and finally, the YBCO was covered by a protective 300 Å layer of $SrTiO_3$. All three samples have the same lateral dimensions of 100×500 μm^2. One film, denoted as REF, was used as a reference sample. The other two, UIR and CIR, were irradiated at GANIL with 2×10^{11} ions/cm^2 5.8 GeV Pb ions along the c axis and along $\theta=\pm45°$, respectively. (UIR and CIR stand for "uniform irradiation" and "crossed irradiation," respec-

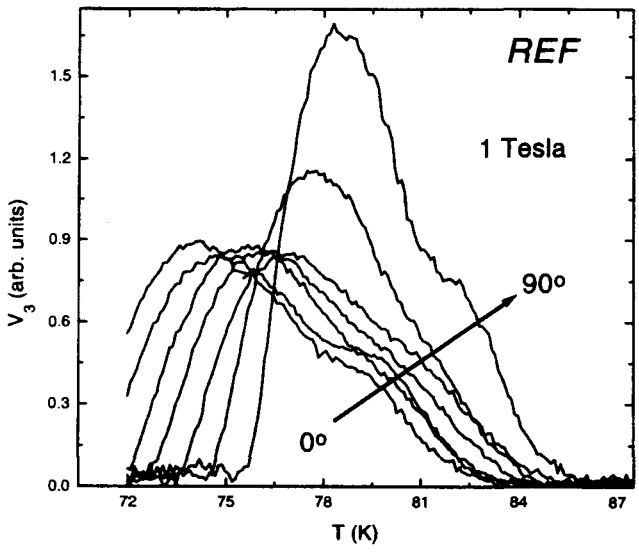

FIG. 1. Third-harmonic signal V_3 vs temperature during field cooling at 1 T for sample REF at θ=0°, 10°, 30°, 40°, 60°, 80°, and 90°.

tively.) The superconducting transition temperatures, measured by a Quantum Design superconducting quantum interference device (SQUID) susceptometer and defined as the onset of the Meissner expulsion in a dc field of 5 G, are $T_c \approx 89$ K for the samples REF and UIR and 88 K for CIR.

For the ac measurements reported below we used a miniature 80×80 μm^2 InSb Hall probe, which was positioned in the center of the sample. The 1 G ac magnetic field, always parallel to the c axis, was induced by a small coil surrounding the sample. An external dc magnetic field, up to $H_a = 1.5$ T, could be applied at any direction θ with respect to the c axis. In our experiments dc magnetic field was always turned on at a fixed angle at $T > T_c$ and then the ac response was recorded during sample cooling. The irreversibility temperature $T_{irr}(\theta)$ is defined as the onset of the third-harmonic signal in the ac response measured by the Hall probe.[44] This procedure was repeated for various dc fields and at various angles θ of the field with respect to the c axis.

III. RESULTS

Figure 1 presents measurements of V_3, the third harmonic in the ac response, versus temperature T, during field cooling at 1 T for the sample REF at various angles between 0 and 90°. Apparently, as the angle θ increases the whole V_3 curve shifts to higher temperatures and becomes narrower. The onset of irreversibility $T_{irr}(\theta)$ is defined by the criterion $V_3^{onset} = 0.05$ in the units of Fig. 1.

Figure 2 exhibits typical $T_{irr}(\theta)$ data for the unirradiated sample REF, measured at two values of the external field: 0.5 T and 1 T. Both curves exhibit a shallow minimum around $\theta = 0$ and they reach their maximum values for H along the ab plane, at angles $\theta = \pm 90°$. We also measured the frequency dependence of T_{irr} for the same values of magnetic field. As shown in Fig. 3, the slope $\partial T_{irr}/\partial \ln(f)$ is larger for larger field.

The sample irradiated along the c axis exhibits an addi-

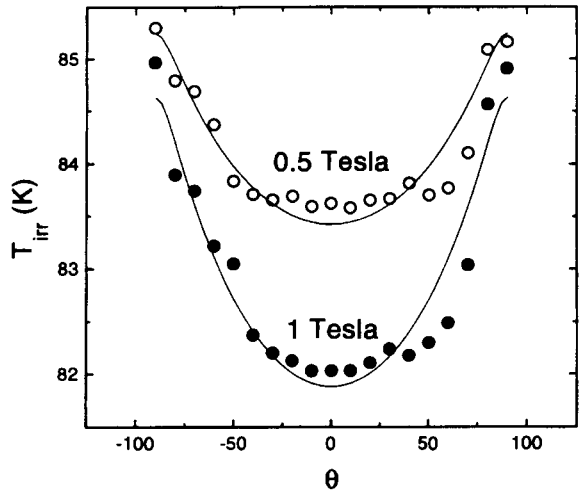

FIG. 2. Irreversibility temperature in the unirradiated sample REF at two values of the external field: $H = 0.5$ and 1 T. The solid lines are fits to Eq. (8).

tional feature, a *peak* around $\theta = 0$. This is clearly shown in Fig. 4 where we compare $T_{irr}(\theta)$ at $H = 1$ T for the samples REF and UIR. As discussed below, this peak is a signature of the unidirectional magnetic anisotropy induced by the columnar defects. Intuitively, one would therefore expect two peaks, along $\theta = \pm 45°$, for the third sample, CIR, crossed irradiated at $\theta = \pm 45°$. Instead, we find one strong peak around $\theta = 0$, similar to that found in Bi-Sr-Ca-Cu-O crystals.[42] This is demonstrated in Fig. 5 where we compare $T_{irr}(\theta)$ at $H = 0.5$ T for this sample (CIR) and for the unirradiated sample (REF). We argue below that the peak around $\theta = 0°$ is a result of a collective action of the crossed columnar defects, and its origin is the same as that for unidirectional enhancement of critical current density observed in Bi-Sr-Ca-Cu-O crystals.[41,42]

IV. ANALYSIS

The "true" irreversibility temperature T_0 is defined as a temperature below which the irreversibility sets in. Such

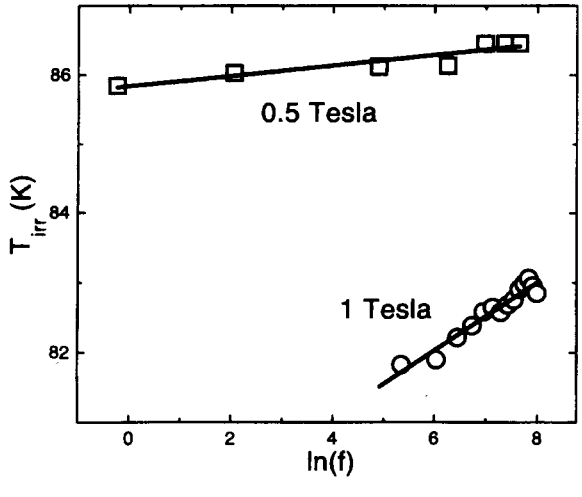

FIG. 3. Frequency dependence of T_{irr} in the unirradiated sample REF at two values of the external field: $H = 0.5$ and 1 T. The solid lines are fits to Eq. (9).

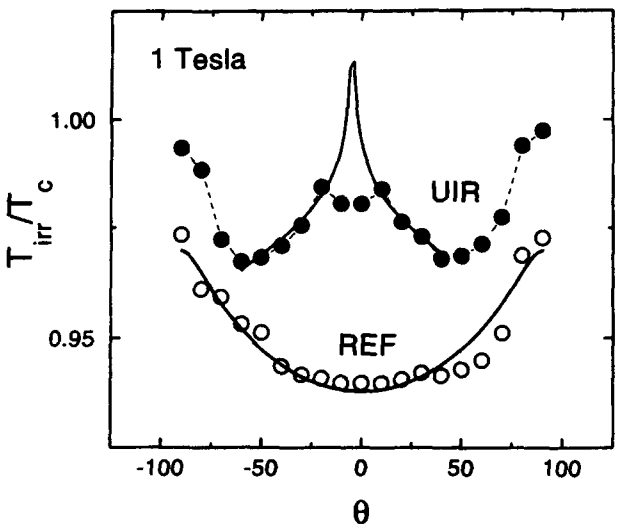

FIG. 4. Irreversibility temperature for two samples: REF (unirradiated, open circles) and UIR (irradiated along the c-axis sample, solid circles) at $H=1$ T. Solid lines are fits to Eq. (8) and Eq. (12), respectively.

appearance of pinning can be of static (true phase transition), as well as of dynamic origin (gradual freezing, pinning in liquid). In practice, one determines the irreversibility temperature $T_{irr}(\Delta)$ as the temperature above which the critical current density is less than some threshold value Δ. Therefore, by definition, $T_0=\lim_{\Delta\to 0}[T_{irr}(\Delta)]$. The apparent current depends on temperature T, magnetic field B, and the frequency f of the exciting field which defines a characteristic time scale $1/f$ for the experiment. By solving the equation $j(T,B,f)=\Delta$ with respect to T one finds the experimental irreversibility temperature T_{irr} for constant B and f. In the following we argue that in our experiments the measured T_{irr} is a good approximation of T_0. In order to estimate T_{irr}

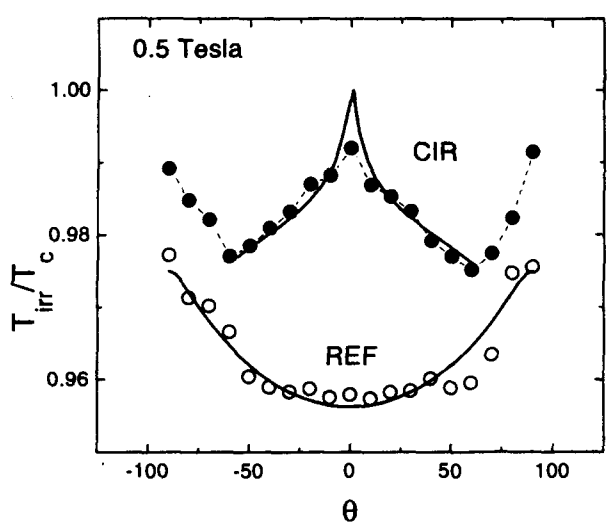

FIG. 5. Irreversibility temperature for two samples: REF (unirradiated, open circles) and CIR (irradiated along $\theta=\pm 45°$, solid circles) at $H=0.5$ T. Solid lines are fits to Eq. (8) and Eq. (12), respectively.

we employ a general form for the apparent current density *in the vicinity of the irreversibility line* (IRL):[4-6,48]

$$j(T,B,f)\propto j_c(0)\frac{(1-T/T_0)^{\alpha}}{(B/B_0)^{\beta}}\left(\frac{f}{f_0}\right)^{\gamma}, \tag{1}$$

where the parameters B_0 and f_0 are temperature independent [Eq. (1) is thus valid only in a narrow temperature interval near the IRL and for fields larger than H_{c1}]. From Eq. (1) we get

$$T_{irr}=T_0(B)\left\{1-\left[\frac{\Delta}{j_c(0)}\left(\frac{B}{B_0}\right)^{\beta}\left(\frac{f_0}{f}\right)^{\gamma}\right]^{1/\alpha}\right\}. \tag{2}$$

Inserting reasonable numerical estimates $j_c(0)\simeq 10^7$ A/cm^2, $\Delta\simeq 100$ A/cm^2 for our experimental resolution, $B_0\simeq 10^3$ G, $B\simeq 10^4$ G, $\beta\simeq 1$,[48] $\gamma\simeq 1$,[6] $f\simeq 10^2$ Hz, and $f_0\simeq 10^7$ Hz,[6] we get, from Eq. (2), $T_{irr}=T_0(B)(1-0.005^{1/\alpha})$. Thus, with 0.5% accuracy we may say that T_{irr}, the measured onset of the third-harmonic component in the ac response, marks some "true" irreversibility crossover line $T_0(B)$. The nature of this line $T_0(B)$ is our main interest, since, as discussed in the Introduction, it is directly related to the pinning properties of vortex lattice in type-II superconductors at elevated temperatures.

A. Unirradiated YBCO film

We turn now to consider the effect of the intrinsic anisotropy on $T_{irr}(\theta)$. Following the anisotropic scaling approach proposed by Blatter *et al.*,[49,50] we replace T by εT and B by $B_{eff}=\varepsilon_\theta B$, where $\varepsilon_\theta=\sqrt{\cos^2(\theta)+\varepsilon^2\sin^2(\theta)}$ and $\varepsilon\approx 1/7$ is the anisotropy parameter for YBCO. It should be emphasized that we can use this scheme only in the case of *intrinsic* anisotropy $\varepsilon=\sqrt{m_{ab}/m_c}$, where m_c and m_{ab} denote the effective masses of the electron along the c axis and in the ab plane, respectively. In the case of some *extrinsic* magnetic anisotropy (columnar defects or twin planes), the critical current depends on the angle not only via the effective magnetic field B_{eff}, but also because of this extrinsic anisotropy.

As we have already indicated in the Introduction, there are several possible origins for a crossover from irreversible to reversible magnetic behavior in unirradiated samples. We exclude the vortex-glass to vortex-fluid transition as a possible origin for the IRL, because this transition was shown to occur at temperatures lower than the onset of dissipation.[23,25,51] The thermal depinning temperature *increases* with increase of field,[5] $T_{dp}\propto\sqrt{B}$, and therefore is excluded as well. Vortex-lattice melting transition is believed to be responsible for the appearance of reversibility.[15,16,18,19] The explicit angular dependence of T_m was derived by Blatter *et al.*[5,49] using their scaling approach:

$$T_m(\theta)\simeq 2\sqrt{\pi}\varepsilon\varepsilon_0 c_L^2(\Phi_0/B\varepsilon_\theta)^{1/2}$$

$$\approx\frac{c_L^2 T_c}{\sqrt{\beta_m G i}}\left(1-\frac{T_m}{T_c}\right)\left(\frac{H_{c2}(0)}{\varepsilon_\theta B}\right)^{1/2}, \tag{3}$$

where Φ_0 is the flux quantum, ξ is the coherence length, $\beta_m\approx 5.6$ is a numerical factor, estimated in Ref. 5, $c_L\simeq 0.1$ is

the Lindemann number, $Gi=[T_c/\varepsilon H_{c2}(0)\xi^3(0)]^2/2$ is the Ginzburg number, and $H_{c2}(0)$ is the *linear* extrapolation of the upper critical field from T_c to zero. Solving Eq. (3) with respect to T_m we get

$$T_m(\theta)\simeq\frac{T_c}{1+[\beta_m Gi/c_L^4 H_{c2}(0)]^{1/2}(\varepsilon_\theta B)^{1/2}}\equiv\frac{T_c}{1+C\sqrt{\varepsilon_\theta B}}. \tag{4}$$

Equation 4 predicts that the melting temperature decreases as $B_{\rm eff}$ increases. This is due to the fact that the intervortex distance $a_0^2\propto 1/B_{\rm eff}$ decreases faster than the characteristic amplitude of fluctuations $\langle u^2(B_{\rm eff},T_m)\rangle_{\rm th}\propto 1/\sqrt{B_{\rm eff}}$. Therefore, the condition for the vortex-lattice melting $\langle u^2(B_{\rm eff},T_m)\rangle_{\rm th}\simeq c_L^2 a_0^2$ implies larger melting temperatures for smaller effective fields, i.e., for larger angles. In agreement with this prediction, the experimental data of Fig. 2 show that $T_{\rm irr}$ increases with the angle, i.e., decreases with $B_{\rm eff}$. The solid lines in Fig. 2 are fits to Eq. (4). From this fit we get $C\simeq 0.0005$. However, a reasonable estimate of $C\simeq\sqrt{[\beta_m Gi/c_L^4 H_{c2}(0)]}$ yields $C\simeq 0.01$, where we take $H_{c2}(0)=5\times10^6$ G, $c_L=0.1$, $Gi=0.01$, and $\beta_m=5.6$.[5] Also, Yeh *et al.* showed that the onset of irreversibility occurs above the melting temperature (Ref. 28, Fig. 4). In addition, the important effect of the frequency (see Fig. 3) is not included in Eq. (4).

We discuss now another possibility for the onset of the irreversibility, namely, pinning in the vortex liquid (for a discussion see Chap. VI in Blatter *et al.*[5] and references therein). Any fluctuation in the vortex structure in the liquid state has to be averaged over the characteristic time scale for pinning $t_{\rm pin}$. In the absence of viscosity the only fluctuations in the liquid state are thermal fluctuations, which have a characteristic time $t_{\rm th}\ll t_{\rm pin}$. (As shown in Ref. 5, $t_{\rm pin}/t_{\rm th}\propto j_0/j_c$, where j_0 is the depairing current.) Thus, such a liquid is always unpinned. The situation is different for a liquid with finite viscosity. In this case there exists another type of excitations in the vortex structure, i.e., *plastic* deformations with a characteristic time scale $t_{\rm pl}$. The energy barrier, corresponding to plastic deformation is shown to be[5,12]

$$U_{\rm pl}\simeq\gamma\varepsilon\varepsilon_0 a_0\simeq\gamma\left(\frac{H_{c2}}{4Gi}\right)^{1/2}(T_c-T)B^{-1/2}, \tag{5}$$

where γ is a coefficient of the order of unity. The corresponding characteristic time scale is

$$t_{\rm pl}\sim t_{\rm th}\exp(U_{\rm pl}/T). \tag{6}$$

Thus, depending on the viscosity, $t_{\rm pl}$ can be smaller or larger than $t_{\rm pin}$. In the latter case, after averaging over a time $t_{\rm pin}$, the vortex structure remains distorted and such a liquid shows irreversible magnetic behavior. Thus, on the time scale of $t_{\rm pin}$ the distorted vortex structure is pinned. The crossover between pinned and unpinned liquid occurs at temperature T_k where the characteristic relaxation time for pinning $t_{\rm pin}(T)$ becomes comparable to that for plastic motion $t_{\rm pl}(T)$. Thus, using Eqs. (5) and (6) we obtain

$$T_k=\frac{T_c}{1+(1/\gamma)[4Gi/H_{c2}(0)]^{1/2}\ln(t_{\rm pin}/t_{\rm th})\sqrt{B}}. \tag{7}$$

Finally, using the anisotropic scaling[49] we may rewrite Eq. (7) for $f_{\rm pin}<f<f_{\rm th}$ as

$$T_{\rm irr}(\theta)=T_k(\theta)=\frac{T_c}{1+(1/\gamma)[4Gi/H_{c2}(0)]^{1/2}\ln(f_{\rm th}/f)\sqrt{B\varepsilon_\theta}}$$
$$\equiv\frac{T_c}{1+A\sqrt{\varepsilon_\theta B}}, \tag{8}$$

with $f_{\rm th}\equiv 1/t_{\rm th}$ and $f_{\rm pin}\equiv 1/t_{\rm pin}$. Note the apparent similarity with the expression for the melting temperature, Eq. (4). The numerical estimate for

$$A=\frac{1}{\gamma}\left(\frac{4Gi}{H_{c2}(0)}\right)^{1/2}\ln(f_{\rm th}/f)$$

gives $A\simeq 10^{-4}\ln(f_{\rm th}/f)/\gamma$. This is in agreement with the value found from the fit (solid line in Fig. 2) for $H_{c2}(0)=5\times10^6$ G, $Gi=0.01$, $f_{\rm th}\sim10^{10}$ Hz, and $\gamma\simeq 4$.

To further confirm that in our YBCO films the most probable physical mechanism for the onset of irreversibility is a dynamic crossover from unpinned to pinned vortex liquid we discuss now the frequency dependence of $T_{\rm irr}$. Equation (8) has a clear prediction for the frequency dependence of $T_{\rm irr}$. To see it directly we may simplify it by using the experimentally determined value of the fit parameter $A\simeq 0.0005$. This small value allows us to expand Eq. (8) (for not too large fields) as

$$T_k\simeq T_c\left[1-\frac{1}{\gamma}\left(\frac{4Gi}{H_{c2}(0)}\right)^{1/2}\ln(f_{\rm th}/f)\sqrt{\varepsilon_\theta B}\right], \tag{9}$$

which results in a linear dependence of $T_{\rm irr}$ upon $\ln(f)$ with a slope

$$S\equiv\partial T_{\rm irr}/\partial\ln(f)\simeq\frac{T_c}{\gamma}\left(\frac{4Gi}{H_{c2}(0)}\right)^{1/2}\sqrt{\varepsilon_\theta B}$$
$$=T_c A\sqrt{\varepsilon_\theta B}\ln(f/f_{\rm th}).$$

Note that the slope is proportional to $\sqrt{B}$. This is indeed confirmed by the experimental data, as is demonstrated by the solid lines in Fig. 3. From this fit we get $S/\sqrt{B}=0.004$ and we can independently verify the parameter A appearing in Eq. (8), $A=S/[T_c\sqrt{\varepsilon_\theta B}\ln(f/f_{\rm th})]=0.0008$, which is in an agreement with the value obtained above.

We note that the approximated expression for the frequency dependence of $T_{\rm irr}$, Eq. (9), is valid in the whole experimentally accessible range of magnetic field since Eq. (8) predicts a *maximum* in the slope S at $B_{\max}=(A\sqrt{\varepsilon_\theta})^{-2}\approx 400$ T for the experimental parameters. This value is, of course, beyond the experimental limits and, probably, even exceeds H_{c2}.

Another support for the onset of the irreversibility in a vortex liquid is the ac field amplitude dependence of the IRL. In both thermal-activated (TAFF) and pure flux-flow (FF) regimes the *I-V* curves are linear and the onset of the third harmonic is due to a change in the slope (from $\rho_{\rm FF}$ to $\rho_{\rm TAFF}$). In this case we expect the amplitude dependence for this onset. Contrary, at the melting transition the onset of irreversibility is sharp and is not expected to depend upon

the amplitute of the ac field. In our experiments we find a pronounced amplitude dependence of the IRL, thus confirming the above scenario.

B. Irradiated YBCO films

For the irradiated films the situation is quite different. The models for $T_{irr}(\theta)$ in unirradiated films cannot explain the experimental features exhibited in Figs. 4 and 5, in particular the increase in T_{irr} in the vicinity of $\theta=0$. Such a discrepancy can only be due to the angular anisotropy introduced by columnar defects, i.e., the angle-dependent pinning strength. It was shown, both theoretically[5,30] and experimentally,[37] that for a magnetic field oriented along the defects the irreversibility line is shifted upward with respect to the unirradiated system. Thus, our results in Fig. 4 suggest that the measured $T_{irr}(\theta)$ is a superposition of the angular variation of T_{irr} in unirradiated film (denoted in this section as T_{irr}^{REF}) and the anisotropic enhancement of the pinning strength due to irradiation.

We can estimate the latter contribution by employing the concept of a "trapping angle" θ_t, the angle between the external field and the defects at which vortices start to be partially trapped by columnar tracks. (For a schematic description, see Fig. 43 in Blatter *et al.*[5]) as we show in the Appendix,

$$\tan(\theta_t)\approx\sqrt{2\varepsilon_r/\varepsilon_l}, \tag{10}$$

where $\varepsilon_r(T)$ is the trapping potential of a columnar defect and ε_l is the line tension. In the experiment we cool down at a fixed θ, and the onset of irreversibility must occur when $\theta=\theta_t(T)$, provided that the temperature is still larger than $T_{irr}^{REF}(\theta)$. Otherwise, the onset occurs at T_{irr}^{REF}. This defines the condition for the irreversibility temperature T_{irr} for angles $\theta\leq\theta_c\equiv\theta_t(T_{irr}^{REF}(\theta_t))\simeq 50°$ in our case:

$$\tan(\theta)=\tan[\theta_t(T_{irr})]\approx\sqrt{2\varepsilon_r/\varepsilon_l}. \tag{11}$$

At high temperatures $\varepsilon_r(T)\propto\exp(-T/\tilde{T}_{dp}^r)$, where $\tilde{T}_{dp}^r$ is the depinning energy.[5] Thus, we can write for T_{irr}

$$T_{irr}(\theta)=\begin{cases} T_{irr}^{REF}(\theta)-D\ln[C|\tan(\theta t)|], & \theta\leq\theta_c, \\ T_{irr}^{REF}(\theta), & \theta>\theta_c, \end{cases} \tag{12}$$

where D and C are constants. This expression is in an agreement with our results shown in Fig. 4 (solid line). We note, however, some discrepancy in the vicinity of $\theta=0$, where we find quite weak dependence of T_{irr} on angle. We explain this deviation by considering the influence of relaxation, which, in the case of parallel defects, depends on angle. The relaxation rate is maximal, when vortices are aligned along the defects, and retains its normal "background" value for perpendicular direction.[52] A vortex, captured by a defect, can nucleate a double kink which slides out resulting in a displacement of a vortex on a neighboring column. In our irradiated samples the defect lattice is very dense (the matching field $B_\phi=4$ T, i.e., distance between columns $d\approx 220$ Å) and such a double-kink nucleation is an easy process. Thus, the irreversibility temperature should be shifted down around $\theta=0$ as compared to the "ideal," nonrelaxed value, Eq. (12). This explains the reduction in T_{irr} in Fig. 4.

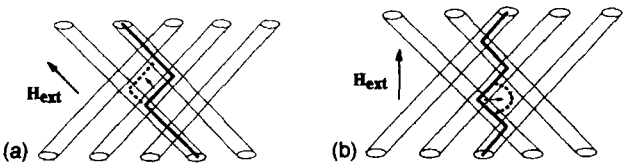

FIG. 6. Schematic description of a possible depinning modes of a vortex line in the case of crossed columnar defects: (a) magnetic field is directed along $\theta=45°$; (b) magnetic field is along $\theta=0$.

We may now conclude that in irradiated films, for angles less than the critical angle θ_c, the irreversibility line is determined by the *trapping angle* θ_t. The Bose-glass transition can probably only be found for small angles within the lock-in angle $\theta_L\leq 10°$. This conclusion is also indirectly confirmed in Ref. 53.

As was pointed out in the Introduction, crossed defects should hinder the relaxation due to forced entanglement of vortices. Thus, the irreversibility temperature is expected to be closer to that predicted by Eq. (12). Figure 5 shows a good agreement of the experimental data with Eq. (12) (solid line). To explain why defects crossed at large angle act collectively and force unidirectional magnetic anisotropy, we follow here the approach outlined in Ref. 41, and extend that description to account for arbitrary orientation of the external field with respect to the crossed columnar defects and to the c axis. In Ref. 41 the authors consider the possible motion of vortices in a "forest" of crossed defects for field oriented along the c axis. In our case of a dense lattice we may exclude from consideration free kink sliding and consider only depinning from the intersections. We sketch in Fig. 6 the two limiting situations: (a) the external field is parallel to one subsystem of the columnar defects ($\theta=45°$) and (b) the external field is oriented along the c axis, between crossed columns ($\theta=0$). In case (a), Fig. 6(a), vortices can depin just by nucleation the single kinks which are sliding from intersection to intersection or by nucleation of superkinks, resulting in a kind of motion, similar to a variable-range hopping. This type of thermally assisted vortex depinning does not cost any additional energy on vortex bending. Another situation arises for field along the c axis, Fig. 6(b). Now vortices can depin *only* via nucleation of multiple half-loops, which characteristic size depends upon current density. This results in an additional barrier for vortex depinning, which even diverges at zero current.[5] As a result, the relaxation rate is anisotropic; i.e., it is suppressed when the external field is oriented along the mid-direction between the two subsystems of the crossed columnar defects. This is just opposite to a situation in uniformly irradiated samples.

V. CONCLUSIONS

We presented angle-resolved measurements of the irreversibility temperature in unirradiated $YBa_2Cu_3O_{7-\delta}$ film and in two films with columnar defects, induced by 5.8-GeV Pb-ion irradiation, either parallel to the c axis or "crossed" in $\theta=\pm 45°$. We find that in the unirradiated film the transition from irreversible to reversible state occurs *above the melting line* and marks the *crossover from a pinned to an unpinned vortex liquid*. In irradiated films, within the critical

angle $\theta_c \simeq 50°$, the irreversibility line is determined by the temperature-dependent *trapping angle*. For larger angles T_{irr} is determined by the intrinsic anisotropy via the effective field. The formulas for $T_{irr}(\theta)$ for both unirradiated and irradiated films are given. We also discuss the possible influence of anisotropic enhancement in relaxation rate which leads to a smearing of the expected cusp at $\theta=0$ in the $T_{irr}(\theta)$ curve in the uniformly irradiated film. Finally, we demonstrate the collective action of crossed columnar defects, which can lead to suppression of relaxation and enhancement of pinning strength along the mid direction.

ACKNOWLEDGMENTS

We are grateful to V. Vinokur, L. Burlachkov, and P. Kes for illuminating comments. We thank S. Bouffard for help with Pb irradiation at GANIL, Caen (France). This research was supported in part by the Israeli Science Foundation administered by the Israeli Academy of Science and Humanities and the Heinrich Hertz Minerva Center for High Temperature Superconductivity, and in part by the DG XII, Commission of the European Communities, and the Israeli Ministry of Science and the Arts (MOSA). A.S. and R.P. acknowledge a support from the Israeli-France cooperation program AFIRST. R.P. acknowledges a support from the Clore Foudations and the hospitality of LSI at Ecole Polytechnique during part of this research.

APPENDIX

We describe here the derivation of our Eq. (10), which differs slightly from the analogous Eq. (9.173) of Blatter *et al.*[5] We derive it using exactly the same approach (and notions) as in Ref. 5, but in view of the experimental situation avoid the assumption of small angles, which allows Blatter *et al.* to approximate $\tan(\theta) \approx \sin(\theta) \approx \theta$. In order to estimate the trapping angle one has to optimize the energy change due to the vortex trapping by columnar defects. This energy is written as[5]

$$\varepsilon(r,\theta)=\varepsilon_l\left\{r+\left[d^2+\left(\frac{d}{\tan(\theta)}-r\right)^2\right]-\frac{d}{\sin(\theta)}\right\}-r\varepsilon_r, \tag{A1}$$

where $r(\theta)$ is the length of the vortex segment trapped by a defect, d is the distance between the columns, ε_l is the line tension, and ε_r is the trapping potential of the defects. The variation of Eq. (A1) with respect to r at fixed angle θ defines the angular dependence of $r(\theta)$. The trapping angle θ_t can be found by solving the equation $r(\theta_t)=0$. This results in

$$\tan(\theta_t)=\frac{\sqrt{\varepsilon_r(2\varepsilon_l-\varepsilon_r)}}{(\varepsilon_l-\varepsilon_r)}, \tag{A2}$$

which, at sufficiently small ε_r, can be approximated as

$$\tan(\theta_t)=\sqrt{\frac{2\varepsilon_r}{\varepsilon_l}}+O(\varepsilon_r^{3/2}). \tag{A3}$$

Apparently, at very small angles we recover the original result of Ref. 5. In the paper, for the sake of simplicity, we use Eq. (A3) instead of the full Eq. (A2). However, as noted above we cannot limit ourselves to small angles and, generally speaking, the trapping angle may be quite large ($\theta_t \approx 40°$ in our case). The error due to use of Eq. (A3) can be estimated as follows: At $\theta \approx 40°$ Eq. (A2) gives $\varepsilon_r/\varepsilon_l \simeq 0.24$, whereas Eq. (A3) gives $\varepsilon_r/\varepsilon_l \simeq 0.35$, which is suitable for our implication of Eq. (A3), since we consider exponential decrease of ε_r. Also, as shown in Ref. 5 in a system with anisotropy ε, the trapping angle is enlarged by a factor of $1/\varepsilon$.

*Permanent address: Laboratoire EPM Matformag, CNRS BP166, 38042 Grenoble Cedex, France

[1] K. A. Müller, M. Takashige, and J. G. Bednorz, Phys. Rev. Lett. **58**, 1143 (1987).
[2] Y. Yeshurun and A. P. Malozemoff, Phys. Rev. Lett. **60**, 2202 (1988).
[3] E. H. Brandt, Physica B **169**, 91 (1991); Rep. Prog. Phys. **58**, 1465 (1995); Phys. Rev. Lett. **63**, 1106 (1989).
[4] E. H. Brandt, Rep. Prog. Phys. **58**, 1465 (1995).
[5] G. Blatter, M. V. Feigelman, V. B. Geshkenbein, A. I. Larkin, and V. M. Vinokur, Rev. Mod. Phys. **66**, 1125 (1994).
[6] T. Matsushita, A. Matsuda, and K. Yanagi, Physica C **213**, 477 (1993); T. Matsushita, Physica C **214**, 100 (1993).
[7] D. Majer, E. Zeldov, and M. Konczykowski, Phys. Rev. Lett. **75**, 1166 (1995).
[8] E. Zeldov, D. Majer, M. Konczykowski, V. B. Geshkenbein, V. M. Vinokur, and H. Shtrikman, Nature **375**, 373 (1995).
[9] E. Zeldov, A. I. Larkin, V. B. Geshkenbein, M. Konczykowski, D. Majer, B. Khaikovich, V. M. Vinokur, and H. Shtrikman, Phys. Rev. Lett. **73**, 1428 (1994).
[10] V. M. Vinokur, M. V. Feigel'man, V. B. Geshkenbein, and A. I. Larkin, Phys. Rev. Lett. **65**, 259 (1990).
[11] M. V. Feigel'man, V. B. Geshkenbein, and A. I. Larkin, Physica C **167**, 177 (1990).
[12] V. Geshkenbein, A. Larkin, M. Feigel'man, and V. Vinokur, Physica C **162-164**, 239 (1989).
[13] T. T. M. Palstra, B. Batlogg, R. B. van Dover, L. F. Schneemeyer, and J. V. Waszczak, Phys. Rev. B **41**, 6621 (1990).
[14] A. Neminsky, J. Dumas, C. Schlenker, H. Karl, and B. Stritzker, Physica C **235-240**, 2907 (1994).
[15] T. K. Worthington, M. P. A. Fisher, D. A. Huse, J. Toner, A. D. Marwick, T. Zabel, C. A. Feild, and F. Holtzberg, Phys. Rev. B **46**, 11 854 (1992).
[16] A. Houghton, R. A. Pelcovits, and S. Sudbø, Phys. Rev. B **40**, 6763 (1989); H. Pastoriza, M. F. Coffman, A. Arribére, and F. de la Cruz, Phys. Rev. Lett. **72**, 2951 (1994).
[17] M. V. Feigel'man, Physica A **168**, 319 (1990).
[18] R. de Andrade, Jr. and Oscar F. de Lima, Phys. Rev. B **51**, 9383 (1995).
[19] O. B. Hyun, H. Suhara, T. Nabatame, S. Koike, and I. Hirabayashi, Solid State Commun. **95**, 519 (1995).
[20] R. G. Beck, D. E. Farrell, J. P. Rice, D. M. Ginsberg, and V. G. Kogan, Phys. Rev. Lett. **68**, 1594 (1992).
[21] W. K. Kwok, S. Fleshler, U. Welp, V. M. Vinokur, J. Downey, G. W. Crabtree, and M. M. Miller, Phys. Rev. Lett. **69**, 3370 (1992); W. K. Kwok, J. A. Fendrich, C. J. van der Beek, and G. W. Crabtree, *ibid.* **73**, 2614 (1994).

[22] M. P. A. Fisher, Phys. Rev. Lett. **62**, 1416 (1989); D. S. Fisher, M. P. A. Fisher, and D. A. Huse, Phys. Rev. B **43**, 130 (1991); A. T. Dorsey, M. Huang, and M. P. A. Fisher, *ibid.* **45**, 523 (1992).

[23] J. Deak, M. McElfresh, J. R. Clem, Z. Hao, M. Konczykowski, R. Muenchausen, S. Foltyn, and R. Dye, Phys. Rev. B **49**, 6270 (1994); J. Deak, M. McElfresh, R. Muenchausen, S. Foltyn, and R. Dye, *ibid.* **48**, 1337 (1993); J. Deak, M. McElfresh, J. R. Clem, Z. Hao, M. Konczykowski, R. Muenchausen, and S. Foltyn, *ibid.* **47**, 8377 (1993).

[24] M. Giura, S. Sarti, E. Silva, R. Fastampa, F. Murtas, R. Marcon, H. Adrian, and P. Wagner, Phys. Rev. B **50**, 12 920 (1994); F. Murtas, R. Fastampa, M. Giura, R. Marcon, S. Sarti, and E. Silva, Physica C **235-240**, 2677 (1994).

[25] H. Obara, A. Sawa, and S. Kosaka, Phys. Rev. B **49**, 1224 (1994).

[26] X. G. Qiu, B. Wuyts, M. Maenhoudt, V. V. Moshchalkov, and Y. Bruynseraede, Phys. Rev. B **52**, 559 (1995).

[27] T. R. Chien, T. W. Jing, N. P. Ong, and Z. Z. Wang, Phys. Rev. Lett. **66**, 3075 (1991).

[28] N. C. Yeh, W. Jiang, D. S. Reed, U. Kriplani, F. Holtzberg, M. Koncykowski, C. C. Tsuei, and C. C. Chi, Physica A **200**, 374 (1993).

[29] M. Konczykowski, L. Burlachkov, Y. Yeshurun, and F. Holtzberg, Phys. Rev. B **43**, 13 707 (1991); Physica C **194**, 155 (1992).

[30] M. P. A. Fisher, P. B. Weichman, G. Grinstein, and D. S. Fisher, Phys. Rev. B **40**, 546 (1989); D. R. Nelson and V. M. Vinokur, Phys. Rev. Lett. **68**, 2398 (1992); Phys. Rev. B **48**, 13 060 (1993).

[31] C. J. van der Beek, M. Konczykowski, V. M. Vinokur, T. W. Li, P. H. Kes, and G. W. Crabtree, Phys. Rev. Lett. **74**, 1214 (1995); C. J. van der Beek, M. Konczykowski, V. M. Vinokur, G. W. Crabtree, T. W. Li, and P. H. Kes, Phys. Rev. B **51**, 15 492 (1995).

[32] W. Jiang, N.-C. Yeh, D. S. Reed, U. Kriplani, D. A. Beam, M. Konczykowski, and T. A. Tombrello, Phys. Rev. Lett. **72**, 550 (1994).

[33] A. I. Larkin and V. M. Vinokur, Phys. Rev. Lett. **75**, 4666 (1995).

[34] R. C. Budhani, W. L. Holstein, and M. Suenaga, Phys. Rev. Lett. **72**, 566 (1994).

[35] M. Konczykowski, N. Chikumoto, V. M. Vinokur, and M. V. Feigelman, Phys. Rev. B **51**, 3957 (1995).

[36] A. Ruyter, V. Hardy, C. Goupil, J. Provost, D. Groult, and C. Simon, Physica C **235-240**, 2663 (1994).

[37] L. Krusin-Elbaum, L. Civale, G. Blatter, A. D. Marwick, F. Holtzberg, and C. Feild, Phys. Rev. Lett. **72**, 1914 (1994).

[38] D. Zech, S. L. Lee, H. Keller, G. Blatter, B. Janossy, P. H. Kes, T. W. Li, and A. A. Menovsky, Phys. Rev. B **52**, 6913 (1995).

[39] T. Hwa, P. Le Doussal, D. R. Nelson, and V. M. Vinokur, Phys. Rev. Lett. **71**, 3545 (1993).

[40] L. Civale, L. Krusin-Elbaum, J. R. Thompson, R. Wheeler, A. D. Marwick, M. A. Kirk, Y. R. Sun, F. Holtzberg, and C. Feild, Phys. Rev. B **50**, 4104 (1994).

[41] T. Schuster, H. Kuhn, M. V. Indenbom, M. Leghissa, M. Kraus, and M. Konczykowski, Phys. Rev. B **51**, 16 358 (1995); T. Schuster, H. Kuhn, M. V. Indenbom, G. Kreiselmeyer, M. Leghissa, and S. Klaumunzer, *ibid.* **53**, 2257 (1996).

[42] Wen Jiang (unpublished).

[43] E. Yacoby, A. Shaulov, Y. Yeshurun, M. Konczykowski, and F. Rullier-Albenque, Physica C **199**, 15 (1992).

[44] Y. Wolfus, Y. Abulafia, L. Klein, V. A. Larkin, A. Shaulov, Y. Yeshurun, M. Konczykowski, and M. Feigel'man, Physica C **224**, 213 (1994).

[45] R. Prozorov, A. Tsameret, Y. Yeshurun, G. Koren, M. Konczykowski, and S. Bouffard, Physica C **235-240**, 3063 (1994); Y. Wolfus, R. Prozorov, Y. Yeshurun, A. Shaulov, Y. Abulafia, A. Tsameret, and K. Runge, *ibid.* **235-240**, 2719 (1994).

[46] Y. Iye, T. Terashima, and Y. Bando, Physics C **177**, 393 (1991).

[47] G. Koren, E. Polturak, B. Fisher, D. Cohen, and G. Kimel, Appl. Phys. Lett. **50**, 2330 (1988).

[48] C. P. Bean, Phys. Rev. Lett. **8**, 250 (1962); Y. B. Kim, C. F. Hempstead, and A. R. Strand, Phys. Rev. **129**, 528 (1963); P. W. Anderson and Y. B. Kim, Rev. Mod. Phys. **36**, 39 (1964); A. M. Campbell and J. E. Evetts, *Critical Currents in Superconductors* (Taylor & Francis Ltd., London, 1972); H. Ullmaier, *Irreversible Properties of Type-II Superconductors* (Springer-Verlag, Berlin, 1975).

[49] G. Blatter, V. B. Geshkenbein, and A. L. Larkin, Phys. Rev. Lett. **68**, 875 (1992).

[50] Z. Hao and J. R. Clem, Phys. Rev. Lett. **71**, 301 (1993); G. Blatter, V. B. Geshkenbein, and A. L. Larkin, Phys. Rev. Lett. **71**, 302 (1993).

[51] J. Kötzler, G. Nakielski, M. Baumann, R. Behr, F. Goerke, and E. H. Brandt, Phys. Rev. B **50**, 3384 (1994).

[52] M. Konczykowski, Physica C **235-240**, 197 (1994); A. Kramer and M. L. Kulic, Phys. Rev. B **50**, 9484 (1994).

[53] A. V. Samoilov, M. V. Feigel'man, M. Konczykowski, and F. Holtzberg, Phys. Rev. Lett. **76**, 2798 (1996).

LT 21

Proceedings of the 21st International Conference on Low Temperature Physics
Prague, August 8-14, 1996
Part S3 - Superconductivity 2: HTS - Vortices (experiment)

Observation of Defect-Independent ab-Plane Vortex Dynamics in $YBa_2Cu_3O_7$ Single Crystals with the Third Harmonic Transmittivity Measurements*

W. Jiang[a], N.-C. Yeh[a], C.-C. Fu[a], B. Schmidt[b], and M. Konczykowski[b]

[a] Department of Physics, California Institute of Technology, Pasadena, CA 91125, U.S.A.
[b] Laboratoire des Solides Irradies, Ecole Polytechnique, 91128 Palaiseau, FRANCE

Anisotropic vortex dynamics of $YBa_2Cu_3O_7$ single crystals with heavy-ion induced parallel and canted columnar defects are investigated and compared with that of the as-grown single crystals. Novel vortex dynamics are observed when magnetic field is applied close to the ab-plane ($\vec{H} \perp \hat{c}$). The amplitude of the third harmonic transmittivity exhibits a secondary peak at lower temperatures in addition to a sharper peak at higher temperatures. The possible relevance of this observation to the theoretical model of "smectic crystal" to vortex-liquid phase transitions is discussed.

1. INTRODUCTION

In the vortex system of high-temperature superconductors(HTSs) with correlated columnar defects, there exist two types of anisotropies, one arises from the vortex pinning by columnar defects extended, the other from the intrinsic vortex pinning due to the periodic structure of the copper-oxide layers (ab-plane). A Bose-glass model[1] and a splayed-glass model[2] have been predicted for YBCO single crstyals with parallel and canted columnar defects, respectively, for applied magnetic fields nearly parallel to the c-axis of the sample. Experimental evidences supporting these models have been provided by both dc and ac electrical transport measurements and critical scaling analysis[3].

Recently Balents and Nelson have proposed an anisotropic vortex phase diagram for vortices pinned by the periodic layered structure[4]. According to this model, upon cooling, the vortex liquid first condenses into a smectic liquid crystal phase through an XY-like transition, and subsequently freezes into a more ordered vortex crystal/glass phase at lower temperatures. The smectic liquid crystal phase is found to be stable upon strong point disorder[4].

In this work, we present our experimental observations of ab-plane vortex dynamics in YBCO single crystals with the third harmonic transmittivity($T' = 1 + \mu_0\chi', T'' = \mu_0\chi''$) measurements. The results will be discussed in the context of the Balents-Nelson theory.

2. EXPERIMENTAL

The experimental technique involves using a miniature Hall probe under the sample and in the center of an ac excitation coil to pick up the magnetic induction of the sample. The details of the setup have been described elsewhere[5]. A rotatable dc magnet enables the variation of the angle (θ) between the c-axis of the sample and the dc magnetic field. Two samples have been investigated, one with columnar defects parallel to the c-axis and the other with two sets of columnar defects canted relative to the c-axis by $\pm 7.5°$. The columnar defects are created by Pb ion irradiations at GANIL Cean, France. The matching fields for both samples are 6.2 kG. All the measurements are field-cooled measurements.

3. RESULT & DISCUSSION

The amplitude of the third harmonic transmittivity ($|T_{H3}|$) as a function of θ for the sample with parallel columnar defects is plotted in Fig.1(a) and Fig.1(b), respectively. The anisotropic vortex response is manifested by the distinct difference in the $|T_{H3}|$ signals for the field aligned nearly along the c-axis ($\theta = 0°$) from that nearly in the ab-plane ($\theta = \pm 90°$). Similar data are obtained for the sample with canted columnar defects except that these two special angular regions where distinct features occur are more confined. For comparison, T_{H3} -vs.- T for $\vec{H} \parallel \hat{c}$ and $\vec{H} \perp \hat{c}$ are shown in Fig.2 for both samples. In contrast to a single peak in $|T_{H3}|$ for $\vec{H} \parallel \hat{c}$, a broad secondary peak appears at lower temperatures for $\vec{H} \perp \hat{c}$.

Such a secondary peak in $|T_{H3}|$ has been observed earlier in twinned as-grown YBCO crystals for $\vec{H} \perp \hat{c}$ as reported in Ref.5. The explanation provided in Ref.5 was based on the concept of ac field penetration such that increasing ac excitation currents reduce the strong-pinning Campbell regime, thereby enhancing the nonlinear response of the third-harmonic signals. This concept is also consistent with our observation in this work. However, questions remain whether this secondary peak reflects the thermal fluctuation effects near a phase transition or a crossover. From our previous transport measurements, an XY-like vortex phase transition has been observed for

* Jointly supported by NSF grant #9401315, ONR grant #N00014-91-J-1556 , NASA, and Packard fundation

$\vec{H} \perp \hat{c}$ at temperatures near the onset of the first peak in $|T_{H3}|$[3]. Therefore we propose, as illustrated in Fig.3(a), that the onset of the first peak at T_{IS} of $|T_{H3}|$ is related to a second-order phase transition from a vortex liquid to a smectic liquid crystal, as predicted by Balents and Nelson's theory, and that of the second peak at T_{IX} is indicative of a crossover from the smectic phase to a vortex crystal/glass phase.

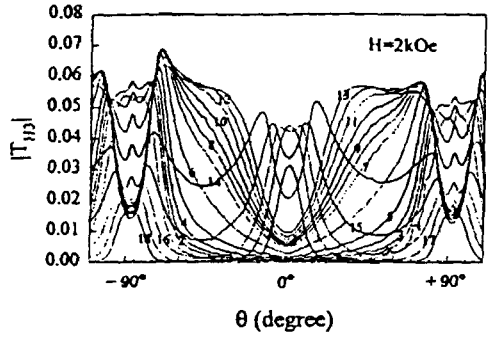

Fig.1: The amplitude of the third harmonic transmittivity ($|T_{H3}|$) versus the angle (θ) between the applied magnetic field ($\vec{H}$) and the c-axis of a YBCO single crystal with c-axis parallel columnar defects. The curves are numbered in the order of increasing temperatures from 82.0 K to 91.5 K.

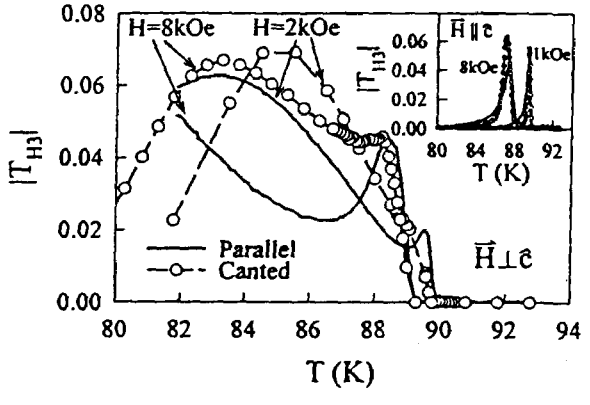

Fig.2: The third harmonic transmittivity $|T_{H3}|$ as a function of temperature for $\vec{H} \perp \hat{c}$ (main frame), and that for $\vec{H} \parallel \hat{c}$ (inset).

Further support for this scenario comes from the dependence of $|T_{H3}|$ on the dc magnetic field (H) and the frequency(f) at reduced ac excitation currents: According to Balents and Nelson's theory, the smectic phase can exist over a broader temperature range if the pinning provided by the point disorder is stronger. Since columnar defects provide strong point-like pinning to the vortices in the ab-plane, and the pinning strength increases with increasing field, the temperature interval between the two peaks in $|T_{H3}|$ increases with the increasing H as shown in Fig.3, suggesting that the smectic phase extends over a broad temperature range at hogher fields. Furthermore, as shown in Fig.3(b), the elasticity of flux lines increases with increasing excitation frequency f, giving rise to a more stable and therefore broader crystal/glass phase. Finally, the fact that similar behavior exists in twinned as-grown crystals for $\vec{H} \parallel \hat{c}$ also suggests that twin boundaries provide another source of periodic pinning potential. However, the same picture may not be applicable to a highly twinned sample in which case the periodic pinning potential is only local and the overall vortex dynamics may be complicated by the random distribution of domains of different twin plane orientations.

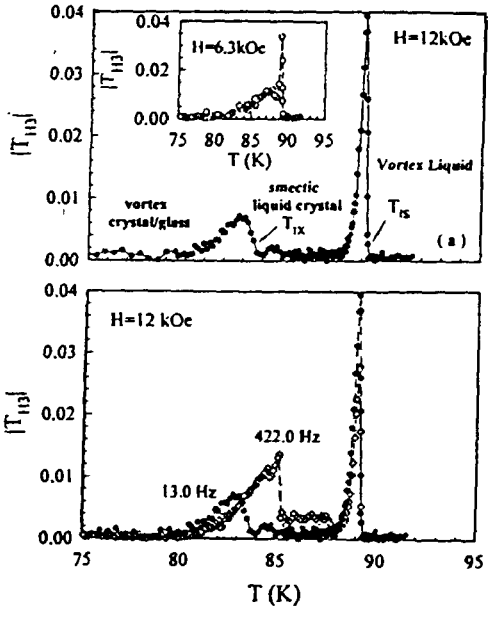

Fig.3: The (a) dc magnetic field (H) dependence and (b) ac excitation frequency (f) dependence of the amplitude of the third harmonic transmittivity $|T_{H3}|$.

4. SUMMARY

A secondary peak feature at low temperatures is observed in the third harmonic transmittivity in YBCO single crystals with parallel and canted columnar defects. The experimental observations can be qualitatively explained by Balents and Nelson's model which suggests the existence of a smectic to vortex liquid phase transition in the presence of a periodic pinning potential.

REFERENCES

[1] D. R. Nelson, and V. M. Vinokur, Phys. Rev. Lett. 68, 2398(1992); Phys. Rev. B. 48, 13060(1993).

[2] T. Hwa et al, Phys. Rev. Lett. 71, 3545(1993).

[3] N.-C. Yeh et al, Proceedings of ISS'94 and the references therein; D. S. Reed et al, Intern. J. of Mod. Phys. B, 1996 (in print).

[4] L. Balents and D. R. Nelson, Phys. Rev. Lett. 73, 2618(1994); Phys. Rev. B 52, 12951(1995).

[5] M. Konczykowski, F. Holtzberg and P. Lejay, Supercond. Sci. Tech., 4 S331(1991); M. Konczykowski et al, Physica A 200, 305(1993).